

# Investigation of Failure Modes of Fiber Reinforced Polymer Composite Flywheel Rotors for Energy Storage Systems

by

Miles Skinner

A thesis submitted in partial fulfillment of the requirements for the degree of

Doctor of Philosophy

Department of Mechanical Engineering  
University of Alberta

© Miles Skinner, 2022

## Abstract

High-velocity and long-lifetime operating conditions of modern high-speed energy storage flywheel rotors may create the necessary conditions for failure modes not included in current quasi-static failure analyses. The central hypothesis for this thesis research is that (i) viscoelastic effects and shear stress effects can cause creep rupture, matrix cracking, or hub-rim interfacial failure in composite flywheel rotors, and that (ii) these failure modes can be prevented employing an appropriate modeling approach in the flywheel energy storage system (FESS) design process. In this thesis, a computational algorithm based on an accepted analytical model was developed. This model progresses in two phases. First, the viscoelastic behavior of fiber reinforced polymer composite (FRPC) flywheel rotors was investigated by simulating a 10-year operational lifetime. The simulations indicate that viscoelastic effects are likely to reduce peak stresses in the FRPC material and the hub-rim interface while also increasing stress in the metallic hub. Second, flywheel rotors also experience a large number of acceleration/deceleration cycles, which raises concerns regarding the effects of shear stresses on flywheel rotor reliability. The computational models were used to describe the transient behavior of radial, circumferential, and shear stresses in FRPC flywheel rotors during constant power demands. This thesis discusses failure predictions using the maximum stress and Tsai-Wu failure criteria. The Tsai-Wu criterion predicted failure to occur at higher loadings compared to a maximum stress threshold. A strength ratio determined from the Tsai-Wu criterion indicates a changing peak stress location from the inner radius at the start of rotor acceleration to approximately the center of the rotor thickness at top speed. The results from this study indicate strong variability in the loading conditions, which may promote damage, crack initiation and crack propagation, and fatigue effects, posing possible risks to the long-term structural health of composite flywheel rotors.

Predicting the behavior of the flywheel rotor over the lifetime of the system requires a thorough understanding of the evolution of the composite material properties. To assess the viscoelastic behavior of the FRPC, an effective experimental test platform and methodology was developed to conduct elevated temperature tensile creep testing of FRPC tube specimens. Using this methodology, the creep compliance of a glass fiber reinforced polymer composite (GFRP) was measured at various elevated temperatures. Then a time-temperature superposition approach was applied to shift the compliance curves along the time axis to create a master curve. The resulting transverse master curve can accurately predict the material compliance over an approximate 67-year period. Additionally, the compliance values compare well with published values of other similar materials.

The findings from this thesis research provide evidence to conclude that viscoelasticity can significantly affect the reliability of flywheel rotors over an average 10-year operational lifetime. Shear stress, however, was found to be minimally impactful on the evolution of internal stresses, and, in isolation, is unlikely to lead to rotor failure. Finally, viscoelastic creep testing of a common GFRP composite proved successful and a compliance master curve was developed.

## Preface

Certain sections of this thesis document have been published previously by the author or will be published in peer reviewed journal papers. Following is a list describing the publication status of this research work.

- Chapter 2 has been published in *Energy Storage Flywheel Rotors – Mechanical Design* published in Encyclopedia volume 2 issue 1 pages 301-324.
- Chapter 3 has been published in *Effects of Viscoelasticity on the Stress Evolution of the Lifetime of Filament-Wound Composite Flywheel Rotors for Energy Storage* published in Applied Sciences volume 11 number 20 page 9544
- Chapter 4 has been prepared for submission to Applied Composite Materials (journal - Springer)

Chapter 5 has been partially published in Canadian International Conference on Composites (CANCOM 2022). This publication focused on the testing and data processing methodology, as well as validating the test platform performance. Table 5.1 clearly identifies which sections of this chapter were included or omitted from this publication.



## Acknowledgements

I would like to thank Dr. Pierre Mertiny for the opportunities and support that were afforded to me throughout the project. His unique styles of teaching and supervision helped me to develop and grow into the person and researcher I am today. The insistence on independence and self motivation forced me to learn to create my own research plans, set goals, and be self reliant. Through this I learned to ask meaningful questions and work through problems. To the rest of the committee, I would like to thank you as well for your support and guidance.

I would also like to acknowledge the support of the NSERC Energy Storage Technology Network which not only funded the flywheel energy storage system project but also goes through great effort to disseminate the content of this and many other energy storage projects to industries, law makers, and the public. Their efforts are truly invaluable to the development of the energy storage technology in Canada.

Finally, I'd like to thank my colleagues and family who have always supported me. To my family who, despite questioning my sanity after I moved from sunny San Diego to the frozen tundra that is Edmonton, never failed to believe in me. To the innumerable friends and colleagues, I met while here, I could not have completed this degree without you. Honestly, you are all wonderful people and I am better for having known you.

# Table of Contents

Abstract .....	ii
Preface.....	iv
Acknowledgements.....	v
List of Tables .....	ix
List of Figures.....	x
Nomenclature.....	xiii
1 Introduction.....	1
1.1 Knowledge Gap.....	2
1.2 Hypothesis and Thesis Objectives.....	3
1.3 References .....	3
2 Literature Review.....	5
2.1 Introduction .....	5
2.2 Applications and Performance .....	6
2.3 Manufacturing .....	7
2.3.1 Hub Construction .....	8
2.3.2 Rim Construction .....	8
2.3.3 Assembly.....	10
2.4 Analytical Modeling.....	11
2.4.1 Energy Storage and Power Capacity.....	11
2.4.2 Material Characterization.....	12
2.4.3 Quasi-static Analysis .....	19
2.4.4 Viscoelastic Analysis .....	22
2.4.5 Shear Stress.....	24
2.5 Failure Analysis.....	26
2.5.1 Failure Criteria .....	26
2.5.2 Maximum Stress Criterion.....	26
2.5.3 Tsai-Wu Criterion .....	27
2.5.4 Progressive Failure Analysis.....	28
2.6 Conclusions and Prospects.....	28
2.7 References .....	29

3	Viscoelastic Modeling .....	34
3.1	Introduction .....	34
3.2	Composite Flywheel Rotor Modeling .....	35
3.2.1	Analytical Model Description.....	35
3.2.2	Tsai-Wu Failure Criterion.....	37
3.2.3	Computational Methodology .....	38
3.3	Modeling Parameters.....	38
3.3.1	Materials .....	38
3.3.2	Flywheel Rotor Simulation Parameters .....	40
3.4	Results and Discussion.....	42
3.4.1	Algorithm Validation .....	43
3.4.2	Viscoelastic Behavior .....	43
3.5	Conclusions .....	53
3.6	References .....	55
4	Study of Acceleration-induced Shear Stresses .....	57
4.1	Introduction .....	57
4.2	Flywheel Stress Analysis .....	58
4.2.1	Radial and Shear Stress.....	58
4.2.2	Tsai-Wu Criteria .....	62
4.2.3	Computational Methodology .....	63
4.2.4	Simulation Parameters .....	63
4.3	Results and Discussion.....	66
4.3.1	Constant Power Demand and Supply .....	67
4.3.2	Flywheel Rotor Failure .....	71
4.4	Conclusion.....	74
4.5	References .....	74
5	Experimental Measurement of Viscoelastic Compliance .....	76
5.1	Introduction .....	76
5.2	Experimental Setup and Methodology.....	77
5.2.1	Specimens .....	77
5.2.2	Testing Equipment.....	79

5.2.3	Specimen Mounts.....	79
5.2.4	Heating Chamber .....	79
5.2.5	Instrumentation and Data Acquisition Equipment.....	79
5.2.6	Experimental Procedures .....	83
5.2.7	Data Reduction.....	84
5.3	Validation of Experimental Procedures .....	88
5.3.1	Applied Load and Temperature .....	88
5.3.2	Strain Measurements and Bending Effects .....	89
5.4	Results and Discussion.....	89
5.4.1	Quasi-Static Results .....	89
5.4.2	Viscoelastic Testing .....	92
5.5	Conclusion.....	101
5.6	References .....	102
6	Conclusions.....	104
7	References.....	107
8	Appendices.....	112
	Appendix I: Burnout Testing Results .....	112
	Appendix II Viscoelastic Test Platform and Sample Technical Drawings.....	113
	Appendix III.....	131
	Appendix IV: Position Test .....	137

## List of Tables

Table 2.1: General range of FESS performance characteristics. ....	6
Table 2.2: Shape factor values (k) for various flywheel rotor cross sections. ....	12
Table 3.1: Material properties for aluminum 7075-T6 [29] and viscoelastic equations for CFRP [30] used in the present study.....	39
Table 3.2: Directionally dependent strengths of CFRP and yield strength of aluminum used to find SR from the Tsai-Wu failure criterion.....	39
Table 3.3: Flywheel rotor rim dimensions, press-fit interference, and energy capacity.....	41
Table 3.4: Rotor peak stress values for interfacial stress, radial peak stress, and circumferential peak stress at 0, 0.5, 1, 5, and 10 years of continuous flywheel operation at limit velocity. ....	46
Table 3.5: Peak stress values at the hub-rim interface and radially and circumferentially in the CFRP rim, and peak SR values for the aluminum hub and the CFRP rim, at various times throughout the simulated one-year period.....	50
Table 4.1: Material properties for the aluminum 7075-T6 [22] and viscoelastic equations for CFRP [23] used in the present study.....	64
Table 4.2: Directionally dependent tensile strength of CFRP and yield strength of aluminum used to find SR from the Tsai Wu failure criterion. ....	64
Table 4.3: Flywheel rotor rim dimensions, press fit width, and energy capacity. ....	65
Table 5.1: List of sections in Chapter 5 detailing the inclusion in conference proceedings.....	76
Table 5.2: Material system and winding parameters used to create composite tubes [16-17]. ....	78
Table 5.3: Strain gauge sensor parameters [20-21]. ....	81
Table 5.4: Elastic modulus calculated from each experiment shown in Figure 5.1 and the average modulus for the material.....	91
Table 5.5: Treatment combinations table showing all the combinations of creep load and testing temperature.....	92
Table 5.6: Elastic modulus predicted by the master curve for the present composite at various times compared to the compliance for similar materials reported in literature. ....	100
Table 7.1: Fiber volume fraction results determined from the burn out tests.....	112

## List of Figures

Figure 2.1: Cut-away schematic of flywheel energy storage system for experimental research. Inset shows actual device [16]. .....	7
Figure 2.2: Composite flywheel rotor rim at the end of filament winding manufacturing process; (a) fiber payout eye and deposition head on winding machine carriage arm, (b) winding mandrel, and (c) completed aramid fiber/epoxy composite rim. ....	9
Figure 2.3: Thermal press-fit accomplished by cooling the aluminum hub with liquid nitrogen before pressing into the composite rims. ....	10
Figure 2.4: Time-temperature superposition experimental data, adopted from [65]. Data was collected from tensile tests for an FRP composite at various temperatures and shifted along the time axis to create a master curve for a reference temperature of 40°C. ....	17
Figure 2.5: Evolution of (a) radial and (b) circumferential stresses at different times of operation (0 to 10 years) of a flywheel rotor with an aluminum hub and carbon FRP composite rim due to viscoelastic stress relaxation [16]. ....	24
Figure 3.1: Simulated flywheel rotor showing dimensions of metallic hub and carbon fiber rim. The axis of rotation (AoR) is shown in blue. ....	41
Figure 3.2: Radial (a) and circumferential (b) stress distribution comparison between the current model and Tzeng et al. [13] for a two-rim press-fit CFRP flywheel rotor. ....	44
Figure 3.3: Radial (a) and circumferential (b) stress predictions for a flywheel rotor constructed of an aluminum hub and CFRP rim, after assembly (zero velocity), at startup, and at various times up to 10 years of continuous operation at the limit velocity of 24,250 rpm. ....	44
Figure 3.4: Normalized rotor peak stress for interfacial pressure, radial stress, and circumferential stress over time, in years, for continuous flywheel operation at limit velocity. Values are normalized by the corresponding stress at time $t = 0$ . ....	47
Figure 3.5: Strength ratio (SR) data for the flywheel rotor (a), and peak SR in the aluminum hub and CFRP rim at various times throughout the simulated lifetime (b). ....	48
Figure 3.6: Radial (a) and circumferential (b) stress results at each velocity on day 1. ....	49
Figure 3.7: SR graphs for all points along the flywheel rotor radius at each velocity on day 1. ....	50
Figure 3.8: Stress results normalized by their initial value on day 1 for (a) interfacial pressure, (b) peak radial tensile stress, and (c) peak circumferential stress in the CFRP rim, (d) peak SR in the aluminum hub, and (e) peak SR in the CFRP rim. ....	53
Figure 4.1: Diagram of simulated flywheel rotor showing dimensions of aluminum hub, CFRP rim, and the axis of rotation (AoR). ....	65
Figure 4.2: Comparison of shear stress calculated by the current model and those published by (a) Ha et al. [29] for radial, circumferential, axial stress, and (b) Salehian et al. [7] for shear stress. ....	66
Figure 4.3: (a, b) radial stress when accelerating and decelerating (c, d) circumferential stress when accelerating and decelerating, and (e) shear stress induced by a constant	

power supply or demand of 725 kW, and (f) SR for various times during the simulation.....	68
Figure 4.4: The (a) radial stress, (b) circumferential stress, (c) shear stress, and (d) SR for all five key points of interest at all velocities during the simulation. Stresses at the interface are reported for the hub outer surface and the CFRP inner surface. The results for accelerating and decelerating are sufficiently similar so only the acceleration results are provided. ....	69
Figure 4.5: SR predicted using the Tsai Wu criteria for (a) all points in the flywheel rotor at various time throughout the simulation and (b) for all velocities in the simulation at five key radii of interest. ....	71
Figure 4.6: Maximum SR and corresponding peak SR location given for all angular velocities. The time index of various key points is provided as well.....	73
Figure 5.1: Cross-sectional diagram of test specimen assembly (dimension in mm).....	78
Figure 5.2: Diagram of creep test setup with labeled components. Some horizontal spars in the support frame have been hidden to provide an unobstructed view of the specimen and load cell. ....	79
Figure 5.3: (a) Cross section of heating chamber and specimen, and (b) tensile machine showing specimen orientation (Insert: top-down view on specimen with strain gauges set to approximately 120° apart for viscoelastic experiments).....	80
Figure 5.4: (a) circuit diagram for sensors and data acquisition system. b,c) Circuit diagram for half and quarter bridge strain gauges. d) Circuit diagram for LC103B-5k load cell where the color of the leads correspond to those from the manufacturer. e) Pin labels for gauge conditioner connector. ....	83
Figure 5.5: Sensor data and best fit approximation used to characterize the load cell. ....	85
Figure 5.6: Schematic of data shifting procedure for compliance master curve. ....	87
Figure 5.7: Data for test equipment validation: (a) Specimen surface and chamber temperature for a 3-hour experiment, and (b) load cell reading for applied load. ....	88
Figure 5.8: (a) Difference between strain data from strain gauges (SG) due to bending stress (Insert: Arrow indicating specimen bending direction from off axis loading), and (b) sample creep strain data. ....	89
Figure 5.9: Strain-time results for glass fiber (GF) samples 08 and 09 collected during quasi-static testing. ....	90
Figure 5.10: Stress-strain results for glass fiber (GF) samples 08 and 09. Strain data was collected from strain gauges set up in either a quarter bridge or half bridge configuration. ....	91
Figure 5.11: Stress results from GF1 as a representative example of (a) stress vs time for the 40%TS creep load and all three experimental temperatures, and (b) detailed view of the stress variation in the first temperature and stress period from the same test.....	93
Figure 5.12: Temperature results from GF1 as a representative example of the heater temperature and sample surface temperature throughout a viscoelastic experiment. ....	94

Figure 5.13: Strain results from GF1 as a representative example of the strain vs time results for a viscoelastic experiment showing strain of all three strain gauges during each temperature step. ....	95
Figure 5.14: (a) Average strain results for the viscoelastic test shown in Figure 5.13. Creep data is plotted against absolute time. (b) Creep data with the recovery period removed and plotted against experimental time. ....	96
Figure 5.15: Thermal output measurements for composite samples. ....	97
Figure 5.16: Calculated compliance at each temperature for 40%TS. ....	98
Figure 5.17: Transverse compliance master curve for 40%TS. The unshifted compliance data (colored) is provided along the shifted curves (black). The solid line represents the best fit power law curve for the master curve. ....	99
Figure 7.1: Stress response from the same sample at constant temperature mounted in position A or position B. Position B is 180° rotation of position A. ....	137



## Nomenclature

Latin Symbol	Name
$A$	Viscoelastic master curve material constant
$A_k$	The area of the overlapping window, used for TTSP
$b$	Master curve initial elastic compliance
$a_T$	Temperature shift factor
$a_{te}$	Age shift factor
$C$	Winding circuits
$C_{ij}$	Material stiffness in the $ij$ direction
$E$	Elastic modulus
$E_K$	Kinetic energy
$E_{\text{hub}}$	Kinetic energy in the hub
$E_{\text{rim}}$	Kinetic energy in the rim
$F$	Tsai-Wu strength parameter
$G_k$	A data set recorded at $T_k$ , used for TTSP
$G_{r\theta}$	Shear modulus
$h$	Rotor height
$I_r$	Moment of inertia for the rotor
$I_{\text{hub}}$	Moment of inertia for the hub
$I_{\text{rim}}$	Moment of inertia for a rim
$k$	Hub cross section shape factor
$L_k$	The first point in $G_k$
$m$	Mass
$N$	Number of rims
$P$	Power
$Q$	Material stiffness
$R$	Failure ratio
$r$	Radius/radial direction
$r_o$	Outer radius
$r_i$	Inner radius
$S$	Compliance
$T$	Temperature
$T$	Torque
$T_k$	The temperature at which data set $G_k$ is recorded
$T_r$	Reference temperature
$T_g$	Glass transition temperature
$t$	Time
$t_{\text{cover}}$	Thickness of each complete filament wound layer
$t_e$	Master curve reference age
$U_k$	The last point in $G_k$
$u$	Displacement
$u_r$	Radial displacement
$V$	Voltage
$v$	Tangential stress
$z$	Axial direction
$ID$	Inner diameter

Tex	Linear density of a fiber tow
Tow	Number of fiber tows

Greek Symbol	Name
$\alpha$	Angular acceleration [rad/sec <sup>2</sup> ]
$\gamma$	Shear strain
$\varepsilon$	Normal strain
$\theta$	Circumferential/hoop direction
$\kappa$	Material constant
$\nu$	Poisson's ratio
$\rho$	Density
$\sigma$	Stress
$\varphi$	Material constant
$\tau$	Shear stress
$\omega$	Angular velocity [rad/sec]

# 1 Introduction

Flywheel energy storage systems (FESS) are a mechanical battery. Electrical energy is transformed into kinetic energy using an electrical machine, i.e., a motor, which physically accelerates a mass in the shape of a disk or cylinder, called the flywheel rotor, to high angular velocity. Energy is retrieved by reversing this process. Kinetic energy is converted to electrical energy again by decelerating the flywheel rotor using the same electrical machine, this time operating as a generator. The primary advantage of FESS over other energy storage devices is their high energy transfer rates and long expected lifetimes. FESS have been implemented in electric grids to reduce power spikes, assist with frequency regulation, improve power quality, and provide uninterrupted power supply. State-of-the-art FESS have several advantageous characteristics including a high charge and discharge rate, lifetimes ranging from  $10^5$  to  $10^7$  charge-discharge cycles, often equated with a service life of 10 to 20 years, and high specific energy, i.e., up to  $100 \text{ Wh kg}^{-1}$ . Further, they do not experience depth of discharge or cycling effects and have a relatively high cycle efficiency – up to 95% depending on the electrical components. While the high efficiency and long expected lifetime make FESS an attractive alternative to other short- and medium-term energy storage options, these same attributes pose significant design and operational challenges [1].

Modern composite flywheel rotors are able to achieve high rotational velocities, greater than 50,000 rpm, to maximize energy storage capacity. However, high angular velocities induce large radial and circumferential stresses on the rotor leading to potential damage and failure. The failure of rotating disks has extensively been studied in both isotropic and anisotropic materials through works such as by Miller [2], Gabrys and Bakis [3], and Hartl et al. [4]. However, the majority of work has focused on developing a greater understanding of the instantaneous, or time-independent, behavior of composite rotors and hubs to maximize potential performance or minimize cost. In these cases, rotor failure is typically seen as a quasi-static process caused by excessive centrifugal loading exceeding transverse material strength. Given the 10+ year expected lifetime of composite flywheel rotors and typical high stress operating conditions, a greater understanding of the viscoelastic, i.e., time-dependent, behavior of composite flywheel rotors is vital for ensuring reliability of rotor designs throughout the system lifetime. The viscoelastic nature of composite materials used in FESS is well documented by the works of Raghavan and Meshii [5, 6] and Arnold et al. [7, 8]. These works and their application [9, 10] have been used to inform the methods and objectives of this thesis.

In addition to long lifetimes creating the potential for viscoelastic failure, modern flywheel rotors experience high cyclic loading which creates the potential for fatigue failure. Their ability to accommodate high energy transfer rates (i.e., power) means the flywheel rotor must accelerate and decelerate rapidly, and, depending on the application, FESS may undergo thousands of charge-discharge cycles every day (e.g., in regenerative braking in rail applications). Energy is added to a FESS using an electrical machine driving and transferring torque to a metallic or composite hub, which thus transfers torque to the rest of the flywheel rotor. Rapid energy transfer

requires high torques, and therefore shear stress, acting on the flywheel rotor, potentially damaging the composite material. Shear stress in rotating disks has been studied in the past [11, 12], especially with respect to turbines and functionally graded materials [13, 14], however, little effort has been focused on the particular conditions experienced by a flywheel rotor.

Recognizing the need to better understand the viscoelastic and shear stress effects affecting the design, development, and operation of flywheel rotors, a physics based computational model was developed capable of predicting the viscoelastic behavior of a rotor over an expected 10-year operation lifetime and the evolution of shear stress in the rotor resulting from an energy transfer demand. The computational model requires a thorough understanding of the flywheel rotor's material properties throughout the simulation to accurately predict its behavior. Significant shear loading only occurs under charge and discharge cycling with relatively high power, meaning the acceleration and deceleration phases are a short-term event, i.e., the FESS can be fully charged or discharged within a period of a few seconds to a few minutes. The behavior of the composite material is not expected to change significantly during this time, so the consideration of only instantaneous material properties is deemed acceptable.

To ensure the validity of a viscoelastic simulation of flywheel rotors, a thorough understanding of the flywheel rotor operation and associated viscoelastic effects is required. The FESS may be expected to remain fully charged for extended periods of time, creating the conditions for significant viscoelastic stress relaxation. To determine the viscoelastic behavior of the composite material, instead of long-term testing at ambient temperature, a series of accelerated viscoelastic tensile testing can be conducted on the composite to measure the material creep subjecting it to constant load and various elevated temperatures. Then, time-temperature superposition can be applied to shift the resulting compliance curves to create a compliance master curve for the material transverse direction, i.e., transverse to the fibers, which is polymer matrix dominated and, contrary to the fiber direction, susceptible to viscoelasticity. The master curve can then be applied in the computational algorithm to predict the viscoelastic behavior of a flywheel rotor constructed from that material [15].

## 1.1 Knowledge Gap

While attempts have been made to more comprehensively predict rotor failure by amending the stiffness matrix for the rotor material(s) with progressive damage models [16], they fail to incorporate viscoelastic behavior and shear stress effects into the stress and failure analysis. The limited work that has been conducted on viscoelastic stress simulations has focused on time frames between  $10^5$  and  $10^{10}$  years which is well outside the presently accepted 10-20 year expected lifetime of FESS systems [1, 17]. Similarly, the impact of shear stress on internal rotor stresses is typically studied by assuming instantaneous loading [12]. Again, this falls outside typical FESS operating conditions where applied shear stress changes continuously as a function of the power demands placed upon it. In both cases this leaves a discontinuity between the operation of FESS and established modeling methods to design and analyze the composite flywheel rotors. This is

exacerbated by the limited availability of viscoelastic material properties necessary to conduct accurate simulations of flywheel rotors. This thesis seeks to address these knowledge gaps in the coming chapters.

## 1.2 Hypothesis and Thesis Objectives

The central hypothesis for this thesis research is that (i) viscoelastic effects and shear stress effects can cause creep rupture, matrix cracking, or hub-rim interfacial failure in composite flywheel rotors, and that (ii) these failure modes can be predicted employing an appropriate modeling approach in the FESS design process.

Analysis of composite flywheel rotors requires a thorough understanding of both the material system and the mechanics of the rotating disk or cylinder. This thesis describes three compounding study objectives, as shown below, which will provide the required information to accept or reject the above hypothesis.

- 1) Develop an analytical algorithm, based on existing flywheel rotor models, to simulate the evolution of the stress-strain field in a flywheel rotor during its expected operational lifetime.
- 2) Conduct simulations to predict the evolution of the stress-strain field in the flywheel rotor subjected to shear stress and viscoelastic stress relaxation.
- 3) Determine the transverse viscoelastic material compliance of filament-wound fiber reinforced polymer composite used to construct flywheel rotor rims.

Each chapter of this paper-based thesis is either intended to be or has been published by the time of submission. Individually each chapter addresses one or more of the abovementioned objectives, and, when taken in aggregate, the chapters provide necessary basis to accept the central hypothesis of this work. Chapter 2 will contextualize the present work and provide background information on FESS construction and analytical modeling of the material and flywheel rotor. This chapter was published in the form of a review article as a book chapter [18]. Chapter 3 discusses the viscoelastic modeling of the flywheel rotor, time-dependent evolution of internal stress, and failure predictions based on the Tsai-Wu failure criteria. This work was published as a journal paper [15]. Chapter 4 discusses the effects of shear stress and acceleration on the flywheel rotor. Internal stress and failure predictions are also discussed. A manuscript based on this chapter is in preparation for publication in the journal *Applied Composite Materials*. Combining the results from Chapters 3 and 4 addresses the first two objectives of this thesis. The final objective is addressed in Chapter 5, which deals entirely with viscoelastic material testing. The experimental test platform and methodology has been published in the conference proceedings of the Canadian-International Conference on Composites, CANCOM 2022 [19].

## 1.3 References

- [1] I. Hadjipaschalis, A. Poullikkas, and V. Efthimiou, "Overview of current and future energy storage technologies for electric power applications," *Renew. Sustain. Energy Rev.*, vol. 13, no. 6–7, pp. 1513–1522, 2009, doi: 10.1016/j.rser.2008.09.028.
- [2] C. A. Miller, "Creep deformation of thick prestressed rings," *Nucl. Eng. Des.*, vol. 7, pp. 87–93, 1968.
- [3] C. W. Gabrys and C. E. Bakis, "Design and Testing of Composite Flywheel Rotors," *Compos. Mater. Test.*

- Des. Thirteen. Vol. ASTM STP 1242*, pp. 1–22, 1997.
- [4] S. Hartl, A. Schulz, H. Sima, T. Koch, and M. Kaltenbacher, “A Static Burst Test for Composite Flywheel Rotors,” *Appl. Compos. Mater.*, vol. 23, no. 3, pp. 271–288, 2016, doi: 10.1007/s10443-015-9460-5.
- [5] J. Raghavan and M. Meshii, “Creep of polymer composites,” *Compos. Sci. Technol.*, vol. 57, no. 97, pp. 1673–1688, 1998.
- [6] J. Raghavan and M. Meshii, “Creep Rupture of Polymer Composites,” *Compos. Sci. Technol.*, vol. 57, pp. 375–388, 1997.
- [7] S. M. Arnold, A. F. Saleeb, and N. R. Al-Zoubi, “Deformation and life analysis of composite flywheel disk systems,” *Compos. Part B Eng.*, vol. 33, no. 6, pp. 433–459, 2002, doi: 10.1016/S1359-8368(02)00032-X.
- [8] A. F. Saleeb, S. M. Arnold, and N. R. Al-Zoubi, “A study of time-dependent and anisotropic effects on the deformation response of two flywheel designs,” *ASTM Spec. Tech. Publ.*, no. 1436, 2003.
- [9] J. Thesken, C. Bowman, S. Arnold, and R. Thompson, “Time-Temperature Dependent Response of Filament Wound Composites for Flywheel Rotors,” *Compos. Mater. Test. Des. Fourteenth Vol.*, no. January 2004, pp. 55–55–20, 2008, doi: 10.1520/stp38404s.
- [10] J. H. Kim, H. H. Han, S. K. Ha, and T. H. Sung, “Real-time life prediction of a high performance composite flywheel rotor using a telemetry system,” 2009.
- [11] J. L. Pérez-Aparicio and L. Ripoll, “Exact, integrated and complete solutions for composite flywheels,” *Compos. Struct.*, vol. 93, no. 5, pp. 1404–1415, 2011, doi: 10.1016/j.compstruct.2010.11.011.
- [12] M. Salehian, B. Shahriari, and M. Yousefi, “Investigating the effect of angular acceleration of the rotating disk having variable thickness and density function on shear stress and tangential displacement,” *J. Brazilian Soc. Mech. Sci. Eng.*, vol. 41, no. 1, pp. 1–11, 2019, doi: 10.1007/s40430-018-1523-8.
- [13] Y. Zheng, H. Bahaloo, D. Mousanezhad, E. Mahdi, A. Vaziri, and H. Nayeb-Hashemi, “Stress analysis in functionally graded rotating disks with non-uniform thickness and variable angular velocity,” *Int. J. Mech. Sci.*, vol. 119, no. October, pp. 283–293, 2016, doi: 10.1016/j.ijmecsci.2016.10.018.
- [14] M. N. M. Allam, R. Tantawy, A. Yousof, and A. M. Zenkour, “Elastic and viscoelastic stresses of nonlinear rotating functionally graded solid and annular disks with gradually varying thickness,” *Arch. Mech. Eng.*, vol. 64, no. 4, pp. 423–440, 2017, doi: 10.1515/meceng-2017-0025.
- [15] M. Skinner and P. Mertiny, “Effects of Viscoelasticity on the Stress Evolution over the Lifetime of Filament-Wound Composite Flywheel Rotors for Energy Storage,” *Appl. Sci.*, vol. 11, no. 20, p. 9544, Oct. 2021, doi: 10.3390/app11209544.
- [16] C. K. Corbin, “Burst failure prediction of composite flywheel rotors: A progressive damage approach via stiffness degradation,” Stanford University, 2005.
- [17] T. N. Ghosh, J. T. Tzeng, R. P. Emerson, D. J. O’Brien, and T. N. Ghosh, “Viscoelasticity Analysis and Experimental Validation of Anisotropic Composite Overwrap Cylinders,” *Trans. Ophthalmol. Soc. U. K.*, vol. 101, no. 02, pp. 200–202, 2012, doi: 10.1106/002199802021464.
- [18] M. Skinner and P. Mertiny, “Energy Storage Flywheel Rotors—Mechanical Design,” *Encyclopedia*, vol. 2, no. 1, pp. 301–324, Jan. 2022, doi: 10.3390/encyclopedia2010019.

## 2 Literature Review

The following chapter provides a literature review and background on flywheel energy storage systems, rotor analytical modeling and failure predictions, and pertinent material testing methods. The chapter was published in the form of a review article as a book chapter:

*Energy Storage Flywheel Rotors – Mechanical Design* published in Encyclopedia volume 2 issue 1 pages 301-324.

### 2.1 Introduction

Between 2019 and 2020, the generation of solar energy grew by 26.0 TWh (24.1%) and 37.1 TWh (16.6%) for the two largest global consumers of energy, the United States of America and the People’s Republic of China, respectively. Over the same timeframe, the growth in energy generation from wind for these two countries was correspondingly 42.0 TWh (14.1%) and 61.2 TWh (15.1%) [1]. For perspective, the total electricity generation of Canada was 643.9 TWh in 2020. Renewable energy generation capacity is expected to continue to increase rapidly as energy demands and pressure to reduce environmental impacts grow [2]. Additionally, the cost of renewable energy production has been falling dramatically over the last half decade [3], which further increases demand. However, as renewable energy production increases the intermittency from these sources necessitates significant energy storage capacity to meet demand at any particular moment [4].

Compounding the intermittency issue is the separation between peak power demands from residences and businesses and peak power production from renewable sources [5]. What is now recognized as the “Duck Curve” shows the difference between hourly demand and renewable energy production [6]. Energy consumption has been shown to peak in the mornings and evening while energy production typically peaks around midday, especially for solar photovoltaic systems.

Energy storage is among the largest obstacles facing modern energy grids as they transition to new renewable sources of energy while attempting to maintain both power supply and power quality. As the demand for renewable energy sources increases and the costs of that energy decrease, the economic and environmental benefits of maintaining large scale energy storage systems increase [7]. The plethora of energy storage options [8] includes flywheel energy storage systems (FESS). FESS are among the oldest forms of energy storage having been used to regulate power output in stone drills as early as 1,000 BCE [9]. While the principal concept of flywheel energy storage, i.e. a large mass spinning on an axis, has changed little in the intervening millennia, the materials, control systems, and applications have continually evolved.

Modern high-speed flywheel energy storage systems have a wide range of applications in renewable energy storage, uninterrupted power supplies, transportation, electric vehicle charging, energy grid regulation, and peak shaving. They are recognized for a number of advantageous characteristics including high charge/discharge rates, expected lifetimes of greater than 20 years, and specific energies in excess of 100 Wh/kg [5]. They are also unaffected by cyclic degradation

or depth of discharge effects common to traditional electrochemical batteries, and their cycle efficiency can be up to 95% [10,11]. As can be inferred from the above applications, the advantage of FESS over more common energy storage technologies, such as electrochemical batteries and pumped hydro storage, is that FESS facilitate applications requiring high power and high specific energy [12,13]. FESS have faster response times than both electrochemical batteries or pumped hydro. Compared to batteries, FESS do not require the same level of delicate control over power and temperature, and, due to their high cycle lifetime and deep depth of discharge, FESS require less installed capacity than batteries while still meeting demand [7].

This is not to say FESS are an ideal solution to address all energy storage challenges. FESS experience high passive discharge losses [10], comparatively high initial investment costs [14], and ongoing efforts to understand long-term behavior of rotor materials and failure [15,16]. In an effort to understand and improve flywheel rotor performance and safe operating limits, analytical models have been developed that consider materials selection, rotor construction, and operating conditions.

This entry focuses on the design and analysis of the flywheel rotor itself. It will begin by highlighting some FESS applications and performance, followed by the design and manufacturing approach commonly used for flywheel rotors. Analytical modeling approaches for typical flywheel rotors will be discussed including the effects of variable angular velocity, viscoelastic stress relaxation, and acceleration. Finally, rotor failure criteria will be discussed.

## 2.2 Applications and Performance

FESS have a wide range of applications for uninterruptible power supplies, energy grid regulation for frequency and power quality, and electric vehicle and rail transportation. A general range of FESS performance characteristics is given in Table 2.1.

*Table 2.1: General range of FESS performance characteristics.*

<b>Parameter</b>	<b>Value</b>
Lifetime [years]	>20 [5]
Charge/discharge cycles	<10 <sup>7</sup> [5]
Energy density [Wh/kg]	<130 [17]
Price [(USD)/kWh]	400 – 6,960 [5, 17]
Power density [W/kg]	~1000 [5]

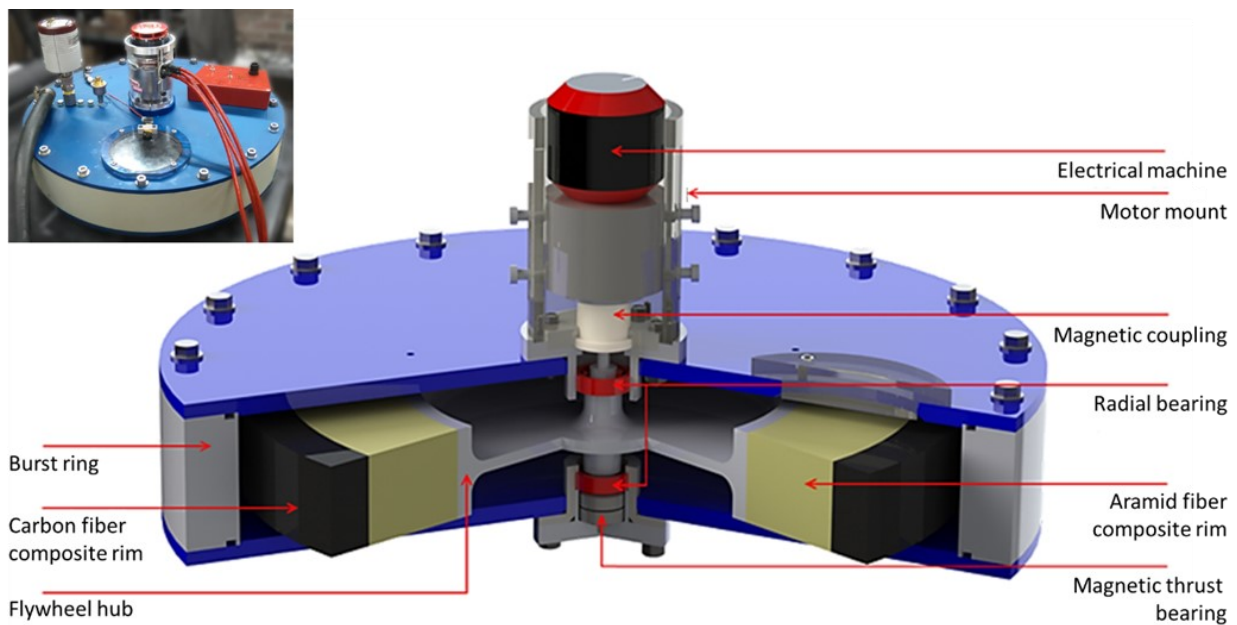
Implementations of FESS are plentiful, so only a few examples are given here. An early application of FESS was the Gyrobus, which began operation in Switzerland and Belgium in 1952 with the goal of servicing low traffic public transport routes where installing overhead electrical catenary wire was deemed too costly [18]. In the late 1990s, Rosen Motors designed a hybrid power train for a vehicle with a gas turbine engine and a high-speed FESS supplementing acceleration in short bursts [19]. Later, Volvo developed a recumbent braking system for their S60



sedan, which recovered and stored energy during braking and subsequent use powering the vehicle [20]. Most recently, Porsche integrated a flywheel into their 911 GT3R race car to extend its range and achieve performance enhancements for long-distance racing [21]. FESS can also be installed on light rail transit systems, either in the cars or along the rail line, as a recumbent braking system to reduce operating costs [22]. Trials for these systems have been conducted in London, New York, Lyon, and Tokyo, among others [23]. Further, utility-scale FESS installations have been implemented as temporary backup power for energy grids in Minto, Ontario [24], Stephentown, New York [25], and De La Salle, Philippines [26].

### 2.3 Manufacturing

The primary components of FESS are the electrical machine (motor/generator unit), housing, flywheel rotor, and bearing assembly. As an illustration, Figure 2.1 depicts a cut-away schematic of a scaled-down FESS that was designed for short-term energy storage from regenerative braking in light-rail transit applications. The shown unit features a rotor with a full-size 400 mm outer diameter, but axial height scaled to 24% of the full-scale design with 1.0 kWh nominal capacity.



*Figure 2.1: Cut-away schematic of flywheel energy storage system for experimental research. Inset shows actual device [16].*

In FESS, the electrical machine is responsible for controlling the energy flow into and from of the system. Notably, the electrical machine can be selected independently from the desired energy capacity to meet the demands of a specific application. The housing, bearings, and rotor work in unison, however, while they have clear interactions with each other, changes to one do not necessarily impact the others. For example, any bearing assembly capable of supporting the rotor is acceptable, and different assemblies can be substituted provided they adequately support the

rotor. In this way FESS are highly modular allowing the system to be finely tuned for optimized performance in a given application. Being the focus of the present entry, the construction of flywheel rotors can be broken down into the two main rotor components - the hub and the rotor rims - and their assembly.

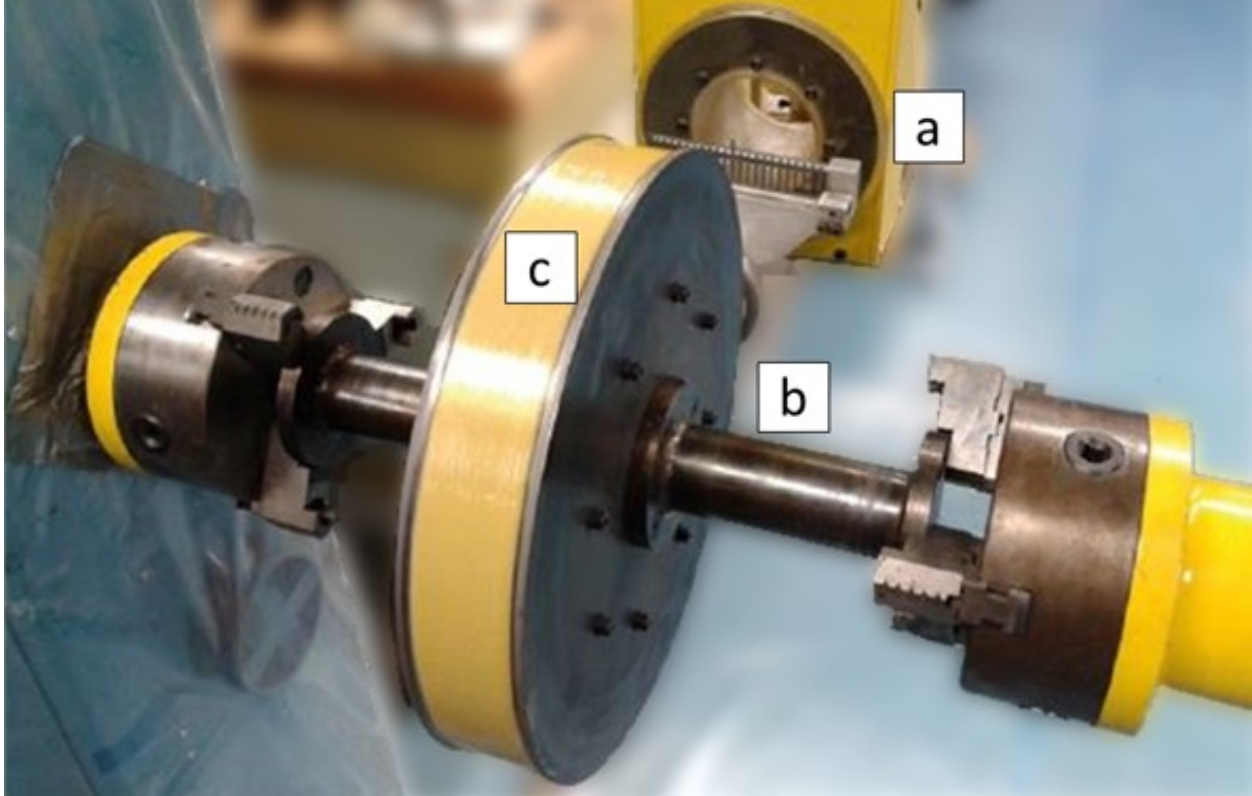
### 2.3.1 Hub Construction

The hub of a flywheel rotor is responsible for supporting the rims and transferring torque from the electrical machine to the rest of the rotor. Rotor hubs are commonly constructed from either high-strength steel, aluminum, or fiber-reinforced polymer (FRP) composites. A metallic hub can be forged or machined into a variety of complex shapes. These shapes have been characterized in detail in a number of different works [13,27]. The advantages of various metallic hub geometries are discussed in greater detail below. Limited studies have been conducted on composite hubs that have been shown to be more compliant than metallic hubs, thus providing advantages supporting the rotor rims [28].

### 2.3.2 Rim Construction

Flywheel rotor rims can also be constructed from metals or FRP composites. Metallic flywheels are a well understood and comparatively low-cost option that can be forged or machined into rather complicated shapes to maximize performance. Additionally, the hub can be integrated with the rim into a single component, simplifying the manufacturing process. Kale et al. [29] developed an optimization method to maximize kinetic energy of metal flywheels by varying the cross-section, speed, and size of the flywheel.

FRP rims are fabricated by either filament winding, as shown in Figure 2.2, or weaving [30,31]. Rectilinear fabric layup techniques have also been studied for constructing rotating disks [32], however, fabric-based methods are uncommon as they have not proven to be advantageous compared other techniques such as filament winding. Filament winding is a highly efficient method for fabricating FRP rotor rims due to the accurate control over fiber placement and orientation, axisymmetry of the finished product, and high fiber volume fraction [33] regardless of the fiber material, such as carbon, glass, and aramid. Attempts have been made to limit viscoelastic behavior and maximize material strength by changing the winding angle or creating complex winding layup patterns, however the additional complexity of these methods has not proven advantageous. These are discussed in more detail below. Rim geometries are usually a simple thick-walled cylinder with rectangular cross section. The process involves passing long filaments through a resin bath to impregnate the dry fibers with a prepolymer. The fibers are then wound onto a mandrel by passing through the deposition head of the filament winding machine, which allows for precise control of fiber positioning and orientation, i.e. winding angle, of the fibers [34]. Filament winding is an additive manufacturing technique which is often automated to produce parts rapidly and efficiently while minimizing cost. After winding and curing, FRP rotors often require machining to their final dimensions, particularly on the outer surface where excess resin tends to accumulate during the winding process.



*Figure 2.2: Composite flywheel rotor rim at the end of filament winding manufacturing process; (a) fiber payout eye and deposition head on winding machine carriage arm, (b) winding mandrel, and (c) completed aramid fiber/epoxy composite rim.*

The majority of FRP composite rims are constructed with winding angles approaching 90 degrees, typically larger than 88 degrees, relative to the axis of rotation, as this maximizes circumferential strength in the rotor. However, investigations into the effects of variable winding angles have shown to improve rotor performance. Wild et al. [35] showed that periodically increasing the winding angle from the inner to outer radius increased compliance of the FRP at inner radii relative to outer radii allowing the inner portion of the rim to move disproportionately outward, preventing the buildup of large tensile radial stress, which is the driver for a primary failure mode. Recognizing the significance of radial tensile stress, Uddin et al. [36] conducted finite element analysis on FRP composite rotors filament-wound with a mosaic pattern. These complicated patterns were created by significantly changing the fiber angle between layers during the winding process. Results showed that radial stress could be significantly reduced, possibly leading to greater rotor energy storage capacities; however, effects on manufacturing cost have not been determined, and further research is therefore needed.

Wang et al. [30] discussed the possibility of creating woven FRP rims with fibers perpendicular to each other radially and circumferentially. They successfully created thin composite disks and conducted finite element analysis on the structures. Their results indicate the radially oriented fibers provide greater support when compared to unidirectional filament-wound

rotors. Similar to the mosaic patten it is not clear if this technique improves specific energy, nor has the effect on manufacturing cost been clearly assessed.

### 2.3.3 Assembly

Assembly of a flywheel rotor is only necessary when it is constructed from multiple components, typically a hub and one or more FRP composite rims. For metallic flywheels, assembly is typically not required as they can be manufactured as a single part. For flywheel rotors constructed from a metallic hub and a single FRP rim, the composite can be wound directly onto the hub as discussed by Tzeng et al. [37] or joined with a press-fit [18]. An example of a thermal press-fit is shown in Figure 2.3.



*Figure 2.3: Thermal press-fit accomplished by cooling the aluminum hub with liquid nitrogen before pressing into the composite rims.*

While there is no consensus on the optimal method for assembling flywheel rotors, press-fitting is often considered for the construction of flywheel rotors with more than a single rim. When press-fitting FRP rims onto a hub or other FRP rims, they can be manufactured with a slight taper to reduce the required pressing force and minimize the risk of damaging the fibers [28]. When dissimilar materials are adjacent to each other it is often expedient to create a thermal press-fit by taking advantage of the different thermal expansion coefficients. This is especially true when assembling an FRP rim and a metallic hub [28]. The final step in flywheel rotor assembly is typically balancing to minimize vibrations and oscillations by ensuring mass is evenly distributed around the axis of rotation.

## 2.4 Analytical Modeling

### 2.4.1 Energy Storage and Power Capacity

Flywheel energy storage systems have often been described as ‘mechanical batteries’ where energy is converted from electrical to kinetic and vice versa. The rate of energy conversion is the power capacity of the system, which is chiefly determined by the electrical machine connected to the rotor [13,39]. The capacity of the FESS is determined by the size, shape, materials, and construction of the flywheel rotor [15]. As indicated above, modern high-speed flywheel rotors are typically constructed from a hub, responsible for torque transfer and structural support, and one or more rims [39]. Here, for the sake of explanation, a monolithic rotor geometry is considered to consist only of a hub without any added rims around its perimeter. Hub and rims can be constructed from either metals, ceramics, or composites [40,41] to maximize rotor performance. The kinetic energy of a rotor, as a rotating body, is defined as

$$E_K = E_{\text{hub}} + \sum_{n=1}^N E_{\text{rim}}^n = \frac{1}{2} I_r \omega^2, \quad 2.1$$

where  $E_K$  is the total kinetic energy of the rotor,  $I_r$  is the total moment of inertia for the rotor,  $\omega$  is the angular velocity in units rad/sec, and  $N$  is the number of rims such that  $n = 1, 2, \dots, N$ . The moment of inertia for the entire rotor is a superposition of the moment of inertia for the hub and all rims,

$$I_r = I_{\text{hub}} + \sum_{n=1}^N I_{\text{rim}}^n, \quad 2.2$$

where  $I_{\text{hub}}$  and  $I_{\text{rim}}^n$  is the moment of inertia for the hub and the  $n$ -th rim, respectively.

Considering the flywheel hub, defining the moment of inertia for simple geometries is straightforward, i.e. for rectangular cross sections of a solid or hollow disk the moment of inertia can be defined as






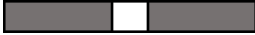
$$I_{\text{hub}} = \frac{1}{2} m (r_o^2 + r_i^2) = \frac{1}{2} \rho \pi h (r_o^4 - r_i^4), \quad 2.3$$

where  $\rho$  is the density of the hub material,  $h$  is the height of the hub (with respect to the axis of rotation), and  $r$  is the radius with the inner and outer dimension defined by subscripts ‘ $i$ ’ and ‘ $o$ ’. In analytical modeling the mass of the hub is calculated using the volume and density. A common approach for handling complex geometries and functionally graded materials is to discretize the shape into a series of uniform disks of arbitrary width and varying height [42], in which case equation 2.3 can be generalized by manipulating  $r_o$ ,  $r_i$ ,  $\rho$ , and  $h$ . As the hub cross section increases in complexity it is common to define the energy density (ratio of energy to mass) [13,27,43] of the hub as

$$\frac{E_{\text{hub}}}{m} = \frac{k\sigma}{\rho}, \quad 2.4$$

where  $k$  is the shape factor of the hub and  $\sigma$  is the stress in the hub. When  $\sigma$  is equal to the ultimate tensile strength in the hub, energy density is maximized and can be used to find the maximum energy capacity of the flywheel rotor. Shape factors for common hub geometries are presented in Table 2.2; additional cross sections  $k$ -values are given in [13,43]. It has been noted [27] that the choice of material for the hub will strongly influence cross sectional geometries. Hub shape factors above 0.5 induce bidirectional stress states, which negatively impact composite materials, especially unidirectional composites, because transverse strength is typically significantly lower than strength in the fiber direction. For this reason, isotropic materials are more appropriate for cross sections with large shape factors. Discontinuous hub geometries, such as the split type hub [44], are either treated as continuous and analyzed as described above, or determined through numerical methods [45].

Table 2.2: Shape factor values ( $k$ ) for various flywheel rotor cross sections.

Shape	Cross section	$k$ -value
Laval disk		1.00
Laval disk real		0.70-0.90
Conical disk		0.70-0.85
Solid disk		0.606
Thin ring		0.50
Thick rim		0.303

Focusing attention now on rotor rims, calculating the energy capacity is analogous to equations (1) to (4). The vast majority of industrial and academic work focusing on flywheel rotors uses rims with rectangular cross sections [46–49]. While it has been shown that variable thickness flywheel rotors can produce a more favorable stress state [50], the energy capacity typically suffers due to the reduction of mass at the largest radial coordinates and limited maximum angular velocity to minimize transverse loading. Variable thickness flywheel rotors with mass concentrated on the outer edges have been presented [45], however, these have not proven to produce higher energy density or a more favorable stress state than traditional rotor designs such as the Laval disk with rims discussed in [43].

#### 2.4.2 Material Characterization

Flywheel rotor material selection depends on a large variety of constraints, including system requirements, cost, operating conditions, and expected lifetime. Equation (1) indicates that energy capacity is quadratically related to angular velocity and radius. Therefore, increasing either one or both values is the most effective method to increase energy capacity. Moreover, equation 2.4 shows that the energy density of a rotating rotor is proportional to the ratio of its material's strength and density. This suggest that high strength, low density materials like carbon FRP

composites are an ideal material for flywheel rotor construction. However, the stress state is also quadratically related to angular velocity and radius. Compounding this issue is the typically limited transverse strength of highly anisotropic materials [27], such as carbon FRP, suggesting that additional design features are required for achieving full energy capacity potential (e.g., press-fit assembly of multiple rotor rims). These considerations lead to the conclusion that the most suitable choice of material and geometry depends heavily on the application requirements and design constraints such as system geometry and cost.

The most common choices for modern flywheel rotors are either metals, such as aluminum and steel, or FRP composites [51]. With respect to single and multi-rim flywheel rotors, it has been shown that the optimal choice depends on the design criteria. When optimizing for specific energy, i.e., energy per unit mass, then FRP composites are usually the ideal choice, whereas metal flywheels are often superior when optimizing for energy per cost [40]. Another consideration is that isotropic materials are also better understood than advanced composite materials, which increases confidence in modeling and failure prediction, especially in design cases aiming for long lifetimes and operation near maximum energy capacity.

Regardless of material selection, it is necessary to describe the stress strain relationship for all materials in the rotor. Assuming time-independent linear elastic behavior [52], Hooke's law in cylindrical coordinates is,

$$\begin{bmatrix} \sigma_{11} \\ \sigma_{22} \\ \sigma_{23} \\ \sigma_{12} \\ \sigma_{13} \\ \sigma_{23} \end{bmatrix} = \begin{bmatrix} C_{11} & C_{12} & C_{13} & C_{14} & C_{15} & C_{16} \\ C_{21} & C_{22} & C_{23} & C_{24} & C_{25} & C_{26} \\ C_{31} & C_{32} & C_{33} & C_{34} & C_{35} & C_{36} \\ C_{41} & C_{42} & C_{43} & C_{44} & C_{45} & C_{46} \\ C_{51} & C_{52} & C_{53} & C_{54} & C_{55} & C_{56} \\ C_{61} & C_{62} & C_{63} & C_{64} & C_{65} & C_{66} \end{bmatrix} \begin{bmatrix} \varepsilon_{11} \\ \varepsilon_{22} \\ \varepsilon_{33} \\ \gamma_{12} \\ \gamma_{13} \\ \gamma_{23} \end{bmatrix}, \quad 2.5$$

where  $\sigma$  is stress,  $C$  is an elastic modulus of elasticity,  $\varepsilon$  is linear strain, and  $\gamma$  the shear strain. The subscripts 1, 2, and 3 in the stress and strain terms indicate the rotor's radial, circumferential, and axial directions, respectively. The stiffness matrix,  $[C]$ , given above, assumes a fully anisotropic material and has 36 independent moduli. However, materials used in flywheel rotor display varying levels of symmetry so this matrix can be simplified based on the materials selection. Orthotropic carbon FRP flywheel rotors have been constructed by stacking woven carbon fiber laminates [30] or developing unique fabric layup patterns [36], discussed in section 4.2, in which case the stiffness matrix becomes,

$$[C] = \begin{bmatrix} C_{11} & C_{12} & C_{13} & 0 & 0 & 0 \\ C_{12} & C_{22} & C_{23} & 0 & 0 & 0 \\ C_{13} & C_{23} & C_{33} & 0 & 0 & 0 \\ 0 & 0 & 0 & C_{44} & 0 & 0 \\ 0 & 0 & 0 & 0 & C_{55} & 0 \\ 0 & 0 & 0 & 0 & 0 & C_{66} \end{bmatrix}. \quad 2.6$$

Further simplifying assumptions can be made for unidirectional FRP composites where the rotor is made by continuously winding long polymer resin impregnated filaments onto a mandrel before polymer solidification [28,38]. In this case the fibers are all oriented circumferentially with the radial and axial directions both being transverse to the fibers. In this case the material is considered transversely isotropic [43],

$$C_{22} = C_{33}; \quad C_{12} = C_{13}; \quad C_{44} = C_{55}. \quad 2.7$$

For fully isotropic materials, such as steel, the stiffness matrix simplifies significantly [54],

$$C_{11} = C_{22} = C_{33}; \quad C_{12} = C_{13} = C_{23}; \quad C_{44} = C_{55} = C_{66} \quad 2.8$$

Transversely isotropic and fully isotropic materials are most common in modern flywheel rotor construction due to their comparatively low cost, high strength, and ease of manufacturing.

A description of elasticity is sufficient to determine the instantaneous or time-independent rotor response to loading, however, this approach does not necessarily reflect the realistic material response to loading. Therefore, it is necessary to develop a description of the materials that depends on time,  $t$ . All engineering materials exhibit some viscoelastic response, meaning they have characteristics of elastic solids and viscous fluids [55]. However, at typical FESS operating temperatures, below 50°C [56], metals display negligible viscoelastic behavior [57], therefore this discussion will focus on FRP composites.

The time-dependent compliance of a material is defined as the inverse of the stiffness matrix such that  $[S(t)] = [C(t)]^{-1}$ . Then, the time-dependent compliance matrix for an orthotropic linearly elastic material is

$$[S(t)] = \begin{bmatrix} S_{11}(t) & S_{12}(t) & S_{13}(t) & 0 & 0 & 0 \\ S_{12}(t) & S_{22}(t) & S_{23}(t) & 0 & 0 & 0 \\ S_{13}(t) & S_{23}(t) & S_{33}(t) & 0 & 0 & 0 \\ 0 & 0 & 0 & S_{44}(t) & 0 & 0 \\ 0 & 0 & 0 & 0 & S_{55}(t) & 0 \\ 0 & 0 & 0 & 0 & 0 & S_{66}(t) \end{bmatrix}. \quad 2.9$$

At this juncture it is worth taking a moment to define the  $S_{ij}$  terms with respect to moduli of elasticity,  $E$ , and Poisson's ratios,  $\nu$ ,



$$[S(t)] = \begin{bmatrix} 1/E_1(t) & -\nu_{12}/E_2(t) & -\nu_{13}/E_3(t) & 0 & 0 & 0 \\ -\nu_{12}/E_1(t) & 1/E_2(t) & -\nu_{23}/E_3(t) & 0 & 0 & 0 \\ -\nu_{13}/E_1(t) & -\nu_{23}/E_2(t) & 1/E_3(t) & 0 & 0 & 0 \\ 0 & 0 & 0 & 1/G_{23} & 0 & 0 \\ 0 & 0 & 0 & 0 & 1/G_{23} & 0 \\ 0 & 0 & 0 & 0 & 0 & 1/G_{12} \end{bmatrix} \quad 2.10$$

As shown earlier, the time-independent compliance matrix for transversely and fully isotropic materials can be found using equations 2.7 and 2.8. For viscoelastic materials, the sustained imposition of a stress causes increasing strain, called creep. Conversely, subjecting a viscoelastic material to constant strain leads to decreasing stress, called relaxation. Creep occurs in three phases characterized by the linearity of the strain response as a function of time. Primary, or phase I, creep is characterized by logarithmic growth. In secondary, phase II, creep, deformation increases linearly with time. Finally, tertiary, phase III, creep is characterized by exponential growth until failure [55]. Methods for calculating the compliance from stress-strain data is well documented [58–61]. These methods typically involve applying a known stress to material samples while measuring strain and time data. From these data, stress-strain curves are constructed and functions are fit to the curves to define the time-dependent change in elastic modulus. It is worth noting that a number of phenomena affect the viscoelastic response of materials, including stress magnitude and direction, temperature, moisture, and age [62].

#### 2.4.2.1 Hygroscopic Effects

The effects of moisture, also known as hygroscopic effects, on material properties have been documented for both elastic and viscoelastic FRP composite materials [63]. However, hygroscopic effects are not expected to significantly affect the operation of flywheel rotors. FESS commonly comprise a vacuum enclosure designed to contain the flywheel and limit the aerodynamic drag acting on the rotor and bearing surfaces [39]. Hence, hygroscopic instability is not expected to affect the rotor material during operation, provided the vacuum environment under which it operates is maintained. Consequently, viscoelastic material characterization should be performed on suitably dry specimens to most accurately describes the material in-situ. If necessary, this can be accomplished by conditioning specimens, e.g., by gently heating specimens to approximately 90°C for up to 24 hours [62].

#### 2.4.2.2 Temperature Effects

Similar to hygroscopic effects, the vacuum condition in the FESS enclosure minimizes the influence of environmental temperature changes on the flywheel rotor during operation. On the other hand, a vacuum environment prevents convective heat transfer and thus impedes the removal of parasitic heat that is generated by energy losses such as friction in bearings and eddy currents in the electrical machine. Hence, a flywheel rotor may still experience considerable temperature

fluctuations depending on the FESS design configuration and operation, and hence, the study of temperature on flywheel rotor creep and relaxation should be considered in FESS design.

Challenges with assessing the creep behavior of FRP composite rotors arise from the projected long lifetimes of FESS. As a solution, time-temperature superposition principle (TTSP) can be used to predict long-term behavior using short-term viscoelastic test data. FRP composites are highly sensitive to temperature fluctuations with linear viscoelastic behavior being observed below the polymer matrix glass transition temperature,  $T_g$ , and non-linear viscoelasticity above. Elevated temperatures facilitate polymer chain mobility causing a decrease in both moduli and strength [60]. For the TTSP, a trade-off is seen where increasing temperature increases the rate of viscoelastic response, and decreasing temperature decreases this response. By conducting short-term experiments at elevated temperatures, it is possible to predict the long-term behavior of the material at low temperatures. The basic procedure for the TTSP is discussed in [64]. First, the material specimens are subjected to constant load at various temperatures during conventional creep testing. These data generate a series of compliance curves when plotted over time in logarithmic scale ( $\log(\text{time})$ ). Second, an arbitrary reference temperature is selected. Third, all compliance curves are shifted along the time axis onto the reference temperature compliance curve to construct a master curve. As a demonstration, consider the data series of tensile experiments in Figure 2.4. Short-term tensile experiments were conducted on an FRP composite material at various temperatures to collect the viscoelastic data [65]. Data for all temperatures but the reference temperature were shifted along the time axis to construct the master curve at a reference temperature,  $T_r$ , of 40°C.

An underlying assumption for the TTSP is that creep is controlled by the same mechanisms under the different temperatures. Therefore, the master curve is expected to be smooth throughout. Since it is constructed on a  $\log(\text{time})$  axis the predicted compliance is sensitive to the shift factor where a small discontinuity could result in errors of years or decades. If a smooth master curve exists by using only horizontal shift factors then the material is considered thermorheologically simple. The need for vertical shift factors has been identified under some conditions [64], in which case materials are referred to as thermorheologically complex. The majority of materials, including FRP composites under normal conditions, are considered thermorheologically simple [64]. Notably, even though TTSP has been employed to characterize the linear viscoelastic behavior of epoxy polymers since at least the 1960s [66], there is still no established convention defining the optimal method to determine shift factors for each curve.

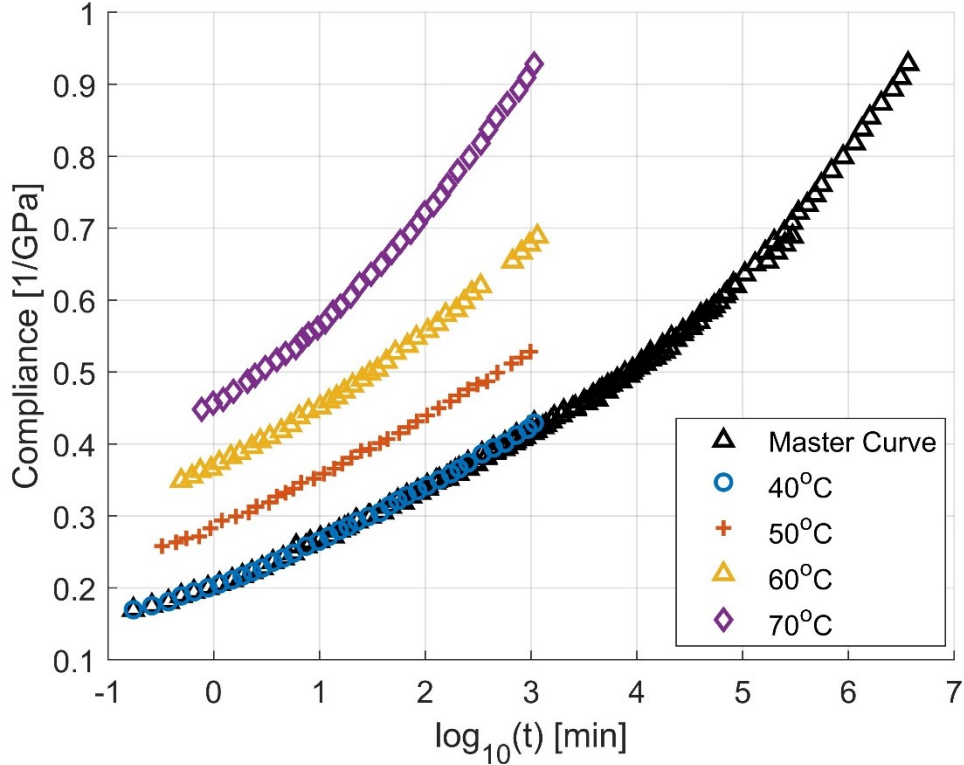


Figure 2.4: Time-temperature superposition experimental data, adopted from [65]. Data was collected from tensile tests for an FRP composite at various temperatures and shifted along the time axis to create a master curve for a reference temperature of 40°C.

The distance each curve is shifted along the time axis is called the shift factor,  $a_T$ . There are several ways to determine the shift factor for each curve, all of which are designed to create a smooth master curve. Brinson [67] studied the time temperature response of Hysol 4290, a common contemporary two-part epoxy. Brinson conducted tensile tests on samples of the material at temperatures between 90°C and 130°C and thus constructed a master curve covering creep at 90°C over approximately 6 months. The shift factor was determined using the William-Landel-Ferry (WLF) equation [68], which requires a knowledge of  $T_g$  and a set of experimentally determined material constants. While WLF can create a smooth master curve it is limited to temperatures above  $T_g$ , so it may not be suitable for all applications. Another common method is using an Arrhenius' equation [69,70], which requires knowledge of the activation energy and gas constant. The activation energy is typically determined using dynamic mechanical analysis [71].

Both of the above mechanistic methods attempt to define a relationship between certain material properties and the creep response. However, Gergesova et al. [72] recognized that a smooth master curve can be constructed without this mechanistic relationship by mathematically minimizing the horizontal distance between two adjacent curves. His algorithm considers overlapping region of data between adjacent curves. Before shifting these regions, one defines an area that is delineated on either side by the experimental data and on top and bottom by the height

of the overlap. This area can be minimized by applying a shift factor to one or both curves depending on the chosen reference temperature. Using this method, the shift factor and master curve can be found without the need for additional experiments or prior knowledge of the activation energy. It is worth noting that Sihm and Tsai [65] used an Arrhenius equation while the master curve in Figure 2.4 was created using the algorithm from Gergesova et al. [72].

Applying a best fit curve to the compliance master curve defines a function used to determine the material stiffness at any time throughout its lifetime,

$$S_{ij}(t, T_r) = S_{ij}(a_T, t, T) \quad 2.11$$

where  $S_{ij}$  is the compliance and  $T$  is the experimental temperature. Tensile experiments must be conducted to determine  $[S]$  for each independent modulus in equation (10), i.e.,  $E_1$ ,  $E_2$ ,  $E_3$ , etc., and will vary depending on whether the material is isotropic, transversely isotropic, orthotropic, or fully anisotropic.

#### 2.4.2.3 Aging Effects

Aging is a continuous process which occurs at all temperatures and is caused by polymer chains evolving toward equilibrium. This is ultimately a densification process which results in a decreased chain mobility and compliance. The effect of aging is similar to temperature in that it is continuous, however, aging always results in a decrease in compliance whereas temperature can result in either an increase or decrease. Aging effects can be included in directional compliance similarly to temperature effects. Compliance is measured from material specimens at various ages and resulting curves are shifted to define the age shift factor,  $a_{te}$ . Then,  $S_{ij}$  becomes,

$$S_{ij}(t_e, T_r) = S_{ij}(a_T, a_{te}, t, T). \quad 2.12$$

where  $t_e$  is the age for which the master curve is created. Under isothermal conditions the aging shift factor can be calculated as a ratio between a reference aging time and an experimental aging time raised to an experimentally determined thermal shift rate [73]. While it is possible to experimentally determine and account for material aging when modeling flywheel rotors it is more practical to thoroughly stabilize the flywheel rotor by aging at an elevated temperature under no load conditions until the rotor reaches equilibrium before operation. This stiffens the material, minimizes creep, and provides a more repeatable starting point for designing flywheel rotors. Sullivan [74] showed that equilibrium can be achieved by aging epoxy polymers at 115°C for 1,000 hours. It is recommended that flywheel rotors be aged to minimize material evolution during operation, which will improve rotor response to applied loads and increase confidence in any simulation or modeling conducted during the design of the rotor.

#### 2.4.2.4 Stress Magnitude

Akin to temperature, the viscoelastic material response is closely linked to the stress magnitude. At low magnitudes, FRP composite materials typically display linear viscoelastic

behavior. As stress magnitude increases the material begins displaying non-linear viscoelastic behavior. Experimental findings on different material systems indicate significant variation in the stress magnitude and temperature levels necessary to predict linear viscoelastic response [62]. Currently, there is no conclusive method for determining at what temperature and stress the material will transition from a linear to non-linear response. However, it has been shown that linear response, necessary for TTSP, and fatigue resistance, necessary for flywheel operation, can be ensured by limiting the temperature to below  $T_g$  [75] and stress to below 50% of the failure strength [76].

### 2.4.3 Quasi-static Analysis

In 1957, Lekhnitskiy [77] defined the stress equilibrium equations for an arbitrary homogeneous anisotropic plate in cylindrical coordinates subjected to rotation. These equations define the radial, circumferential, axial, and tangential (shear) equilibrium for an anisotropic body with applied forces, such as rotation, and the resulting internal stresses. Lekhnitskiy worked with thin plates assuming a plane stress state for the body. If a thin uniform circular disk is in equilibrium, axisymmetric, neither accelerating nor decelerating, and not experiencing out of plane forces means the only the radial equilibrium equation is non-trivial.

Lekhnitskiy's original analysis have been expanded upon with focus specifically on multi-rim FRP composite flywheel rotors. Chamis and Kiraly [78] applied analytical modeling to determine the stress and vibration induced in thin FRP flywheel rotors. They found that high aspect ratio flywheel rotors were the most weight efficient elements of a rotor, and that a flywheel can efficiently provide power in excess of 10 kW for several days when needed.

By the 1990s, analytical modeling of flywheel rotors had been generalized to predict the stress and displacement of multi rim flywheel rotors through work such as Gabrys and Bakis [79], Ha et al. [80], and Wild and Vickers [35]. Gabrys and Bakis developed a complete method for designing composite flywheel rotors from one or more FRP rims press-fitted together. Their method relied on defining an optimization routine that maximizes angular velocity while ensuring radial and circumferential failures occur simultaneously. Through their method the thickness of each rim in a press-fit rotor can be found, thus defining an optimal rotor design. They also state that rim materials should decrease in density and increase in stiffness as rims are positioned further from the axis of rotation. In other words, the densest and least stiff material should be used for the innermost rim while the least dense and most stiff material should form the outer most rim. This recommendation is reasonable considering the largest radial positions will experience the greatest loading from centripetal forces due to rotation and reaction forces from other rims deforming outward. At the same time, this design approach alleviates the buildup of radial tensile stress that acts transverse to the fibers, i.e., the direction with greatest susceptibility to failure.

Ha et al. [80] recognized that solving the analytical equations for multi-rim rotors results in a series of non-linear equations, which led them to develop a unique method for solving all the equation simultaneously, thus minimizing the time and computational effort needed to analyzed

flywheel rotors. They then went on to apply a similar optimization routine as Gabrys and Bakis [79] to optimize the radial thickness of each rim for multi-rim rotors constructed of various materials. Ha et al. considered rotors with an embedded permanent magnet at the inner surface and up to four different rims: glass/epoxy, aramid/epoxy, and two different carbon/epoxy variants, i.e., AS/H3501, T300/5208, and IM6/epoxy. They showed that no multi-rim solution exists when density and stiffness decrease with radius, contrary to typical construction. The optimization algorithm always trended toward eliminating (i.e., zero radial rim thickness) all but the innermost rim.

Methods for solving equation 2.13 to find radial displacement, radial stress, and circumferential stress have been described extensively in literature [16,80,81] so only a brief description is provided here. The radial equilibrium equation is

$$\frac{\partial \sigma_r}{\partial r} + \frac{\sigma_r - \sigma_\theta}{r} + \rho r \omega^2 = 0, \quad 2.13$$

where  $\sigma$  is the internal stress in either the radial, subscript  $r$ , or circumferential, subscript  $\theta$ , direction;  $\rho$  is the density of the material; and  $\omega$  is the angular velocity. The stresses are defined by Hooke's law, equation 2.5, and the stiffness matrix is defined with any of the equations 2.6, 2.7, or 2.8 depending on the material response. Fundamentally, a two-dimensional assumption can be made which is suitable for high aspect ratio flywheel rotors, i.e., thin rotors with radial dimensions significantly larger than axial dimensions. The directional strains are defined as,

$$\varepsilon_\theta = \frac{u_r}{r}; \quad \varepsilon_r = \frac{\partial u_r}{\partial r}; \quad \varepsilon_z = \varepsilon_{\theta z} = 0 \quad 2.14$$

where  $u_r$  is the radial displacement and the subscript  $z$  signifies the rotor axial direction. Then, equation 2.14 can be substituted into Hooke's law which is further substituted into equation 2.13. This yields a second order inhomogeneous ordinary differential equation, which can be solved for the radial displacement and radial stress, yielding

$$\begin{aligned} u_r &= -\rho \omega^2 \varphi_0 r^3 + C_1 \varphi_1 r^\kappa + C_2 \varphi_2 r^{-\kappa} \\ \sigma_r &= -\rho \omega^2 \varphi_3 r^2 + C_1 r^{\kappa-1} + C_2 r^{-\kappa-1} \end{aligned} \quad 2.15$$

where  $\varphi$  and  $\kappa$  are constants based on the material properties of the rim, and  $C_1$  and  $C_2$  are integration constants, detailed in [80], which must be determined by the boundary conditions, see [81].

All research mentioned up to this point, and in fact the majority of flywheel research, has been conducted on relatively thin disks. Such rotor geometries tend to minimize material and fabrication costs and simplify analytical modeling by allowing for a two-dimensional or plane stress assumption. Also, axial stress arises merely due to Poisson's effects from the combination of radial and circumferential stress. Moreover, for typical rotor configurations it is challenging to measure radial deformation experimentally. For these reasons a thin composite disk is beneficial especially for research purposes.

While Ha et al. [82] has extensively explored modeling under plane stress, work by this group of researchers also involved two alternate assumptions: plane strain (PS) and modified generalized plane strain (MGPS). The PS assumption is true for a thick rotor where the axial dimension is significantly larger than the radial dimension, and defines axial strain as zero while axial stress is allowed to vary [81]. Generalized PS and MGPS allow axial strain to vary according to a constant and a linear relation, respectively. Ha et al. compared the axial stress results for single, two and three-rim rotor simulations conducted with PS, MGPS, and finite element modeling (FEM). They found axial stress results to have the best correlation between MGPS and FEM. For the two-dimensional case, such as solved using the model by Lekhnitskiy, plane stress and PS are identical because there is no third dimension for stress or strain. As the flywheel rotor increases in thickness, PS was shown to be more appropriate than plane stress approximately when the rotor radial dimension equals the axial dimension. While MGPS is relatively uncommon in modern flywheel research due to its complexity, PS and generalized PS are still part of contemporary research.

A number of studies have been published discussing analysis that specifically target flywheel rotor design for energy storage applications [14,46,47]. Much of recent research into FRP composite flywheels has focused on optimizing the design to minimize cost, in an effort to make the technology a more attractive alternative to other conventional storage technologies, primarily electrochemical batteries. Hearn et al. [83] and Rupp et al. [22] focused on minimizing FESS cost for public transportation. Both studies found rotors with rectangular cross sections and no more than three rims to be ideal for maximizing storage capacity while minimizing cost; storage capacity of approximately 3 to 5 kWh were targeted as appropriate for public transportation. Recalling equations 2.2 and 2.15, rectangular cross sections maximize the volume of material at a given radius while providing in plane support for material at smaller radial locations. Rectangular cross section rotors are also comparatively easy to manufacture. Recent efforts [84] have employed advanced multi-factor optimization algorithms to develop methods for designing FESS appropriate for a wide range of application, including grid storage, grid regulation [85], and energy storage in addition to public transport.

In the most recent decade, research has shown a trend to move away from either the PS or plane stress assumptions to include full three-dimensional analyses. Pérez-Aparicio and Ripoll [86] describe exact solutions for the analytical equations in the radial, circumferential, axial, and tangential (shear) directions. They also compare two failure criteria, discussed later. Zheng et al. and Eraslan and Akis [41,87] discuss the instantaneous stresses induced in variable thickness functionally graded rotating disks. A functionally graded rotor is one where the material properties smoothly vary as a function of radius, in contrast to a multi-rim rotor where material properties change discretely. These results show carefully controlling rotor thickness and material properties can significantly reduce induced stress and minimizing the risk of failure due to crack initiation and propagation. The methods discussed in these studies are valuable tools in understanding rotor

mechanics, however they fail to consider aspects such as energy storage capacity and manufacturing costs.

While there has been significant development in the understanding and optimization of quasi-static composite rotor stress responses, there has been comparatively little development in the understanding of viscoelastic and dynamic behavior of composite rotors, which is the subject matter of the following two sections. This is especially surprising given one of the primary advantages of FESS over other storage systems is the expected long lifetimes of these systems.

#### 2.4.4 Viscoelastic Analysis

Viscoelastic creep and stress relaxation continuously evolve over the operation of a FRP composite flywheel rotor. Viscoelasticity has been suggested to significantly affect the interface pressure at either the hub-rim or rim-rim interfaces, depending on rotor construction, which is critical for the integrity of rotors assembled via press-fitting. Creep rupture in the composite materials is an additional concern [88]. Trufanov and Smetannikov [89] investigated a flywheel rotor constructed from a variable thickness filament-wound composite wrapped in an organic plastic shell. They tracked the change in radial and circumferential stress at several key points over a simulated period of 10,000 hours. Depending on location in the shell, their results showed that circumferential tensile stresses can increase between 4% and 15% and radial compressive stresses could increase by up to 40%. In the composite rim, the maximum circumferential stress increased by 7.5%. At the same time the maximum radial stress decreased by 33%. The construction of this flywheel is unusual for modern high-speed flywheel rotors, however, these results demonstrate that radial and circumferential stresses are highly variable and the potential for creep rupture or loss of interfacial pressure between rotor components exists.

Portnov and Bakis [90] presented complete solutions to the analytical equilibrium equations including creep. They studied a thick unidirectional FRP composite rim with rectangular cross section filament-wound around a small metallic hub. Their results showed that after complete relaxation, radial strain was maximized at the outer radius of the rotor, with strains being predicted to be approximately three times larger than the circumferential strain at the same position. This further supports the conclusion that creep rupture may be of significant concern.

Subsequent studies by Tzeng et al. [91,92] simulated arbitrarily long composite flywheel rotors press-fit or wound onto metallic hubs similar to those seen in industry [93,94]. They employed the generalized PS assumption due to the assumed length of the rotor and predicted stress and displacement in the radial and circumferential direction after 1 year, 10 years, and infinite time ( $10^{10}$  years). Similar to previous work, Tzeng showed that radial stress could decrease by as much as 35% while circumferential stress could increase by up to 9%. Tzeng also studied flywheels with variable winding angles and found similar though slightly improved results.

While this body of work is compelling, the majority of it has been conducted analytically with relatively little available experimental data. Emerson [62] attempted to resolve this issue by,



first, measuring the transverse strength and modulus of a glass fiber composite used in flywheel rotor construction, to improve simulation reliability, and second, by taking in-situ strain measurements using optoelectronic strain measurements. The material testing was conducted according to the methods described in section 2.4.2. The flywheel measurements were to be conducted using a custom-built test apparatus. Unfortunately, this testing was inconclusive due to a series of mechanical failures and was not able to eliminate the possibility of creep significantly impacting rotor structural integrity.

While some studies suggest that over extremely long times of operation, e.g.  $10^{10}$  years or the time required to reach full relaxation, viscoelastic behavior of the composite can significantly impact rotor structural health by facilitating either creep rupture, the loss of rotor integrity by the loss of interfacial pressures between hub and rims, or both. However, the expected lifetime for flywheel rotors, as discussed, is between 10 and 20 years [5]. Further, many of these studies occurred on either thick composite disks or arbitrarily long flywheel rotors. Skinner and Mertiny addressed this issue in [16] where a carbon FRP composite flywheel rotor was simulated for up to 10 years. The analytical process they followed to simulate the rotor behavior is similar to that pursued by previous researchers, so it is worth taking a brief aside to discuss this work here.

The analytical methodology used for viscoelastic simulations is fundamentally a quasi-static analysis, therefore, the viscoelastic solution procedure requires approximating time-varying behavior through a number of discrete time and load steps. The response at each step is used to calculate stress for the flywheel rotor throughout the simulation. First, the rotor dimensions, material properties, and simulation parameters—time and velocity vectors of interest—are defined as inputs to the algorithm. Then, beginning at the first time and velocity of interest, the material stiffness matrix is calculated for each rim of the flywheel rotor. Next, the boundary conditions at each interface and at the inner and outer surface of the rotor are calculated. Through these steps the rotor response is calculated for the current time and velocity iteration. Finally, the algorithm proceeds to the next time and velocity of interest. Iteration continues for all discrete times and velocities of interest, which yields the induced stress for all points in the flywheel rotor at all times and velocities of interest.

The results from Skinner and Mertiny showed that during operation, radial and circumferential stresses in the carbon FRP composite rotor were predicted to decrease by 1% and 5%, respectively, [Figure 2.5]. Additionally, as was seen by other researchers, interfacial pressure was predicted to have the most significant variation with an overall decrease of up to 36%. Despite these changes, viscoelastic stress relaxation is not expected to cause complete loss of interfacial pressure between hub and rim during the expected lifetime, nor is it expected to be a primary cause of failure. It was postulated that viscoelastic behavior of the material may play a role in other failure modes, such as fatigue damage and matrix cracking, but is ultimately unlikely to be the dominant cause for rotor failure.

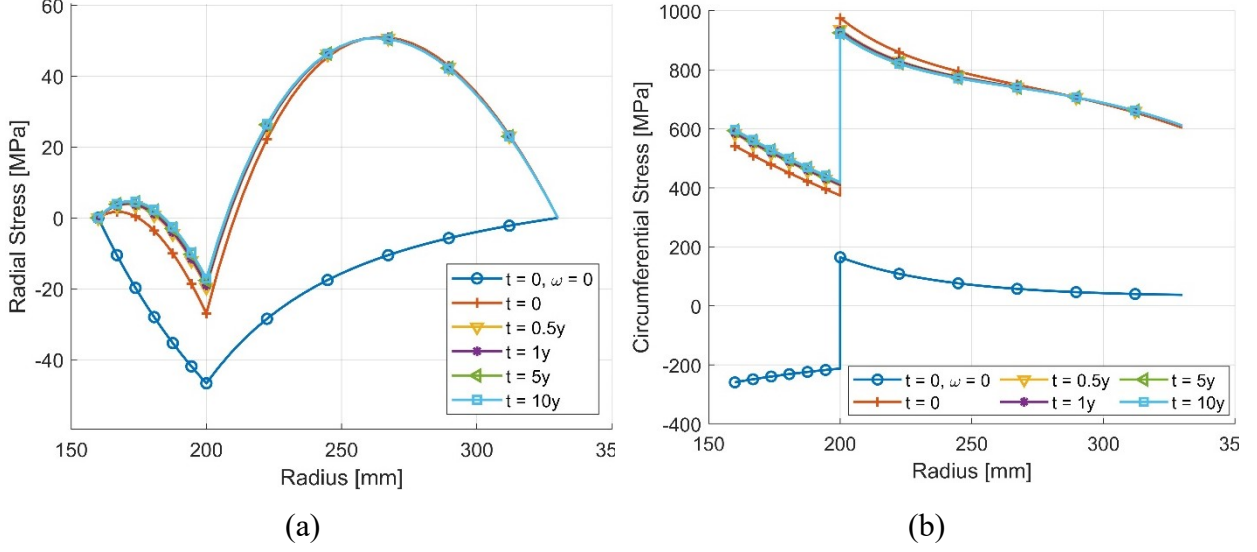


Figure 2.5: Evolution of (a) radial and (b) circumferential stresses at different times of operation (0 to 10 years) of a flywheel rotor with an aluminum hub and carbon FRP composite rim due to viscoelastic stress relaxation [16].

#### 2.4.5 Shear Stress

The presence of shear stresses in FRP composite flywheel rotors has not been studied extensively. Nevertheless, the analytical equilibrium equations have been defined for rotating anisotropic disks, and extensive work has been completed in this field for isotropic and functionally graded rotating disks of constant and variable thickness. An exact solution for the tangential (shear) equilibrium equation of a rotating disk was presented by Pérez Aparicio and Ripoll [86]. The equilibrium equation, given by equation 2.16, has a similar form to the radial equilibrium equation, equation 2.13,

$$\frac{d\tau_{r\theta}}{dr} + \frac{2}{r}\tau_{r\theta} + \rho\alpha r = 0 \quad 2.16$$

where  $\tau_{r\theta}$  is the in-plane shear stress and  $\alpha$  is angular acceleration. Shear strain is defined as,

$$\gamma_{r\theta} = \frac{dv}{dr} - \frac{v}{r} \quad 2.17$$

Solving the resulting second order inhomogeneous ordinary differential equation, in the same manner as previously discussed, yields the tangential stress and displacement equations,

$$v = C_1 r^{-1} + C_2 r + \frac{\rho\alpha}{8G_{r\theta}} r^3; \quad \tau_{r\theta} = G_{r\theta} \left[ -\frac{2C_1}{r^2} + \frac{\rho\alpha}{4G_{r\theta}} r^2 \right] \quad 2.18$$

where  $v$  is the tangential displacement, and  $C_1$  and  $C_2$  are integration constants. Notice that tangential stress depends on a single integration constant because when strain, equation 2.17, is substituted into tangential displacement the second integration constant,  $C_2$ , is eliminated. The integration constants can be found through the boundary conditions as functions of the rotor

geometry, density, shear modulus, and angular acceleration. Pérez Aparicio and Ripoll considered a worst-case scenario where peak shear stress is caused by a severe acceleration of  $3.6 \times 10^5$  rad/sec<sup>2</sup>. For this considered worst-case scenario, resulting stress states were described as possibly critical for the hub rather than the rotor.

Tang [95] conducted an early study on shear stress in accelerating disks mounted to a ridged shaft. They showed that shear stress was dependent on the acceleration and the ratio between the inner and outer rotor radius. When this ratio is greater than 0.15 the shear stress will increase drastically and may need to be considered when designing structural components.

Much of the studies on shear stress in rotating disks focuses on variable thickness and functionally graded materials for applications in turbines and engines. Reddy and Srinath [96] presented a method to study acceleration in high-temperature rotating disks with variable thickness. They showed that the cross section of the disk may have a significant impact on shear stress and should therefore not be discounted. Continuing with rotating disks for turbine applications, Eraslan and Akais [87] and Zheng et al. [41] presented a method to analyze instantaneous shear stress in rotating disks. They showed that carefully controlling the rotor cross section and properties produces an optimum stress profile. Zheng et al. also showed that the presence of shear stress can shift the maximum stress location from the inner radius to near the mid-radius, depending on shear stress magnitude and direction. Note, shear stress directionality is relative to the rotating direction where accelerating the rotor causes positive shear stress and decelerating the rotor causes negative shear stress. Shear direction is important, for example, for predicting failure such as using the Tsai-Wu criteria discussed below.

Salehian et al. [97] investigated instantaneous shear stress in functionally graded constant and variable thickness rotating disks. They conducted both analytical and numerical analyses. The functionally graded flywheels they studied featured increasing material density as a function of radius. They also showed that both methods are equally accurate and that shear stress can be significant for functionally graded materials.

Previous studies were conducted assuming an essentially instantaneous event subjecting a rotating disk to angular acceleration. However, in the context of FESS, shear stress created by accelerating or decelerating the flywheel rotor should be considered for typical FESS energy transfer, i.e., the supply or demand of power. The relationship between power and acceleration is found through the applied torque, such that,

$$P = T\omega; \quad T = I_r\alpha \quad 2.19$$

where  $P$  is power and  $T$  is torque. From equation (19) it is clear that power is related linearly to angular acceleration and velocity at a given instant. Further, from equation (18), shear stress is linearly related to angular acceleration. Therefore, even for constant acceleration, power varies over time, and so do radial and circumferential stresses as velocity changes due to angular

acceleration. Considering the opposite case of constant power, acceleration necessarily needs to vary. For example, at an initially low angular velocity and constant power supply, the flywheel rotor acceleration and shear stresses would be much larger than at a later time when velocity has increased due to the imposed acceleration.

Combining equations 2.18 and 2.19 it is possible to determine the stress state as a result of a given power supply or demand, and vice versa. Recalling the work by Pérez Aparicio and Ripoll [86] mentioned above, a flywheel rotor was simulated with inner radius, outer radius, height, and density of 0.08 m, 0.2 m, 0.06 m, and  $1800 \text{ kg/m}^3$ , respectively. For an angular velocity of 17,425 rpm ( $1,827.6 \text{ sec}^{-1}$ ) a supplied power of 1.67 GW is associated with an angular acceleration of  $3.6 \times 10^5 \text{ sec}^{-2}$  for 0.005 seconds. Pérez Aparicio and Ripoll explained that power supplied at this magnitude would occur in specific applications, such as military artillery, however, it is atypical for energy storage systems.

The shear stress investigations discussed above presented solutions to analytical equilibrium equations and described instantaneous behavior of variable thickness FRP and functionally graded rotating disks. Moreover, shear stress resulting from a given peak acceleration of a flywheel rotor was discussed. However, the technical literature is ambiguous regarding time-dependent behavior, evolution of the rotor stress states, and possible damage events resulting from typical operating conditions, i.e., repeated energy transfer cycles over the flywheel lifetime.

## 2.5 Failure Analysis

### 2.5.1 Failure Criteria

Several criteria have been applied to predicting failure of FRP composite flywheel rotors. A large body of the available research considers rotor failure a quasi-static process caused by excessive loading from centripetal forces due to rotation exceeding material ultimate strengths [45]. The most common failure models are the maximum stress or strain [98], von Mises [41], and Tsai-Wu failure criteria [16,99]. Also, attempts have been made to predict rotor failure with progressive damage models [100]. Other less common methods, such as the Christensen model [86], have been used to a limited extent for predicting the failure of composite flywheel rotors.

### 2.5.2 Maximum Stress Criterion

The maximum stress and maximum strain failure criteria are the most widely used due to their simple application and analysis. The maximum stress failure criterion defines the failure ratio in each material direction to be the ratio of the applied stress to the failure strength. Consider the failure stress in the fiber direction of the material in the tensile or compressive direction to be  $\sigma_{1t}$  or  $\sigma_{1c}$ , respectively. In the transverse directions the material is assumed to be transversely isotropic such that the 2 and 3 directions are congruent, thus  $\sigma_{2t} = \sigma_{3t}$  and  $\sigma_{2c} = \sigma_{3c}$ . Shear stress is dominated by matrix deformation  $\tau_{12}$  and  $\tau_{23}$ . With the applied stress tensor as  $[\sigma_\theta, \sigma_z, \sigma_r, \tau_{r\theta}]$ , the maximum stress failure criterion is defined as,

$$\frac{\sigma_\theta}{\sigma_{1t}} \leq 1 \text{ if } \sigma_\theta \geq 0 \text{ or } \frac{|\sigma_\theta|}{\sigma_{1c}} \leq 1 \text{ if } \sigma_\theta \leq 0,$$

$$\frac{\sigma_z}{\sigma_{2t}} \leq 1 \text{ if } \sigma_z \geq 0 \text{ or } \frac{|\sigma_z|}{\sigma_{2c}} \leq 1 \text{ if } \sigma_z \leq 0,$$

$$\frac{\sigma_3}{\sigma_{3t}} \leq 1 \text{ if } \sigma_r \geq 0 \text{ or } \frac{|\sigma_r|}{\sigma_{3c}} \leq 1 \text{ if } \sigma_r \leq 0,$$

2.20

$$\frac{|\tau_{r\theta}|}{\tau_{12}} \leq 0 \text{ and } \frac{|\tau_{rz}|}{\tau_{23}} \leq 0$$

Failure occurs when any of the above ratios is larger than unity. Similar inequalities can be written for the maximum strain criteria to find the ratio between applied strain and failure strain. While these criteria are well suited to predict failure when the primary failure mode is uniaxial loading, they neglect load interactions in a rotor.

### 2.5.3 Tsai-Wu Criterion

To address multiaxial loading conditions present in flywheel rotors, the Tsai-Wu failure criterion is frequently employed. The Tsai-Wu failure criterion involves independent interaction terms, considers strength parameters both for tension and compression, and enables treating different classes of materials, multi-axial stress, and multi-dimensional space [101]. As presented by Tsai and Wu, this method considers 27 independent terms which normalize the applied stress in a particular direction with the strength parameter in that direction. If the sum of these terms, called the failure index  $F$ , is equal to unity, failure is predicted. When applied to FRP flywheel rotors, the analysis problem is often simplified using material symmetry and certain modeling assumptions. For example, consider a thin, transversely isotropic FRP rotor operating at constant velocity, axial stress terms can be neglected, and all out-of-plane and shear terms vanish. Therefore, the Tsai-Wu criterion can be reduced to six terms. Depending on the material and modeling assumptions the exact number of terms that must be considered will vary. It is worth noting, when applied to an isotropic material with equal tensile and compressive strengths, the Tsai-Wu criteria will simplify to the von Mises failure criterion [102]. Therefore, the Tsai-Wu criterion can expediently be applied to multi-material flywheel rotors where the hub and rims may be constructed from materials that are either isotropic, e.g. metals, or anisotropic, e.g. FRP composites. The Tsai-Wu failure criterion, which has widely been applied for the failure prediction of FRP flywheel rotors for decades [16,32,99,103], is given for a three-dimensional transversely isotropic material as

$$F = F_{11}\sigma_1^2 + F_{22}(\sigma_2^2 + \sigma_3^2) + (2F_{22} - F_{44})\sigma_2\sigma_3 + 2F_{12}\sigma_1(\sigma_3 + \sigma_2) + F_1(\sigma_1 + \sigma_2) + F_2\sigma_3 + F_{44}\tau_{23}^2 + 2F_{66}(\tau_{12}^2) \quad 2.21$$

where  $F_{ij}$  are material coefficients dependent on the tensile and compressive strengths in each direction. A complete list of coefficients is available in [102]. The Tsai-Wu failure criterion can be modified to find the strength ratio ( $SR$ ), which is the ratio between the applied stress and the failure stress [16,80,100]. Failure is predicted when  $SR$  is greater than or equal to unity. This

approach provides an intuitive and easily represented term which facilitates the comparison of combined stresses across the entire flywheel rotor.

#### 2.5.4 Progressive Failure Analysis

Progressive failure analysis (PFA) has been applied to composite rotors and other structures in a number of studies in the preceding decade [30,100,104,105]. The premise underlying this approach is that composite materials may initially experience benign failure modes, e.g., matrix micro-cracking and interlaminar fracture, without complete loss of structural integrity. In this case the structure can continue to support applied loads until the accumulation of damage causes ultimate (catastrophic) failure. As applied to flywheel rotors, matrix damage such as cracking, delamination, and interlaminar fracture can be classified as benign failure modes while fiber rupture is considered catastrophic. This type of failure analysis is iterative. First, rotor simulations are conducted as discussed above to determine the maximum rotor velocity, and failure mode and location. In case of a benign failure mode, a knockdown factor that depends on the failure mode and the material characteristics is applied to the material properties at that location. This process is repeated until catastrophic failure is predicted [99].

PFA has been shown to accurately predict failure dynamics in woven composite disks [30], however, only limited studies have been conducted on filament-wound fly-wheel rotors [100]. In contrast to radially oriented fibers, in the woven disk designs the fibers provide the majority of radial support for the rotor to resist the centripetal forces. However, this is not the case for filament-wound flywheel rotors where radial stresses are borne chiefly by the matrix. Notably, circumferential matrix fracture in a filament-wound rotor would result in practically complete loss of radial integrity. Further, analytical methods described above assume the rotor to be continuous, however, progressive damage events may introduce discontinuities which may or may not violate this assumption. For example, if a damage location, such as a circumferential matrix fracture, is under compressive stress then crack closure may ensue, and hence, a continuity assumption could be upheld. In such as case, the fractured structure could be considered as two separate rims of the same material that are press-fitted together. However, under tensile stress the crack is forced open, violating the continuity assumption. Situation like these have not been addressed in the technical literature so further studies into PFA are needed to better understand its applicability to predicting FRP flywheel rotor failure.

## 2.6 Conclusions and Prospects

The present entry has presented an overview of the mechanical design of flywheel energy storage systems with discussions of manufacturing techniques for flywheel rotors, analytical modeling of flywheel rotors including multi-rim configurations, and contemporary failure criteria. Flywheel construction employing metallic hubs and rotors was also considered, as was the assembly of components by either filament-winding or press-fitting. Analytical techniques for modeling multi-rim flywheel rotors constructed from either metallic or FRP composite materials were described for quasi-static, viscoelastic, and variable angular velocity operating conditions.

Finally, contemporary failure criteria were discussed along with their advantages and limitations. Clearly, the understanding of flywheel rotor construction, analysis, and failure prediction has advanced significantly in the last several decades. Nevertheless, despite flywheel energy storage being a maturing field, some gaps in understanding still exist. For example, further investigations into the cost of manufacturing and the efficacy of variable winding angle flywheel rotors seems warranted. Further studies on the effects of shear stress and time-dependent effects, including cyclic loading and fatigue, in FRP composite rotors may be warranted to better understand behavior and improve failure predictions for flywheel rotors for long-term operation. Additionally, experimental data characterizing long-term behavior of FRP composite materials, especially in the transverse direction, would be valuable for improving the accuracy of long-term modeling of stress and failure predictions. Finally, progressive damage failure analysis, while compelling, would benefit substantially from experimental validation of modeling results to clearly discern its merit compared to other failure predictions.

## 2.7 References

1. British Petroleum Statistical Review of World Energy globally consistent data on world energy markets . and authoritative publications in the field of energy; 2021; Vol. 70;.
2. Chen, H.; Cong, T.N.; Yang, W.; Tan, C.; Li, Y.; Ding, Y. Progress in electrical energy storage system: A critical review. *Prog. Nat. Sci.* **2009**, *19*, 291–312, doi:10.1016/j.pnsc.2008.07.014.
3. Käberger, T. Progress of renewable electricity replacing fossil fuels. *Glob. Energy Interconnect.* **2018**, *1*, 48–52, doi:10.14171/j.2096-5117.gei.2018.01.006.
4. Moriarty, P.; Honnery, D. Can renewable energy power the future? *Energy Policy* **2016**, *93*, 3–7, doi:10.1016/j.enpol.2016.02.051.
5. Hadjipaschalis, I.; Poullikkas, A.; Efthimiou, V. Overview of current and future energy storage technologies for electric power applications. *Renew. Sustain. Energy Rev.* **2009**, *13*, 1513–1522, doi:10.1016/j.rser.2008.09.028.
6. Denholm, P.; O’Connell, M.; Brinkman, G.; Jorgenson, J. Overgeneration from Solar Energy in California: A Field Guide to the Duck Chart; Golden, CO;
7. Amiryar, M.E.; Pullen, K.R. A review of flywheel energy storage system technologies and their applications. *Appl. Sci.* **2017**, *7*, doi:10.3390/app7030286.
8. Sabihuddin, S.; Kiprakis, A.E.; Mueller, M. A numerical and graphical review of energy storage technologies. *Energies* **2015**, *8*, 172–216, doi:10.3390/en8010172.
9. Ilan, D. The ground stone components of drills in the ancient Near East: Sockets, flywheels, cobble weights, and drill bits. *J. Lithic Stud.* **2016**, *3*, 261–277, doi:10.2218/jls.v3i3.1642.
10. Skinner, M. Characterization of passive discharge losses in a flywheel energy storage system, University of Alberta, 2017.
11. Luo, X.; Wang, J.; Dooner, M.; Clarke, J. Overview of current development in electrical energy storage technologies and the application potential in power system operation. *Appl. Energy* **2015**, *137*, 511–536, doi:10.1016/j.apenergy.2014.09.081.
12. Hebner, R.; Beno, J.; Walls, A. Flywheel batteries come around again. *IEEE Spectr.* **2002**, *39*, 46–51, doi:10.1109/6.993788.
13. Bolund, B.; Bernhoff, H.; Leijon, M. Flywheel energy and power storage systems. *Renew. Sustain. Energy Rev.* **2007**, *11*, 235–258, doi:10.1016/j.rser.2005.01.004.
14. Krack, M.; Secanell, M.; Mertiny, P. Rotor Design for High-Speed Flywheel Energy Storage Systems. In *Energy Storage in the Emerging Era of Smart Grids*; InTech, **2011**.
15. Skinner, M.; Suess, M.; Secanell, M.; Mertiny, P. Design of a Composite Flywheel Rotor For Long-Term Energy Storage in Residential Applications. In Proceedings of the The Canadian Society of Mechanical Engineering International Congress; Canadian Society of Mechanical Engineers: Kelowna, BC, Canada, 2016; pp. 1–5.
16. Skinner, M.; Mertiny, P. Effects of Viscoelasticity on the Stress Evolution over the Lifetime of Filament-Wound Composite Flywheel Rotors for Energy Storage. *Appl. Sci.* **2021**, *11*, 9544, doi:10.3390/app11209544.

17. Pullen, K. The Status and Future of Flywheel Energy Storage. *Joule*. **2019**, 3, 1394-1399, doi: 10.1016/j.joule.2019.04.006.
18. The GYROBUS: Something New Under the Sun?". *Motor Trend*. **1952**. p. 37.
19. Wakefield, E. *History of the Electric Automobile: Hybrid Electric Vehicles*; Society of Automotive Engineers: Warrendale, PA, 1998; ISBN 978-0-7680-0125-9.
20. Weiss, C.C., Volvo Confirms Fuel Savings of 25 Percent with Flywheel KERS. Available online: <https://newatlas.com/volvo-flywheel-kers-testing/27273/> (accessed on 01/13/2022)
21. Available online: [https://www.porsche.com/international/\\_iceland\\_/motorsportandevents/motorsport/customerracing/racingcars/991-2nd-gt3-r/](https://www.porsche.com/international/_iceland_/motorsportandevents/motorsport/customerracing/racingcars/991-2nd-gt3-r/) (accessed on 01/13/2022)
22. Rupp, A.; Baier, H.; Mertiny, P.; Secanell, M. Analysis of a Flywheel Energy Storage System for Light Rail Transit. *Energy* **2016**, 107, 625–638, doi:10.1016/j.energy.2016.04.051.
23. Tarrant, C., Kinetic Energy Storage Wins Acceptance, Available online: <https://www.railwaygazette.com/kinetic-energy-storage-wins-acceptance/27250.article> (accessed on 01/13/2022)
24. NRStor Inc., 2 MW Minto Flywheel Facility: A Fast-Ramping Resource for Grid Regulation and other Electricity Services. Available online: <http://nrstor.com/2019/11/21/2-mw-minto-flywheel-facility-market-impact-case-study-power-advisory/> (accessed on: 01/13/2022)
25. Beacon Power, Operating Plants Stephentown, New York. Available online: <https://beaconpower.com/stephentown-new-york/> (accessed on 01/13/2022)
26. Amber Kinetics, The World's Only Flywheel Innovation Hub. Available online: <https://amberkinetics.com/installation/the-worlds-only-flywheel-innovation-hub/> (accessed on 01/13/2022)
27. Genta, G. *Kinetic Energy Storage: Theory and Practice of Advanced Flywheel Systems*; Butterworth-Heinemann: London, UK 2014; ISBN 0-408-01396-6.
28. Ha, S.K.; Han, H.H.; Han, Y.H. Design and manufacture of a composite flywheel press-fit multi-rim rotor. *J. Reinf. Plast. Compos.* **2008**, 27, 953–965, doi:10.1177/0731684407086625.
29. Kale, V.; Thomas, M.; Secanell, M. On determining the optimal shape, speed, and size of metal flywheel rotors with maximum kinetic energy. *Struct. Multidiscip. Optim.* **2021**, 64, 1481–1499, doi:10.1007/s00158-021-02935-x.
30. Wang, Y.; Dai, X.; Wei, K.; Guo, X. Progressive failure behavior of composite flywheels stacked from annular plain profiling woven fabric for energy storage. *Compos. Struct.* **2018**, 194, 377–387, doi:10.1016/j.compstruct.2018.04.036.
31. Ornaghi, H.L.; Neves, R.M.; Monticeli, F.M.; Almeida, J.H.S. Viscoelastic characteristics of carbon fiber-reinforced epoxy filament wound laminates. *Compos. Commun.* **2020**, 21, doi:10.1016/j.coco.2020.100418.
32. Takkar, S.; Gupta, K.; Tiwari, V.; Singh, S.P. Dynamics of Rotating Composite Disc. *J. Vib. Eng. Technol.* **2019**, 7, 629–637, doi:10.1007/s42417-019-00155-8.
33. Eggers, F.; Almeida, J.H.S.; Azevedo, C.B.; Amico, S.C. Mechanical response of filament wound composite rings under tension and compression. *Polym. Test.* **2019**, 78, 105951, doi:10.1016/j.polymertesting.2019.105951.
34. Rejab, R.; Kumar, N.M.; Ma, Q.; Idris, M.S.; Zhang, B.; Merzuki, M.N.M. Wireless technology applied in 3-axis filament winding machine control system using MIT app inventor. In Proceedings of the IOP Conference Series: Materials Science and Engineering; IOP Publishing, **2019**.
35. Wild, P.M.; Vickers, G.W. Analysis of filament-wound cylindrical shells under combined centrifugal, pressure and axial loading. *Compos. Part A Appl. Sci. Manuf.* **1997**, 28, 47–55, doi:10.1016/S1359-835X(96)00093-0.
36. Sayem Uddin, M.; Morozov, E. V.; Shankar, K. The effect of filament winding mosaic pattern on the stress state of filament wound composite flywheel disk. *Compos. Struct.* **2014**, 107, 260–275, doi:10.1016/j.compstruct.2013.07.004.
37. Tzeng, J.T.; Emerson, R.P.; O'Brien, D.J. Viscoelasticity Analysis and Experimental Validation of Anisotropic Composite Overwrap Cylinders. *Vol. 8 Mech. Solids, Struct. Fluids* **2012**, 429, doi:10.1115/IMECE2012-87818.
38. Ertz, G. Development, manufacturing and testing of a Multi-Rim ( Hybrid ) Flywheel Rotor, University of Alberta, 2014.
39. Skinner, M.; Mertiny, P. Experimental Characterization of Low-Speed Passive Discharge Losses of a Flywheel Energy Storage System. *Appl. Mech.* **2021**, 2, 1–15, doi:10.3390/applmech2010001.
40. Kale, V.; Secanell, M. A comparative study between optimal metal and composite rotors for flywheel energy storage systems. *Energy Reports* **2018**, 4, 576–585, doi:10.1016/j.egy.2018.09.003.
41. Zheng, Y.; Bahaloo, H.; Mousanezhad, D.; Mahdi, E.; Vaziri, A.; Nayeb-Hashemi, H. Stress analysis in functionally graded rotating disks with non-uniform thickness and variable angular velocity. *Int. J. Mech. Sci.* **2016**, 119, 283–293, doi:10.1016/j.ijmecsci.2016.10.018.



42. Yeh, K.Y.; Han, R.P.S. Analysis of high-speed rotating disks with variable thickness and inhomogeneity. *J. Appl. Mech. Trans. ASME* **1994**, *61*, 186–191, doi:10.1115/1.2901396.
43. Ertz, G.; Twiefel, J.; Krack, M. Feasibility Study for Small Scaling Flywheel-Energy-Storage Systems in Energy Harvesting Systems. *Energy Harvest. Syst.* **2014**, *1*, 233–241, doi:10.1515/ehs-2013-0010.
44. Ha, S.K.; Kim, M.H.; Han, S.C.; Sung, T.H. Design and spin test of a hybrid composite flywheel rotor with a split type hub. *J. Compos. Mater.* **2006**, *40*, 2113–2130, doi:10.1177/0021998306061324.
45. Hartl, S.; Schulz, A.; Sima, H.; Koch, T.; Kaltenbacher, M. A Static Burst Test for Composite Flywheel Rotors. *Appl. Compos. Mater.* **2016**, *23*, 271–288, doi:10.1007/s10443-015-9460-5.
46. Han, Y.; Ren, Z.; Tong, Y. General Design Method of Flywheel Rotor for Energy Storage System. *Energy Procedia* **2012**, *16*, 359–364, doi:10.1016/j.egypro.2012.01.059.
47. Mittelstedt, M.; Hansen, C.; Mertiny, P. Design and multi-objective optimization of fiber-reinforced polymer composite flywheel rotors. *Appl. Sci.* **2018**, *8*, doi:10.3390/app8081256.
48. Krack, M.; Secanell, M.; Mertiny, P. Cost optimization of hybrid composite flywheel rotors for energy storage. *Struct. Multidiscip. Optim.* **2010**, *41*, 779–795, doi:10.1007/s00158-009-0469-y.
49. Skinner, M.; Secanell Gallart, M.; Mertiny, P. Observed Effects of Vibrationally Induced Fretting on Bearing–Shaft Systems in Flywheel Energy Storage Systems. *J. Fail. Anal. Prev.* **2018**, *18*, doi:10.1007/s11668-018-0469-6.
50. Allam, M.N.M.; Tantawy, R.; Yousof, A.; Zenkour, A.M. Elastic and viscoelastic stresses of nonlinear rotating functionally graded solid and annular disks with gradually varying thickness. *Arch. Mech. Eng.* **2017**, *64*, 423–440, doi:10.1515/meceng-2017-0025.
51. Long, Z.; Zhiping, Q. Review of Flywheel Energy Storage System. In *Proceedings of ISES World Congress 2007 (Vol. I – Vol. V)*; Springer: Berlin, Germany, **2008**; pp. 2815–2819.
52. Lai, W.M.; Rubin, D.; Krempl, E. Chapter 5: The Elastic Solid. In *Introduction to Continuum Mechanics*; 2010; pp. 201–352.
53. Ding, H.; Chen, W.; L., Z. *Elasticity of Transversely Isotropic Materials*; Gladwell, G.M.L., Ed.; Springer: Dordrecht, **2006**; ISBN 9781119130536.
54. Zhao, J.; Song, X.; Liu, B. Standardized compliance matrixes for general anisotropic materials and a simple measure of anisotropic degree based on shear extension coupling coefficient. *Int J Appl Mech* **2011**, *8*, 1–28.
55. Lakes, R. *Viscoelastic Materials*; Cambridge University Press: Edinburgh, Cambridge, UK, **2009**; Vol. 1; ISBN 9780511626722.
56. Buchroithner, A.; Haidl, P.; Birgel, C.; Zarl, T.; Wegleiter, H. Design and experimental evaluation of a low-cost test rig for flywheel energy storage burst containment investigation. *Appl. Sci.* **2018**, *8*, doi:10.3390/app8122622.
57. Rojas, J.I.; Nicolás, J.; Crespo, D. Study on mechanical relaxations of 7075 (Al-Zn-Mg) and 2024 (Al-Cu-Mg) alloys by application of the time-temperature superposition principle. *Adv. Mater. Sci. Eng.* **2017**, *2017*.
58. Mahdavi, R.; Goodarzi, V.; Jafari, S.H.; Saeb, M.R.; Shojaei, S.; Khonakdar, H.A. Experimental analysis and prediction of viscoelastic creep properties of PP / EVA / LDH nanocomposites using master curves based on time – temperature superposition. *J Appl Polym Sci* **2018**, 1–12, doi:10.1002/app.46725.
59. Barbero, E.J. Time-temperature-age superposition principle for predicting long-term response of linear viscoelastic materials; 2nd ed.; Elsevier Ltd., **2019**; ISBN 9780081026014.
60. Yeow, Y.; Morris, D.; Brinson, H. Time-Temperature Behavior of a Unidirectional Graphite/Epoxy Composite. In *Fifth Conference on Composite Materials: Testing and Design*; ASTM International: West Conshohocken, PA, **1979**; pp. 263–263–19.
61. Koyanagi, J.; Sato, M. Time and temperature dependence of transverse tensile failure of unidirectional carbon fiber-reinforced polymer matrix composites; 2nd ed.; Elsevier Ltd., **2019**; ISBN 9780081026014.
62. Emerson, R.P. *Viscoelastic Flywheel Rotors: Modeling and Measurement*, Pennsylvania State University, 2002.
63. Aniskevich, A.; Glaskova-Kuzmina, T. Effect of moisture on elastic and viscoelastic properties of fiber reinforced plastics: Retrospective and current trends; 2nd ed.; Elsevier Ltd., **2019**; ISBN 9780081026014.
64. Alwis, K.G.N.C.; Burgoyne, C.J. Time-temperature superposition to determine the stress-rupture of aramid fibres. *Appl. Compos. Mater.* **2006**, *13*, 249–264, doi:10.1007/s10443-006-9017-8.
65. Sih, S.; Tsai, S. Automated shift for time-temperature superposition. *12th Int. Com. Compos. Mater.* **1999**, *51*.
66. Brinson, H.F.; Griffith, W.I.; Morris, D.H. Creep Rupture of Polymer-matrix Composites. **1981**, *57*, 329–335.
67. Brinson, H.F. Mechanical and optical viscoelastic characterization of Hysol 4290. *Exp. Mech.* **1968**, *8*, 561–566, doi:10.1007/bf02327519.
68. Williams, M.L.; Landel, R.F.; Ferry, J.D. The Temperature Dependence of Relaxation Mechanisms in Amorphous Polymers and Other Glass-forming Liquids. *J. Am. Chem. Soc.* **1955**, *77*, 3701–3707, doi:10.1021/ja01619a008.
69. Krauklis, A.E.; Akulichev, A.G.; Gagani, A.I.; Echtermeyer, A.T. Time-temperature-plasticization superposition principle: Predicting creep of a plasticized epoxy. *Polymers (Basel)*. **2019**, *11*, doi:10.3390/polym11111848.

70. Ganß, M.; Satapathy, B.K.; Thunga, M.; Weidisch, R.; Pötschke, P.; Janke, A. Temperature dependence of creep behavior of PP-MWNT nanocomposites. *Macromol. Rapid Commun.* **2007**, *28*, 1624–1633, doi:10.1002/marc.200700288.
71. Jain, N.; Verma, A.; Singh, V.K. Dynamic Mechanical Analysis and Creep-recovery behaviour of Polyvinyl Alcohol based cross-linked Biocomposite reinforced with Basalt fiber. *Mater. Res. Express* **2019**, *6*, doi:10.1088/2053-1591/ab4332.
72. Gergesova, M.; Zupančič, B.; Saprunov, I.; Emri, I. The closed form t-T-P shifting (CFS) algorithm. *J. Rheol. (N. Y. N. Y.)* **2011**, *55*, 1–16, doi:10.1122/1.3503529.
73. Bradshaw, R.D.; Brinson, L.C. Recovering nonisothermal physical aging shift factors via continuous test data: Theory and experimental results. *J. Eng. Mater. Technol. Trans. ASME* **1997**, *119*, 233–241, doi:10.1115/1.2812250.
74. Sullivan, J.L. Creep and physical aging of composites. *Compos. Sci. Technol.* **1990**, *39*, 207–232, doi:10.1016/0266-3538(90)90042-4.
75. Lou, Y.C. Viscoelastic Characterization of Nonlinear Fiber-Reinforced Plastic. *J. Compos. Mater.* **1971**, *5*, 208–234.
76. Stinchcomb, W.W.; Bakis, C.E. Fatigue Behavior of Composite Laminates. *Compos. Mater. Ser.* **1991**, *4*, 105–180, doi:10.1016/B978-0-444-70507-5.50008-1.
77. Lekhnitskiy, S.G. Anisotropic Plates, Air Force Systems Command: Moscow, **1957**.
78. Chdnis, C.C.; Kiruly, L.J. Rim-Spoke Composite Flywheels - Stress a N D Vibration Analysis. **1976**.
79. Gabrys, C.W.; Bakis, C.E. Design and Testing of Composite Flywheel Rotors. *Compos. Mater. Test. Des. Thirteen. Vol. ASTM STP 1242* **1997**, 1–22.
80. Ha, S.K.; Yang, H.-I.; Kim, D.-J. Optimum design of a hybrid composite flywheel with permanent magnet rotor. *J. Compos. Mater.* **1999**, *33*, 1544–1575.
81. Kelly, P. Mechanics Lecture Notes Available online: <http://homepages.engineering.auckland.ac.nz/~pkel015/SolidMechanicsBooks/index.html>.
82. Ha, S.K.; Kim, D.J.; Sung, T.H. Optimum design of multi-ring composite flywheel rotor using a modified generalized plane strain assumption. *Int. J. Mech. Sci.* **2001**, *43*, 993–1007, doi:10.1016/S0020-7403(00)00047-3.
83. Hearn, C.S.; Flynn, M.M.; Lewis, M.C.; Thompson, R.C.; Murphy, B.T.; Longoria, R.G. Low cost flywheel energy storage for a fuel cell powered transit bus. *VPPC 2007 - Proc. 2007 IEEE Veh. Power Propuls. Conf.* **2007**, 829–836, doi:10.1109/VPPC.2007.4544239.
84. Krack, M.; Secanell, M.; Mertiny, P. Advanced optimization strategies for cost-sensitive design of energy storage flywheel rotors. *J. Adv. Mater.* **2011**, *43*, 65–78, doi:10.1002/lary.24014.
85. Kheawcum, M.; Sangwongwanich, S. A Case Study on Flywheel Energy Storage System Application for Frequency Regulation of Islanded Amphoe Mueang Mae Hong Son Microgrid. In Proceedings of the 17th International Conference on Electrical Engineering/Electronics, Computer, Telecommunications and Information Technology, ECTI-CON 2020; **2020**; pp. 421–426.
86. Pérez-Aparicio, J.L.; Ripoll, L. Exact, integrated and complete solutions for composite flywheels. *Compos. Struct.* **2011**, *93*, 1404–1415, doi:10.1016/j.compstruct.2010.11.011.
87. Eraslan, A.N.; Akis, T. On the plane strain and plane stress solutions of functionally graded rotating solid shaft and solid disk problems. *Acta Mech.* **2006**, *181*, 43–63, doi:10.1007/s00707-005-0276-5.
88. Saleeb, A.F.; Arnold, S.M.; Al-Zoubi, N.R. A study of time-dependent and anisotropic effects on the deformation response of two flywheel designs. *ASTM Spec. Tech. Publ.* **2003**.
89. Trufanov, N.A.; Smetannikov, O.Y. Creep of Composite Energy Accumulators. *Strength Mater.* **1991**, *23*, 671–675.
90. Portnov, G.G. Estimation of Limit Strains in Disk-Type Flywheels Made of Compliant Elastomeric Matrix Composite Undergoing Radial Creep. *Mech. Compos. Mater.* **2000**, *36*, 55–58.
91. Tzeng, J.T. Viscoelastic analysis of composite flywheel for energy storage; Army Research Laboratory, **2001**;
92. Ghosh, T.N.; Tzeng, J.T.; Emerson, R.P.; O'Brien, D.J.; Ghosh, T.N. Viscoelasticity Analysis and Experimental Validation of Anisotropic Composite Overwrap Cylinders. *Trans. Ophthalmol. Soc. U. K.* **2012**, *101*, 200–202, doi:10.1106/002199802021464.
93. Levistor Boosting Forecourt Grid Power for the Next Generation of Fast Charging Electric Vehicles Available online: <https://levistor.com/#about>.
94. Stornetic GmbH Powerful Storage System for Grid Services Available online: [https://stornetic.com/assets/downloads/stornetic\\_general\\_presentation.pdf](https://stornetic.com/assets/downloads/stornetic_general_presentation.pdf).
95. Tang, S. Note on acceleration stress in a rotating disk. *Int. J. Mech. Sci.* **1970**, *12*, 205–207, doi:10.1016/0020-7403(70)90020-2.
96. Reddy, T.Y.; Srinath, H. Effects of acceleration stresses on the yielding of rotating disks. *Int. J. Mech. Sci.* **1974**, *16*, 593–596.

97. Salehian, M.; Shahriari, B.; Yousefi, M. Investigating the effect of angular acceleration of the rotating disk having variable thickness and density function on shear stress and tangential displacement. *J. Brazilian Soc. Mech. Sci. Eng.* **2019**, *41*, 1–11, doi:10.1007/s40430-018-1523-8.
98. Li, S. The Maximum Stress Failure Criterion and the Maximum Strain Failure Criterion: Their Unification and Rationalization. *J. Compos. Sci.* **2020**, *4*, doi:10.3390/jcs4040157.
99. Ha, S.K.; Lee, D.G.; Kim, D.J. Optimization of hybrid composite rotor in flywheel battery. *SAE Tech. Pap.* **1998**, doi:10.4271/981899.
100. Corbin, C.K. Burst failure prediction of composite flywheel rotors: A progressive damage approach via stiffness degradation, Stanford University, **2005**.
101. Tsai, S.W.; Wu, E.M. A General Theory of Strength for Anisotropic Materials. *J Comp Mater* **1971**, *5*, 58–80.
102. Li, S.; Sitnikova, E.; Liang, Y.; Kaddour, A.S. The Tsai-Wu failure criterion rationalised in the context of UD composites. *Compos. Part A Appl. Sci. Manuf.* **2017**, *102*, 207–217, doi:10.1016/j.compositesa.2017.08.007.
103. Roy, A.K.; Tsai, S.W. Design of Thick Composite Cylinders. *J. Press. Vessel Technol.* **2009**, *110*, 255, doi:10.1115/1.3265597.
104. Chen, Q.; Li, C.; Tie, Y.; Liu, K. Progressive Failure Analysis of Composite Flywheel Rotor Based on Progressive Damage Theory. *J. Mech. Eng.* **2013**, *49*, 1–6.
105. Kotelnikova-Weiler, N.; Baverel, O.; Ducoulombier, N.; Caron, J.F. Progressive damage of a unidirectional composite with a viscoelastic matrix, observations and modelling. *Compos. Struct.* **2018**, *188*, 297–312, doi:10.1016/j.compstruct.2017.12.067.

### 3 Viscoelastic Modeling

The following chapter is reproduced verbatim from *Effects of Viscoelasticity on the Stress Evolution of the Lifetime of Filament-Wound Composite Flywheel Rotors for Energy Storage* published in *Applied Sciences*, 2021 volume 11 number 20 page 9544. An analytical model capable of predicting the viscoelastic behavior of the flywheel rotor is developed. Then this model is used to simulate an expected 10-year operation lifetime time and the Tsai-Wu failure criteria is applied to predict rotor failure. Analytical modeling will progress in two directions. The first, discussed here, investigates the longer term behavior of the rotor by holding energy transfer into or out of the FESS at zero, i.e. acceleration is zero, while simulating the rotor spinning at a high angular velocity for extended periods of time. The second, discussed in chapter 4, assumes energy transfer is a constant non-zero value, i.e. acceleration is greater than zero. Chapter 3 addresses the viscoelastic concerns in the first two primary objectives of this thesis.

#### 3.1 Introduction

State-of-the-art high-speed flywheel energy storage systems (FESS) are recognized for several advantageous characteristics including a high charge and discharge rate, lifetimes ranging from 10 to 20 years and high specific energy up to  $100 \text{ Wh}\cdot\text{kg}^{-1}$  [1]. Further, they are unaffected by depth of discharge or cycling effects common to electrochemical batteries and have a relatively high cycle efficiency—up to 95% depending on the electrical components [2]. While the high efficiency and long expected lifetime make FESS an attractive alternative over other short- and medium-term energy storage options, these same attributes pose design and operational challenges.

The majority of studies on fiber reinforced polymer (FRP) composite flywheel rotors have focused on instantaneous, or time-independent, behavior of composite rotors and hubs to optimize performance or minimize cost [3–5]. If rotor failure is considered, it is typically seen as a quasi-static process caused by excessive centrifugal loading exceeding material ultimate strengths [6]. While attempts have been made to predict rotor failure with progressive damage models [7], they largely neglect to incorporate viscoelasticity into the stress and failure analyses. It has been theorized that changes in the interfacial compressive forces could lead to rim separation or creep rupture [8], yet the number of studies on viscoelastic behavior in composite rotors supporting this notion are limited.

Some works presented solutions for the boundary-value problem presented by flywheel rotors constructed of viscoelastic materials and discussed creep effects [9, 10]. Trufanov and Smetannikov [9] focused on flywheel rotors with an outer shell supporting an inner composite rim. Additionally, the rim is of non-uniform cross sections and features a variable winding angle, neither of which are commonly used in modern FESS [11, 12]. Portnov [10] discussed a solution to the equilibrium equations to determine creep strain in rotating disks. Tzeng [13] expanded on previous works by simulating filament-wound composite flywheel rotors with uniform rotor cross section and discussing viscoelastic behavior at 10 years and infinite time ( $10^{10}$  h). Tzeng showed that viscoelastic stress relaxation of approximately 35% in the radial direction and a corresponding

increase of approximately 9% in the circumferential direction can occur over the lifetime of the rotor. Emerson [14] conducted experimental investigations on flywheel rotors subjected to three temperatures and speed profiles over the course of 2 months using optoelectronic strain measurements. While rotor creep tests were inconclusive due to a mechanical failure, this work did not rule out any significant impact of creep on strains imposed for the press-fit assembly of the rotor. A similar conclusion was found elsewhere [15].

While there have been developments in the understanding of viscoelastic behavior of flywheel rotors, related insights do not necessarily translate well to typical use cases. For example, FESS in public transit [16] are installed with a vacuum enclosure that minimizes temperature fluctuations, and expected lifetimes are 10 to 20 years. In addition, load cycling occurs every few minutes, with viscoelastic effects effectively being negligible in between cycles. For other promising FESS applications, such as electric vehicle (EV) charging and renewable energy grid support, cycle times are likely much longer than for FESS in public transit, yet temperature conditions and timeframes would be similar.

The present study seeks to describe the viscoelastic behavior of composite flywheel rotors during their expected lifetimes using a computational algorithm to predict the stress evolution in the rotor. Additionally, the Tsai-Wu criterion is used to describe the total stress state, combining radial, circumferential, and axial stress to predict rotor failure. The simulated rotor material is a filament-wound carbon fiber reinforced polymer (CFRP) composite [17–19], similar to those typically used in flywheel rotor construction, making its application here appropriate. The rotor also includes an aluminum hub that facilitates the connection between the motor/generator unit and the bearing system. The effects of creep and viscoelastic stress relaxation on a flywheel rotor are examined with respect to the stress evolution over the lifetime of the system.

## 3.2 Composite Flywheel Rotor Modeling

### 3.2.1 Analytical Model Description

The analytical model has been discussed in several publications, therefore only a brief description will be provided here. While the present study focuses on the solution of a single-rim rotor, the analysis can be generalized to multi-rim rotors as described in [20], variable thickness rotors [21], and functionally graded materials [22]. The stress development in the thick composite rotor is assumed to be axisymmetric, meaning the resultant stresses and strains are independent of the circumferential coordinate. The material used for these rotors is a unidirectional filament-wound FRP composite where the winding angle is taken to be circumferential, i.e.,  $90^\circ$ . Hence, the composite is assumed to be transversely isotropic. Additionally, it was assumed the aluminum hub and composite rim are permanently bonded, that is, the model is unable to simulate separation between hub and rim. However, the latter condition is indicated by interfacial radial stress being greater than or equal to zero. Due to axisymmetry, the rotor response must only satisfy the governing equation in the radial direction [23]. The stress equilibrium equation in cylindrical coordinates is given as [24]

$$\frac{\partial \sigma_r}{\partial r} + \frac{\sigma_r - \sigma_\theta}{r} + \rho r \omega^2 = 0, \quad 3.1$$

where  $\sigma_r$  and  $\sigma_\theta$  are the radial and circumferential hoop stresses, which are the only non-trivial terms in the stress matrix;  $\rho$  is the material density; and  $\omega$  is the rotor angular velocity. The stress-strain relationship is defined as

$$\begin{Bmatrix} \sigma_\theta \\ \sigma_z \\ \sigma_r \\ \sigma_{\theta z} \end{Bmatrix} = \begin{bmatrix} Q_{11} & Q_{12} & Q_{13} & 0 \\ Q_{21} & Q_{22} & Q_{23} & 0 \\ Q_{31} & Q_{32} & Q_{33} & 0 \\ 0 & 0 & 0 & Q_{66} \end{bmatrix} \begin{Bmatrix} \varepsilon_\theta \\ \varepsilon_z \\ \varepsilon_r \\ \varepsilon_{\theta z} \end{Bmatrix}, \quad 3.2$$

where  $[Q]$  is the stiffness matrix and  $\{\varepsilon\}$  is the strain vector. Note that the  $z$ -coordinate is associated with the rotor axial direction. The  $[Q]$  matrix is the inverse of the compliance matrix  $[S]$  [25], such that

$$[Q] = [S]^{-1} = \begin{bmatrix} S_{11} & S_{12} & S_{13} & 0 \\ S_{21} & S_{22} & S_{23} & 0 \\ S_{31} & S_{32} & S_{33} & 0 \\ 0 & 0 & 0 & S_{66} \end{bmatrix}^{-1}. \quad 3.3$$

Considering equation 3.2, the compliance matrix must define the behavior in the circumferential (parallel to fibers), radial (transverse to fibers), axial (transverse to fibers), and shear directions. Since the rotor material is assumed to be transversely isotropic with no applied shear forces, the symmetric matrix simplifies from 10 unique terms to seven. The strain in the circumferential and radial directions can be written as, respectively,

$$\varepsilon_\theta = \frac{u_r}{r} \text{ and } \varepsilon_r = \frac{\partial u_r}{\partial r}, \quad 3.4$$

where  $u_r$  is the displacement in the radial direction and  $r$  is an arbitrary location along the rotor radial direction. Invoking a plane strain assumption, strain in the axial and shear directions is defined correspondingly by Equation 3.5. The appropriateness of this assumption will be discussed later in this text.

$$\varepsilon_z = 0 \text{ and } \varepsilon_{\theta z} = 0. \quad 3.5$$

Combining Equations 3.1, 3.2, and 3.4 yields a second order inhomogeneous ordinary differential equation. Solving this equation gives the local displacement and local stress at an arbitrary radius defined as

$$u_r = -\rho\omega^2\varphi_0r^3 + C_1\varphi_1r^\kappa + C_2\varphi_2r^{-\kappa}, \quad 3.6$$

$$\sigma_r = -\rho\omega^2\varphi_3r^2 + C_1r^{\kappa-1} + C_2r^{-\kappa-1}. \quad 3.7$$

The  $C$  parameters are integration constants dependent on the boundary conditions and material properties. The  $\kappa$  and  $\varphi$  coefficients are intermediate terms dependent on the stiffness matrix, defined as follows:

$$\begin{aligned}\kappa &= \sqrt{\frac{Q_{11}}{Q_{33}}}, \\ \varphi_0 &= \frac{1}{(9-\kappa^2)Q_{33}}, \varphi_1 = \frac{1}{Q_{13}+\kappa Q_{33}}, \\ \varphi_2 &= \frac{1}{Q_{13}-\kappa Q_{33}}, \varphi_3 = \frac{3Q_{33}+Q_{13}}{(9-\kappa^2)Q_{33}}.\end{aligned}\tag{3.8}$$

Then, upon determining the integration constants, the radial displacement (Equation 3.6) and radial stress (Equation 3.7) can be found using Equation 3.8. Circumferential stress can be found by combining Equations 3.4, 3.6, and 3.8 in conjunction with the stress-strain relationship (Equation 3.2).

Generalizing to a multi-rim flywheel rotor with an arbitrary number of rims, i.e., the rotor is constructed from  $N$  rims labeled  $j$  and can vary between  $j = 1, 2, 3 \dots N$ , then the continuity condition at the interface states,

$$\sigma_{r,r_o}^j = \sigma_{r,r_i}^{j+1}; \quad u_{r,r_o}^j = u_{r,r_i}^{j+1}.\tag{3.9}$$

where  $\sigma_{r,r_o}^j$  is the radial stress at the outer radius,  $r_o$ , in the  $j^{\text{th}}$  rim, and  $\sigma_{r,r_i}^{j+1}$  is the radial stress at the inner radius,  $r_i$ , of the next,  $j+1$ , rim. The same notation is used to describe the radial displacements,  $u_r$ , at the interface.

### 3.2.2 Tsai-Wu Failure Criterion

The general Tsai-Wu failure criterion, described in [6, 7, 26, 27], can be reduced to nine terms for a transversely isotropic material and considering the absence of shear stresses. This criterion finds a relationship,  $F$ , between the applied stress tensor and the material tensile strengths and predicts failure when  $F \geq 1$ . At failure, the stress tensor represents the maximum allowable stress and  $F$  equals unity. Hence, the Tsai-Wu failure criterion can be written as

$$\begin{aligned}F &= F_{11}(\sigma_1^{\text{all}})^2 + F_{22}(\sigma_2^{\text{all}})^2 + F_{33}(\sigma_3^{\text{all}})^2 + 2F_{12}\sigma_1^{\text{all}}\sigma_2^{\text{all}} + 2F_{13}\sigma_1^{\text{all}}\sigma_3^{\text{all}} \\ &\quad + 2F_{23}\sigma_2^{\text{all}}\sigma_3^{\text{all}} + F_1\sigma_1^{\text{all}} + F_2\sigma_2^{\text{all}} + F_3\sigma_3^{\text{all}} = 1,\end{aligned}\tag{3.10}$$

where  $[\sigma_i^{\text{all}}]$  is the allowable, or failure, stress tensor where  $i = 1, 2$ , or  $3$ . Note as applied herein, the 1 and 3 directions refer to the circumferential and radial stress, respectively, while the 2 direction refers to the axial direction. While the plane strain condition eliminates axial strain, it allows for axial stress; therefore, it is included in the failure criterion. Then,

$$\begin{aligned}F_{11} &= \frac{1}{\sigma_{1t}\sigma_{1c}}, F_{22} = F_{33} = \frac{1}{\sigma_{3t}\sigma_{3c}}, F_1 = \frac{1}{\sigma_{1t}} - \frac{1}{\sigma_{1c}}, \\ F_2 = F_3 &= \frac{1}{\sigma_{3t}} - \frac{1}{\sigma_{3c}}, F_{12} = F_{13} = \frac{-1}{2\sqrt{\sigma_{1t}\sigma_{1c}\sigma_{3t}\sigma_{3c}}}, F_{23} = F_{22} - \frac{1}{2\tau_{13}^2},\end{aligned}\tag{3.11}$$

where the subscripts  $t$  and  $c$  refer to the tensile and compressive strengths, respectively. The strength coefficients in the 2 and 3 directions are equal due to the transversely isotropic assumption, discussed further in Section 3.1.

It is common, and more valuable, to define the relationship between maximum allowable stress and the applied stress as the failure ratio ( $R$ ) [7]. This relationship is found by combining the

maximum allowable stress tensor,  $(\sigma_i^{\text{all}})$ , with the applied stress tensor,  $(\sigma_i^{\text{app}})$ , multiplied with  $R$  such that

$$\sigma_1^{\text{all}} = R\sigma_1^{\text{app}}, \sigma_2^{\text{all}} = R\sigma_2^{\text{app}}, \sigma_3^{\text{all}} = R\sigma_3^{\text{app}}. \quad 3.12$$

Then, substituting Equation (12) into Equation (10) yields a quadratic equation, i.e.

$$0 = \left[ F_{11}(\sigma_1^{\text{app}})^2 + F_{22}(\sigma_2^{\text{app}})^2 + F_{33}(\sigma_3^{\text{app}})^2 + 2F_{12}\sigma_1^{\text{app}}\sigma_2^{\text{app}} + 2F_{13}\sigma_1^{\text{app}}\sigma_3^{\text{app}} + 2F_{23}\sigma_2^{\text{app}}\sigma_3^{\text{app}} \right] R^2 + \left[ F_1\sigma_1^{\text{app}} + F_2\sigma_2^{\text{app}} + F_3\sigma_3^{\text{app}} \right] R - 1. \quad 3.13$$

Solving this quadratic equation for  $R$  defines the failure ratio. When  $(\sigma_i^{\text{app}})$  equals  $(\sigma_i^{\text{all}})$ , then  $R$  equals unity, indicating failure, whereas  $R > 1$  indicates  $(\sigma_i^{\text{app}})$  is less than  $(\sigma_i^{\text{all}})$  and no failure is predicted. It is convenient to define a strength ratio ( $SR$ ) to be  $1/R$ , as this is more intuitive conceptually and graphically [7]. Failure under this criterion is predicted when  $SR \geq 1$ .

### 3.2.3 Computational Methodology

The computational methodology has been discussed elsewhere [13, 14], so only a brief description is provided here. The analytical model, described in Section 3.2.1, assumes constant loads, therefore the viscoelastic solution procedure requires approximating time-varying behavior through a number of discrete time and load steps. The response at each step is used to calculate stresses and  $SR$  for the flywheel throughout the simulation. First, the rotor dimensions, material properties, and simulation parameters—including time and velocity vectors of interest—are defined as inputs to the algorithm. Then, beginning at the first time and velocity of interest, the material stiffness matrix is calculated for each rim of the flywheel rotor (here, a single-rim rotor is considered). Next, the boundary conditions at each interface and at the inner and outer surface of the rotor are calculated. Using this information, the rotor response and  $SR$  are calculated for the given time and velocity. Finally, the algorithm iterates to the next time and velocity. This continues for all discrete times and velocities of interest, which yields the induced stresses and  $SR$  for all points in the flywheel rotor at all times and velocities of interest.

## 3.3 Modeling Parameters

The flywheel rotor simulated in this study is constructed from a single CFRP rim press-fitted to an aluminum hub. The hub and rim are simulated as cylinders with rectangular cross sections.

### 3.3.1 Materials

The aluminum and CFRP are both assumed to be uniform throughout the rotor and free of defects. Referring to [28], the aluminum exhibits negligible viscoelastic response at temperatures below 50 °C, therefore viscoelastic behavior in the aluminum is not considered. The material properties of the chosen 7075-T6 aluminum are found in [29].

The composite considered in this study is IM7 carbon fiber (Hexcel Corp., Stamford, CT, USA) with an 8552 epoxy resin system (Hexcel Corp., Stamford, CT, USA), as described by Tzeng



et al. [30]. The filament winding process employed for fabricating CFRP flywheel rotors utilizes continuous unidirectional fiber reinforcement, which creates a transversely isotropic behavior [31].

In the CFRP rim, the fibers run circumferentially and display only subtle viscoelastic characteristics. The long-term behavior of a CFRP in the transverse direction is often described using a time-temperature superposition (TTSP) master curve. This curve is created by measuring short-term creep data at various elevated temperatures. Then, a shift factor is applied to the elevated temperature experimental data to shift them temporally, increasing the time axis while decreasing the temperature. Shifting all elevated temperature experimental data creates a smooth master curve representing the lifetime strain and compliance behavior, provided the applied stress from experimentation is known. Finally, curve fitting is performed on the master curve to generate empirical equations for the creep compliance. TTSP is applicable for modeling linear viscoelasticity, which is acceptable for this application as permanent damage, material aging, and other higher order effects are excluded from this simulation. The transverse compliance equations published by Tzeng et al. [30] are given in Table 3.1 and Equation 3.14, as are the aluminum properties, where variable  $t$  indicates time. The tensile strengths of the CFRP and yield strength of the aluminum necessary for the Tsai-Wu criteria are given in Table 3.2.

*Table 3.1: Material properties for aluminum 7075-T6 [29] and viscoelastic equations for CFRP [30] used in the present study.*

<b>Material</b>	$S_{11}$ [Pa <sup>-1</sup> ]	$S_{22}$ [Pa <sup>-1</sup> ]	$S_{33}$ [Pa <sup>-1</sup> ]	$S_{66}$ [Pa <sup>-1</sup> ]	$\nu$
Aluminum	$1.39 \times 10^{-11}$	$1.39 \times 10^{-11}$	$1.39 \times 10^{-11}$	$3.72 \times 10^{-11}$	0.33
CFRP	$S_{11}^0(t)^{0.01}$	$S_{22}^0(t)^{0.03}$	$S_{33}^0(t)^{0.03}$	$S_{66}^0(t)^{0.03}$	0.31

$$S_{11}^0 = 9.0 \times 10^{-12} \text{ Pa}^{-1}; S_{22}^0 = S_{33}^0 = 1.1 \times 10^{-10} \text{ Pa}^{-1}; S_{66}^0 = 2.0 \times 10^{-10} \text{ Pa}^{-1}. \quad 3.14$$

*Table 3.2: Directionally dependent strengths of CFRP and failure strength of aluminum used to find SR from the Tsai-Wu failure criterion.*

<b>Material</b>	$\sigma_{1t}$ [MPa]	$\sigma_{1c}$ [MPa]	$\sigma_{3t}$ [MPa]	$\sigma_{3c}$ [MPa]	$\tau$ [MPa]
CFRP	2,720	1,689	64.1	307	137
Aluminum	572	572	572	572	331

### 3.3.2 Flywheel Rotor Simulation Parameters

The vast majority of operational flywheel rotors are constructed from a metallic hub and composite rim, so it was decided the present study would maintain this trend to increase its applicability. Further, the objective of this study is to investigate the effects of viscoelastic behavior on a filament wound composite flywheel rotors suitable for energy storage, so the overall dimensions were chosen to highlight this behavior. Consider, energy storage capacity increase with radius and angular, however these same parameters also increase centrifugal stresses. A parametric investigation was conducted to better understand the effect of increasing the inner and outer radii of the rim and hub. The present dimensions were chosen because they are an advantageous balance between maximizing energy capacity, minimizing induced stresses, and highlighting the viscoelastic behavior. These parameters should not be viewed as an optimal solution to this problem, merely one possible solution chosen specifically for the objectives of this study.

Two cases were considered to investigate the effects of viscoelastic behavior on the flywheel rotor. The first case simulates a worst-case scenario for creep and viscoelastic stress relaxation in the flywheel rotor. The second case more closely simulates a realistic scenario of an FESS experiencing daily charge/discharge cycles. The FESS capacity and flywheel rotor dimensions are identical between the two cases. Recent studies on appropriate sizing of FESS have identified various values ranging between 3 kWh and 20 kWh for residential applications, light rail transit, electric vehicle charging, and frequency regulation for microgrid applications [16,31,32]. For the present study, a capacity of 10 kWh was chosen as it is situated in the middle of the range for the applications mentioned above. Note that energy storage capacity scales linearly with rotor height (axial dimension), and scaling is not expected to affect creep behavior appreciably, so the chosen rotor configuration can easily be scaled up or down to adjust for a given application. This scaling could be done, as suggested in [33], by stacking individual composite disks on top of one another to form the rotor, in which case, the analysis for each individual disk is performed as described herein while capacity may be increased or decreased as needed. To illustrate the chosen capacity, a recent study [34] on residential photovoltaic (PV) potential in Lethbridge, Alberta, Canada, identified that the majority of residential homes had roof space for up to 10 kW of solar PV, meaning the FESS in this study could reasonably be expected to reach full capacity throughout the day even under less-than-ideal irradiation conditions, in order to provide power during high demand times such as in the evening. The simulated flywheel rotor dimensions and energy capacity used in this study are given in Figure 3.1 and Table 3.3. Note that changing power demand would necessarily require accelerating or decelerating the flywheel rotor, imposing shear stresses, which is not included in the current model, hence justifying the aforementioned biaxial stress condition.

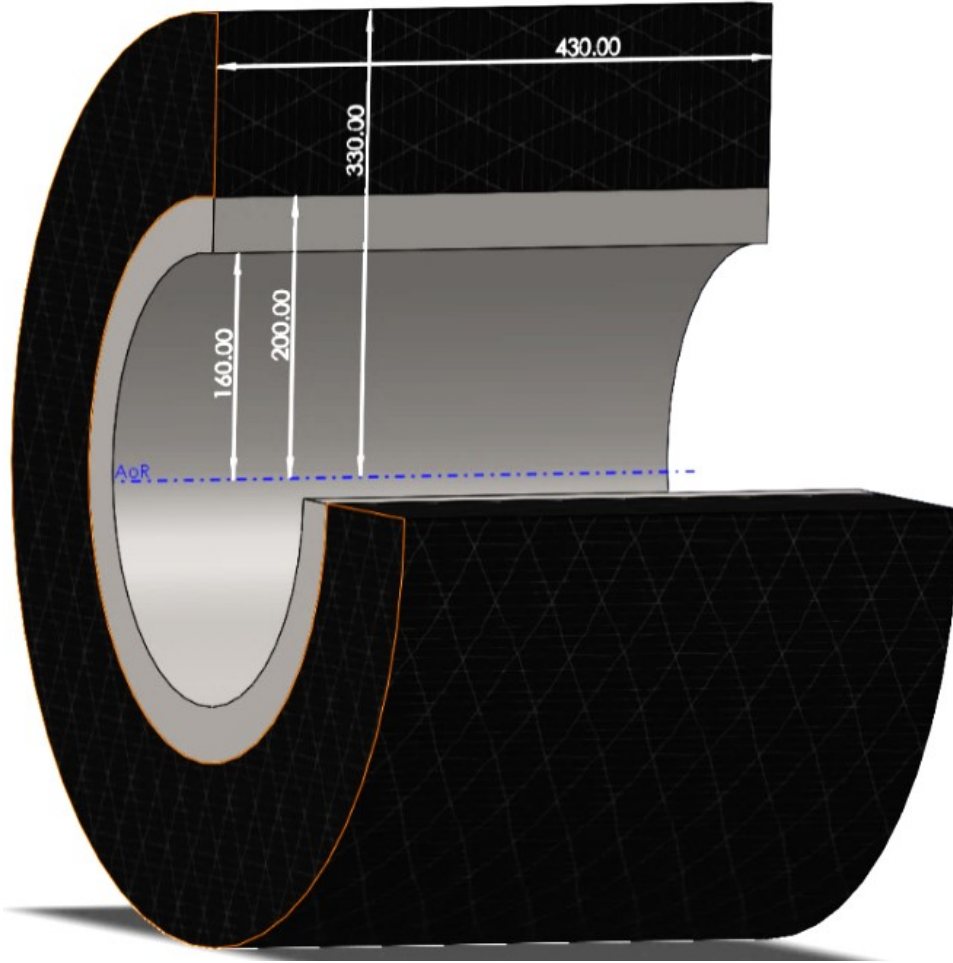


Figure 3.1: Simulated flywheel rotor showing dimensions of metallic hub and carbon fiber rim. The axis of rotation (AoR) is shown in blue.

Table 3.3: Flywheel rotor rim dimensions, press-fit interference, and energy capacity.

Parameter	Aluminum Hub	CFRP Rim	Complete Rotor
Inner radius	160 mm	200 mm	-
Outer radius	200 mm	330 mm	-
Press-fit interference	-	-	0.8 mm
Rotor height	-	-	430 mm
Energy capacity	-	-	11.19 kWh

Case 1: The worst-case scenario for viscoelastic effects is simulated by assuming the flywheel rotor is operated at its limit load at all times. The model was used to simulate 10 years of operation. Based on the Tsai-Wu failure criterion, a critical or limit velocity,  $\omega_{\text{limit}}$ , was determined as 24,250 rpm. Note that failure is initially indicated at this velocity, for an *SR* lightly above unity (1.01); however, viscoelastic stress relaxation will improve the stress state, allowing for safe operation at this velocity over the long term.

Case 2: This scenario is intended to more realistically simulate the application of a FESS in solar PV electric grids or EV charging support. For these applications, the FESS is assumed to experience a single charge/discharge cycle every day as the system charges during off-peak hours and discharges during peak hours. Peak electricity demands are typically observed in the mornings and evenings [35], which are also when PV systems have low productivity; therefore, a household would rely on the FESS during these times to operate appliances or support the charging of a vehicle. It should be mentioned here that the considered FESS capacity is not sufficient to fully charge typical EVs on the market. Rather, energy storage is seen as a means to support EV fast charging and associated peak loads. Minimum demands are observed in the middle of the day when a PV system is most productive, thereby recharging the system. For this study, each day is divided into three 8-h phases and assigned a different average velocity for each period. These are referred to as the maximum phase, intermediate phase, and minimum phase. It is recognized that charging or discharging the FESS may occur over a period of hours; therefore, the intermediate phase represents the average velocity during the charge-discharge periods. Attempting to simulate a real-world scenario, the rotor is assumed to operate below  $\omega_{\text{limit}}$ ; therefore, the velocity during the maximum phase,  $\omega_{\text{Pmax}}$ , is set at  $0.9 \omega_{\text{limit}}$ . For the minimum phase, the angular velocity,  $\omega_{\text{Pmin}}$ , is chosen to be  $0.25 \omega_{\text{limit}}$ , as discussed in [36]. Finally, the intermediate phase angular velocity,  $\omega_{\text{Pint}}$ , is halfway between  $\omega_{\text{Pmax}}$  and  $\omega_{\text{Pmin}}$ , i.e.,  $0.575 \omega_{\text{limit}}$ . The rotor is simulated to rotate at each velocity, i.e.,  $\omega_{\text{Pmax}}$ ,  $\omega_{\text{Pint}}$  and  $\omega_{\text{Pmin}}$ , for 8 h each day, for 365 days per year.

### 3.4 Results and Discussion

Filament-wound composite flywheel rotors may be subject to a variety of failure modes. Considering viscoelasticity and typical composite flywheel rotor construction, two failure modes are of primary concern. First, the rotor structural integrity is dependent on maintaining compressive loading at the interface between the hub and the composite rim, created by the press-fit during assembly. Therefore, in view of possible stress relaxation, a significant reduction or loss of this compressive loading may lead to rotor failure. Second, it has been shown that the prevalent polymer matrix materials for composite rotor fabrication, epoxy resins, experience creep embrittlement as they undergo viscoelastic stress relaxation, leading to an increased size and density of micro-cracks under subcritical loading conditions [37], i.e., applied loads which approach but do not exceed the matrix strength. Therefore, substantial viscoelastic stress increases the potential for micro-crack networks to substantially damage the matrix, which ultimately may lead to failure.

Notice, a factor of safety is not included in the design of this study as any such artificial limitations on the load bearing capacity of the flywheel rotor are highly dependent on the intended application of the system. Selecting a particular decision here would decrease the applicability of this study. Additionally, including a factory of safety in this study would be counteractive to the objectives by limiting the maximum allowable stresses and depressing the viscoelastic behavior of the system. Based on these factors, a factor of safety is not included in the simulations.

### 3.4.1 Algorithm Validation

The computational algorithm was validated by comparing simulation results with stress distributions for viscoelastic stress effects published by Tzeng et al. [13]. In their work, the rotor is constructed from two CFRP rims press-fitted together. The CFRP is an IM7/8552 transversely isotropic composite with no viscoelastic behavior in the fiber direction. Material properties are given in [13]. The simulation results are plotted alongside the published data in Figure 3.2. The close congruence that is observed between the published results and the current model provides validation that the present modeling approach is capable of accurately predicting the stress response in the flywheel rotor. Hence, model stress responses will herein be used in conjunction with the Tsai-Wu criterion to predict failure location and behavior.

Recalling the plane strain assumption made for the present analysis, modeling results validated the chosen approach, which simplified solving the radial inhomogeneous equilibrium equation. Contrasting present work with published literature, see e.g. [14,29,37,38,39], comparable results were achieved. It should be noted that some of these studies assume generalized plane strain. In addition, analyses that quantified axial stress [40] showed it to be an order of magnitude less than radial stress, and two orders less than the circumferential stress. Given the body of published works that impose and validate the plane strain assumption, and the comparatively small magnitude of axial stress, applying a plane strain assumption for the present analysis was seen as appropriate.

### 3.4.2 Viscoelastic Behavior

#### 3.4.2.1 4.2.1. Case 1

Simulation results in terms of radial and circumferential stress are shown in Figure 3.3 for the flywheel rotor constructed from an aluminum hub with a thick CFRP rim. While the hub, located between  $r = 160$  mm and  $r = 200$  mm, was not inherently subject to viscoelastic behavior, its stress state changed as compressive loading from the composite rim decreased.

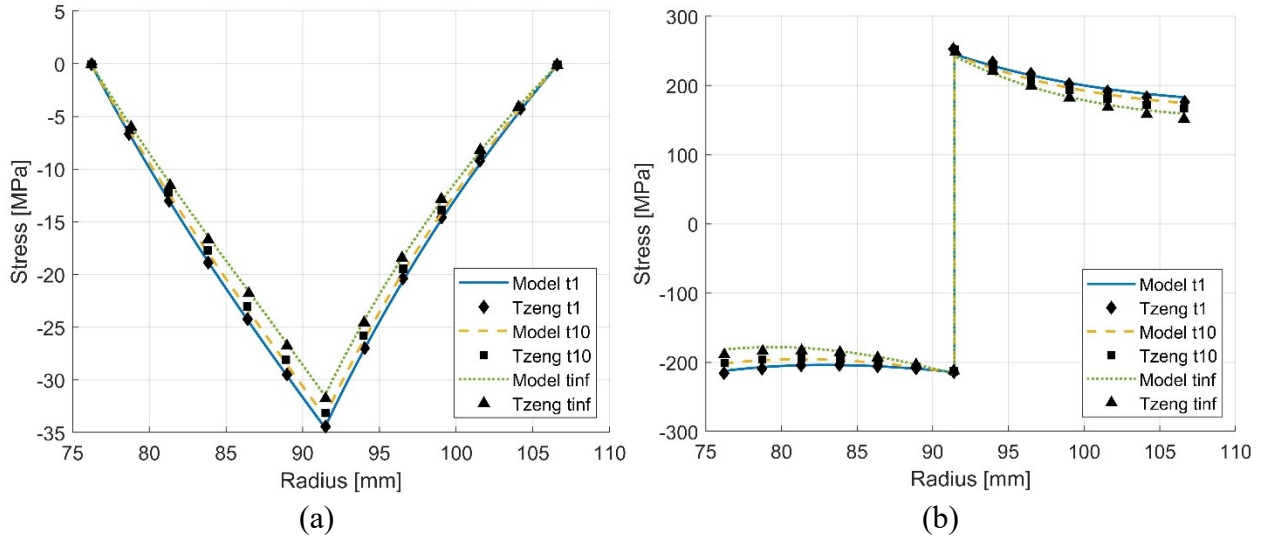


Figure 3.2: Radial (a) and circumferential (b) stress distribution comparison between the current model and Tzeng et al. [13] for a two-rim press-fit CFRP flywheel rotor.

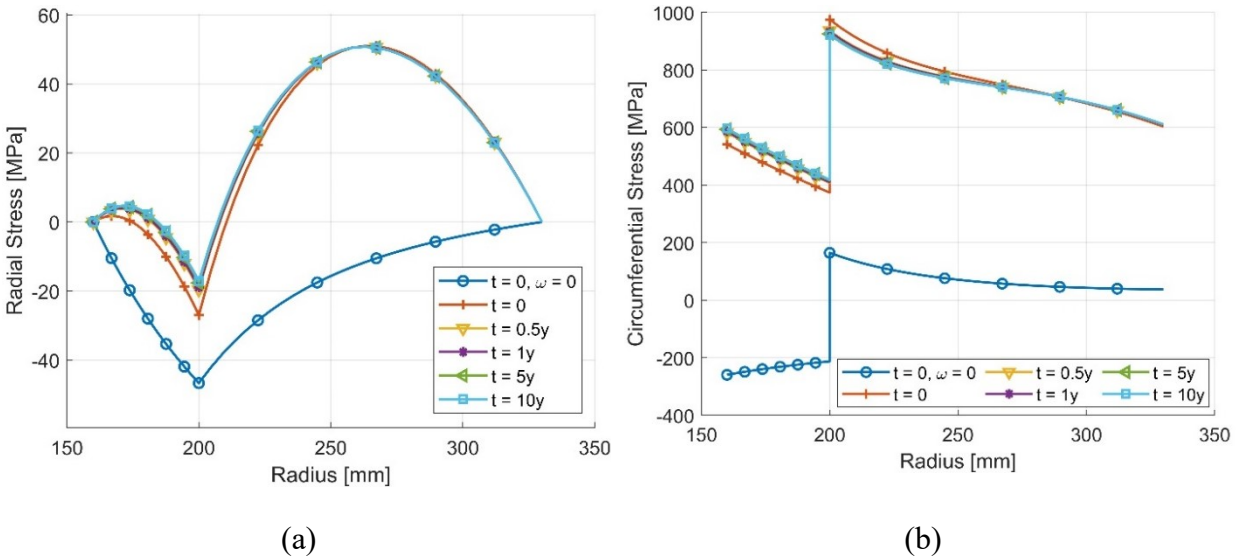


Figure 3.3: Radial (a) and circumferential (b) stress predictions for a flywheel rotor constructed of an aluminum hub and CFRP rim, after assembly (zero velocity), at startup, and at various times up to 10 years of continuous operation at the limit velocity of 24,250 rpm.

Considering the radial stress data depicted in Figure 3.3, the composite rim, in a pristine state post-manufacturing ( $t = 0$  and  $\omega = 0$ ), experiences high compressive loading, approximately  $-46.7$  MPa, due to the press-fit assembly. After startup to  $\omega_{\text{limit}}$ , the peak compressive load decreases to  $-27$  MPa. This change is induced by the radial position of the hub and rim leading differences in centrifugal loads, as well as differences in elastic modulus between the two materials. For comparison, the aluminum elastic modulus is 71 GPa while the CFRP longitudinal and transverse modulus is 111 GPa and 9.1 GPa, respectively. As a consequence, the outer rim

deforms more than the aluminum hub, reducing the interfacial pressure. Note that this ability to compensate for differential deformation while maintaining rotor integrity is one advantage of a press-fit assembly.

It can further be seen in Figure 3.3 that circumferential stress in the aluminum hub increases over time. At the inner hub surface, circumferential stress increases from 542 MPa to 596 MPa after 10 years; an increase of 9.2%. Note, even though this circumferential stress exceeds yield strength, the hub does not undergo failure because the stress coordinate for the given stress state still resides within the failure envelope, invoking, e.g., maximum distortion energy theory. Additionally, the increased circumferential stress is coupled with a decrease in radial compressive stress, i.e., radial stress becomes less compressive in the aluminum hub. These changes in radial and circumferential stress are attributed to the increased compliance of the CFRP rim during this time period, allowing the hub to deform radially.

Regarding the composite rim, radial and circumferential peak stresses are predicted to decrease moderately between 1% and 5.5%, respectively, over the 10 year simulation period, which is to be expected based on previous research [14]. For greater clarity, peak stress values in the rotor over the simulated 10-year period were determined for (i) the interfacial pressure measured in the radial direction, (ii) the radial stress, and (iii) the circumferential stress. Corresponding values are given in Table 3.4. To illustrate their change over the simulated operation, they were normalized by their initial value at  $t = 0$  and plotted in Figure 3.4. Within the first year of (continuous) operation, the rotor undergoes viscoelastic stress changes as the interfacial compressive stress decreases from -27 MPa to -19 MPa, or approximately 70.4% of the initial value. After 1 year, interfacial compressive stress decreases at a reduced rate, decreasing to 63.3% after 10 years. These results indicate that the composite material experiences rapid non-linear relaxation over the first year of operation, which to a large extent is ascribed to primary or transient creep (phase I). In the subsequent years of the rotor's service life, stress relaxation is significantly reduced, indicating the material has fully transitioned into secondary or steady-state creep (phase II). Conceivably, the initial rapid relaxation could be avoided by subjecting the composite rim to a suitable conditioning process prior to rotor assembly. In this case, only a relative minor decrease in interfacial pressure of about 7% would be expected.

Based on present findings, while viscoelastic stress relaxation leading to hub-rim separation is a conceivable scenario, it is controllable provided adequate interfacial pressure is achieved during assembly, or substantial initial creep effects can effectively be mitigated otherwise (e.g., by CFRP rim conditioning). It is interesting to note that for a reduced press-fit interference of 0.45 mm between the hub and rim (instead of 0.8 mm), creep effects are sufficient to cause zero interfacial pressure over the considered operating time, that is, separation between hub and rim would occur. Clearly, these results demonstrate that a viscoelastic analysis is warranted for the engineering design of FESS rotors.

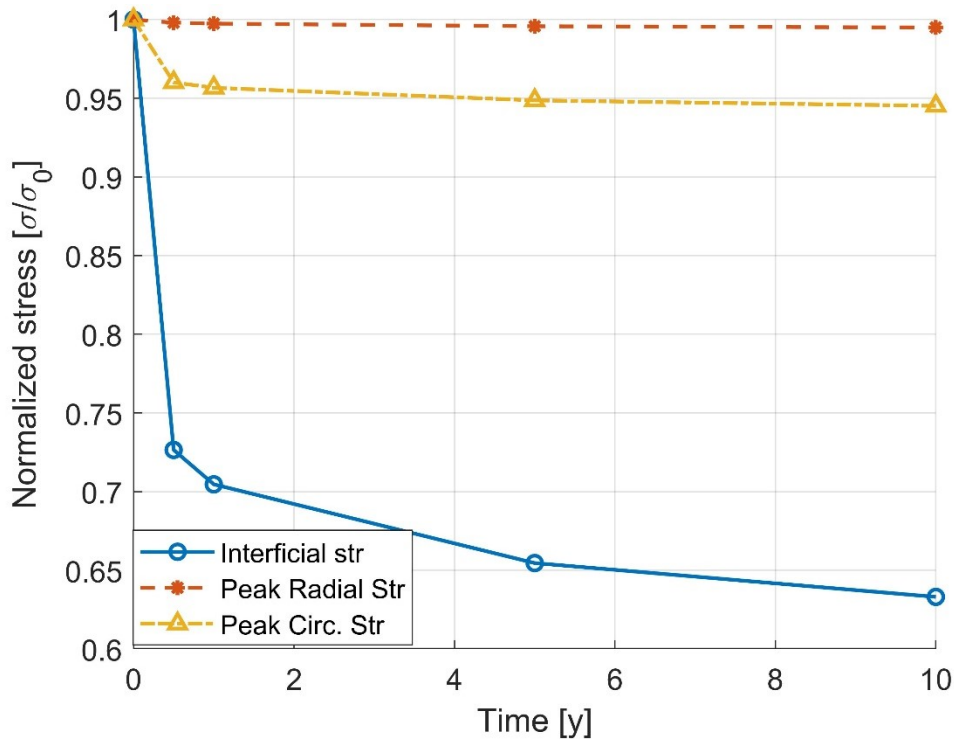
Table 3.4: Rotor peak stress values for interfacial stress, radial peak stress, and circumferential peak stress at 0, 0.5, 1, 5, and 10 years of continuous flywheel operation at limit velocity.

Time [Year]	0	0.5	1	5	10
Interface pressure [MPa]	-26.98	-19.60	-19.01	-17.66	-17.08
Radial peak stress [MPa]	50.96	50.86	50.83	50.75	50.71
Circumferential peak stress [MPa]	975.51	936.54	933.20	925.40	922.01

The Tsai-Wu failure criteria were used to determine the  $SR$  data and predict the location and angular velocity associated with rotor failure.  $SR$  data facilitate predicting failure since these data are based on the combined stresses exceeding the strength threshold. In other words, the  $SR$  analysis provides an understanding of the total stress state of the rotor.  $SR$  data for the current rotor are provided in Figure 3.5.

The CFRP rim initially has the highest  $SR$  of 1.01 and is located at the midplane of the rim; however, viscoelastic stress relaxation improves the stress state of this rim, so  $SR$  decreases to 0.975 within 6 months, then continues to slowly decrease to about 0.96 after 10 years. The same cannot be said for the aluminum hub, which exhibits an evolution of stresses approaching failure. The  $SR$  for the hub, while initially substantially less than the composite rim, increases from 0.836 to 0.9 within 6 months, then continues to increase to 0.92 over the following 10 years. With an increase by 6.8%, changes in  $SR$  for the hub are rapid in the first year of operation, while the  $SR$  is predicted to increase by only another 2% over the next 9 years. Referring to Figure 3.3, this  $SR$  growth is caused by a rising circumferential stress in conjunction with a lessening of compression in the radial direction. This behavior can be understood recalling Equation 3.13, which is composed of radial, circumferential, axial, and coupled terms. The linear term for radial direction is  $SR_{\text{radial}} = F_3 \sigma_3^{\text{app}} R$ . Since the peak radial stress is compressive, a large negative value is introduced into Equation 3.13, thus reducing  $SR$  accordingly. As the CFRP rim undergoes viscoelastic deformation, the radial compressive load diminishes, so  $SR_{\text{radial}}$  diminishes as well, thus removing the negative term from the equation, causing the observed  $SR$  increase for the hub.





*Figure 3.4: Normalized rotor peak stress for interfacial pressure, radial stress, and circumferential stress over time, in years, for continuous flywheel operation at limit velocity. Values are normalized by the corresponding stress at time  $t = 0$ .*

In summary, viscoelastic stress relaxation of the CFRP rim can improve its stress state to the detriment of the aluminum hub. It is reasonable to conclude that for a given rotor geometry, changing stresses may lead to damage of the aluminum hub and/or separation between hub and rim components. Viscoelastic effects should therefore be considered in flywheel rotor design. Nevertheless, based on the present observations, limited viscoelastic stress relaxation in the rotor may also be beneficial to the overall rotor performance. While substantial phase I creep may be a concern from a risk assessment point-of-view, mechanical conditioning and/or thermal aging could be a means to mitigate large initial viscoelastic effects after rotor assembly and operational startup while allowing for phase II creep to gradually evolve over the rotor's operational lifetime.

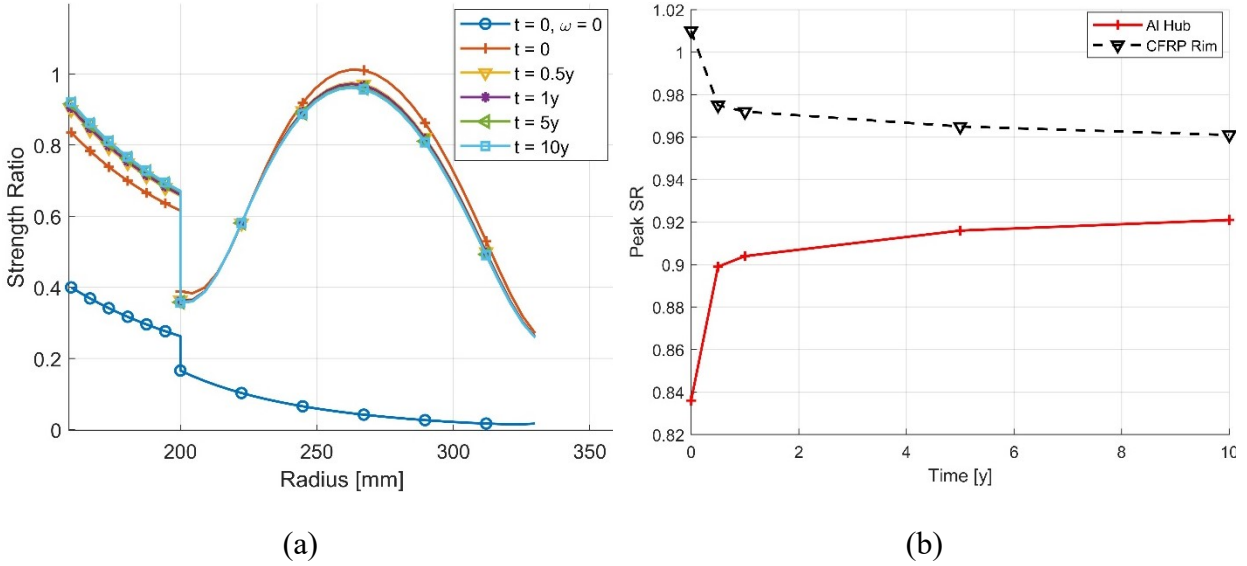


Figure 3.5: Strength ratio (SR) data for the flywheel rotor (a), and peak SR in the aluminum hub and CFRP rim at various times throughout the simulated lifetime (b).

### 3.4.2.2 Case 2

As mentioned earlier, the load profile for case 2 is intended to more closely simulate the operation of an FESS in actual applications, such as for solar PV electric grids or EV charging. Graphs with the radial and circumferential stresses on day 1 of operation are given in Figure 3.6. These graphs serve as representative examples of the stress distribution for the simulated operation. While the magnitude of the radial and circumferential stresses was found to decrease in the rim and increase in the hub over time, the overall shape of the stress response at each velocity (minimum phase,  $\omega_{Pmin}$ , intermediate phase,  $\omega_{Pint}$ , maximum phase,  $\omega_{Pmax}$ ) was found to be similar for any day of the simulated operation, so only data for the first day are provided. Comparing case 1 (Figure 3.3) and case 2 (Figure 3.6), the stress responses at  $\omega_{Pmin}$  and  $\omega_{Pmax}$  closely resemble those from case 1 at  $t = 0, \omega = 0$  and at  $t = 0, \omega = \omega_{limit}$ , respectively, as is expected given the similarity between angular velocities and the non-linear relationship between stress and velocity. Notably, for both cases, the circumferential stress in the hub is seen to change from initially having a positive slope ( $\omega = 0, \omega = \omega_{Pmin}$ ) to having a negative slope at high-velocity operation ( $\omega_{limit}, \omega_{Pmax}$ ). Between both extremes, stresses switch from tensile to compressive with the magnitude occurring at the hub inner surface. This loading scenario resembles fatigue loading with a negative stress ratio, positive mean stress, and a comparatively high stress range. The hub design should therefore include a fatigue analysis, especially for FESS that experiences high cycle rates, i.e., numerous cycles per day.

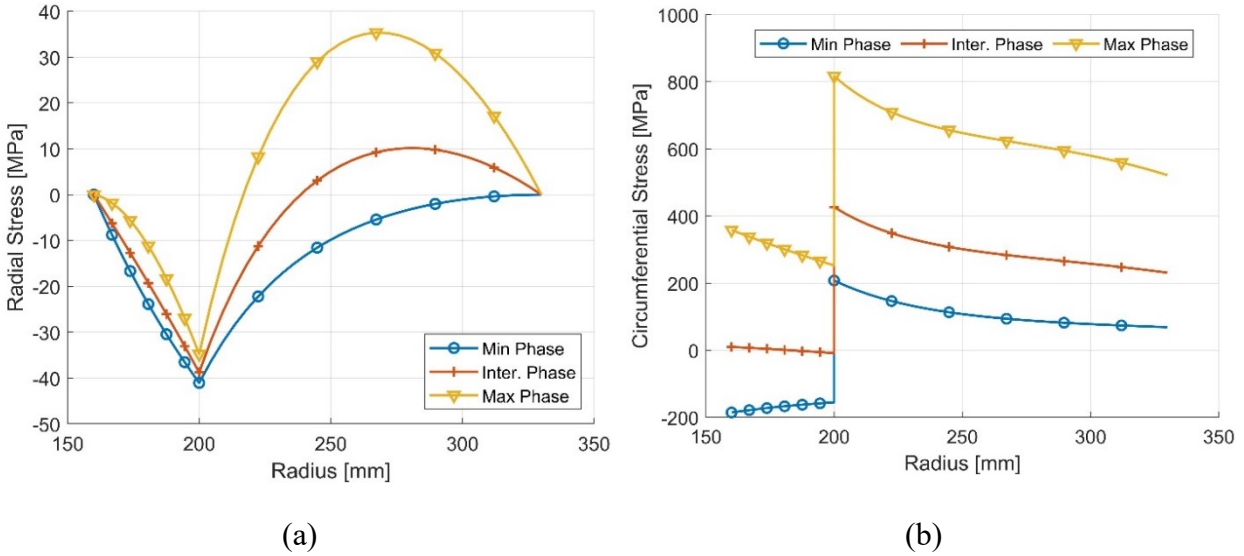


Figure 3.6: Radial (a) and circumferential (b) stress results at each velocity on day 1.

Figure 3.7 depicts *SR* data for all points along the rotor radial direction at each velocity for day 1 and day 365. Again, while magnitudes at each point are seen to vary for the different velocities, the overall shape of the *SR* curves at each velocity bear distinct similarities. Broadly, *SR* graphs exhibit similar trends as in case 1. After year 1, *SR* values at  $\omega_{P_{max}}$  increase in the hub but decrease in the composite rim. As one would expect, *SR* values in Figure 3.7 are lower compared to data in Figure 3.5, due to the overall lower stress levels and the reduced time that the rotor operates at high velocity.

During each phase, five key indicators are tracked throughout the simulation: (i) interface stress, (ii) peak radial tensile stress (i.e., neglecting compressive stresses, as these are found at the interface), (iii) peak circumferential stress in the CFRP rim, (iv) peak *SR* in the hub, and (v) peak *SR* in the CFRP rim. Values for each indicator recorded on day 1, 90, 180, 270, and 365 are given in

Table 3.5. To facilitate comparisons with case 1, data from

Table 3.5 were normalized using the day 1 value at each velocity and each location or component of interest, as depicted in Figure 3.8. Noting that since the peak radial tensile stress at  $\omega_{P_{min}}$  is negligible throughout the simulation (see

Table 3.5), this dataset was omitted in Figure 3.8.

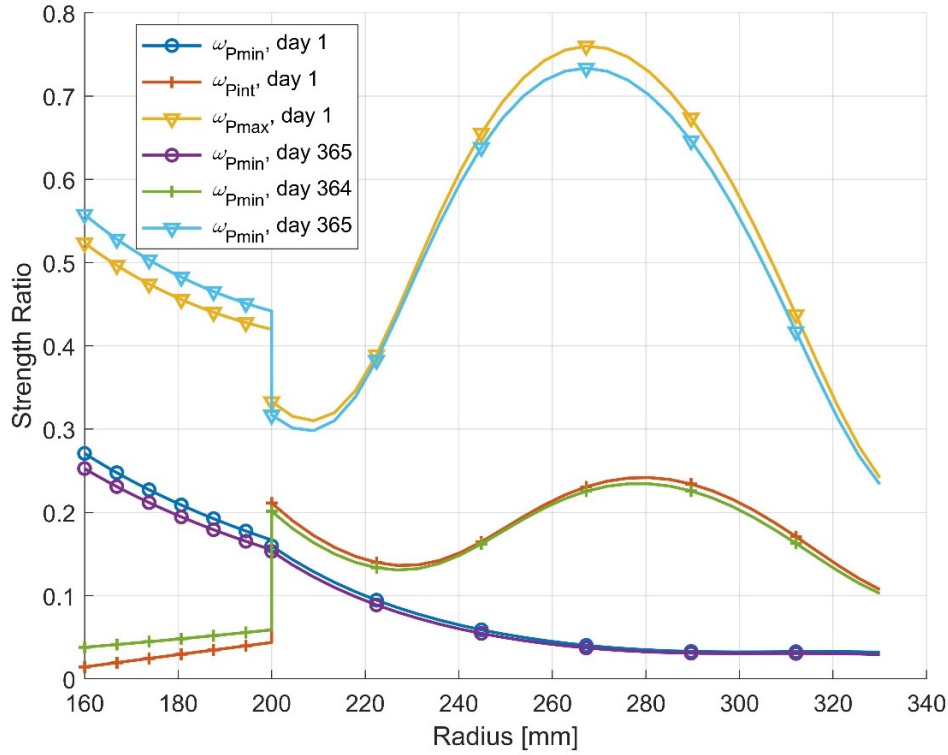


Figure 3.7: SR graphs for all points along the flywheel rotor radius at each velocity on day 1.

Table 3.5: Peak stress values at the hub-rim interface and radially and circumferentially in the CFRP rim, and peak SR values for the aluminum hub and the CFRP rim, at various times throughout the simulated one-year period.

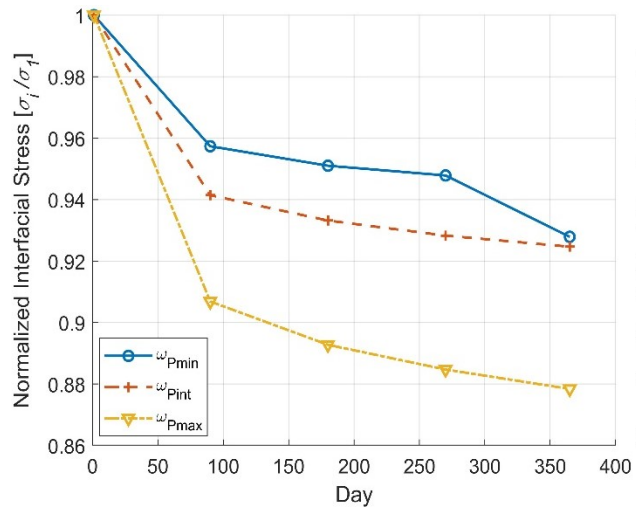
	Phase	Day 1	Day 90	Day 180	Day 270	Day 365
Peak interface pressure [MPa]	$\omega_{Pmin}$	-41.04	-39.26	-39.03	-38.90	-38.80
	$\omega_{Pint}$	-38.76	-36.49	-36.17	-35.98	-35.84
	$\omega_{Pmax}$	-34.78	-31.54	-31.05	-30.77	-30.55
Peak radial tensile stress in CFRP rim [MPa]	$\omega_{Pmin}$	0.0	0.001	0.010	0.012	0.014
	$\omega_{Pint}$	10.19	10.35	10.37	10.38	10.39
	$\omega_{Pmax}$	35.33	35.26	35.24	35.23	35.22
Peak circumferential stress in CFRP rim [MPa]	$\omega_{Pmin}$	207.9	207.3	207.2	207.1	207.1
	$\omega_{Pint}$	426.8	420.2	419.3	418.7	418.3
	$\omega_{Pmax}$	816.7	800.9	798.4	797.0	795.9
SR for aluminum hub [ ]	$\omega_{Pmin}$	0.271	0.256	0.255	0.253	0.253
	$\omega_{Pint}$	0.044	0.056	0.057	0.058	0.059
	$\omega_{Pmax}$	0.524	0.550	0.554	0.556	0.557
SR for CFRP rim [ ]	$\omega_{Pmin}$	0.160	0.155	0.154	0.153	0.153
	$\omega_{Pint}$	0.242	0.236	0.235	0.235	0.234
	$\omega_{Pmax}$	0.760	0.740	0.737	0.735	0.734

Akin to case 1, values for the interfacial pressure exhibit the most significant change during the case 2 simulation, as shown in Figure 3.8a. This observation again substantiates conclusions in previous work [30] which suggested that stress relaxation at the interface could pose a risk to a flywheel rotor's structural integrity. After 1 year of operation, the interfacial pressure is predicted to decrease by approximately 7%, 7.5%, and 12% at the minimum, intermediate, and maximum velocities, respectively. However, these reductions are significantly less compared to case 1, for which a decrease of 29% is predicted after year 1. Again, lower predicted interface pressures in case 2 are due to the rotor being subjected to lower average angular velocities than in case 1, and the rotor spending less time subjected to high velocity loading conditions. Since for each charge-discharge cycle the rotor transitions from low to high velocity and vice versa, high cycle rates will typically subject the rotor to reduced viscoelastic effects, as it will spend less time at or near maximum velocities.

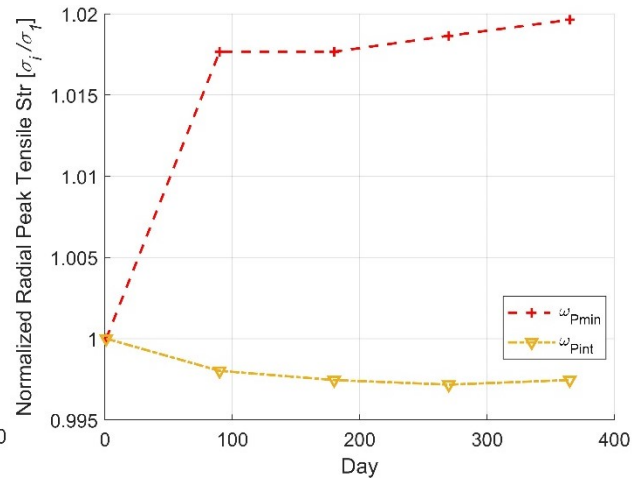
Considering Figure 3.8b,c, changes in peak stresses are rather benign. The peak radial tensile stress increases by a maximum of about 2%, which is comparable to the corresponding decrease seen in case 1. The peak circumferential stress shows a reduction of 0.5% at  $\omega_{Pmin}$  and 3% at  $\omega_{Pmax}$ . Reductions in both peak stress components are less than those for case 1 for the same reasons as discussed earlier.

In Figure 3.8d, peak *SR* values for the aluminum hub are indicated to decrease for  $\omega_{Pmin}$  but to rise for the other two velocities. *SR* changes at  $\omega_{Pmin}$  and  $\omega_{Pint}$ , being seemingly high at the latter velocity, are largely irrelevant given the comparatively low absolute *SR* values for the hub at these operating conditions (see Figure 3.7). The rise in *SR* at  $\omega_{Pmax}$  is considerable but is still confined to below 10% and remains uncritical. Referring to Figure 3.8e, the *SR* evolution for the CFRP rim is favorable, as observed for case 1, as values decrease over the considered operating period.

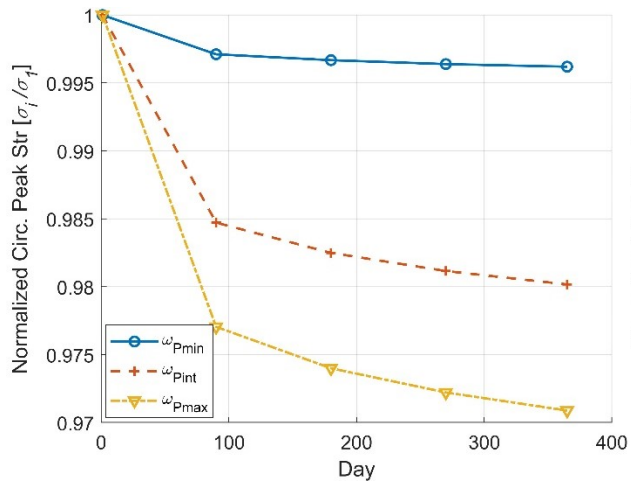
Considering relative *SR* changes between case 1 and case 2 at high velocity and at critical locations with respect to the rotor radial direction, i.e., the hub inner surface and the rim's cylindrical midsection, it is apparent that magnitudes in case 2 remain below those in case 1, which is to be expected given that the rotor is subjected to an overall reduced average velocity while also operating for less time under high velocity loading conditions. For example, in case 1, after the first year, the *SR* for the hub increases by 6.8%, while in case 2 (at  $\omega_{Pmax}$ ) over the same period, the increase is 3.3%.



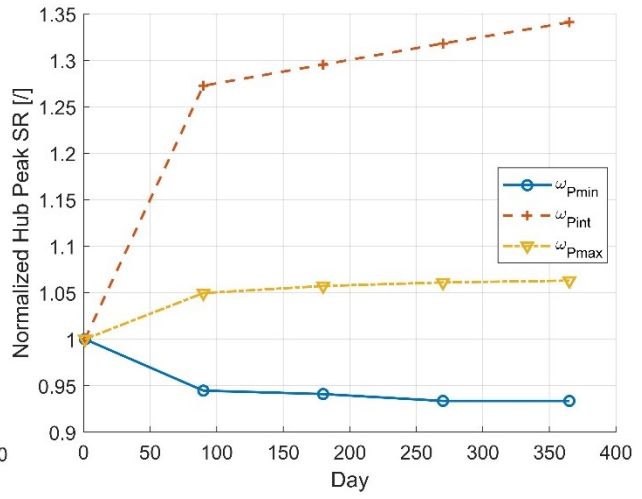
(a)



(b)



(c)



(d)

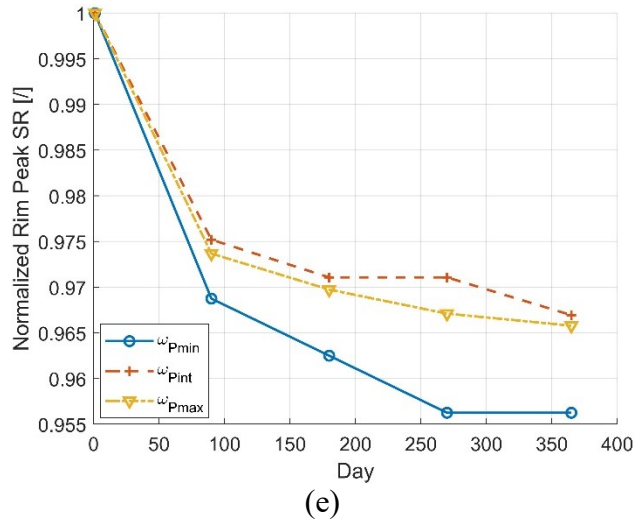


Figure 3.8: Stress results normalized by their initial value on day 1 for (a) interfacial pressure, (b) peak radial tensile stress, and (c) peak circumferential stress in the CFRP rim, (d) peak SR in the aluminum hub, and (e) peak SR in the CFRP rim.

### 3.5 Conclusions

The high-stress and long-lifetime operating conditions of modern composite flywheel rotors create the necessary conditions for viscoelastic failure modes not included in contemporary quasi-static failure analyses. In this study, a computational algorithm, based on an accepted analytical modeling approach, was developed to investigate the viscoelastic behavior of fiber reinforced polymer composite rotors during their lifetimes. Additionally, the Tsai-Wu failure criterion was used to compute strength ratios along the rotor radial direction. The values were used to assess the conditions for rotor failure. A composite flywheel rotor design was considered that meets capacity requirements to support an electrical vehicle charging system or solar PV residential electric grid. The rotor consists of a press-fit assembly of an aluminum hub with a carbon fiber polymer composite rim. The viscoelastic behavior of the flywheel rotor was studied for two cases: (i) a worst-case scenario of the rotor operating with an angular velocity at the failure threshold for a simulated lifetime of 10 years, and (ii) a charging/discharging cycle in which the rotor experiences a minimum, intermediate, and maximum velocity for 8 h each per day over a one-year period.

The case 1 simulation indicated that due to viscoelastic stress relaxation, the radial and circumferential stresses in the composite rotor reduce over time. After 10 years, peak stress in the radial and circumferential directions were found to decrease by approximately 1% and 5%, respectively. Given that rim stresses continually decrease over time, the risk of rim failure is diminishing during operation, provided no external factors, such as matrix cracking, affect the rotor's structural integrity. In contrast, circumferential stresses in the aluminum hub increase while radial stresses decrease. This behavior was attributed to an increasing compliance of the composite rim, allowing it to deform radially outward. Thus, radial compressive stresses in the rotor are reduced, and in turn, circumferential stresses in the hub are increased. The peak strength ratio for

the composite rim decreases by approximately 4% compared to an 8% increase in the hub after 10 years. The latter is of concern, as the peak strength ratio in the aluminum hub converges toward unity, suggesting an increased risk of hub failure. The interfacial press-fit pressure is subject to the largest decrease, approximately 36%. Still, taken on its own, this behavior represents a low risk to the flywheel rotor's structural integrity as long as the rotor design prescribes a sufficient initial press-fit interference that upholds compressive interfacial pressure over the rotor's lifetime. Based on the observation in case 1, failure may occur in the rim at startup if the rotor reaches a critical velocity but would decrease over time even if the critical velocity is maintained as viscoelastic stress relaxation improves the overall stress state in the composite rim. However, this behavior does not preclude possible failure due to other effects such as fatigue and matrix cracking, which warrants including such effects in flywheel rotor design and analysis.

The daily charge-discharge cycle considered in case 2 imposes cyclic loading conditions upon the rotor. In this scenario, strength ratios never reached unity, so failure is not predicted for any part of the rotor. Consistent with case 1, viscoelastic stress relaxation allows the radial and circumferential stress in the composite rim to decrease over time, creating a more favorable stress state regardless of angular velocity or time. However, the viscoelastic effects that improve the stress state for the rim are detrimental to the metallic hub. Moreover, charge-discharge cycles were found to impose fatigue loading with a negative stress ratio, positive mean stress, and a comparatively high stress range at the inner surface of the hub.

As was discussed earlier, this study did not include a factor of safety as an artificial limitation on the load bearing capacity of the flywheel rotor. One could incorporate these limitations by modifying the strength factors,  $F$ , in the Tsai-Wu criterion. These factors are dependent on the material strength tensor, so applying a scalar to this tensor would decrease the allowable combined stress before failure. This effectively shrinks the failure envelope of the Tsai-Wu criterion.

In summary, the present study satisfies the first two primary objectives of this thesis by conducting simulations on flywheel rotors of appropriate size and over appropriate time frames for applications such as in residential PV energy systems or EV charging stations. While previous studies began to explore this topic, the present study investigated the evolution of stresses in each principal direction between 6 months and 10 years of operation. Findings from these data are vital to consider when designing flywheel rotors for similar and other applications. The simulations conducted in the present study support the notion that viscoelastic effects reduce peak stresses in a composite rim over time. However, this study also showed that viscoelasticity may affect stresses in other parts of the rotor, i.e., the hub and the hub-rim interface, in ways that may lead to rotor failure. Moreover, it was noted that charge-discharge cycles of the flywheel energy storage device may create significant fatigue loading conditions. Therefore, it is concluded that flywheel rotor design should include viscoelastic and fatigue analyses to ensure safe operation, especially for devices experiencing high cycle rates and long-time operation near critical velocities.



## 3.6 References

1. Hadjipaschalis, I.; Poullikas, A.; Efthimiou, V. Overview of current and future energy storage technologies for electric power applications. *Renew. Sustain. Energy Rev.* **2009**, *13*, 1513–1522, <https://doi.org/10.1016/j.rser.2008.09.028>.
2. Luo, X.; Wang, J.; Dooner, M.; Clarke, J. Overview of current development in electrical energy storage technologies and the application potential in power system operation. *Appl. Energy* **2015**, *137*, 511–536, <https://doi.org/10.1016/j.apenergy.2014.09.081>.
3. Takkar, S.; Gupta, K.; Tiwari, V.; Singh, S.P. Dynamics of Rotating Composite Disc. *J. Vib. Eng. Technol.* **2019**, *7*, 629–637, <https://doi.org/10.1007/s42417-019-00155-8>.
4. Yang, L.; Crawford, C.; Ren, Z. A Fuzzy Satisfactory Optimization Method Based on Stress Analysis for a Hybrid Composite Flywheel. *IOP Conf. Ser. Mater. Sci. Eng.* **2018**, *398*, 012032, <https://doi.org/10.1088/1757-899X/398/1/012032>.
5. Mittelstedt, M.; Hansen, C.; Mertiny, P. Design and multi-objective optimization of fiber-reinforced polymer composite flywheel rotors. *Appl. Sci.* **2018**, *8*, 1256, <https://doi.org/10.3390/app8081256>.
6. Hartl, S.; Schulz, A.; Sima, H.; Koch, T.; Kaltenbacher, M. A Static Burst Test for Composite Flywheel Rotors. *Appl. Compos. Mater.* **2016**, *23*, 271–288, <https://doi.org/10.1007/s10443-015-9460-5>.
7. Corbin, C.K. *Burst Failure Prediction of Composite Flywheel Rotors: A Progressive Damage Approach via Stiffness Degradation*; Stanford University: Stanford, CA, USA, **2005**.
8. Arnold, S.M.; Saleeb, A.F.; Al-Zoubi, N.R. Deformation and life analysis of composite flywheel disk systems. *Compos. Part B Eng.* **2002**, *33*, 433–459, [https://doi.org/10.1016/S1359-8368\(02\)00032-X](https://doi.org/10.1016/S1359-8368(02)00032-X).
9. Trufanov, N.A.; Smetannikov, O.Y. Creep of Composite Energy Accumulators. *Strength Mater.* **1991**, *23*, 671–675.
10. Portnov, G.G. Estimation of Limit Strains in Disk-Type Flywheels Made of Compliant Elastomeric Matrix Composite Undergoing Radial Creep. *Mech. Compos. Mater.* **2000**, *36*, 55–58.
11. Levistor Boosting Forecourt Grid Power for the Next Generation of Fast Charging Electric Vehicles. Available online: <https://levistor.com/#about> (August 2021).
12. Stornetic GmbH Powerful Storage System for Grid Services. Available online: [https://stornetic.com/assets/downloads/stornetic\\_general\\_presentation.pdf](https://stornetic.com/assets/downloads/stornetic_general_presentation.pdf) (August 2021).
13. Tzeng, J.T. Viscoelastic Analysis of Composite Cylinders Subjected to Rotation. *Trans. Ophthalmol. Soc. U. K.* **2001**, *101*, 200–202, <https://doi.org/10.1106/002199802021464>.
14. Emerson, R.P. *Viscoelastic Flywheel Rotors: Modeling and Measurement*; Pennsylvania State University: State College, PA, USA, **2002**.
15. Emerson, R.P.; Bakis, C.E. Relaxation of press-fit interference pressure in composite flywheel assemblies. In Proceedings of the 43rd International SAMPE Symposium and Exhibition, Anaheim, CA, USA, 31 May–4 June 1998; SAMPE: Anaheim, CA, USA, **1998**; Volume 43, pp. 1904–1915.
16. Rupp, A.; Baier, H.; Mertiny, P.; Secanell, M. Analysis of a Flywheel Energy Storage System for Light Rail Transit. *Energy* **2016**, *107*, 625–638, <https://doi.org/10.1016/j.energy.2016.04.051>.
17. Toray CARBON FIBER T700G. Available online: <https://www.toraycma.com/wp-content/uploads/T700G-Technical-Data-Sheet-1.pdf.pdf> (August 2021).
18. Majda, P.; Skrodzewicz, J. A modified creep model of epoxy adhesive at ambient temperature. *Int. J. Adhes. Adhes.* **2009**, *29*, 396–404, <https://doi.org/10.1016/j.ijadhadh.2008.07.010>.
19. Almeida, J.H.S.; Ornaghi, H.L.; Lorandi, N.P.; Bregolin, B.P.; Amico, S.C. Creep and interfacial behavior of carbon fiber reinforced epoxy filament wound laminates. *Polym. Compos.* **2018**, *39*, E2199–E2206, <https://doi.org/10.1002/pc.24537>.
20. Thakur, P.; Sethi, M. Creep deformation and stress analysis in a transversely material disk subjected to rigid shaft. *Math. Mech. Solids* **2019**, *25*, 17–25, <https://doi.org/10.1177/1081286519857109>.
21. Debljinom, P.; Teorije, P.; Napona, P. Modelling of creep behaviour of a rotating disc in the presence of load and variable thickness by using SETH transition theory. *Struct. Integr. Life* **2018**, *18*, 153–160.
22. Zharfi, H. Creep relaxation in FGM rotating disc with nonlinear axisymmetric distribution of heterogeneity. *Theor. Appl. Mech. Lett.* **2019**, *9*, 382–390, <https://doi.org/10.1016/j.taml.2019.05.005>.
23. Tzeng, J.T., *Viscoelastic Analysis of Composite Flywheel for Energy Storage*; Army Research Laboratory: Adelphi, MD, USA, **2001**.
24. Lekhnitskiy, S.G. *Anisotropic Plates*; Air Force Systems Command: Moscow, Russia, **1957**.
25. Ha, S.K.; Jeong, H.M.; Cho, Y.S. Optimum design of thick-walled composite rings for an energy storage system. *J. Compos. Mater.* **1998**, *32*, 851–873.
26. Li, S.; Sitnikova, E.; Liang, Y.; Kaddour, A.S. The Tsai-Wu failure criterion rationalised in the context of UD composites. *Compos. Part A Appl. Sci. Manuf.* **2017**, *102*, 207–217, <https://doi.org/10.1016/j.compositesa.2017.08.007>.
27. Tsai, S.W.; Wu, E.M. A General Theory of Strength for Anisotropic Materials. *J. Compos. Mater.* **1971**, *5*, 58–80.
28. Rojas, J.I.; Nicolás, J.; Crespo, D. Study on mechanical relaxations of 7075 (Al-Zn-Mg) and 2024 (Al-Cu-Mg) alloys by application of the time-temperature superposition principle. *Adv. Mater. Sci. Eng.* **2017**, *2017*, 2602953.
29. ASM International Handbook Committee. *Metals Handbook Properties and Selection: Nonferrous Alloys and Special-Purpose Materials*; ASM International: Geauga County, OH, USA, **1990**; Volume 2, ISBN 978-0-87170-378-1.
30. Tzeng, J.T. Viscoelastic Modeling of Press-Fitted Composite Cylinders. *J. Compos. Tech. Res.* **2001**, *23*, 21–27.
31. Ding, H.; Chen, W.; Zhang, L. *Elasticity of Transversely Isotropic Materials*; Gladwell, G.M.L., Ed.; Springer: Dordrecht, The Netherlands, 2006; ISBN 9781119130536.

32. Sadananda, K.; Nani Babu, M.; Vasudevan, A.K. The unified approach to subcritical crack growth and fracture. *Eng. Fract. Mech.* **2019**, *212*, 238–257, <https://doi.org/10.1016/j.engfracmech.2019.03.010>.
33. Kheawcum, M.; Sangwongwanich, S. A Case Study on Flywheel Energy Storage System Application for Frequency Regulation of Islanded Amphoe Mueang Mae Hong Son Microgrid. In Proceedings of the 17th International Conference on Electrical Engineering/Electronics, Computer, Telecommunications and Information Technology, ECTI-CON 2020, Phuket, Thailand, 24–27 June **2020**; pp. 421–426.
34. Amiryar, M.E.; Pullen, K.R. A review of flywheel energy storage system technologies and their applications. *Appl. Sci.* **2017**, *7*, 286, <https://doi.org/10.3390/app7030286>.
35. Mansouri Kouhestani, F.; Byrne, J.; Johnson, D.; Spencer, L.; Hazendonk, P.; Brown, B. Evaluating solar energy technical and economic potential on rooftops in an urban setting: The city of Lethbridge, Canada. *Int. J. Energy Environ. Eng.* **2019**, *10*, 13–32, <https://doi.org/10.1007/s40095-018-0289-1>.
36. Andersen, F.M.; Baldini, M.; Hansen, L.G.; Jensen, C.L. Households' hourly electricity consumption and peak demand in Denmark. *Appl. Energy* **2017**, *208*, 607–619, <https://doi.org/10.1016/j.apenergy.2017.09.094>.
37. Peña-Alzola, R.; Sebastián, R.; Quesada, J.; Colmenar, A. Review of flywheel based energy storage systems. In Proceedings of the 2011 International Conference on Power Engineering, Energy and Electrical Drives, Malaga, Spain, 11–13 May 2011; <https://doi.org/10.1109/PowerEng.2011.6036455>.
38. Odegard, G.M.; Bandyopadhyay, A. Physical aging of epoxy polymers and their composites. *J. Polym. Sci. Part B Polym. Phys.* **2011**, *49*, 1695–1716, <https://doi.org/10.1002/polb.22384>.
39. Ha, S.K.; Yang, H.-I.; Kim, D.-J. Optimum design of a hybrid composite flywheel with permanent magnet rotor. *J. Compos. Mater.* **1999**, *33*, 1544–1575.
40. Pérez-Aparicio, J.L.; Ripoll, L. Exact, integrated and complete solutions for composite flywheels. *Compos. Struct.* **2011**, *93*, 1404–1415, <https://doi.org/10.1016/j.compstruct.2010.11.011>.

## 4 Study of Acceleration-induced Shear Stresses

The following chapter is intended for publication, in its present form, in Applied Composite Materials. As mentioned above this chapter is closely related to the previous one. In many ways this chapter is the antithesis of previous viscoelastic modeling efforts. Where the previous chapter was concerned with the rotor behavior over many years while angular velocity was constant, this chapter focuses on variable angular velocity over a period of seconds. Despite this the computational algorithm is broadly similar. Additionally, the same Tsai-Wu failure criteria is employed to predict the potential failure modes. This chapter addresses the shear stress concerns from the first two primary objectives of this thesis.

### 4.1 Introduction

High performance flywheel energy storage systems (FESS) employ a rotating disk—the flywheel rotor—frequently constructed from filament-wound fiber reinforced polymer composites (FRPC) [1]. The high ultimate tensile strength of these materials in fiber direction allows the rotor to reach large angular speeds before failure, which substantially increases its energy storage capacity. FESS can facilitate high energy transfer rates for both charging and discharging, and are claimed to have substantially longer lifetimes than other traditional energy storage systems [2]. These are desirable attributes for applications requiring recurrent energy storage cycles with high energy transfer rates. Examples are electric vehicle charging infrastructure or electric rail transit systems employing recuperation of regenerative braking energy. High cycle lifetimes and high energy transfer rates are synonymous with frequent acceleration and deceleration of the flywheel rotor over short periods of time.

The flywheel rotors simulated in this study are a filament-wound carbon fiber reinforced polymer (CFRP) of constant rectangular cross section. The quasi-static method for analyzing rotating disks of this type is well understood, having first been explored by Lekhnitskiy [3] and expanded on by Reddy and Srinath [4] and Roy and Tsai [5]. More recent studies discussed analytical methods for analyzing the stress field created in a composite flywheel rotor subjected to angular acceleration [6, 7]. Pérez-Aparicio and Ripoll [6] presented analytical solutions to equilibrium equations in every direction including shear. Their analysis included the effects of acceleration, hub stiffness, composite curing, moisture absorption, and thermomechanical effects. Salehian et al. [7] compared analytical and numerical rotor analysis techniques in functionally graded rotating disks with variable thickness. Their study showed that analytical and numerical analysis methods are equally capable of predicting shear stress and radial displacement in rotating disks.

Shear stresses are imposed by angular acceleration which necessarily also changes the angular velocity thus causing variation in the radial and circumferential stresses. As the flywheel rotor accelerates from minimum to maximum speed, internal stresses will increase. The transient behavior of composite flywheel rotors has received little attention in the technical literature

regarding stress analysis and failure prediction, even though transient behavior may affect damage initiation and growth, cause cyclic fatigue, and thus lead to rotor failure.

FRPC rotor design and optimization has typically been based on strength in the principal material directions as the failure criterion [8]. For this method, the ultimate strength in a principal material direction is compared to the applied load in that direction, and failure is expected if the applied load exceeds this threshold. This is the maximum stress failure criteria. However, this approach neglects the interaction of stresses in different directions at a given point. For example, at the inner surface of the rotor, maxima of both shear stress and circumferential stress are to be expected. Further, during acceleration, directional stress components vary continuously with time, yet stress components at a given point do not necessarily change proportionally, meaning that the peak stress location and stress gradients also vary continuously, both of which may affect damage behavior.

For the above reasons, other failure criteria were explored for the present study. From the technical literature, the considered criteria were progressive damage [9], Tsai-Wu [10], and the four parameter Christensen models [11]. A progressive damage failure criterion was not adopted in the present study as this approach creates discontinuities within the rotor model which violates the material continuity assumption of the employed analytical approach. The Christensen model would be an applicable failure criterion for composite flywheel rotors however it considers out of plane stresses which are unnecessary given the current analytical model assumes plane strain conditions. The Tsai-Wu criterion readily incorporates shear stress, and some recent studies applied the Tsai-Wu criterion to composite FRP rotor analysis, thus its application therefore considered appropriate [12,13].

The objective of present study is to describe the transient behavior of stresses in a composite FRP flywheel rotor during acceleration and deceleration. Beginning from quasi-static analysis, the baseline stress response at minimum and maximum velocities will be established. Then maximum and minimum acceleration and deceleration will be defined using maximum stress and Tsai Wu failure criteria. Finally, simulations will be conducted to discuss the stress response of an FRPC flywheel rotor subjected to parameters appropriate to EV charging.

## 4.2 Flywheel Stress Analysis

### 4.2.1 Radial and Shear Stress

For the flywheel stress analysis, analytical equations are derived for the radial, circumferential, and shear stresses in the flywheel rotor. This analysis is based on the following assumptions:

- The rotor is modeled as a plane strain problem.
- The model is axisymmetric with respect to the axis of rotation.
- Angular rotor acceleration is smooth and continuous.
- The rotor material is transversely isotropic and continuous throughout the simulation.

The goal of this analysis is to define the radial and tangential stress as a function of the rotor geometry, material properties, velocity, and angular acceleration. As will be seen, the radial displacement leads directly to stress and strain in both the radial, circumferential, and tangential (shear) directions. Deriving these relationships begins with the radial and tangential stress equilibrium equations which are found directly from the free body diagram of the flywheel as discussed in [7]. The equilibrium equations are,

$$\frac{d\sigma_r}{dr} + \frac{\sigma_r - \sigma_\theta}{r} + \rho r \omega^2 = 0; \quad \frac{d\tau_{r\theta}}{dr} + \frac{2}{r} \tau_{r\theta} + \rho r \alpha = 0, \quad 4.1$$

where  $\sigma$  and  $\tau$  are the principle stress and shear stress acting in the directions indicated by subscripts  $r$  and  $\theta$  for the radial and circumferential directions, respectively;  $\omega$  in  $rad/sec$  and  $\alpha$  in  $rad/sec^2$  are correspondingly the angular velocity and angular acceleration. Note that the  $z$  coordinate denotes the axial direction, and shear stress acts in the  $\theta$ - $z$  cylindrical face. The rotor is constructed from unidirectional filament wound FRPC and is considered transversely isotropic, stress is defined with Hooke's law such that,

$$\begin{bmatrix} \sigma_\theta \\ \sigma_z \\ \sigma_r \\ \tau_{r\theta} \end{bmatrix} = \begin{bmatrix} Q_{\theta\theta} & Q_{\theta z} & Q_{\theta r} & 0 \\ Q_{\theta z} & Q_{zz} & Q_{zr} & 0 \\ Q_{\theta r} & Q_{zr} & Q_{rr} & 0 \\ 0 & 0 & 0 & Q_{r\theta} \end{bmatrix} \begin{bmatrix} \varepsilon_\theta \\ \varepsilon_z \\ \varepsilon_r \\ \gamma_{r\theta} \end{bmatrix}, \quad 4.2$$

where  $Q$  and  $G$  are the material stiffnesses in the principal material directions, and  $\varepsilon$  and  $\gamma$  are the directional strain and shear strain. The strain terms are defined as,

$$\varepsilon_\theta = \frac{u_r}{r}; \quad \varepsilon_r = \frac{du_r}{dr}; \quad \varepsilon_z = 0; \quad \gamma_{r\theta} = \frac{dv}{dr} - \frac{v}{r}, \quad 4.3$$

where  $u_r$  and  $v$  are the radial and tangential displacements respectively. Invoking the plane strain assumption eq 4.3 can be substituted into 4.2 which is then substituted into eq 4.1 yielding a second order inhomogeneous ordinary differential equations. After simplification these equations are

$$Q_{rr} \frac{d^2 u_r}{dr^2} + \frac{Q_{rr}}{r} \frac{du_r}{dr} + (Q_{\theta r} - Q_{\theta\theta}) \frac{u_r}{r^2} = -\rho r \omega^2; \quad 4.4$$

$$\frac{d^2 v}{dr^2} + \frac{1}{r} \frac{dv}{dr} - \frac{2v}{r^2} = -\frac{\rho r \alpha}{G_{r\theta}}.$$

Clearly, the radial and tangential equilibrium equations are in a similar form indicating the solution to both equations is found using the same process. It is also worth noting, due to the assumption of transverse isotropy, the existence of tangential stress has no effect on the radial equilibrium set of equations, and vice versa. This may not be intuitive, however, considering the stiffness matrix in eq 4.2, it is clear the principal stress and shear stress behavior should be

independent of each other given the coupling terms,  $Q_{61}$  to  $Q_{63}$ , are zero. Notice this condition is only true if the material is transversely isotropic. Since the rotors considered herein are filament wound with a  $90^\circ$  winding angle transverse isotropy is appropriate, therefore radial and circumferential strains have no effect on in-plane shear stress,  $\tau_{r\theta}$  [6].

For brevity the remainder of the derivation is limited to solving the radial displacement equation while recognizing the shear equation is solved identically. The second order inhomogeneous ordinary differential equation is simplified by changing its base from  $r$  to  $t$  using the following relationships,

$$r = e^t; \quad \ln(r) = t; \quad \frac{dt}{dr} = \frac{1}{r}. \quad 4.5$$

Then invoking the chain rule, eq 4.5 is substituted into eq 4.4 to yield

$$Q_{rr} \frac{d^2 u_r}{dt^2} + (Q_{\theta r} - Q_{rr}) u_r = -\rho \omega^2 r^3, \quad 4.6$$

which is also a second order inhomogeneous ordinary differential equation but now with constant coefficients, thus having the general form

$$A \frac{d^2 u_r}{dt^2} + E u_r = -\rho \omega^2 r^3. \quad 4.7$$

The characteristic homogeneous solution to eq 4.7 is

$$u_r(t) = C_1 e^{\lambda_1 t} + C_2 e^{\lambda_2 t}, \quad 4.8$$

where constants  $C_1$  and  $C_2$  are discussed later, and  $\lambda_1$  and  $\lambda_2$  are determined from the homogeneous solution of eq 4.7 with the substitution  $u_r = e^{\lambda x}$  and using the chain rule once again yielding

$$(A e^{\lambda x}) \lambda^2 + E e^{\lambda x} = 0. \quad 4.9$$

Solving the quadratic equation gives  $\lambda_1$  and  $\lambda_2$ . The particular solution can be found with the homogeneous solution to isolate the appropriate radial displacement function from all possible solutions. Then, changing the base back to the  $r$  basis yields the radial displacement equation

$$u_r(r) = C_1 \varphi_1 r^\kappa + C_2 \varphi_2 r^{-\kappa} - \rho \omega^2 \varphi_3 r^3, \quad 4.10$$

Using equations 4.2, 4.3, and 4.10 the radial stress is

$$\sigma_r = C_1 r^{\kappa-1} + C_2 r^{-\kappa-1} - \rho \omega^2 \varphi_4 r^2 \quad 4.11$$

where  $C_1$  and  $C_2$  are found from the boundary conditions, and  $\kappa$  and  $\varphi_i$  with  $i = 1, 2, 3$  are functions of the stiffness matrix, i.e.,

$$\begin{aligned} \kappa &= \sqrt{\frac{Q_{\theta\theta}}{Q_{rr}}}; & \varphi_1 &= \frac{1}{Q_{\theta r} + \kappa Q_{rr}}; \\ \varphi_2 &= \frac{1}{Q_{\theta r} - \kappa Q_{rr}}; & \varphi_3 &= \frac{1}{(9 - \kappa^2)Q_{rr}}; & \varphi_4 &= \frac{3Q_{rr} + Q_{\theta r}}{(9 - \kappa^2)Q_{rr}}. \end{aligned} \quad 4.12$$

The same solution path can be used to determine the tangential displacement equation is found as

$$v(r) = D_1 r + D_2 r^{-1} - \frac{\rho \alpha r^3}{8G_{r\theta}}. \quad 4.13$$

Similarly, referring to eq 4.10,  $D_1$  and  $D_2$  are constants found using the boundary conditions. Shear stress is found by combining equation 4.14 with the shear strain condition in equation 4.3.

$$\tau_{r\theta} = G_{r\theta} \left( -\frac{2D_2}{r^2} + \frac{\rho \alpha r^2}{4G_{r\theta}} \right) \quad 4.14$$

Applying this to multi-rim flywheel rotors with an arbitrary number of rims, i.e. the rotor is constructed from  $j = 1, 2, 3 \dots N$  rims, requires radial and tangential continuity and boundary conditions to be satisfied. Radially,

$$\sigma_{r,r_o}^j = \sigma_{r,r_i}^{j+1}; \quad u_{r,r_o}^j = u_{r,r_i}^{j+1} \quad 4.15$$

where  $\sigma_{r,r_o}^j$  is the radial stress at the outer radius,  $r_o$ , in the  $j^{\text{th}}$  rim, and  $\sigma_{r,r_i}^{j+1}$  is the radial stress at the inner radius,  $r_i$ , of the next,  $j+1$ , rim. The same notation is used to describe the radial displacements,  $u_r$ , at the interface as well. The boundary conditions are

$$\sigma_{r,0} = -\sigma_0; \quad \sigma_{r,r_{\max}} = 0, \quad 4.16$$

Where  $\sigma_0$  is the applied stress at the inner surface, such as from a press fit, and  $\sigma_r(r_{\max})$  is the stress on the outer surface of the flywheel rotor. Using equations 4.16 and 4.17,  $C_1$  and  $C_2$  can be found. Tangentially the continuity conditions are,

$$\tau_{r\theta,r_o}^j = \tau_{r\theta,r_i}^{j+1}; \quad v_{r_o}^j = v_{r_i}^{j+1}, \quad 4.17$$

and the boundary conditions are

$$\tau_{r\theta,0} = \tau_0; \quad \tau_{r\theta,r_{\max}} = 0. \quad 4.18$$

Here shear stress at the inner most and outer most surfaces are  $\tau_0$  and 0. Notice, shear stress is dependent on a single integration constant which can be found using the boundary and continuity conditions in equations 4.17 and 4.18. For each rim,

$$D^{j-1} = \left( \frac{\rho^{j-1}\alpha}{G_{r\theta}^{j-1}} - \frac{\rho^j\alpha}{G_{r\theta}^j} \right) \frac{r_{j,o}^4}{8} + \frac{G_{r\theta}^j}{G_{r\theta}^{j-1}} D^j; \quad D^N = \frac{\rho^N \alpha r_{\max}}{8G_{r\theta}} \quad 4.19$$

Consider equation 4.19 left, when  $j - 1 = N$  then  $G_{r\theta}^{j-1}$  is the shear modulus of the  $N^{\text{th}}$  rim; therefore,  $G_{r\theta}^j$ ,  $\rho^j$  and  $D^j$  must refer to the shear modulus, density, and integration constant for a rim which does not exist so these values must be zero. In this case equation 4.19 left simplifies to 4.19 right.

#### 4.2.2 Tsai-Wu Criteria

The general Tsai-Wu failure criterion, described in [10,14–16], can be reduced to 10 terms by employing the same transversely isotropic assumption used above. This criterion finds a relationship,  $F$ , between the applied stress tensor and the material tensile strengths and it predicts failure when  $F \leq 1$ . At failure, the stress tensor represents the maximum allowable stress and  $F = 1$ . The Tsai-Wu failure criterion is written as,

$$F = F_{11}(\sigma_1^{\text{all}})^2 + F_{22}(\sigma_2^{\text{all}})^2 + F_{33}(\sigma_3^{\text{all}})^2 + F_{66}(\tau_{12}^{\text{all}})^2 + 2F_{13}\sigma_1^{\text{all}}\sigma_3^{\text{all}} + 2F_{12}\sigma_1^{\text{all}}\sigma_2^{\text{all}} + 2F_{23}\sigma_2^{\text{all}}\sigma_3^{\text{all}} + F_1\sigma_1^{\text{all}} + F_2\sigma_2^{\text{all}} + F_3\sigma_3^{\text{all}} = 1, \quad 4.20$$

where  $[\sigma_i^{\text{all}}]$  is the allowable, or maximum, stress tensor in the  $i = 1, 2, \text{ or } 3$  directions at an arbitrary point in the rotor. Where the  $i$  directions correspond to the  $\theta, z, \text{ and } r$  directions respectively. Additionally, while the plane strain condition was used to simplify the rotor analysis, this does not preclude the possibility of axial stress; therefore, it is included in the failure criteria for completeness [13]. The  $F$  coefficients are,

$$\begin{aligned} F_{11} &= \frac{1}{\sigma_{1t}\sigma_{1c}}; & F_1 &= \frac{1}{\sigma_{1t}} - \frac{1}{\sigma_{1c}}; & F_{22} = F_{33} &= \frac{1}{\sigma_{3t}\sigma_{3c}}; \\ F_2 = F_3 &= \frac{1}{\sigma_{3t}} - \frac{1}{\sigma_{3c}}; & F_{12} = F_{13} &= \frac{-1}{2\sqrt{\sigma_{1t}\sigma_{1c}\sigma_{3t}\sigma_{3c}}}; & F_{23} &= F_{22} - \frac{1}{2\tau_{13}^2}; \\ F_{66} &= \frac{1}{\tau_{13}^2}, \end{aligned} \quad 4.21$$

where the subscripts  $t$  and  $c$  refer to the tensile and compressive failure strengths, respectively.

Its common, and more valuable, to define the relationship between maximum allowable stress and the currently applied stress as the failure ratio ( $R$ ) [15]. This relationship is found by combining the maximum allowable stress tensor,  $[\sigma_i^{\text{all}}]$ , with the applied stress tensor,  $[\sigma_i^{\text{app}}]$ , multiplied with  $R$  such that,



$$\sigma_1^{\text{all}} = R\sigma_1^{\text{app}}; \quad \sigma_2^{\text{all}} = R\sigma_2^{\text{app}}; \quad \sigma_3^{\text{all}} = R\sigma_3^{\text{app}}; \quad \tau_{13}^{\text{all}} = R\tau_{13}^{\text{app}}. \quad 4.22$$

Then, eq 4.23 is substituted into eq 4.21 which yields a quadratic equation, i.e.

$$\begin{aligned} 0 = & \left[ F_{11}(\sigma_1^{\text{app}})^2 + F_{22}(\sigma_2^{\text{app}})^2 + F_{33}(\sigma_3^{\text{app}})^2 + F_{66}(\tau_{12}^{\text{app}})^2 + 2F_{13}\sigma_1^{\text{app}}\sigma_3^{\text{app}} \right. \\ & \left. + 2F_{12}\sigma_1^{\text{app}}\sigma_2^{\text{app}} + 2F_{23}\sigma_2^{\text{app}}\sigma_3^{\text{app}} \right] R^2 \\ & + [F_1\sigma_1^{\text{app}} + F_2\sigma_2^{\text{app}} + F_3\sigma_3^{\text{app}}]R - 1. \end{aligned} \quad 4.23$$

Solving this quadratic equation for  $R$  defines the strength ratio. When  $[\sigma_i^{\text{app}}]$  equals  $[\sigma_i^{\text{all}}]$  then  $R$  equals unity indicating failure, whereas  $R > 1$  indicates  $[\sigma_i^{\text{app}}]$  is less than  $[\sigma_i^{\text{all}}]$  showing no failure is predicted. It is common to define a strength ratio ( $SR$ ) to be  $1/R$  as this is more intuitive conceptually and graphically [15]. Failure under this criterion is predicted when  $SR \geq 1$ .

### 4.2.3 Computational Methodology

The computational methodology applied here is similar to that discussed in [13,17,18]. The analytical methodology discussed above is fundamentally a quasi-static analysis valid for constant loads and time. To adapt this for time dependent behavior the rotor response is approximated through a number of discrete time and load steps. However, the present work differs from previous studies by iterating through both angular velocity and time instead of only time as has been done previously. The rotor dimensions, material properties, and simulation parameters—including the time vector, minimum and maximum angular velocities, and the function according to equation (26) discussed below—are defined inputs to the model. Then beginning at the initial time step, angular velocity is calculated and used to determine the boundary conditions, rotor response, and  $SR$ . Then the algorithm iterates to the next time step and begins again. This yields the induced stress and  $SR$  for all points in the flywheel rotor at all times and velocities of interest. The simulation ends when either the maximum time is reached or when the rotor no longer has enough energy to satisfy the power requirement without exceeding the maximum angular velocity or passing below the minimum angular velocity.

### 4.2.4 Simulation Parameters

During operation, a flywheel rotor will experience many charge-discharge cycles which can be divided into an acceleration phase and a deceleration phase. For example, the rotor of an EV charging station may accelerate slowly over a long period of time while no vehicle is charging, i.e. charge phase. Then, when a vehicle is connected to the charging station, the rotor will decelerate rapidly, i.e. discharge phase. Clearly, the discharge phase will have more significant shear stresses due to the high power required to charge the EV battery. For this study, a flywheel rotor appropriate for EV charging or LTR recumbent braking is designed and subjected to various loading conditions. The simulated flywheel rotor is constructed from filament wound carbon fiber reinforced polymer composite with constant rectangular cross section intended for short to medium term energy storage applications. The winding angle is taken to be  $90^\circ$  with respect to the rotor

axis of rotation to maximize circumferential strength. The material properties are given in Table 4.1 based on an IM7/8552 carbon fiber filament and epoxy resin (Hexcel Corp., Stamford CT, Hexion Inc., Columbus OH) [19–21]. The composite rim is press fit around a 7075-t6 aluminum rim used to simulate a metallic hub. The material properties given in Table 4.1 and Table 4.2.

*Table 4.1: Material properties for the aluminum 7075-T6 [22] and viscoelastic equations for CFRP [23] used in the present study.*

Material	$Q_{\theta\theta}$ [Pa]	$Q_{zz}$ [Pa]	$Q_{rr}$ [Pa]	$Q_{r\theta}$ [Pa]	$\nu$	$\rho$ [ $\frac{kg}{m^3}$ ]
Aluminum	$7.19 \times 10^{10}$	$7.19 \times 10^{10}$	$7.19 \times 10^{10}$	$2.69 \times 10^{10}$	0.33	2795
CFRP	$1.11 \times 10^{11}$	$9.09 \times 10^9$	$9.09 \times 10^9$	$5.0 \times 10^9$	0.31	1560

*Table 4.2: Directionally dependent tensile strength of CFRP and failure strength of aluminum used to find SR from the Tsai Wu failure criterion.*

Material	$\sigma_{1t}$ [MPa]	$\sigma_{1c}$ [MPa]	$\sigma_{3t}$ [MPa]	$\sigma_{3c}$ [MPa]	$\tau$ [MPa]
CFRP	2,720	1,689	64.1	307	137
Aluminum	572	572	572	572	331

The angular velocity of the rotor is defined as

$$\omega(t) = \omega_{t-1} + \alpha(t)\Delta t, \quad 4.24$$

where  $\omega_{t-1}$  is the initial angular velocity in rad/s and  $\alpha(t)$  is the acceleration in  $\text{rad/sec}^2$ , and  $\Delta t$  is an arbitrary time step. The acceleration,  $\alpha(t)$ , is determined by the power requirements for each case according to,

$$\alpha(t) = \frac{P}{I\omega(t)} \quad 4.25$$

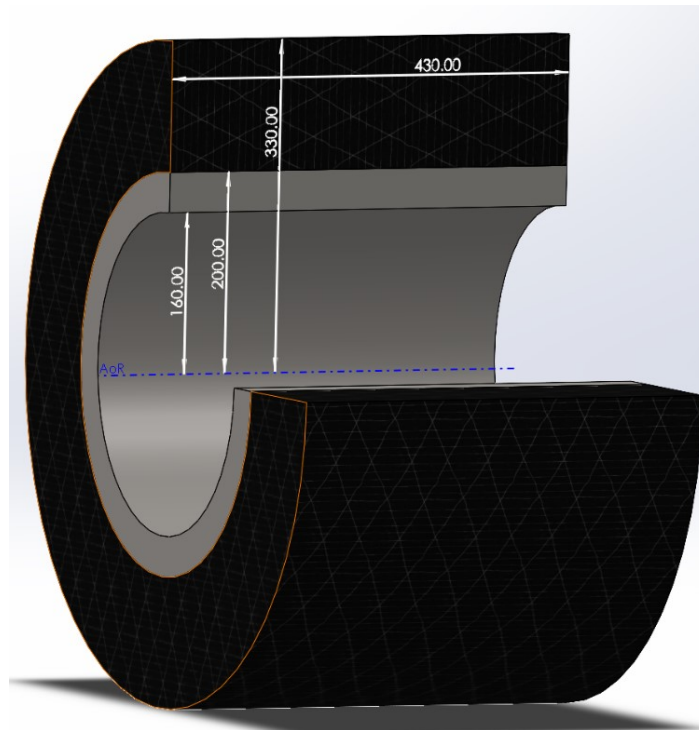
where  $P$  is the power, and  $I$  is the rotor moment of inertia which can be calculated as described in [24]. Notice the maximum acceleration, and in turn shear stress, will occur at the lowest angular velocities. This is also when principle stresses—radial, circumferential, and axial—are minimized.

The initial rotor parameters are based on the requirements for an FESS used in recumbent breaking in light rail transit (LRT) [25]. The power requirements for EV charging were found to

be similar [26]. This case simulates a flywheel rotor providing power to a light rail transit vehicle to assist the vehicle’s acceleration out of a station. The flywheel rotor simulated here has a filament wound CFRP composite rim with uniform rectangular cross section. The fiber angle is taken to be 90° from the axis of rotation. This is press fit around an aluminum 7050-t6 metallic hub also with rectangular cross section. Given the plane strain assumption the rotor thickness is taken to be 43 cm with a corresponding to an energy capacity of 11.19 kWh at  $\omega_{\max} = 24,150$  rpm. The minimum state of charge is taken to be 25% of the maximum angular velocity [27],  $\omega_{\min} = 6,037.5$  rpm. These parameters are given in Table 4.3 and Figure 4.1.

*Table 4.3: Flywheel rotor rim dimensions, press fit width, and energy capacity.*

Parameter	Aluminum hub	CFRP rim	Complete rotor
Inner radius	160 mm	200 mm	-
Outer radius	200 mm	330 mm	-
Press fit interference	-	-	0.8 mm
Rotor length	-	-	430 mm



*Figure 4.1: Diagram of simulated flywheel rotor showing dimensions of aluminum hub, CFRP rim, and the axis of rotation (AoR).*

Demand from LRT systems may be as high as 725 kW [25] while peak demands from EV charging stations can reach 120 kW [28]. Applied to the LRT the flywheel could maintain the required power supply for a maximum of approximately 52 seconds before reaching the minimum state of charge. As applied to EV charging this flywheel rotor could maintain 120 kW for approximately 5 minutes 35 seconds. For the purposes of this study the larger power demand and simulation time will be used as this creates greater shear stresses within the rotor.

### 4.3 Results and Discussion

To validate the analytical model discussed above predictions from the current model are compared to those in published literature, Figure 4.2. The circumferential, radial, and axial results are compared to those reported by Ha et al. [29], results are from their analytical model, and the shear stress predictions are compared to Salehian et al. [7], results from their FEA model. It can be seen the current model produces identical results in all directions as those in literature. Note, the Ha et al. [29] results include a simulated internal pressure resulting in the compressive load at the inner surface. As was discussed previously this analysis is fundamentally a quasi-static analysis where only velocity changes with time. These results show the current analysis is capable of accurately predicting the rotor stress at an arbitrary velocity and angular acceleration, and, given this is fundamentally a quasi-static analysis, it is reasonable to believe that the model works as expected.

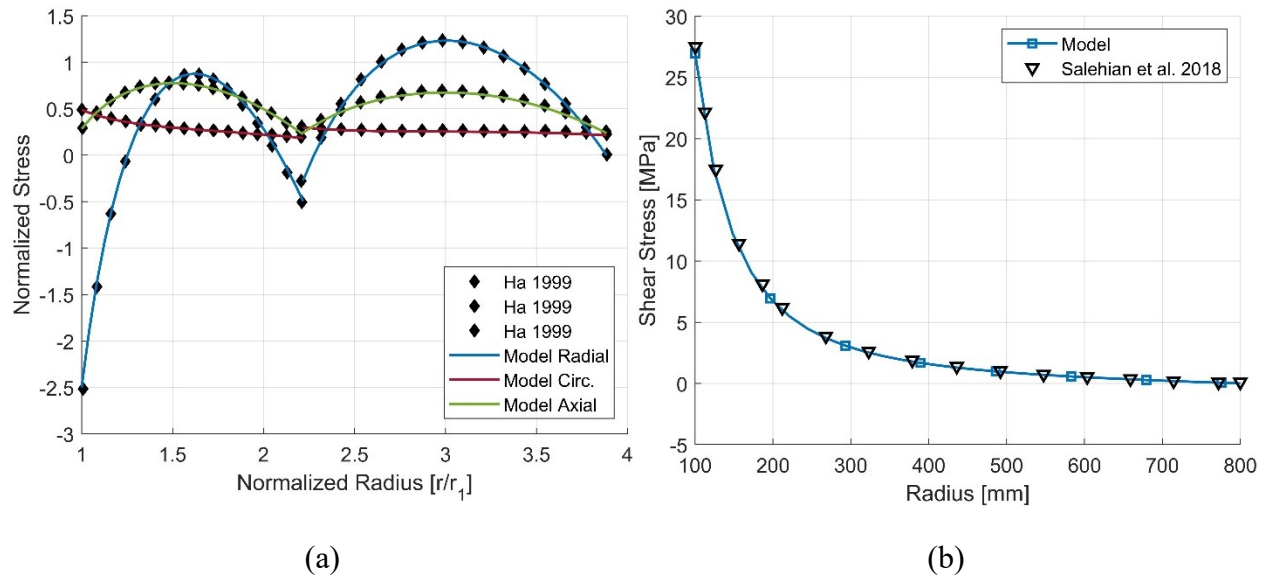


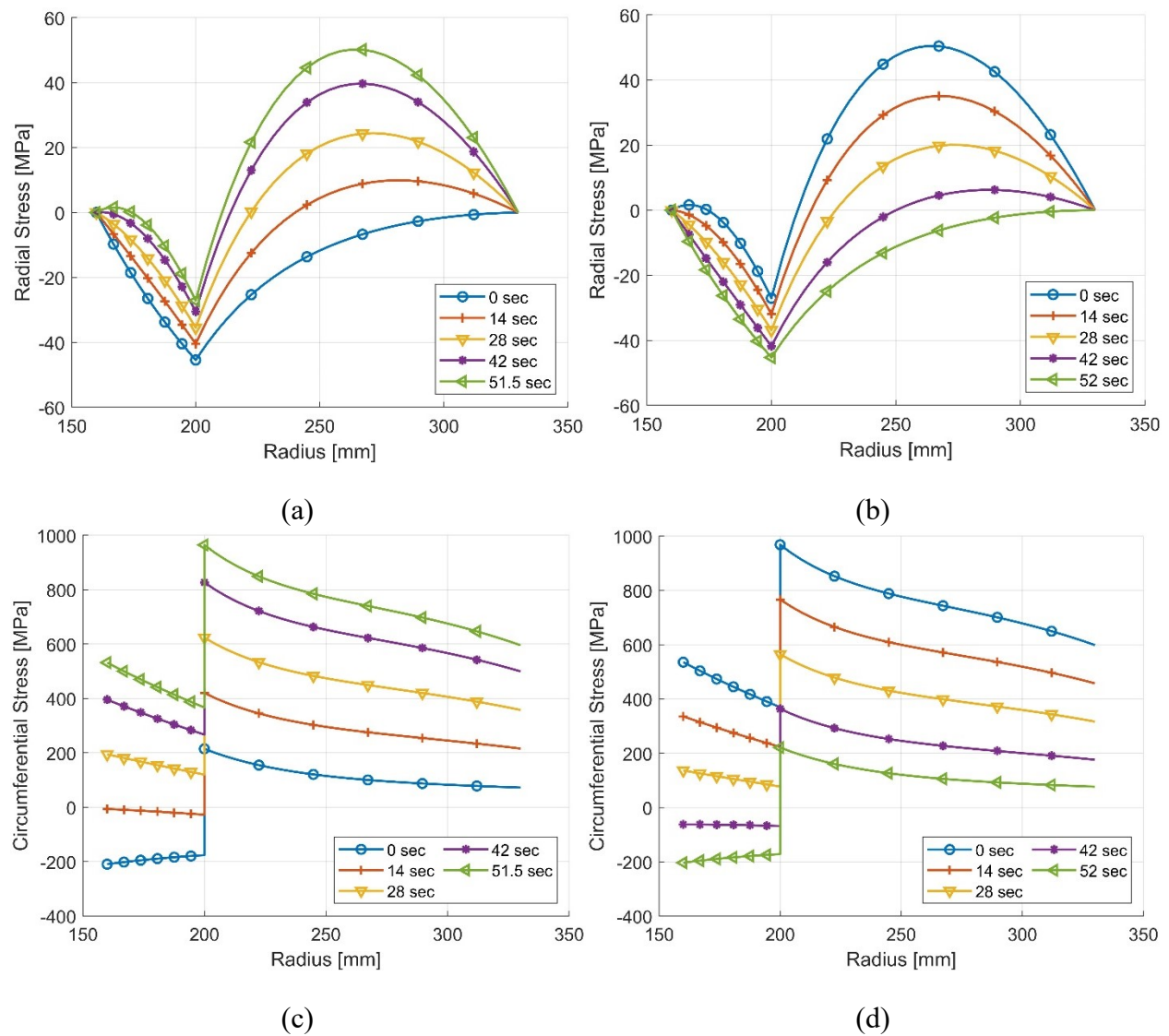
Figure 4.2: Comparison of shear stress calculated by the current model and those published by (a) Ha et al. [29] for radial, circumferential, axial stress, and (b) Salehian et al. [7] for shear stress.

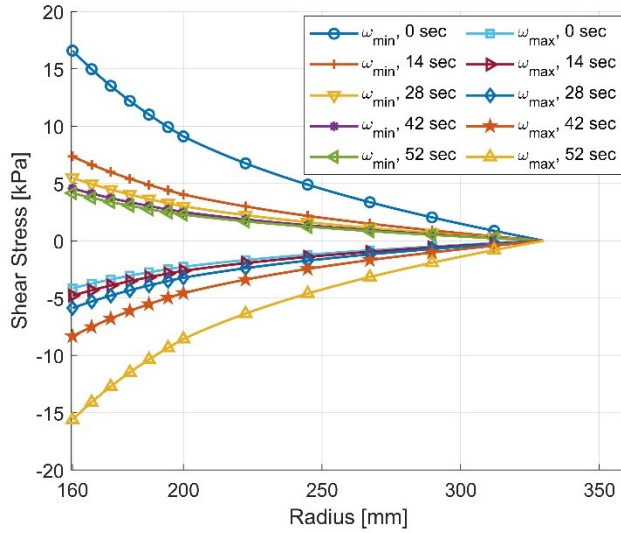
Recalling the plane strain assumption made for the present analysis, modeling results validate the taken approach, which simplifies solving the radial inhomogeneous equilibrium equation. Contrasting present work with published literature, see e.g. [6,7,29,30], comparable results are achieved. It should be noted that some of these studies assume generalized plane strain. Given the

body of published works that impose and validate the plane strain assumption, its application in the present analysis is seen as appropriate.

### 4.3.1 Constant Power Demand and Supply

The flywheel rotor simulation will predict the stress caused by constant power supply or demand of 725 kW as discussed previously. For the purposes of this discussion, supply will be used to indicate energy entering the FESS and accelerating the flywheel rotor while demand will indicate energy leaving the system thus decelerating the rotor. The simulation will always begin from either  $\omega_{\max}$ , in which case power and acceleration will be negative, or  $\omega_{\min}$ , in which case power and acceleration will be positive. The resulting radial, circumferential, and shear stress for both the supply and demand cases is given in Figure 4.3.





(e)

Figure 4.3: (a, b) radial stress when accelerating and decelerating (c, d) circumferential stress when accelerating and decelerating, and (e) shear stress induced by a constant power supply or demand of 725 kW.

From this figure several key points stand out and will be considered further. These points are the inner and outer rotor surface at  $r=160$  mm and  $r=330$  mm, the CFRP radial peak tensile stress location at  $r=262.8$  mm, and the interface at  $r=200$  mm. Interfacial stress is unique because it acts on both the hub and CFRP rim. While the radial stress is equal at this radius, the circumferential stress and SR varies significantly. For these radii of interest, the stress in each direction is given at all velocities in Figure 4.4. These figures, Figure 4.3 and Figure 4.4, provide complimentary information. Consider Figure 4.4a, radial stress at the inner and outer surface is zero and is identical at all velocities for the hub/rim interface, as is expected. The same data is shown in Figure 4.4a for all times during the simulation. This example identifies the relationship between the predicted radial stress, angular velocity, and simulation time for these four points. Similar deductions can be made for any of the radii of interest at any time and velocity during the simulation.

The radial and circumferential stress are observed to grow nonlinearly with angular velocity in Figure 4.4. At the interface, magnitude of pressure between the rim and hub decreases with velocity from 45.3 MPa to 27.0 MPa. The maximum tensile stress for the radial direction at  $\omega_{\max}$  is 50.4 MPa near the rim mid-surface at  $r=262.8$  mm and is in the same position whether accelerating or decelerating. Below  $\omega_{\max}$  the location of peak tensile stresses, shown in Figure 4.3a and b, is seen to move outward when decelerating.

Peak stress in the circumferential direction always occurs at the inner surface of the composite rim and is approximately 968 MPa. In the hub maximum stress was predicted at the inner surface of approximately 532 MPa and the minimum stress is -209.5 MPa.

Under the plane strain assumption axial stresses cannot be entirely discounted. The isotropic aluminum has a Poisson's ratio of 0.33 leading to peak axial stresses between -73 MPa and 243 MPa at the inner surface of the hub at maximum velocity. The composite rim is a slightly more complicated case due to anisotropy. In this case peak axial stress varied between 0 and 36.3 MPa. Circumferential stress in the CFRP has little impact on the axial stress because the material's high stiffness prevents significant strain. Therefore, axial stress in the CFRP is caused almost entirely by radial strain.

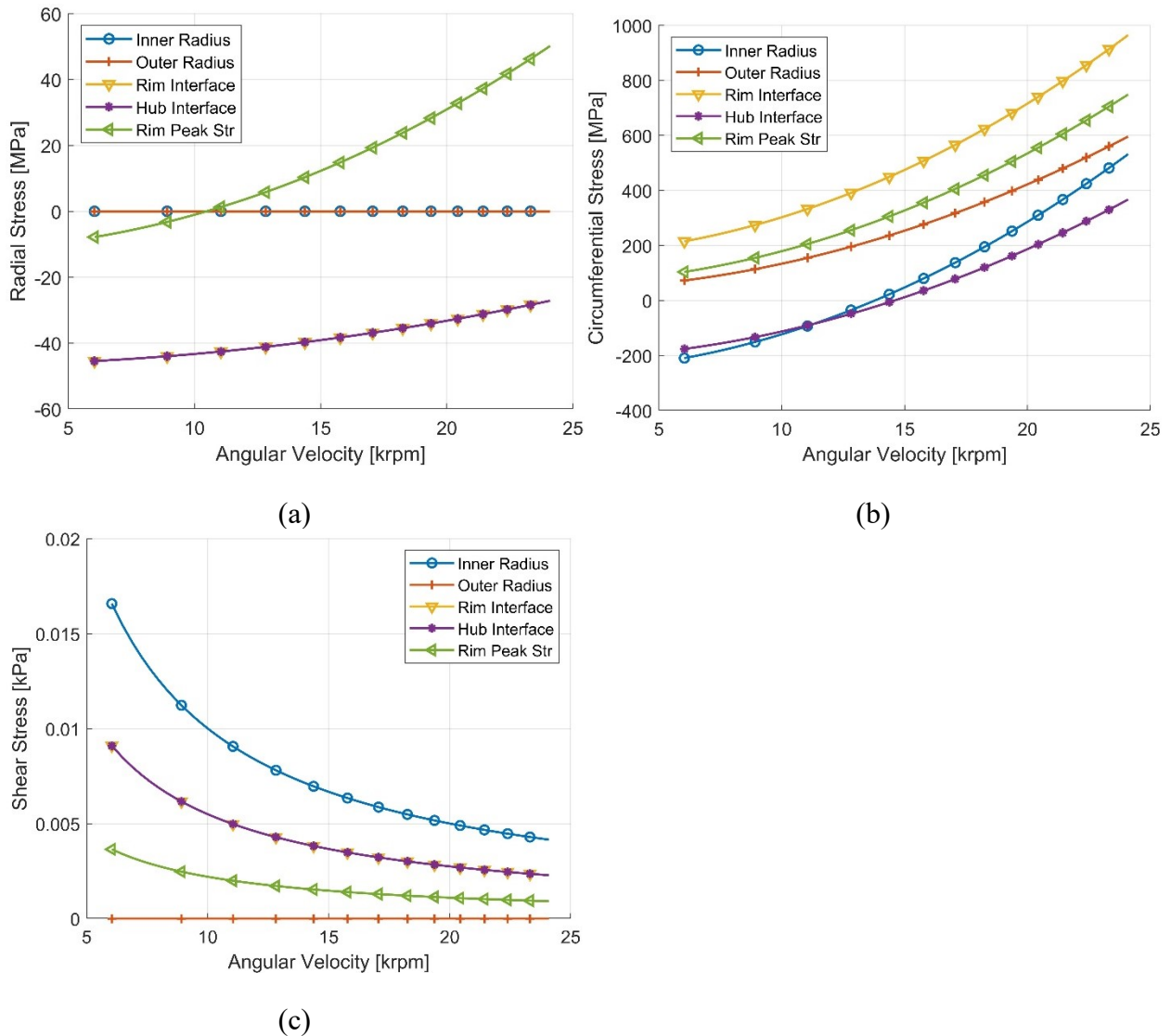


Figure 4.4: The (a) radial stress, (b) circumferential stress, (c) shear stress. Stresses at the interface are reported for the hub outer surface and the CFRP inner surface. The results for accelerating and decelerating are sufficiently similar so only the acceleration results are provided.

Figure 4.3e includes the shear stress while the rotor is both accelerating and decelerating, and Figure 4.4c includes the shear stress at all velocities for the five radii of interest. When the

rotor has an initial velocity of  $\omega_{\min}$  it is subjected to a shear stress at the inner of 16.6 kPa at  $t=0$  s decreasing to 4.15 kPa at  $t=52$  s. The exponential decay is clearly seen in both figures. The inverse behavior is seen when decelerating the rotor from  $\omega_{\max}$ . The initial high velocity allows for minimal deceleration, and therefore a minimal shear stress of -4.14 kPa. After decelerating from  $\omega_{\max}$  for 52 sec the rotor the shear stress is large due to the high acceleration required to maintain the power demand, the shear stress is 15.6 kPa. As was seen in section 3.1, minimum velocities result in maximum acceleration and shear stress.

The acceleration and deceleration do not produce exactly symmetric shear stress because the velocity at each simulated time iteration is not identical. Compare the acceleration and deceleration cases. In the first, the rotor begins at  $\omega_{\min}$  when  $t=0$  s. In the second, the rotor begins at  $\omega_{\max}$  and decelerates for  $t=52$  s before the simulation ends. In the first case, the angular velocity is exactly 6,037.5 rpm because the simulation begins at the minimum angular velocity. However, in the second case the simulation begins at the maximum and decelerates for 52 seconds ending at 6,411 rpm. At this point the rotor cannot meet the power requirement without passing below the minimum velocity so the simulation ends. For this reason, accelerating from the minimum velocity resulted in the simulation ending 0.5 seconds earlier than when decelerating from the maximum velocity.

The interfacial stress combined with the coefficient of friction between aluminum and CFRP can be used to determine the maximum allowable shear stress before the rim slips on the hub. The coefficient of friction between aluminum and CFRP is 0.68 [31] and the minimum interfacial stress, i.e. normal force acting on the cylindrical surface of the hub, is  $\pm 27$  MPa meaning the maximum shear stress must be less than  $\pm 18.36$  MPa to prevent sliding at the interface. Comparing Figure 4.3e and Figure 4.4c it is clear that interfacial friction is not a limiting factor for this flywheel rotor.

As the rotor undergoes a full charge discharge cycle circumferential and axial stress in the hub alternates between tensile and compressive stress. The difference between the maximum and minimum stress for each direction is 741.5 MPa for the circumferential and 316 MPa for the axial. Similarly, radial stress in the composite rim alternates tensile and compressive, however the difference between the maximum and minimum stress at  $r=262.8$  mm is 55.7 MPa, an order of magnitude less. Circumferential stress in the CFRP rim is the only region of the rotor which continuously experiences tensile stress. The largest difference in magnitude between the maximum and minimum stress occurs at the inner surface and has a range of 754 MPa. Taken in aggregate, these results suggest fatigue is a significant concern. Cracks can be initiated and propagate due to the large magnitude cyclic loading. Of particular concern is the inner surface of the hub, and the mid plane of the CFRP rotor. Circumferential stress in the hub can initiate a crack which would propagate radially outward [32]. Additionally, radial stress in the rim could initiate a crack which propagates circumferentially through the matrix [33].



### 4.3.2 Flywheel Rotor Failure

The Tsai-Wu criteria combines all four stress dimensions into the  $SR$  where a value greater than or equal to unity indicates failure. While accelerating from  $\omega_{\min}$ , the  $SR$  for all points along the flywheel rotor is given in Figure 4.5a and for all velocities at key points in Figure 4.5b. The  $SR$  while decelerating is not provided as the overall stress state between the two cases is sufficiently similar as to produce no significant difference between these two cases. Initially, the highest combined loading is seen in the aluminum hub, however this quickly changes as the rotor accelerates. The CFRP rim has lower radial stiffness than the aluminum and experiences greater centrifugal loading due to its radial position meaning radial stress quickly grows to dominate  $SR$  in this region of the rotor. In the hub,  $SR$  initially decreases as the circumferential and radial stresses, both caused by the press fit, decrease toward zero. As the rotor continues to accelerate stress continues to grow within the hub. This initial drop in  $SR$  is caused by the stresses transitioning from tensile to compressive. The phenomenon is most apparent in the hub because the radial, circumferential, and axial stress all transition from compressive to tensile unlike the CFRP rim where only the radial stress undergoes this transition.

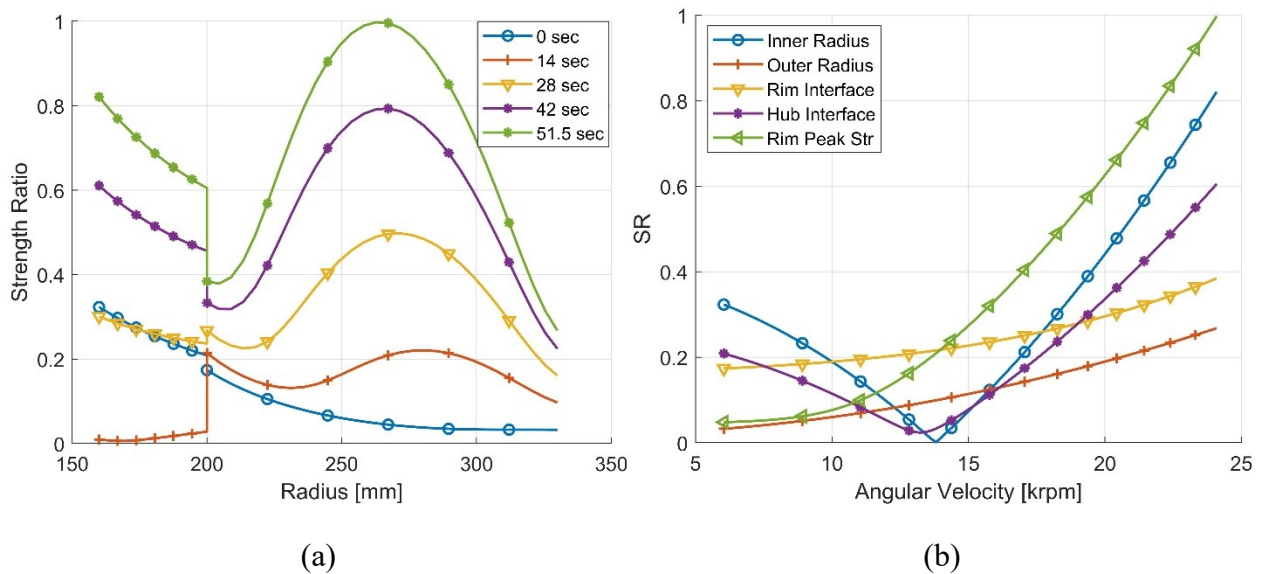


Figure 4.5:  $SR$  predicted using the Tsai Wu criteria for (a) all points in the flywheel rotor at various time throughout the simulation and (b) for all velocities in the simulation at five key radii of interest. Note the peak radial stress location changes with angular velocity, discussed below.

Based on quasi-static loading,  $SR$  predicts failure will occur in the composite rim at  $r=262.8$  mm. Considering the results in Figure 4.5b and Figure 4.3a failure is likely to occur in the radial direction as tensile stress exceeds the radial tensile strength. Quasi static failure is not predicted for any other points in the flywheel rotor.

Figure 4.5b shows the largest  $SR$  variations are seen in the hub which corresponds to the conclusions from Figure 4.3. At the hub inner and outer surfaces, the  $SR$  is seen to decrease to zero and 0.024 respectively before increasing to 0.82 and 0.61, among the largest values predicted anywhere in the rotor. The unusual shape of  $SR$  curves in the hub is caused by the change from

compressive to tensile stress. In the hub radial stress is typically dominated by the circumferential stress because aluminum is isotropic, and the magnitude of radial stress is significantly less than the circumferential stress. Below  $\omega=13,810$  rpm the circumferential stress is compressive loading, above that velocity it is tensile, and at that velocity circumferential stress is negligible. Consider the effect of radial stress on equation (21). This applied stress is always less than 10% of the yield strength, meaning the radial quadratic term,  $F_{33}(\sigma_3^{\text{app}})^2$ , will always have a value less than 0.01. Further, aluminum is isotropic, so all linear terms in equation 4.22 are zero. In aggregate this suggests radial stress in the hub has a negligible effect on SR when compared to the combined effect of circumferential and axial stress.

The slope of the *SR* curves in the hub is also larger than for any other region indicating that changing angular velocity disproportionately impact the hub when compared to the rim. The large magnitude *SR* variation and rapid growth and decay further support the conclusion that fatigue in the metallic hub is of significant concern to rotor failure.

Continuing, it can be seen *SR* is dependent on angular acceleration entirely though the quadratic term  $F_{66}(\tau_{13}^{\text{app}})^2$ . It has been shown the largest shear stress is 16.6 kPa at the inner surface of the hub while the circumferential stress at the same location and velocity is approximately -200 MPa and radials stress is zero.  $F_{66}$  is on the order of  $10^{-12}$  and  $(\tau_{13}^{\text{app}})^2$  is  $10^{-6}$ . Despite radial stress being zero clearly the circumferential stress is the only significant factor in *SR*. Conducting the same order of magnitude analysis for all velocities and times shows shear stress is never a significant factor in *SR* during the simulation. Figure 4.5 shows the *SR* curve for this flywheel regardless of acceleration and can be used for fatigue and lifetime assessment throughout the rotor's operation.

This is not to say shear stress is insignificant. Shear stress can have a significant impact on the induction and propagation of cracks, especially within the metallic hub where the magnitude and direction of stress varies wildly. While it has been shown the flywheel rotor is capable of withstanding these applies shear stresses that does not necessarily mean an FESS has the same capabilities. Rather this discussion shows shear stress, independently, may not be significant, however other factors dependent on shear, such as fatigue, are likely more significant than quasi static loading. Finally, shear stress can be used to define an upper bound on power supplies and demands acceptable to a flywheel rotor. While this upper bound may not be practical from an energy storage perspective it can become extremely relevant for other applications as discussed in [6].

Considering all velocities, the maximum *SR* and its corresponding location is shown in Figure 4.6. Maximum *SR*, shown in red, and peak stress location is blue. The time index of various key points is provided as well. The *SR* predicts the peak stress location change as the rotor accelerates. Initially, the circumferential stress dominates the stress response, and the peak stress location is at the inner surface of the rim,  $r=160$  mm. However, the peak stress location briefly

moves to the hub-rim interface before the CFRP rim radial stress grows to dominate the response, at approximately 13,620 rpm and  $t=14$  s, and the peak stress location moves to its largest radial distance at  $r=280$  mm. From here the peak stress location moves inward. At  $t=31$  s and  $t=47$  s peak stress is found at  $r=267.2$  and  $262.8$  mm respectively. This is just inside the rim mid plane due to the compressive loading at the interface. While the peak stress location is typically between the inner radius and the mid plane [6,29,34] of the CFRP rim the presence of the hub applying pressure to the inner surface of the rim forces the peak stress location further out than if the hub were not present.

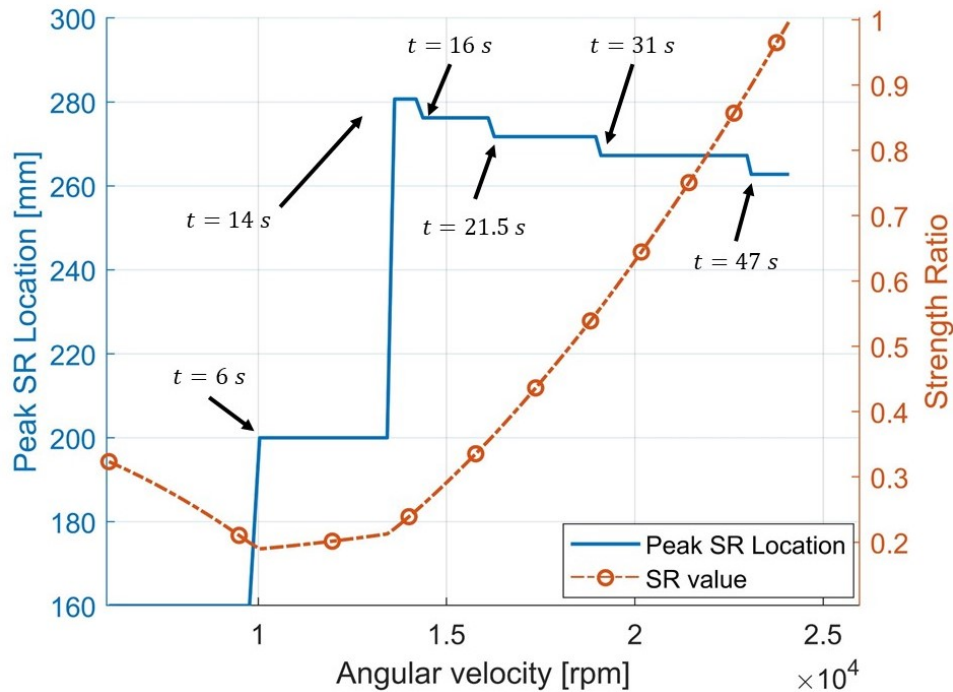


Figure 4.6: Maximum SR and corresponding peak SR location given for all angular velocities. The time index of various key points is provided as well.

To better understand the effect of the hub, a brief exploratory investigation was conducted by, first, allowing the rotor to accelerate continuously regardless of predicted failure until the peak stress location is constant, and, second, determining the peak stress location when the hub was not present. Note that shear stress decreases as velocity increases so shear stress will become a diminishing factor as velocity grows. After reaching 48,800 rpm, the peak stress location reached  $r=253.8$  mm but did not continue inward. When the hub was not present the peak stress location was always  $r=253.8$  mm. This confirmed the hub forces the peak stress location further outward which compounds with the greater circumferential stress at this larger radial position. Recognizing cyclic stress is most significant in the hub it may be beneficial to limit the minimum angular velocity of the rotor to 13,620 rpm. This would ensure the circumferential stress in the hub is always positive, thus minimizing cyclic fatigue. However, the increased minimum velocity reduces the available energy capacity to 68.2% of the total kinetic energy of the rotor.

## 4.4 Conclusion

High performance composite FRP flywheel rotors experience large cycle lifetimes and high-power capacities. This necessarily requires rotor acceleration and deceleration raising concerns regarding the effect shear stress has on the flywheel rotor. An analytical model capable of predicting radial, circumferential, and shear stress was developed to simulate filament wound FRP composite flywheel rotors. Additionally, the Tsai-Wu failure criterion was applied to predict failure velocity, location, and mode.

A constant power supply and demand 725 kWh was provided to the flywheel rotor to predict the stress evolution during a charge-discharge cycle. Five key points along the rotor were identified and used to track the predicted stress and *SR* at all velocities during the simulation. It was seen that in radial tensile stress in the rim was the most likely quasi-static failure mode. However, based on the wide range of predicted stress and *SR* there exists significant variability in the loading conditions suggesting crack initiation, crack propagation, and cyclic fatigue pose serious risk to the long-term health of the flywheel rotor, especially in the metallic hub. Recognizing shear stress has a minimal impact on stress magnitude, it is theorized that *SR* can be used to determine cyclic fatigue and failure.

Finally, it was seen that the peak stress location was not fixed, but rather moved from the inner surface to the interface, then to the CFRP rim. In the rim peak stress is first found at a large radial coordinate but moved slowly inward as angular velocity increases.

When discussing flywheel rotor failure, it is important to consider the wide variety of potential failure modes which exist simultaneously during operation. While the maximum radial stress criterion predicts failure before the Tsai-Wu criterion, it does not consider the complex interactions of each stress, nor does it provide insight on other potential failure modes such as cyclic fatigue and cracking. For this reason, when designing and analyzing composite FRP flywheel rotors, multiple failure modes should be considered in combination to determine the optimal design for a given application.

## 4.5 References

1. Amiryar, M.E.; Pullen, K.R. A review of flywheel energy storage system technologies and their applications. *Appl. Sci.* **2017**, *7*, doi:10.3390/app7030286.
2. Hadjipaschalis, I.; Poullikkas, A.; Efthimiou, V. Overview of current and future energy storage technologies for electric power applications. *Renew. Sustain. Energy Rev.* **2009**, *13*, 1513–1522, doi:10.1016/j.rser.2008.09.028.
3. Lekhnitskiy, S.G. *Anisotropic Plates*, Air Force Systems Command: Moscow, 1957.
4. Reddy, T.Y.; Srinath, H. Effects of acceleration stresses on the yielding of rotating disks. *Int. J. Mech. Sci.* **1974**, *16*, 593–596.
5. Roy, A.K.; Tsai, S.W. Design of Thick Composite Cylinders. *J. Press. Vessel Technol.* **2009**, *110*, 255, doi:10.1115/1.3265597.
6. Pérez-Aparicio, J.L.; Ripoll, L. Exact, integrated and complete solutions for composite flywheels. *Compos. Struct.* **2011**, *93*, 1404–1415, doi:10.1016/j.compstruct.2010.11.011.
7. Salehian, M.; Shahriari, B.; Yousefi, M. Investigating the effect of angular acceleration of the rotating disk having variable thickness and density function on shear stress and tangential displacement. *J. Brazilian Soc. Mech. Sci. Eng.* **2019**, *41*, 1–11, doi:10.1007/s40430-018-1523-8.

8. Kale, V.; Secanell, M. A comparative study between optimal metal and composite rotors for flywheel energy storage systems. *Energy Reports* **2018**, *4*, 576–585, doi:10.1016/j.egy.2018.09.003.
9. Wang, Y.; Dai, X.; Wei, K.; Guo, X. Progressive failure behavior of composite flywheels stacked from annular plain profiling woven fabric for energy storage. *Compos. Struct.* **2018**, *194*, 377–387, doi:10.1016/j.compstruct.2018.04.036.
10. Li, S.; Sitnikova, E.; Liang, Y.; Kaddour, A.S. The Tsai-Wu failure criterion rationalised in the context of UD composites. *Compos. Part A Appl. Sci. Manuf.* **2017**, *102*, 207–217, doi:10.1016/j.compositesa.2017.08.007.
11. Christensen, R.M. Stress based yield/failure criteria for fiber composites. *Int. J. Solids Struct.* **1997**, *34*, 529–543, doi:10.1016/S0020-7683(96)00038-8.
12. Mittelstedt, M.; Hansen, C.; Mertiny, P. Design and multi-objective optimization of fiber-reinforced polymer composite flywheel rotors. *Appl. Sci.* **2018**, *8*, doi:10.3390/app8081256.
13. Skinner, M.; Mertiny, P. Effects of Viscoelasticity on the Stress Evolution over the Lifetime of Filament-Wound Composite Flywheel Rotors for Energy Storage. *Appl. Sci.* **2021**, *11*, 9544, doi:10.3390/app11209544.
14. Hartl, S.; Schulz, A.; Sima, H.; Koch, T.; Kaltenbacher, M. A Static Burst Test for Composite Flywheel Rotors. *Appl. Compos. Mater.* **2016**, *23*, 271–288, doi:10.1007/s10443-015-9460-5.
15. Corbin, C.K. Burst failure prediction of composite flywheel rotors: A progressive damage approach via stiffness degradation, Stanford University, 2005.
16. Tsai, S.W.; Wu, E.M. A General Theory of Strength for Anisotropic Materials. *J Comp Mater* **1971**, *5*, 58–80.
17. Tzeng, J.T. Viscoelastic Modeling of Press-Fitted Composite Cylinders. *J Comps Tech Res* **2001**, *23*, 21–27.
18. Emerson, R.P. Viscoelastic Flywheel Rotors: Modeling and Measurement, Pennsylvania State University, 2002.
19. Ghosh, T.N.; Tzeng, J.T.; Emerson, R.P.; O'Brien, D.J.; Ghosh, T.N. Viscoelasticity Analysis and Experimental Validation of Anisotropic Composite Overwrap Cylinders. *Trans. Ophthalmol. Soc. U. K.* **2012**, *101*, 200–202, doi:10.1106/002199802021464.
20. Jordan, J.L.; Foley, J.R.; Siviour, C.R. Mechanical properties of Epon 826/DEA epoxy. *Mech. Time-Dependent Mater.* **2008**, *12*, 249–272, doi:10.1007/s11043-008-9061-x.
21. P.J. Charitidis Criteria for the Selection of Carbon Fiber Composite Materials for Fighter Aircraft. *Adv. Mater. Sci. Eng. An Int. J.* **2018**, *5*, 01–13, doi:10.5121/msej.2018.5401.
22. *Metals Handbook Properties and Selection: Nonferrous Alloys and Special-Purpose Materials*; ASM International, 1990; Vol. 2; ISBN 978-0-87170-378-1.
23. Tzeng, J.T. Viscoelastic Analysis of Composite Cylinders Subjected to Rotation. *Trans. Ophthalmol. Soc. U. K.* **2001**, *101*, 200–202, doi:10.1106/002199802021464.
24. Skinner, M. Characterization of passive discharge losses in a flywheel energy storage system, University of Alberta, 2017.
25. Rupp, A.; Baier, H.; Mertiny, P.; Secanell, M. Analysis of a Flywheel Energy Storage System for Light Rail Transit. *Energy* **2016**, *107*, 625–638, doi:10.1016/j.energy.2016.04.051.
26. Li, X.; Hu, L.; Palazzolo, A. A lightweight , high-speed kinetic battery for hybrid and electric vehicles. **2019**.
27. Peña-Alzola, R.; Sebastián, R.; Quesada, J.; Colmenar, A. Review of flywheel based energy storage systems. *Int. Conf. Power Eng. Energy Electr. Drives* **2011**, doi:10.1109/PowerEng.2011.6036455.
28. Longo, M.; Zaninelli, D.; Viola, F.; Romano, P.; Miceli, R.; Caruso, M.; Pellitteri, F. Recharge stations: A review. *2016 11th Int. Conf. Ecol. Veh. Renew. Energies, EVER 2016* **2016**, doi:10.1109/EVER.2016.7476390.
29. Ha, S.K.; Yang, H.-I.; Kim, D.-J. Optimum design of a hybrid composite flywheel with permanent magnet rotor. *J. Compos. Mater.* **1999**, *33*, 1544–1575.
30. Emerson, R.P.; Bakis, C.E. Optoelectronic strain measurement for flywheels. *Exp. Mech.* **2002**, *42*, 237–246, doi:10.1177/001448502321548300.
31. Schön, J. Coefficient of friction for aluminum in contact with a carbon fiber epoxy composite. *Tribol. Int.* **2004**, *37*, 395–404, doi:10.1016/j.triboint.2003.11.008.
32. Ren, J. Assessment of fatigue and fracture strength of transportation energy storage flywheel using finite element simulation. In *Damage and Fracture Mechanics VII*; **2002**; Vol. 37, pp. 235–244 ISBN 1853129267.
33. Ertz, G. Development, manufacturing and testing of a Multi-Rim ( Hybrid ) Flywheel Rotor, University of ALberta, **2014**.
34. Allam, M.N.M.; Tantawy, R.; Yousof, A.; Zenkour, A.M. Elastic and viscoelastic stresses of nonlinear rotating functionally graded solid and annular disks with gradually varying thickness. *Arch. Mech. Eng.* **2017**, *64*, 423–440, doi:10.1515/meceng-2017-0025.

## 5 Experimental Measurement of Viscoelastic Compliance

The parts of the following chapter have been published in the proceedings of the Canadian International Conference on Composites (CANCOM 2022). Table 5.1 identifies which sections are part of this publication and which are new to this thesis. Partially published sections are a combination of published and unpublished paragraphs or subsections. Appendices were not part of the original publication. This chapter addresses the third and final objective of this thesis.

*Table 5.1: List of sections in Chapter 5 detailing the inclusion in conference proceedings.*

Section Name	Published
5.1 Introduction	Partial
5.2 Experimental Setup and Methodology	Included
5.2.6 Experimental Procedures	Partial
5.2.7.1 Load Cell Characterization	Omitted
5.2.7.2 TTSP and Master Curve	Included
5.3 Validation of Experimental Procedures	Included
5.4 Results	Omitted
5.5 Conclusion	Partial

### 5.1 Introduction

The application of filament-wound fiber-reinforced polymer composites (FRPC) to the construction of flywheel rotors for energy storage has been a common practice for over 40 years and the study of composite material properties independent of application goes back even further [1]. Measurement methods for quasi-static elasticity are well-documented [2-3], and well reported in literature [4-5], however documentation for viscoelastic material properties is less comprehensive. Moreover, due to the existence of edge effects, measurement of transverse viscoelastic compliance of unidirectional FRPCs, such as those used in flywheel rotors, presents unique challenges for traditional coupon testing. Further, accurately measuring the anisotropic viscoelastic compliance of composite materials is critical to design and modeling of flywheel rotors [6-7]. Recognizing that FRPC that are filament-wound in the hoop direction are transversely isotropic [8-9], axial testing of tubular specimen is postulated to accurately represent the axial and radial transverse elasticity of thick-walled cylinders, such as those used in the construction of multi-rim flywheel rotors [10].

Skinner and Mertiny [7] showed that accounting for viscoelastic compliance is critical for designing and modeling composite flywheel rotors throughout their expected lifetime. The same is true for any application requiring long term prediction of composite material behavior. Specifically, it is necessary to determine the compliance master curve of the material for its entire lifetime. ASTM D2990 [11] states the creep strain of a composite specimen can be found by heating test specimens to an elevated temperature while applying a known load and measuring creep strain. Then, viscoelastic compliance is calculated from creep strain using the known stress.

Typically, the compliance master curve is constructed using employing the time temperature superposition (TTSP) approach which relates short term high temperature compliance with long-term low temperature compliance by shifting the short-term compliance measurements along a  $\log(\text{time})$  abscissa [12]. The shifting factors are commonly determined by applying an Arrhenius equation using the empirically derived creep activation energy [13-14]. However, this method requires an additional set of experiments, to determine the activation energy, and may not be feasible. Other methods for determining shifting factors have been described in literature including the computational algorithm discussed in [15].

This chapter presents a low-cost experimental platform capable of conducting viscoelastic testing on thin walled filament wound FRPC tubular specimens with the goal of constructing the transverse compliance master curve. The experimental platform and specimens are discussed in detail including the data acquisition system, sensors, and testing procedure. Additionally, the validation of data processing and test platform is presented. The objective of this chapter is to document the method for determining the compliance master curve of filament-wound composite specimens and reduce the barrier to entry for future researchers. The present study is conducted with glass fiber reinforced polymer composites (GFRP); however, the experimental platform and methodology is appropriate for any transversely isotropic material.

## 5.2 Experimental Setup and Methodology

### 5.2.1 Specimens

As shown in Figure 5.1, specimens comprise a composite tube and two aluminum tabs machined from 6061 aluminum. Tubes were filament-wound using glass fiber filament (Advantex Type 30, Owens Corning, Toledo, OH, USA) [16] onto a steel mandrel with a diameter of 25.4 mm. The matrix was a two-part epoxy (EPON 826 resin and EPIKURE 9551 hardener, Hexion, Columbus, OH, USA) [17] with a mixing ratio of 100:36. Table 1 gives further information on the composite material system and winding parameters. The winding angle was  $88^\circ$  to closely approximate a circumferential fiber orientation.

After winding, the resulting tubular part was cured on the rotating mandrel in an oven at  $80^\circ\text{C}$  for 1 hour, followed by  $120^\circ\text{C}$  for 2.5 hours. Tubes were then cut to length using a diamond saw. In preparation for adhesive bonding the tabs, the tube extremities were abraded and cleaned to create a uniform bonding surface. Prior to bonding, tubes and tabs were dried in an oven at  $50^\circ\text{C}$ , then the adhesive (DP460, 3M, Maplewood, MN, USA) was applied to bond the tabs to the tubes. Tubes and tabs were kept in alignment during room temperature cure using an alignment jig.

As manufactured, the composite tubes have a thin resin-rich area on the outer surface of the specimen. This layer contributes only marginally to the sample stiffness, so an effective wall thickness was used for analyses using the method described in [18]. In this method the effective wall thickness is found from the volume of the deposited fiber material and the fiber volume fraction, according to equations Eq.(5.1). The fiber volume fraction,  $v_f$ , was found by performing

burn-out tests using five composite tube sections collected when cutting the specimens to length. The fiber volume fraction was found to be 0.667, yielding an effective wall thickness of 2.88 mm, which agrees well with the measured wall thickness of 3 mm, assuming a resin-rich surface layer of about 0.1 mm—data provided in Appendix 1.

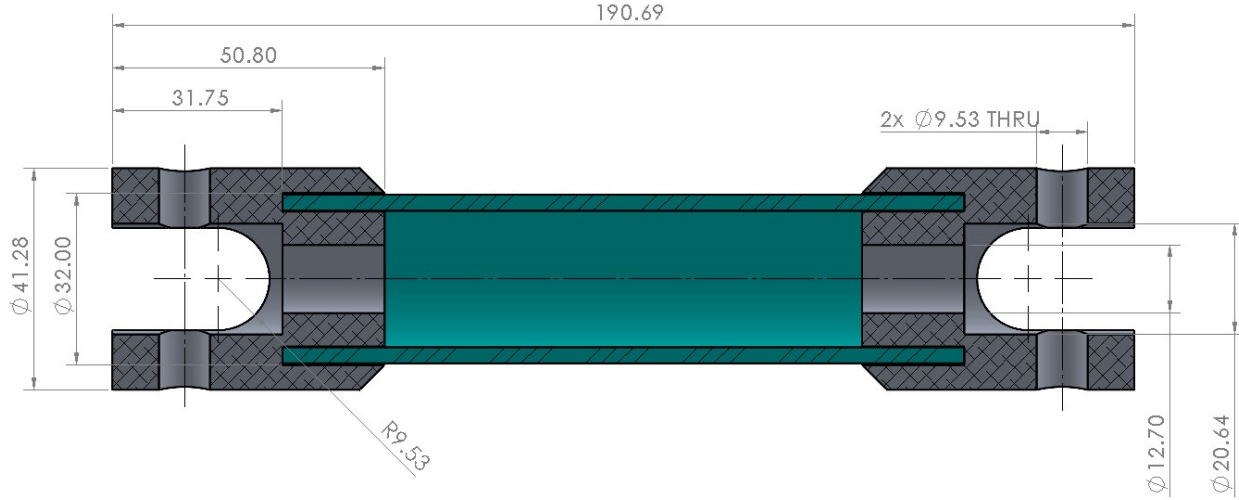


Figure 5.1: Cross-sectional diagram of test specimen assembly (dimension in mm).

Table 5.2: Material system and winding parameters used to create composite tubes [16-17].

Property	Value
Fiber density, $\rho_f$	2560 kg/m <sup>3</sup>
Matrix density, $\rho_m$	1160 kg/m <sup>3</sup>
Linear density of fiber tow, $TEX$	0.735 g/m
Number of fiber tows, $TOW$	2
Winding circuits, $C$	1
Winding angle, $\alpha$	88°
Number of layers, $N$	5
Inner diameter of composite tube, $ID$	25.4 mm

$$s = \sum_{n=1}^N t_{cover_n} \quad 5.1$$

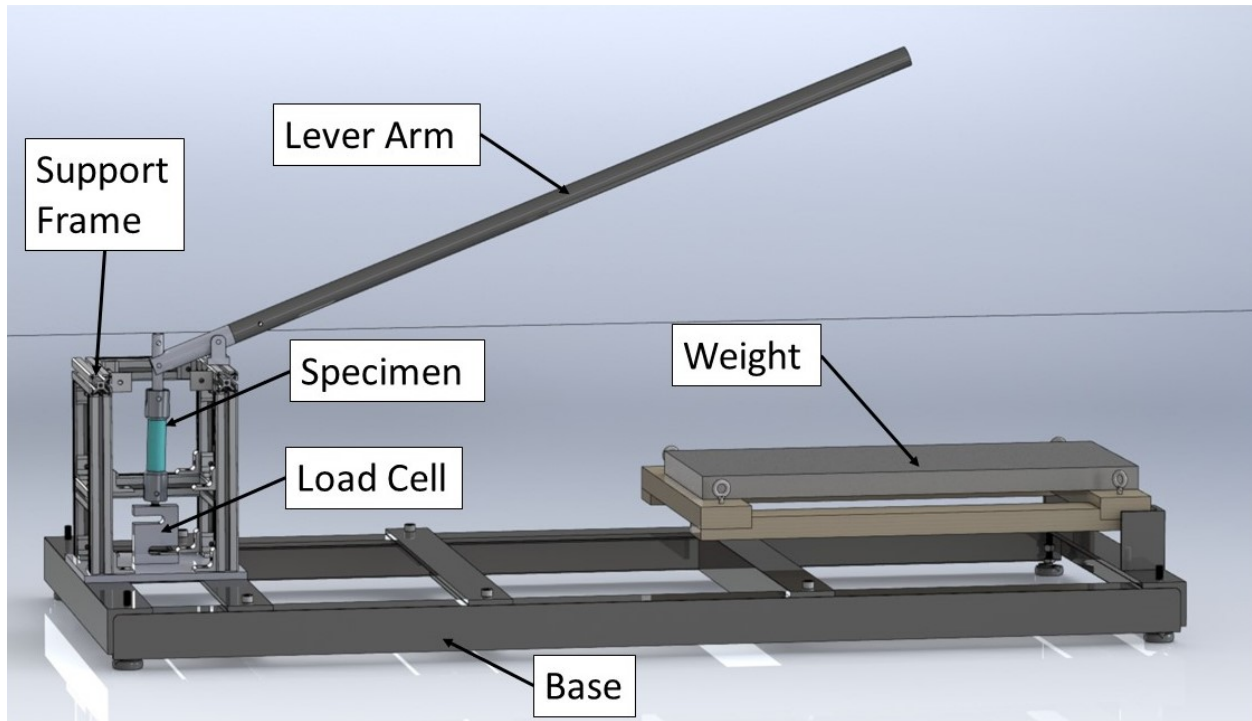
where

$$t_{cover_n} = \frac{(TEX)(TOW)C}{v_f \rho_f \pi \left( \frac{ID}{2} + \sum_{i=1}^{n-1} t_{cover_i} \right) \cos(\alpha)} \quad 5.2$$



### 5.2.2 Testing Equipment

An experimental setup was designed to satisfy the requirements established by ASTM D2990-17 [11]. Figure 5.2 depicts a diagram of the setup, consisting of a base, a support frame, a load cell, a mounted specimen, and lever arm with attached weight. Technical drawings and a bill of materials is provided in Appendix II.



*Figure 5.2: Diagram of creep test setup with labeled components. Some horizontal spars in the support frame have been hidden to provide an unobstructed view of the specimen and load cell.*

### 5.2.3 Specimen Mounts

The specimen is affixed in the load train with 4.76 mm (3/16 inch) steel pins slip fit in the specimen tabs and tensile machine fixtures. This allows the specimen to rotate freely in the machine and minimize off-axis loading.

### 5.2.4 Heating Chamber

The specimen can be placed inside a heating chamber, which gently heats the specimen and maintains it at the desired temperature. Figure 5.3a shows a schematic of the heating unit assembled with a specimen. Heat is supplied by a custom silicone strip heater (Wattco Inc., LaSalle, QC, Canada) wrapped around a cylindrical steel housing. The top, bottom, and outside of the cylinder is insulated with fiberglass insulation.

### 5.2.5 Instrumentation and Data Acquisition Equipment

Specimens are instrumented with three types of sensors: strain gauges, a load cell, and a thermocouple. Diagrams for the data acquisition (DAQ) system and all sensors are provided in

Figure 4. The load cell is an S-type load cell (type LC103B-5k, Omega Engineering, Norwalk, CT, USA).

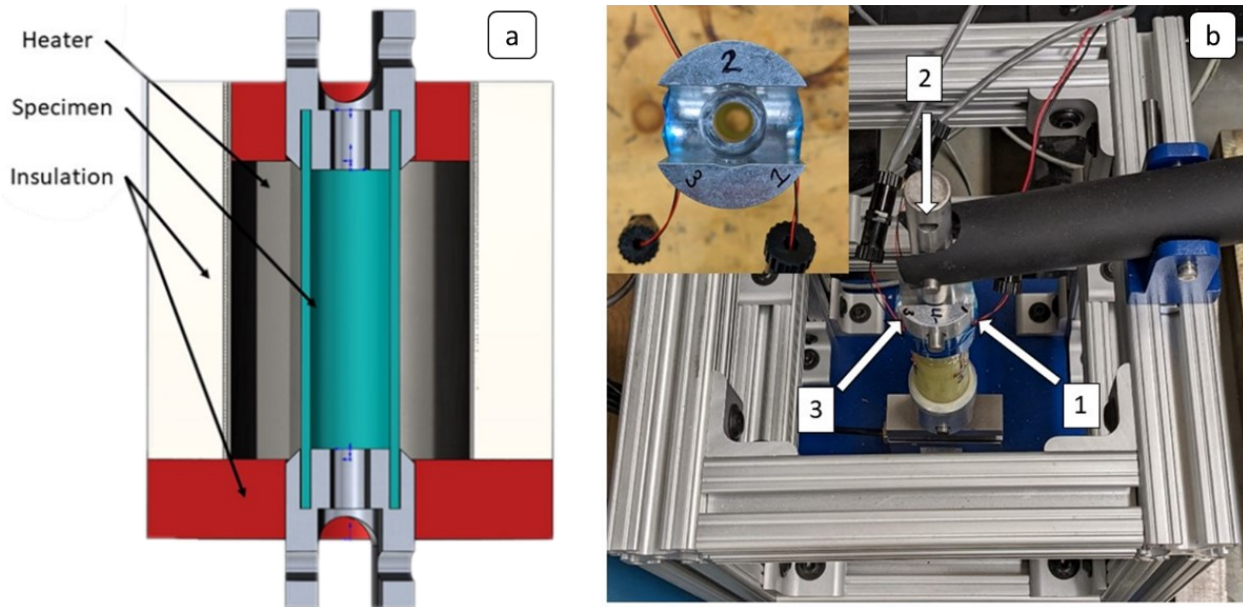


Figure 5.3: (a) Cross section of heating chamber and specimen, and (b) tensile machine showing specimen orientation (Insert: top-down view on specimen with strain gauges set to approximately  $120^\circ$  apart for viscoelastic experiments).

The strain gauge setup was altered between initial quasi-static and later viscoelastic testing in response to issues encountered during the former. Due to the possibility of off-axis loading creating bending stress in the sample, multiple strain gauges were attached to each sample. For quasi-static testing two strain gauges were applied to the surface of each sample approximately  $90^\circ$  apart. During quasi-static testing, off axis loading proved to be a reasonable concern so three strain gauges applied approximately  $120^\circ$  apart were used for creep testing. Hence, strain is collected from three independent gauges with the objective to assess whether the specimen is subjected to bending. If bending occurs, the magnitude and direction of bending can be determined. Moreover, data from the three gauges can be averaged to compensate for bending effects, similarly to [19]. A photograph of the specimen and strain gauge setup is shown in Figure 5.3b.

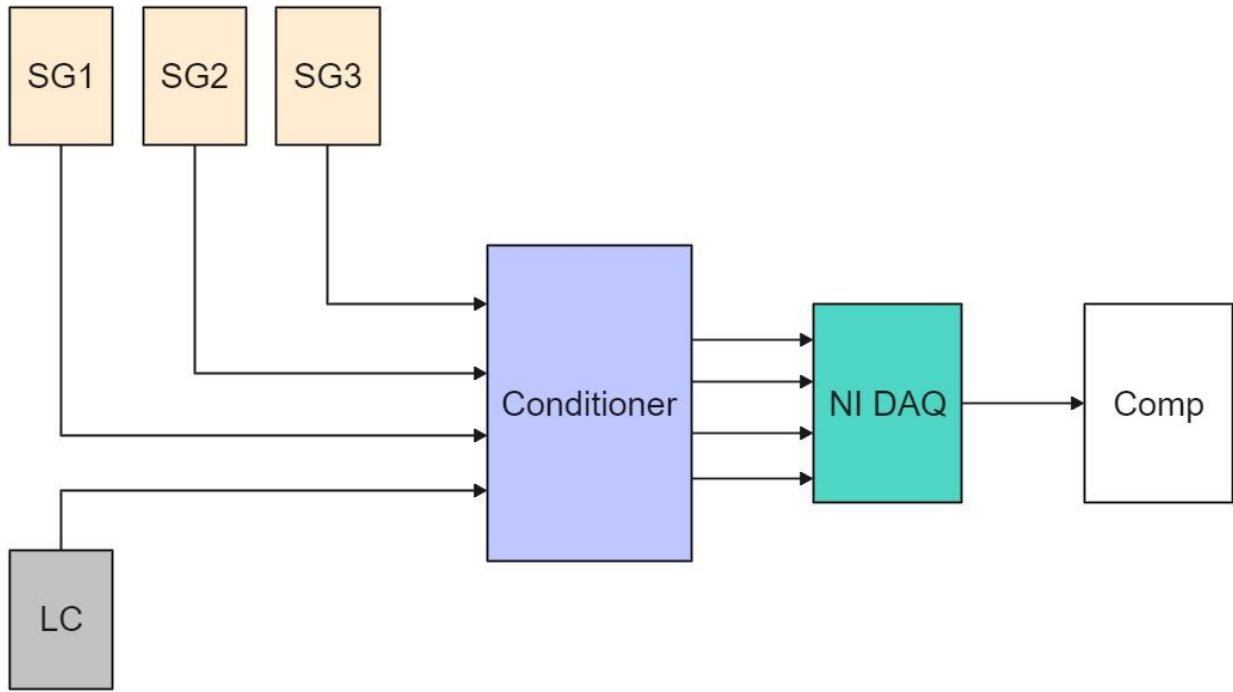
Two different strain gauges have been used, i.e., a dual-grid gauge CEA-13-125WT-350 and a single-grid gauge CEA-13-500UW-350 (both types by Vishay Precision Group Inc., Raleigh, NC, USA) [20-21]. Gauges are attached to the specimen using M-Bond 200 strain gauge adhesive, and aligned transverse to the fiber direction. The dual-grid and single-grid gauge are wired in a half-bridge and quarter bridge configuration, respectively. The gauges are connected to a Vishay 2100 gauge conditioner [22], which is used to balance the gauges before testing and apply amplifier gain.

Table 5.3: Strain gauge sensor parameters [20-21].

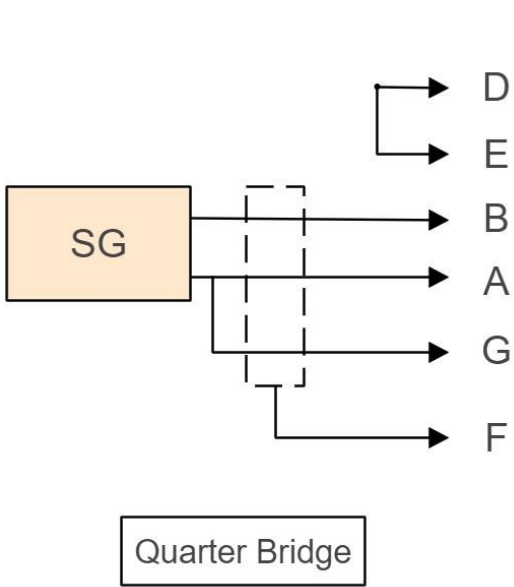
Parameter	CEA-13-125WT-350	CEA-13-500UT-350
Resistance [ $\Omega$ ]	$350 \pm 0.5\%$	$350 \pm 0.3\%$
Strain Range	$\pm 3\%$	$\pm 5\%$
Temperature Range [ $^{\circ}\text{C}$ ]	$-75^{\circ} - 65^{\circ}$	$-75^{\circ} - 175^{\circ}$
Gauge Length [mm]	3.13	12.7
Overall Length [mm]	8.2	17.78
Grid Width [mm]	4.57	4.57
Overall Width [mm]	8.26	4.57
Matrix Length [mm]	10.7	20.3
Matrix Width [mm]	10.7	6.9

The specimen temperature is recorded with a custom-built PID controller that continuously monitors the sample temperature with a thermocouple and regulates the heating power to control the temperature. Three K-type thermocouples (BQLRZ, Shenzhen, China) are used to measure the ambient, heater, and specimen temperatures throughout an experiment. The PID settings for the temperature controller are 0.1, 100, and 1.0 respectively. A detailed description of the controller and standard operating procedures is included in Appendix III.

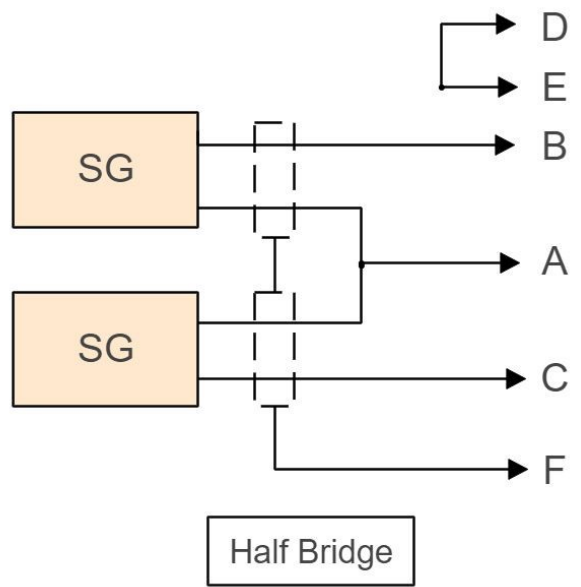
During testing, specimen strain and temperature, and applied load are collected continuously over time,  $t$ , at a sample rate of 1 Hz, using the NI DAQExpress software in conjunction with a NI 6008-USB device (National Instruments, Austin, TX, USA).



(a)



(b)



(c)

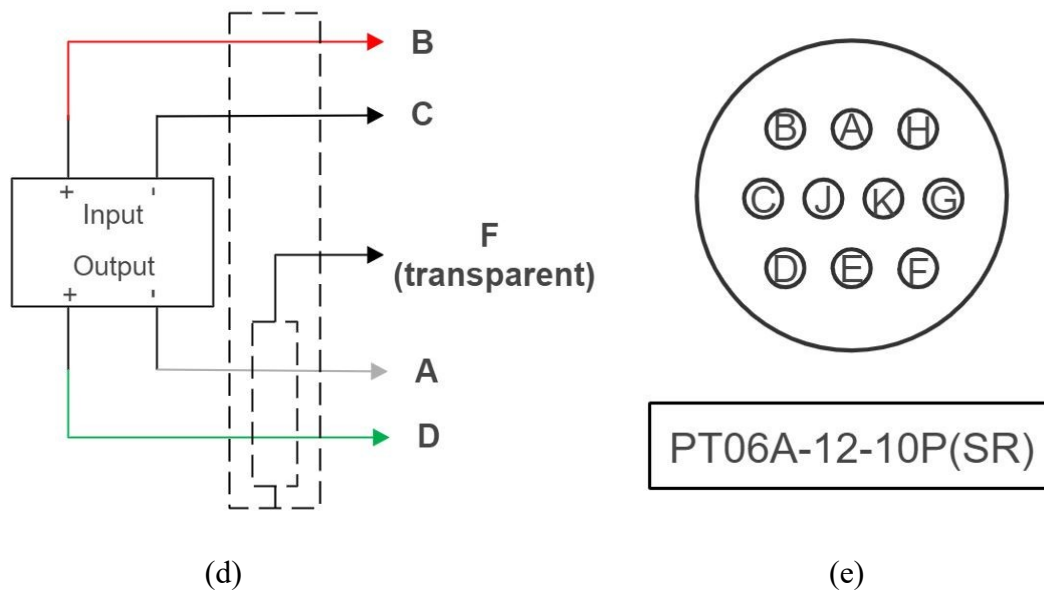


Figure 5.4: (a) circuit diagram for sensors and data acquisition system. b,c) Circuit diagram for half and quarter bridge strain gauges. d) Circuit diagram for LC103B-5k load cell where the color of the leads correspond to those from the manufacturer. e) Pin labels for gauge conditioner connector.

## 5.2.6 Experimental Procedures

### 5.2.6.1 Quasi-Static Testing

Quasi-static testing was performed using a universal testing machine (MTS 810, MTS, Eden Prairie, MN, USA) to determine the transverse tensile strength of GFRP specimens. Load was applied at 500 N/min until failure. Specimen strain was acquired with the sensor setup described above. Applied load and strain data were recorded by the control and DAQ computer of the testing machine.

The testing procedure was:

1. Connect strain gauges sensors to the DAQ and ensure the sensors are functioning properly, and sample rate is correct.
2. Ensure load rate and sample frequency are correct.
3. Load sample into the MTS 810 machine.
4. Begin data recording and experiment and monitor data acquisition throughout.

### 5.2.6.2 Viscoelastic Testing

To determine the transverse compliance master curve of the material, a series of elevated temperature experiments (30°C, 45°C, 60°C) were performed at two applied loads. Testing at 30°C, rather than room temperature, was conducted to ensure a constant temperature can be maintained using the heater. The 45°C and 60°C settings were selected based on ASTM D2990 which stipulates characterizing a material over the useful temperature range in suitable increments that reflect creep variation with temperature and transitions of the material. The applied loads were

set at 40% to fosters significant creep deformation while minimizing the risk of crack initiation, as shown in [19] where limiting stress to below 50% TS was found improve fatigue performance.

The technical literature diverges on the need for specimen conditioning. In [23], conditioning was deemed necessary for measuring nonlinear viscoelasticity, while virgin specimens were used in [24] to directly measure linear viscoelastic behavior. Recognizing that time-temperature superposition is only valid for linear viscoelastic behavior, specimen conditioning was not performed.

After instrumenting and installing a specimen and starting the control and DAQ system, the testing procedure begins by heating the sample at the required temperature until it reaches equilibrium (2 hours). Note that test data is recorded continuously during all stages of the experiment. Once at equilibrium, the first specified load is applied by engaging the weight in a steady manner using the scissor jack. The ensuing creep test stage runs for 30 minutes. Afterwards, the load is removed and the sample is heated to 65°C for 2 hours to allow for specimen recovery. This step is followed by equilibrating the sample at the next required temperature. Then, the load is applied for the second creep test stage, again for 30 minutes. The recovery-heating-loading sequence is repeated in the same manner for the final temperature. Notice that strains are noted after each heating stage and before applying the load as this data is needed to separate thermo-mechanical from elastic and viscoelastic effects. A concern with the above procedure is using a single specimen for multiple creep test stages. However, this concern is alleviated by examining the recovery behavior. It has been shown that post-recovery strain of less than 5  $\mu\epsilon$  indicated minimal permanent damage, so the specimen could be used for the next treatment [19].

## 5.2.7 Data Reduction

### 5.2.7.1 Load Cell Characterization

Applied stress was found by combining the specimen cross sectional area with the applied load recorded during testing with the load cell. The load cell voltage data was converted to applied load in Newtons using an empirically determined characteristic equation. The load cell was placed in the MTS 810 tensile test machine to apply known loads between 0 N and 19,613.3 N (4,409 lbf) while recording voltage. The results of this characterization are given in Figure 5.5 and the best fit equation found in Matlab is equation 5.3. The adjusted r2 value for this fit is 0.999, and was thus deemed acceptable. This will be used to convert the applied creep load to force.

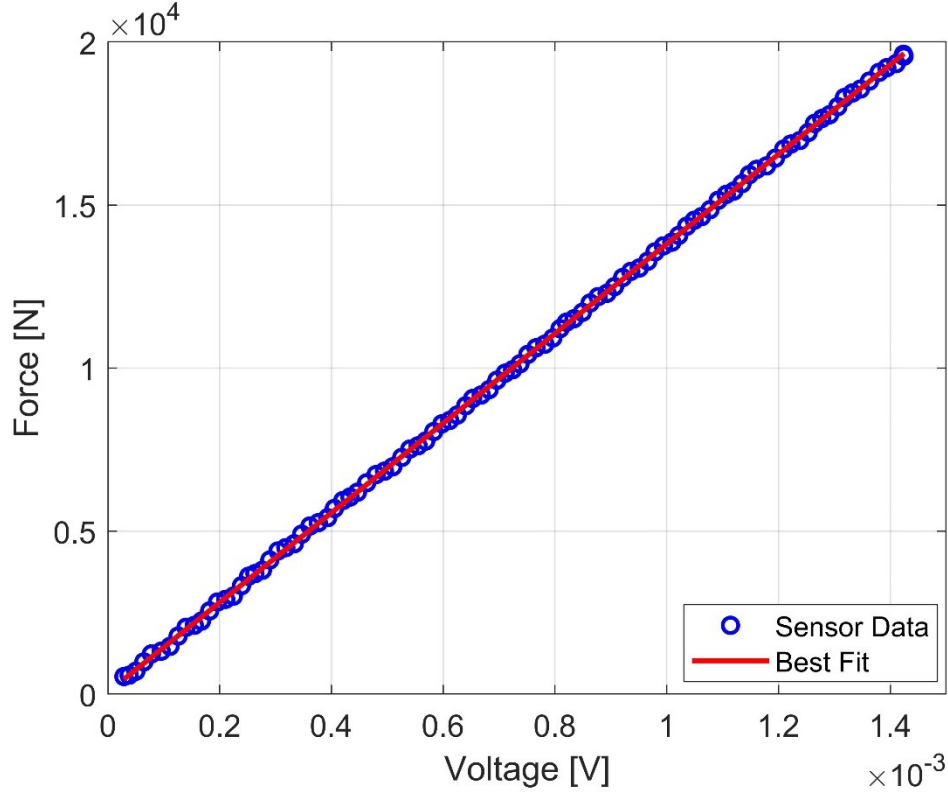


Figure 5.5: Sensor data and best fit approximation used to characterize the load cell.

$$F = (1.401E6)V + 5.88 \quad 5.3$$

#### 5.2.7.2 TTSP and Master Curve

Voltage signals recorded during the experiments were reduced to pertinent physical data. A linear voltage-force response was ascertaining for the load cell, allowing force and thus applied tensile stress to be determined using the specimen cross-sectional area. Recorded strain gauge data were isolated from the start to the end of each test stage. Gauge data from the quarter-bridge or half-bridge arrangement was converted to strain,  $\varepsilon$ , using Eqs.(5.4) and (5.5). Strain were then combined with applied stress to determine the time-dependent transverse compliance at each treatment temperature and load according to Eq.(5.6).

$$\varepsilon_{\text{quarter}}(t) = \frac{-4V_r(t)}{GF(1 + 2V_r(t))} \left(1 + \frac{R_L}{R_G}\right), \text{ or} \quad 5.4$$

$$\varepsilon_{\text{half}}(t) = \frac{-4V_r(t)}{GF[(1 + \nu) - 2V_r(t)(\nu - 1)]} \left(1 + \frac{R_L}{R_G}\right)$$

$$V_r(t) = \frac{V_{\text{strained}}(t) - V_{\text{unstrained}}(0)}{V_{\text{excitation}}}, \quad 5.5$$

where  $RL$  and  $RG$  are correspondingly the lead wire and strain gauge resistance,  $GF$  is the gauge factor,  $V$  is the measured voltage, and  $\nu$  is the Poisson's ratio of the material (here,  $RL \approx 0$ ).

$$S_{22}(t) = \frac{\varepsilon(t)}{\sigma} \quad 5.6$$

Employing TTSP the compliance master curve was constructed an employing shift factor, at. While there is no established convention for determining shift factors, it is common to calculate them using activation energy in an Arrhenius equation [26-27] or the Williams-Landel-Ferry equation [28-29]. However, this approach requires empirically determining the activation energy, which was not feasible in this study. Alternatively, the shift for each curve was determined analytically using the closed-form shifting algorithm described in [15], which determines the shift factor by minimizing the distance between the reference temperature compliance curve and the elevated temperature compliance data. Figure 5.6 illustrates this shifting algorithm. Consider two datasets,  $G_k$  and  $G_{k+1}$ , recorded at different temperatures,  $T_k$  and  $T_{k+1}$ , where each set contains  $N$  elements. Notably,  $G$  may denote any dataset, for example, creep strain data. The objective is to shift  $G_{k+1}$  along the abscissa to create a smooth curve. To accomplish this, the overlapping region from each data set is identified and used to define the boundaries of an overlapping window. These overlapping regions are

$$U_{k+1} = \{\log G_{k+1,n}, \log t_{k+1,n}, n = 1, 2, \dots, u_{k+1}\}, \quad 5.7$$

$$L_k = \{\log G_{k,n}, \log t_{k,n}, n = l_k, l_{k+1}, N_k\}. \quad 5.8$$

The location of the last point  $U_{k+1}$  is defined by an abscissa parallel passing through the last point in  $G_k$ , and intersecting  $G_{k+1}$ . Similarly, the first point in  $L_k$  is defined by an abscissa parallel containing the first point in  $G_{k+1}$  and intersecting  $G_k$ . With the overlapping window defined,  $a_{k+1}$  is found by minimizing the area of this window. Hence,

$$A = A_k - A_{k+1} = 0 \quad 5.9$$

where

$$A_k = \sum_{n=L_k}^{N_k-1} \left[ \frac{\log t_{k,n+1} + \log t_{k,n}}{2} (\log G_{k,n+1} - \log G_{k,n}) \right]. \quad 5.10$$

Using Eqs.(5.7) and (5.8), the shift factor for the segment dataset measured at  $T_{k+1}$  is,

$$\log a_{k+1} = \frac{A_k - \sum_{n=1}^{U_{k+1}-1} \left[ \frac{\log t_{k+1,n+1} + \log t_{k+1,n}}{2} (\log G_{k+1,n+1} - \log G_{k+1,n}) \right]}{\log G_{k,N_k} - \log G_{k+1,1}} \quad 5.11$$



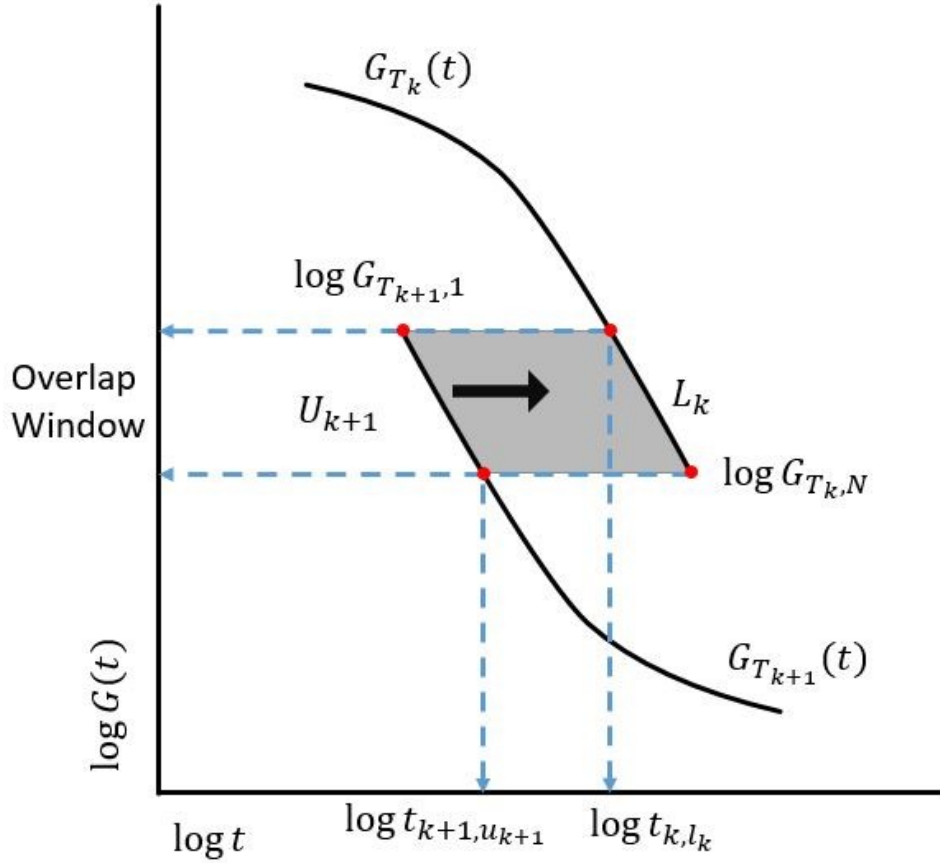


Figure 5.6: Schematic of data shifting procedure for compliance master curve.

There are several factors that affect the goodness of the shift resulting from the algorithm. It is important to control these factors to minimize shift errors. First, considering the size of the overlap window. Errors can be reduced by increasing the number of elements in the two overlap regions and the duration of the reference time in the window, both of which can be achieved by increasing the experiment duration. Second, considering the slope of the overlap regions, the error is minimized for moderately sloped overlapping regions and increases as the slope decreases toward zero and toward infinity. It has been shown in [15] that the ideal slope is approximately 0.05. The third and fourth factor for reducing shift errors are the magnitude of the experimental error that is controlled by the experimental setup, and the number of discrete data points per time unit in the reference frame, respectively.

The first step to applying the shift algorithm to the compliance data collected at the various temperatures is to select the lowest temperature as the reference temperature,  $T_k$ . The compliance at the next temperature  $T_{k+1}$  is shifted onto the reference temperature. Then, the two datasets are combined into a larger combined compliance, yielding the master curve at the reference temperature. Accordingly, the compliance at subsequent temperatures is shifted onto the master curve and added to the combined dataset. The master curve is complete when all elevated temperature compliance datasets have been shifted to the reference temperature. The final step is

to determine a best fit equation that can be used to reproduce the master curve for the life of the material. Findley’s power law is a common empirical model used to predict time-dependent compliance and creep of fiber reinforced polymer composites [30-31]. In terms of compliance, Findley’s power law is written as

$$S_{22} = At^n + b \quad 5.12$$

where  $b$  is the initial elastic compliance, and  $A$  and  $n$  are material constants. In the current study, curve fitting was performed using the built-in fitting tools in the Matlab programming environment (MathWorks, Natick, MA, USA).

### 5.3 Validation of Experimental Procedures

#### 5.3.1 Applied Load and Temperature

Preliminary testing with a target load of 5,000 N was performed to validate the applied loading. A mass of 43.1 kg was suspended 122 cm from the fulcrum. The steel lever, inclined at approximately 15° from horizontal, imposes a mass of 2.52 kg at its half-length (66.5 cm). For the mechanical advantage of 10.5:1, the predicted force applied to the specimen is 4,577 N compared to the load cell measurement 4,593 N ± 7 N, yielding an error of 0.3%. Figure 5.7a confirms that the applied loading is constant without drift.

The controller for the heater measures the chamber temperature and the specimen surface temperature. The latter is used for control purposes. The graph in Figure 5.7b depicts the surface and chamber temperatures for a 3-hour experiment. Notably, the chamber temperature is 55°C for a target specimen surface temperature 45°C. The graph confirms that the heater closely maintains the desired specimen temperature after about 2 hours of equilibrating.

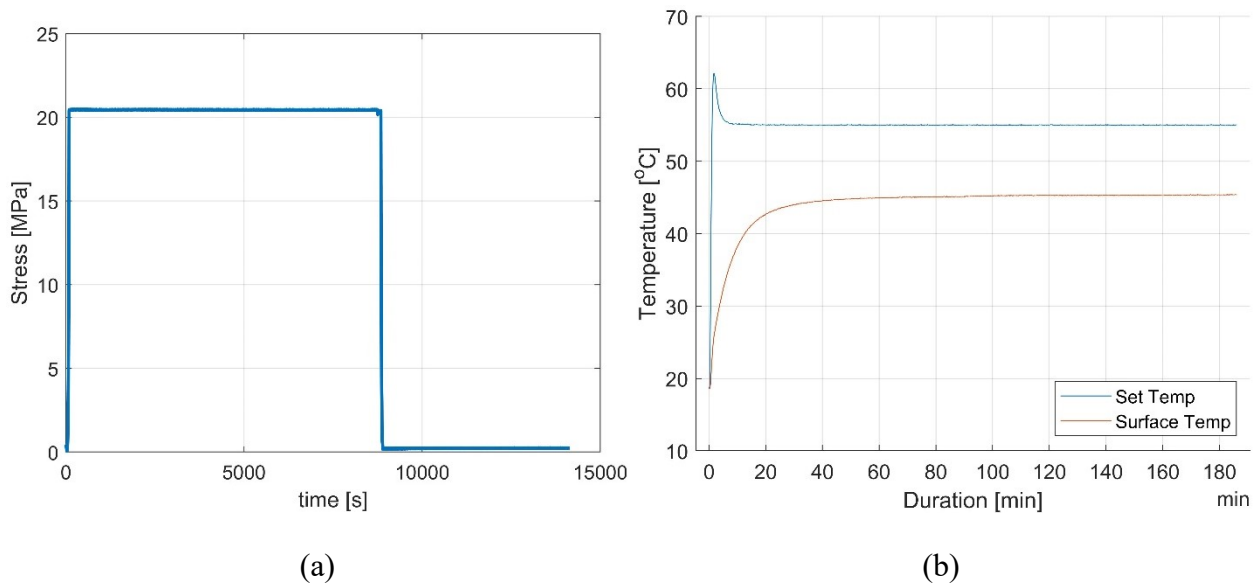


Figure 5.7: Data for test equipment validation: (a) Specimen surface and chamber temperature for a 3-hour experiment, and (b) load cell reading for applied load.

### 5.3.2 Strain Measurements and Bending Effects

In some instances, during quasi-static testing, differences in strain readings were observed between the three gauge locations along the specimen circumference, presumably due to bending effects. Example strain data is shown in Figure 5.8a, where gauges 1 and 3 recorded the largest strain indicating these gauges are on the outside of the bend radius while gauge 2 shows the least strain indicating it is on the inside of the bend radius. From a top-down perspective, the specimen is bending as indicated by the inset in Figure 5.8a. Bending is thought to originate from misalignment, either from imperfect mounting the specimen in the machine and/or a lack of cylindrical concentricity between specimen tube and metallic end tabs. Misalignments effects can be corrected by changing the specimen, or as mentioned above, by employing a procedure for compensating for bending effects as described in e.g. [19].

Figure 5.8b depicts sample creep strain data for a specimen subjected to the load described above. The strain measurements from each strain gauge have been averaged together to compensate for off-axis loading as discussed. The elastic strain caused by quasi-static loading and the recovery data have been removed from this graph to better display the creep strain results. The small discontinuity seen at 6,000 s is possibly due to a material defect or failure. The data in Figure 5.8b confirms the capability of the developed test setup and procedure to yield the transverse compliance master curve for FRPC specimens.

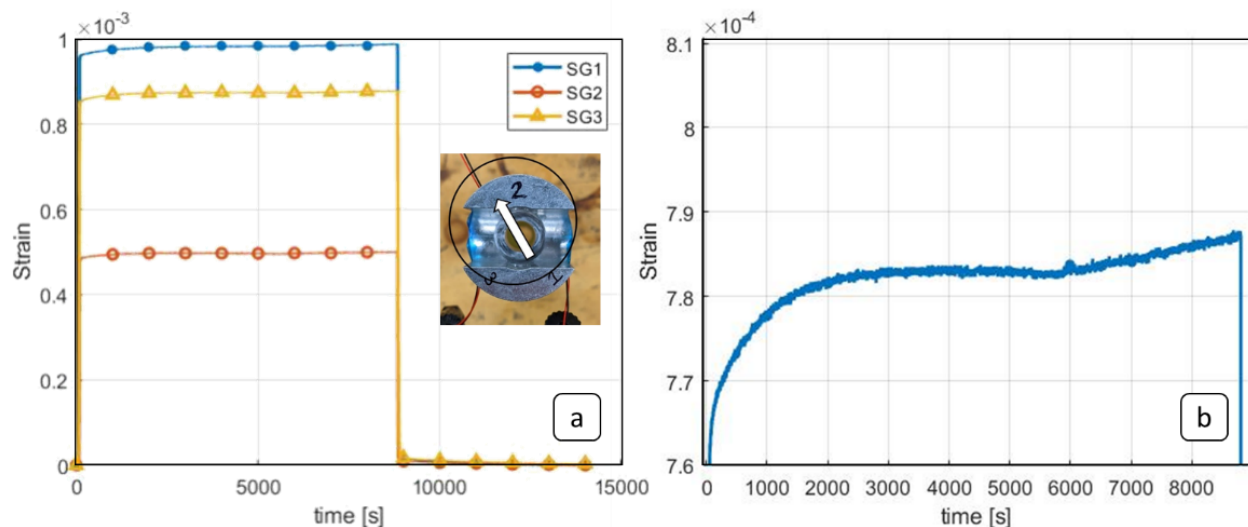


Figure 5.8: (a) Difference between strain data from strain gauges (SG) due to bending stress (Insert: Arrow indicating specimen bending direction from off axis loading), and (b) sample creep strain data.

## 5.4 Results and Discussion

### 5.4.1 Quasi-Static Results

The goal of quasi-static testing conducted in the MTS810 tensile test machine was to determine the elastic modulus and ultimate tensile strength of the GFRP material. Testing was

conducted as described in section 5.2.6.1. Load was applied to the specimens at 500 N/min. Strain is recorded on two strain gauges configured as either a half bridge or quarter bridge. Force is recorded by the tensile machine. The strain for two specimens is shown in Figure 5.9 below. The significant variability seen in the strain results is unexpected given that all specimens are cut from the same GFRP tube and subjected to the same loading conditions. This variability is attributed to off-axis bending stress, discussed in greater detail below.

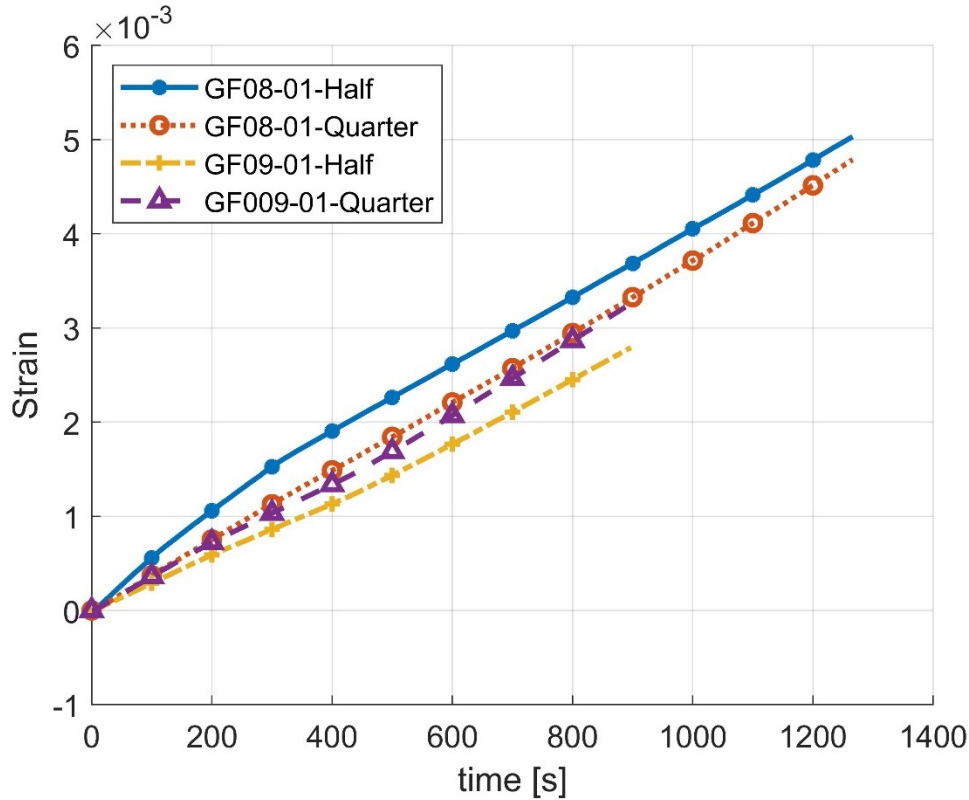


Figure 5.9: Strain-time results for glass fiber (GF) samples 08 and 09 collected during quasi-static testing.

The strain results of two specimens is shown in Figure 5.10 below. Data is labeled in four parts. In order these are a material, glass fiber (GF) in this case, a two or three digit specimen number, a two digit test number, and the strain gauge configuration. For example, label GF08-01-Half is glass fiber specimen 08 test number 01 from the half bridge strain gauge configuration. Note that specimens GF01 through GF07 were used for preliminary testing or were failure caused by off-axis loading. The elastic modulus for each data set can be found as the slope of the line in the stress strain curve, given in Table 5.4. These results for transverse elastic modulus and ultimate strain are consistent with results from similar materials published in literature [32].

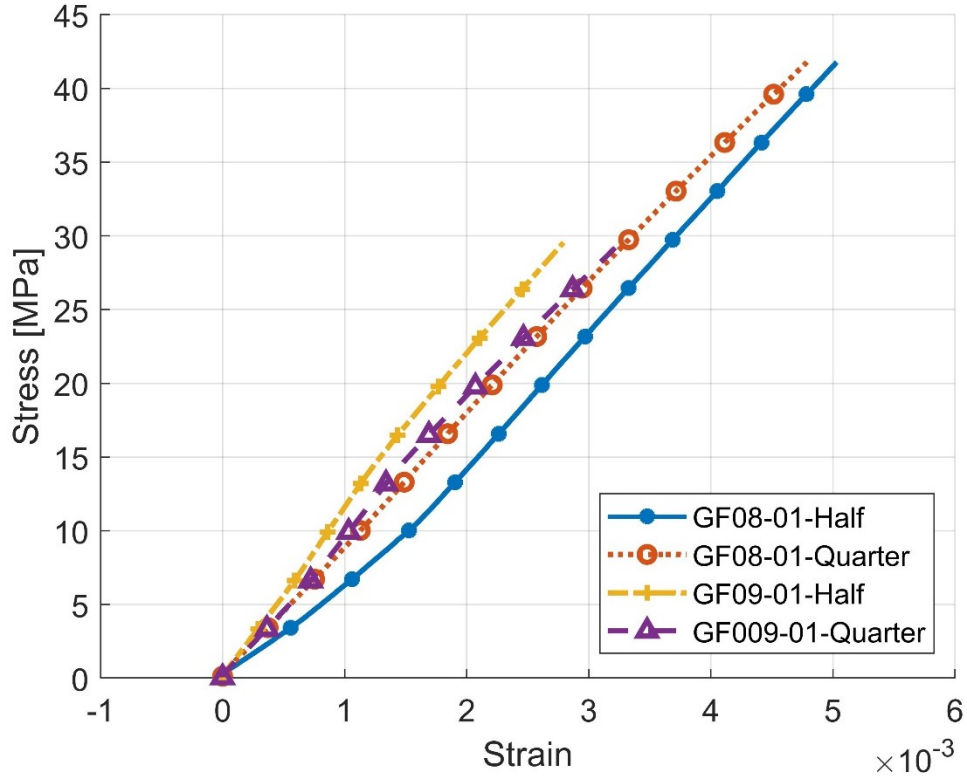


Figure 5.10: Stress-strain results for glass fiber (GF) samples 08 and 09. Strain data was collected from strain gauges set up in either a quarter bridge or half bridge configuration.

Table 5.4: Elastic modulus calculated from each experiment shown in Figure 5.10 and the average modulus for the material.

Test number	Elastic Modulus [GPa]	Ultimate Strain [%]
GF08-01-Half	8.416	0.478
GF08-01-Quarter	8.547	0.503
GF09-01-Half	10.452	--
GF09-01-Quarter	8.958	--
Average	9.06	0.491

Significant variability is seen between these data sets due to off-axis bending forces applied during testing. These specimens were designed for use in the viscoelastic test platform described above, however this creates an issue with mounting the specimen in the MTS machine and an adaptor had to be used. During earlier testing the adaptor was not in line with the central axis of the specimen causing bending. Additionally, the tubular shape also facilitates off axis loading because of its large radius compared to traditional coupon or dog bone samples. These issues combined lead to the variability seen in the quasi-static testing. The GF09-01 test was not intended to reach failure so it was stopped after the specimen reached 30 MPa. The GF08-01 test did

continue until failure reaching an ultimate failure stress of approximately 41 MPa. The elastic modulus and failure stress are within the expected range of GFRP material properties reported in literature [14], so these results will be used to define the applied creep load used in the viscoelastic testing.

#### 5.4.2 Viscoelastic Testing

The EPON 826/ EpiCure-W GFRP composite tube samples are tested at a creep stress of 16.4 MPa for the 40%TS with two repetitions. Table 5.5 gives all viscoelastic test parameters. Viscoelastic testing was conducted according to the procedure outlined in section 5.2.6.2.

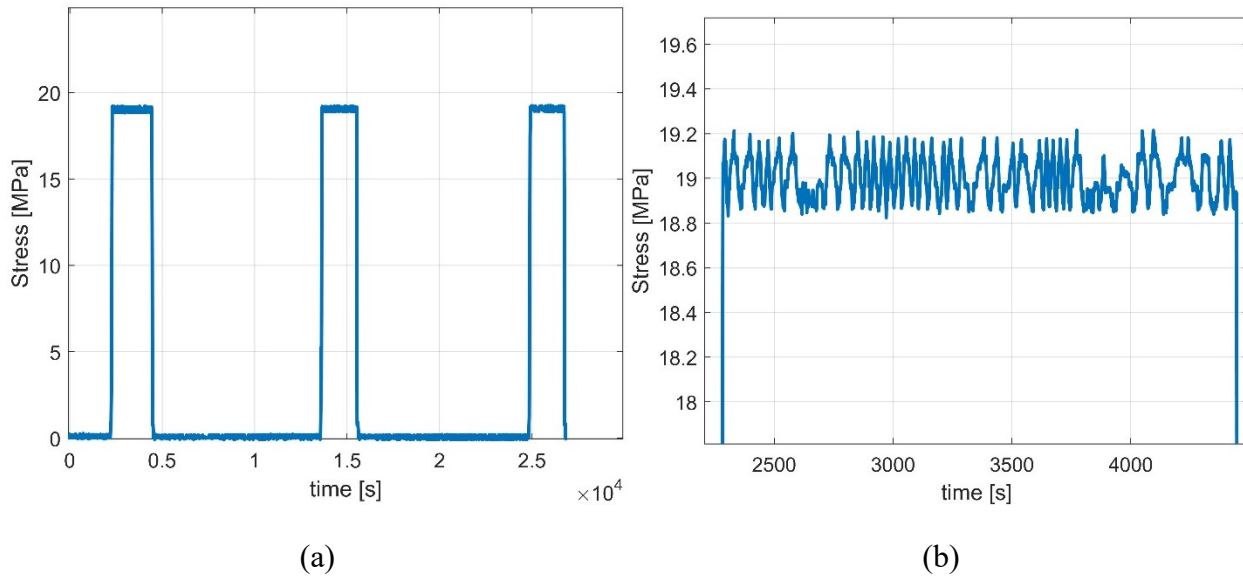
*Table 5.5: Treatment combinations table showing all the combinations of creep load and testing temperature.*

Applied Load	Test Temperature [°C]	Creep Duration [min]
16.4 MPa (40% TS)	30	~30
	45	~30
	60	~30

The effective wall thickness was found to be 2.88 mm, and the lever arm as manufactured provides a mechanical advantage of 10.49:1 meaning the lift platform and counter weight are 42.58 kg. The stress results for the 40%TS creep load repetitions shown in Figure 5.11 (a) as well as a detailed view of the first loading period in this figure. This figure is representative of the stress vs time results across all viscoelastic testing. The average stress value for this test is approximately 19.5 MPa which is 46%TS and exceeds the intended stress by 2.6 MPa. The variance in Figure 5.11 is approximately  $\pm 0.15$  MPa, however this was not constant throughout all tests. In the worst case, stress variations of between 0.5 MPa and 1 MPa were observed. This was attributed to a number of causes. First and most significantly, oscillations of the lever arm were observed just after applying the load and seen to continue for several minutes after the viscoelastic test began. These were caused by non-uniform application of the creep load. The counter weights are placed in the approximate center of the lift platform, however small deviations from the exact center can cause the platform to swing which acts like a pendulum varying the load throughout its period. Additionally, the load is applied manually by lowering a scissor lift which allows the lift platform to hang from the lever arm. If this is not done smoothly this can induce oscillations in the lever arm. A secondary influence on the creep load is other activity in the lab area which can create vibrations due to the operation of other equipment.

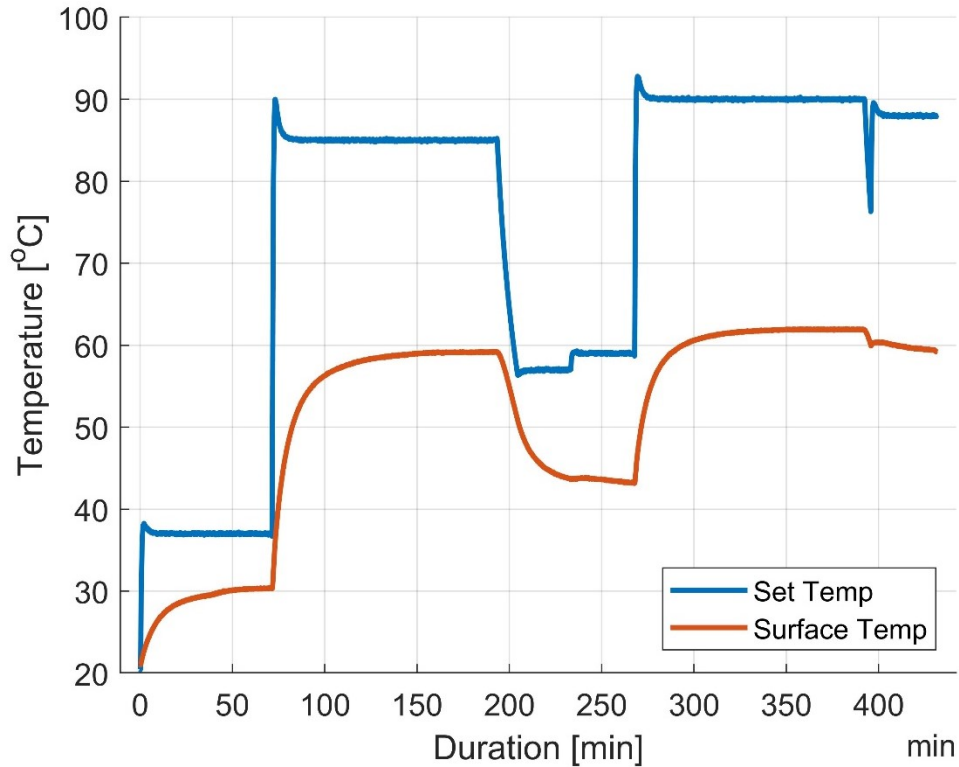
The oscillations can be addressed in several ways. First, shortening the lever arm and increasing its stiffness will reduce bending. Secondly, decreasing the size of the lift platform and balancing the center of gravity below the center of lift will reduce its tendency to swing. Finally, the machine can be better isolated from its surroundings by increasing the mass of the machine

and changing its footing to a more stable alternative thus reducing interference from outside influences.



*Figure 5.11: Stress results from GF1 as a representative example of (a) stress vs time for the 40%TS creep load and all three experimental temperatures, and (b) detailed view of the stress variation in the first temperature and stress period from the same test.*

The temperature results for this experiment is shown in Figure 5.12. Again, this was a representative example of the temperature profile of the sample throughout a viscoelastic experiment. Notice the offset between the set temperature and the sample surface temperature. The size of the offset varied significantly between experiments largely due to the air temperature in the lab during testing. It took approximately 30 to 40 minutes to reach equilibrium at all temperatures and small adjustments were made to the set temperature before applying the load to ensure the sample is at the appropriate temperature for each part of the experiment. For the example shown the measured temperature during each test was 30.3°C, 44°C, and 61°C which is within the limits specified by ASTM for creep testing [2]. The sample temperature was always within  $\pm 2^\circ\text{C}$  of the desired temperature for all experiments.



*Figure 5.12: Temperature results from GF1 as a representative example of the heater temperature and sample surface temperature throughout a viscoelastic experiment.*

The specimen strain was recorded on three strain gauges placed uniformly around the sample. The strain results for a representative experiment are shown in Figure 5.13. Significant variation is seen from each gauge and at each temperature. This variation is consistent with those shown in Figure 5.8, however the direction and magnitude of off axis loading is not consistent. Strain variation changes between samples, between temperatures, and between orientations of the sample in the machine. The variation between samples can be likely attributed to manufacturing errors in either the aluminum tabs, the composite sample, or both. Manufacturing errors can be created when cutting the samples to length and assembling them with the tabs. Additionally due to the manual application, the strain gauges may not be aligned perfectly with the central axis creating systematic errors. Further, in the composite sample manufacturing defects, such as void space and resin rich areas, are randomly created and are typically assumed to be uniformly dispersed throughout the sample. However, it is possible to create a network of defects negatively impacting homogeneity, though it is worth nothing this is likely a less significant effect than manufacturing errors.



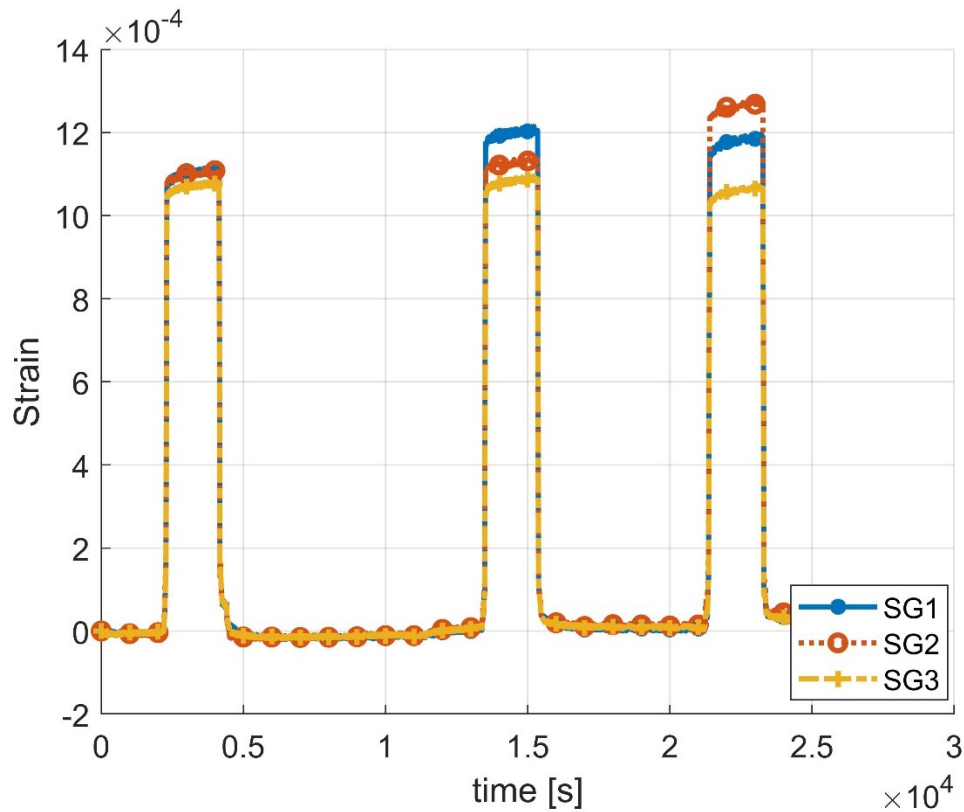


Figure 5.13: Strain results from GF1 as a representative example of the strain vs time results for a viscoelastic experiment showing strain of all three strain gauges during each temperature step.

Regarding the sample position in the machine, it was observed that a sample at constant temperature placed in the machine will produce different strain results than the same sample rotated  $180^\circ$ . Additionally, the magnitude of difference between the different orientations suggests a positive interaction between manufacturing errors of the machine and manufacturing errors in the sample.

These issues can be addressed by enacting tighter tolerances on the shape and size of the composite tube samples and on the sample assembly. The development of a jig to assist with assembly and placing strain gauges which further eliminates possible sources of error. Finally, an investigation should be conducted into the construction and use of the tensile platform to minimize systematic errors.

As discussed earlier the effects of off axis loading and random errors is minimized by averaging the results from all three strain gauges. The average result for the above strain is given in Figure 5.14a. This is the total strain including thermal, elastic, and creep strains. These are the data collected throughout the entire experiment including the recovery periods, therefore they are plotted against absolute time. By looking at the stress-time data, Figure 5.11, the load and unload times for each temperature can be clearly identified. This allows the creep data to be isolated from the recovery periods. The creep data is then plotted against experimental time which begins when

the creep load is fully applied at  $t=0$ , Figure 5.14b. At this point it is important to remove thermal effects from these data to ensure the compliance is calculated only based on the viscoelastic response of the material.

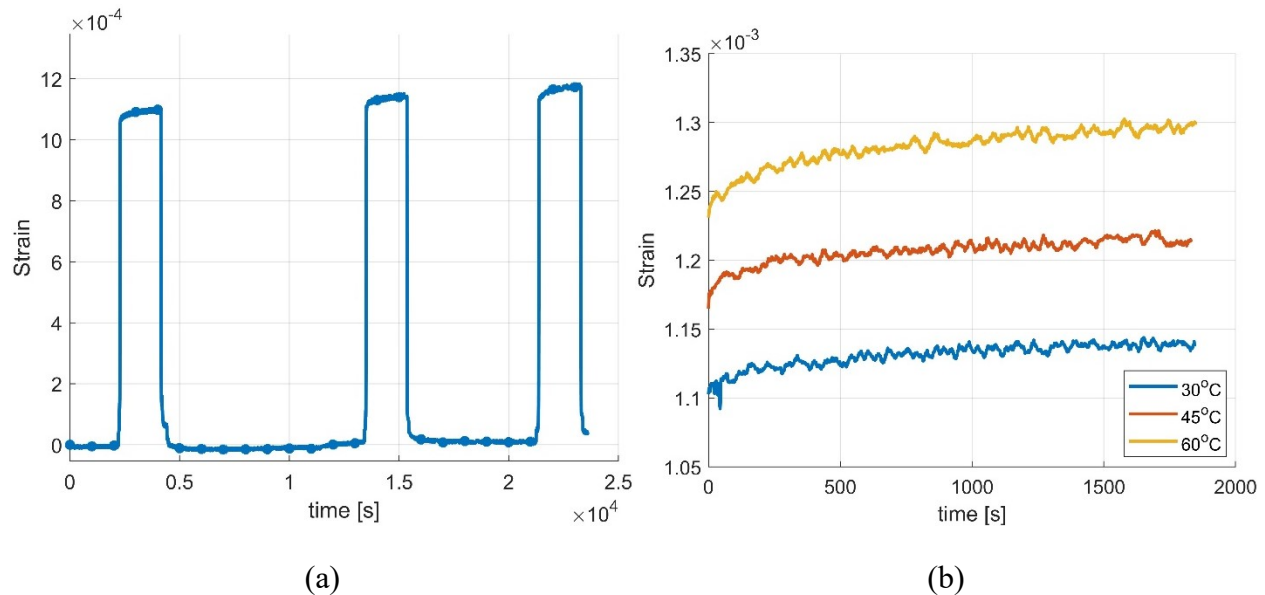


Figure 5.14: (a) Average strain results for the viscoelastic test shown in Figure 5.13. Creep data is plotted against absolute time. (b) Creep data with the recovery period removed and plotted against experimental time.

Thermal compensation is a superposition of the ratio of the thermal expansion coefficient between the composite and the strain gauges as well as the electrical resistivity of the strain gauge. This is to say the electrical resistivity of the strain gauge will vary depending on temperature and thermal strain, both of which effect the strain measurement and interfere with measuring the coefficient of thermal expansion for the composite [33]. The manufacturer recommends the overall thermal output be measured by heating the sample to each test temperature with no applied load while measuring strain. The resulting value, in strain units, can then be subtracted from the experimental strain data to compensate for temperature changes. This value can be either positive or negative, meaning that compensating for temperature variations can increase or decrease the experimental strain depending on the interaction between the gauge and the sample. Thermal compensation results are given in Figure 5.15. At 30°C, 45°C, and 60°C the measured output is  $-8.19 \mu\epsilon$ ,  $-29.4 \mu\epsilon$ , and  $-43.3 \mu\epsilon$  respectively. These results are consistent with manufacturer published estimates between materials with differing CTE. The negative values do not necessarily indicate the sample or strain gauge is under compression, rather that the that the output of the strain gauge has decreased relative to its initial starting position as a result of the increasing temperature. These values will be subtracted from the strain measurements, i.e. subtracting a negative value, in order to compensate for thermal output.

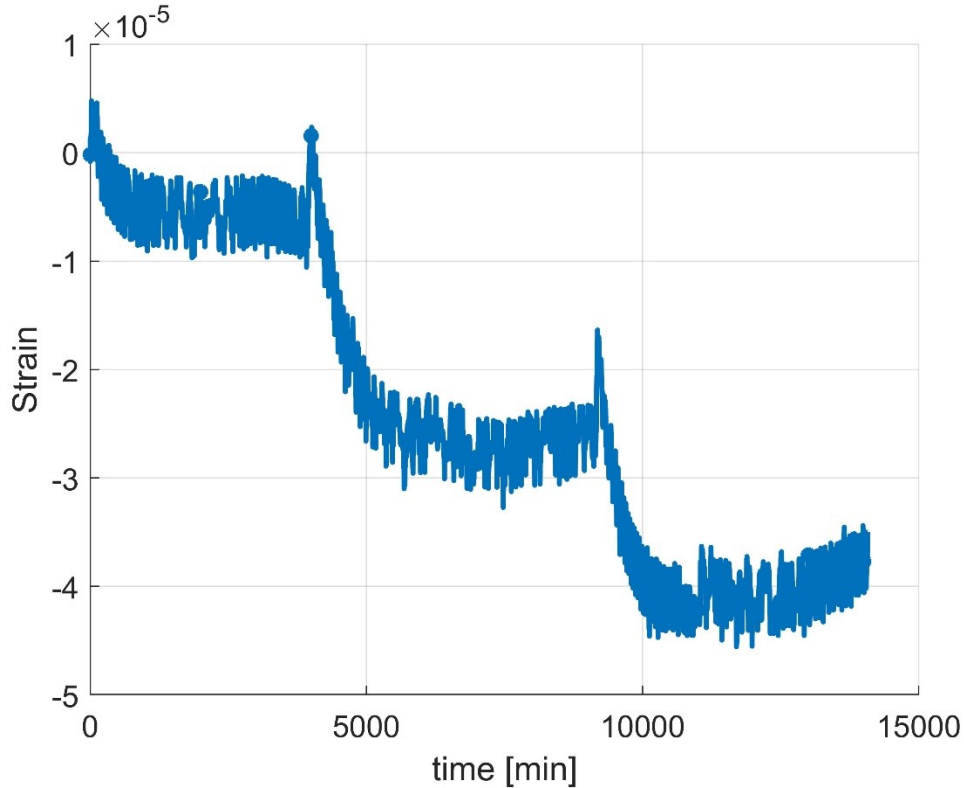


Figure 5.15: Strain variation due to thermal response of the strain gauge and sample.

As discussed previously, compliance is the inverse of elastic modulus and found by dividing the time dependent strain by the constant creep load, eq 5.4. The compliance for each temperature shown in Figure 5.16. Note the time axis on these graphs is the experimental time which starts,  $t=0$  min, when the creep load is applied and ends,  $t \approx 30$  min, when the load is removed. The experimental time varied by a few minutes between test temperatures because of the manual operation of the lift platform. For these compliance results there is no overlapping region between either the 30°C and 45°C or the 45°C and 60°C test. Recognizing the master curve is smooth and continuous and that TTSP is valid for linear viscoelastic behavior this can be address by extrapolating the compliance beyond the experimental time at each temperature.

The shifting algorithm uses the 30°C compliance curve as the reference onto which all other data will be shifted. Once each elevated temperature compliance curve is shifted onto the reference it is then added to that reference before moving onto the next temperature. The shifting algorithm requires some overlap between the reference curve and the next compliance curve to be shifted, so that it can minimize the overlapping region, see section 5.2.7. To alleviate the issue of the highest temperature curve lacking an overlapping region with the reference data additional compliance data is extrapolated based on the existing reference compliance. Note, this method recognizes that the master curve is a smooth and continuous. Extrapolation is accomplished by applying the best fit approximation of these data which matches the power law curve, eq 5.10, discussed above. The best fit curve is then extended to create an overlapping region which is then

used by the shifting algorithm to shift the final compliance curve. Another best fit curve, in the same form, is found for the new reference data and the goodness of fit parameters are recorded. Finally, the shift factor is adjusted slightly to move the curve left and right and curve fitting is repeated. The goodness of fit parameters are compared for each best fit curve are compared to each other and the shift factor which creates the best fitting master curve is selected. In the 40%TS data, the best shift factor is also the one determined by the shifting algorithm.

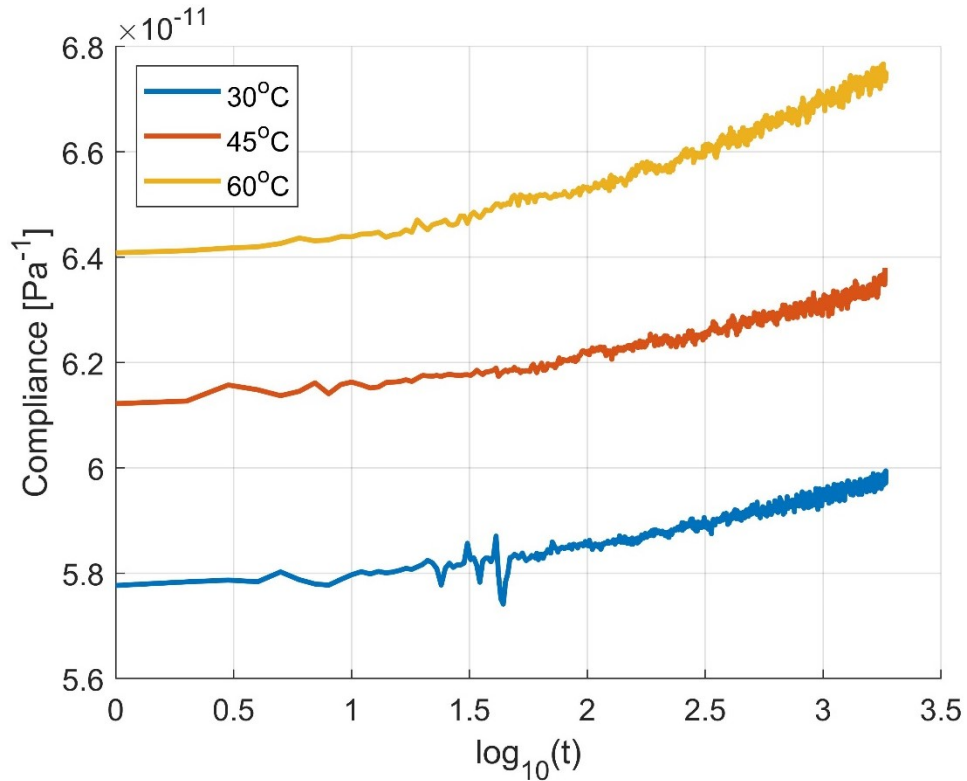


Figure 5.16: Calculated compliance at each temperature for 40%TS.

Applying the shifting algorithm to these data yields the transverse compliance master curves for the GFRP composite at 30°C, shown in Figure 5.17. The master curve equation is given eq 5.13. This figure shows the unshifted compliance data on the left side of the graph with the corresponding shifted data, in black. The solid line is the best fit power law curve for these data, this is the master curve.

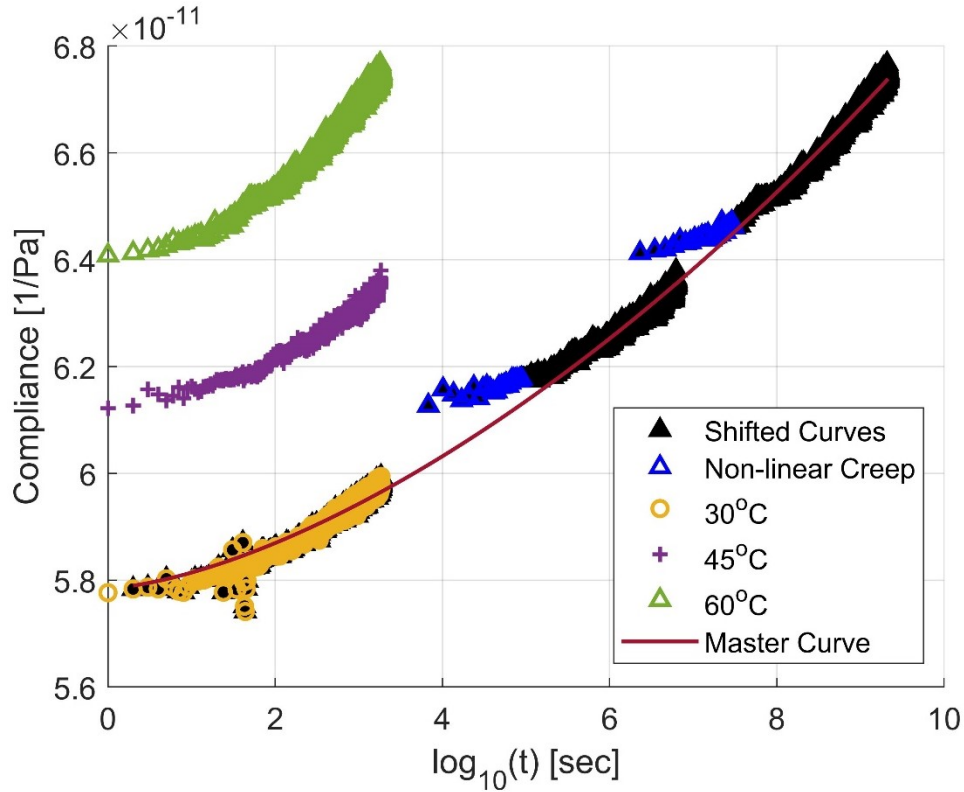


Figure 5.17: Transverse compliance master curve for 40%TS. The unshifted compliance data (colored) is provided along the shifted curves (black). The solid line represents the best fit power law curve for the master curve.

$$\log_{10} S_{22}(t) = A(\log_{10}(t))^n + b \quad 5.13$$

Parameter	Value
$A$	0.00218
$n$	1.529
$b$	-10.24

In this figure, significant periods of creep data can be seen lying away from the master curve, shown in blue triangles. These tails come from the non-linear, i.e. phase I creep, which occurs immediately after the creep load is applied. Phase I creep is also clearly seen in Figure 5.14b at the beginning of each temperature test. This is indicative of a high degree of sample recovery between test periods. These non-linear periods are left displayed in the figure for completeness, however they are not used to determine the shift factor because TTSP is only valid for linear viscoelastic behavior. The time frame for this master curve spans 100 years which covers the entire expected lifetime of a flywheel rotor as discussed in section 3. Notice, the master curve predicts the mechanical compliance of the material independent of creep saturation or rupture. In the elevated temperature experiments both phase I and phase II creep could be clearly seen,

however there was no indication of the material entering phase III creep so no comment can be made on the potential creep failure of the material due to creep under these conditions.

The compliance at  $\log(t)=0$  is the quasi-static elastic modulus and is 17.4 GPa. This is significantly larger than the elastic modulus measured during tensile testing, section 5.4.1. The primary contributor to this difference is likely the differing strain rates. Consider the creep test have the full load applied in approximately 80 seconds—note some variation due to the manual application of load—and produces a maximum strain of 0.12% $\epsilon$ , or 0.0014 % $\epsilon/s$ . Contrast this with the tensile testing which applies the full load after 1250 second and produces a strain of 0.5 % $\epsilon$ , or 0.0004 % $\epsilon/s$ . Gurusideswar et al. [34] showed the elastic modulus of glass epoxy resins is proportional to the strain rate meaning the increased strain of creep tests is expected to produce the result seen here. Additionally, less significant effects will have also increased the elastic modulus. The period between the tensile and creep experiments was approximately nine months during which the samples were stored at room temperature and humidity, both of which varied greatly during fall, winter, and spring. While unintentional, this aging period is expected to increase the material stiffness, however this is likely a minor effect compared to the strain rate effects.

The elastic modulus predicted by the master curve, eq 5.13, is compared to the modulus reported for other materials Table 5.6. Comparing the elastic modulus of the Epon 826/ EpiCure W GFRP tested here is difficult due to variations in strain rate—as already discussed— fiber volume fraction, curing and aging parameters, reporting temperature, and reporting duration. However, the transverse elastic modulus of unidirectional fiber reinforced composites is given at various times. Reporting temperature and fiber volume fraction, where applicable, is also provided to aid in comparison. The transverse compliance is primarily a matrix dominated phenomenon, therefore the inclusion of IM7 and AS4 is deemed appropriate.

*Table 5.6: Elastic modulus predicted by the master curve for the present composite at various times compared to the compliance for similar materials reported in literature.*

Material (temp, fvf)	Elastic modulus [GPa]			
	0 years	1 year	3 years	10 years
E-glass/ Epon826 (30°C, 66.3%)	17.4	15.6	15.4	15.2
IM7/ 8552 CFRP (75°C, -) [6]	11.6	6.9	6.6	6.4
E-glass/ Epon826 (room temp, 50%) [32]	14.1 ±0.9			
E-glass/ Dow 383 (30°C, 62%) [19]	20.6	17.4	17.0	
AS4/3501-6 (21°C, 60%) [35]	14.00			

The GFRP tested here is most closely related the E-glass/ Epon 826 reported by [32] differing primarily by the fiber volume fraction and the hardener, EpiCure W verses DDS HY 976 which are similar compounds produced by different companies. While [32] did not report the long-term behavior of the material, the present GFRP is seen to be stronger after 10 years due to the higher glass fiber volume fraction limiting polymer chain mobility in the matrix. Comparing with the E-glass/ Dow 383 composite shows significant correlation. The initial modulus of the present material is approximately 3 GPa less than the E-glass/Dow 383 composite, and they approximately maintain this different after three years. A 10 year comparison was not possible as the author's data did not extend that far, however given compliance is logarithmic, see Figure 5.14b, it is expected to follow this same trend after 10 years.

The IM7/8552 CFRP reported in [6] does cover the same time range, however it is significantly softer than the GFRP discussed here due to the elevated temperature at which the compliance is reported. Considering the results discussed in sections 3 and 4 relied primarily on this material it is expected the present GFRP would produce less viscoelastic stress relaxation than the IM7/8552 CFRP.

## 5.5 Conclusion

Determining the transverse viscoelastic compliance master curve for FRPC presents unique challenges for traditional coupon testing due the existence of edge effects. Additionally, testing requirements, specimen preparation, and data collection and processing are significant challenges to overcome. This article presented an experimental test platform and process capable of conducting elevated temperature testing employing tubular filament-wound FRPC specimens. Specimens discussed herein were made from glass-fiber/epoxy composites with circumferential fiber orientation. The specimen fabrication parameters and experimental methods for viscoelastic material characterization were discussed in detail. The process for constructing the compliance master curve from collected creep strain data was described. Finally, the performance of the experimental setup was validated, confirming its ability to apply the desired loads and temperatures while recording pertinent data for computing stress and strain. It was observed that off-axis loading (bending) may be a concern, however, its effects can be accounted for during data processing. In closing, the experimental platform along with the methodology for conducting viscoelastic material testing was ascertained to successfully yield the data required for constructing the transverse compliance master curve for FRPC specimens.

Quasi-static failure testing was conducted to determine the failure strength and elastic modulus of the GFRP samples. The failure strain and stress were measured at 0.5 % $\epsilon$  and 41 MPa respectively. Then viscoelastic creep experiments were conducted at approximately 46%TS and 30°C, 45°C, and 60°C while recording temperature, creep load, and creep strain. It was seen that the compliance curves did not overlap, as intended, however this was address by creating best fit curves to extrapolate the material behavior and facilitate TTSP. When all curves were shifted the transverse compliance master curve was determined by finding a best fit power law curve.

Significant differences were seen between the compliance and quasi-static testing, however these differences were attributed, primarily, to difference in testing parameter and, to a lesser extent, aging and hygroscopic effects. In comparison with similar materials the E-glass/Epon 826 GFRP discussed here displays a relatively high, but not unreasonable, elastic modulus. Based on these results the master curve for the E-glass/Epon 826 GFRP composite studied here was determined. This master curve can be used to predict the transverse compliance, i.e.  $S_{22}$  and  $S_{33}$ , of the material throughout an approximately 100 year period, significantly longer than the expected lifetime of a flywheel energy storage system. When combined with fiber direction, i.e.  $S_{11}$ , elastic modulus these results can be used to predict the response of a composite flywheel rotor due to viscoelastic stress relaxation.

## 5.6 References

1. M. Skinner and P. Mertiny, Energy Storage Flywheel Rotors—Mechanical Design, *Encyclopedia*, **2022**, 2, 1, 301–324.
2. ASTM, ASTM D3039/D3039M, **2014**, pp. 1–13.
3. ASTM, ASTM D7205, **2011**, 1–13.
4. M. Y. Khalid, A. Al Rashid, Z. U. Arif, N. Akram, H. Arshad, and F. P. G. Márquez, Characterization of failure strain in fiber reinforced composites: Under on-axis and off-axis loading, *Crystals*, **2021**, 11, 2, 1–11.
5. A. Saleeb, S. Arnold and N. Al-Zoubi, A study of time-dependent and anisotropic effects on the deformation response of two flywheel designs, *ASTM Spec. Tech. Publ.*, **2003**, 1436, 1–27.
6. J. T. Tzeng, Viscoelastic Analysis of Composite Cylinders Subjected to Rotation, *Trans. Ophthalmol. Soc. U. K.*, **2001**, 101, 2, 200–202.
7. M. Skinner and P. Mertiny, Effects of Viscoelasticity on the Stress Evolution over the Lifetime of Filament-Wound Composite Flywheel Rotors for Energy Storage, *Appl. Sci.*, **2021**, 11, 20, 9544.
8. H. Ding, W. Chen and Z. L., Elasticity of Transversely Isotropic Materials. Springer, **2006**.
9. L. Di Gennaro, F. Daghia, M. Olive, F. Jacquemin, and D. Espinassou, A new mechanism-based temperature-dependent viscoelastic model for unidirectional polymer matrix composites based on Cartan decomposition, *Eur. J. Mech. A/Solids*, **2021**, 90, 104364.
10. M. Skinner and P. Mertiny, Experimental Characterization of Low-Speed Passive Discharge Losses of a Flywheel Energy Storage System, *Appl. Mech.*, **2021**, 2, 1, 1–15.
11. ASTM, “ASTM D2990-09,” **2009**, 1–20.
12. S. Sihm and S. Tsai, Automated shift for time-temperature superposition, *Proceedings of 12th Int. Com. Compos. Mater.*, **1999**, 51.
13. B. T. Werner and K. Nelson, Time Temperature Superposition Shift Factors for Fabric Composites, *Proceedings of Proc. Soc. Exp. Mech. Ser.*, **2021**, 95–98.
14. N. Nosrati, A. Zabet, and S. Sahebian, Long-term creep behaviour of E-glass/epoxy composite: time-temperature superposition principle, *Plast. Rubber Compos.*, **2020**, 49, 6, 254–262.
15. M. Gergesova, B. Zupančič, I. Saprunov, and I. Emri, The closed form t-T-P shifting (CFS) algorithm, *J. Rheol.*, **2011**, 55, 1, 1–16.
16. Owens Corning, SE12000 Single-End Type 30 Roving, **2019**.
17. Hexion, EPON Resin 826 Technical Data Sheet, **2005**.
18. P. Mertiny and F. Ellyin, Influence of the filament winding tension on physical and mechanical properties of reinforced composites, *Compos. Part A Appl. Sci. Manuf.*, **2002**, 33, 12, 1615–1622.
19. R. P. Emerson, Viscoelastic Flywheel Rotors: Modeling and Measurement, Pennsylvania State University, **2002**.
20. Vishary Precision Group, General Purpose Strain Gages 500UW, *Vishary Precision Group*, Malvern, PA, USA, **2018**.
21. Vishary Precision Group, General Purpose Strain Gages 125WT — Tee Rosette, *Vishary Precision Group*, Malvern, PA, USA, **2015**.



22. Vishay Precision Group, Vishay 2100 Strain Gauge Conditioner-Amplifier System, *Vishay Precision Group*, Malvern, PA, USA, 1–9.
23. Y. C. Lou, Viscoelastic Characterization of Nonlinear Fiber-Reinforced Plastic, *J. Compos. Mater.*, **1971**, 5, 208–234.
24. Y. Y. T. Yeow, D. D. H. Morris, and H. H. F. Brinson, The Time-Temperature Behavior of a Unidirectional Graphite/Epoxy Composite, *Fifth Conf. Compos. Mater. Test. Des.*, **1979**, 263–19.
25. J. L. Sullivan, E. J. Blais, and D. Houston, Physical aging in the creep behavior of thermosetting and thermoplastic composites, *Compos. Sci. Technol.*, **1993**, 47, 4, 389–403.
26. M. Durante, A. Formisano, L. Boccarusso, A. Langella, and L. Carrino, Creep behaviour of polylactic acid reinforced by woven hemp fabric, *Compos. Part B Eng.*, **2017**, 124, 16–22.
27. C. M. Wu, P. C. Lin, and R. Murakami, Long-term creep behavior of self-reinforced PET composites, *Express Polym. Lett.*, **2017**, 11, 10, 820–831.
28. M. L. Williams, R. F. Landel, and J. D. Ferry, The Temperature Dependence of Relaxation Mechanisms in Amorphous Polymers and Other Glass-forming Liquids, *J. Am. Chem. Soc.*, **1955**, 77, 14, 3701–3707.
29. A. Koutsomichalis, T. Kalampoukas, and D. E. Mouzakis, Mechanical testing and modeling of the time–temperature superposition response in hybrid fiber reinforced composites, *Polymers (Basel)*, **2021**, 13, 7.
30. N. P. Lorandi, M. O. H. Cioffi, C. Shigue, and H. L. Ornaghi, On the creep behavior of carbon/epoxy non-crimp fabric composites, *Mater. Res.*, **2018**, 21, 3, 1–8.
31. D. C. T. Cardoso and K. A. Harries, A viscoelastic model for time-dependent behavior of pultruded GFRP, *Constr. Build. Mater.*, **2019**, 208, 63–74.
32. K. Benzarti, L. Cangemi, F. Dal Maso, Transverse Properties of Unidirectional Glass/Epoxy Composites: Influence of Fibre Surface Treatments, *Compos Part A – Appl S*, **2001**, 32, 2, 197-206.
33. Micromeritics, Strain Gauge Thermal Output and Gage Factor Variation with Temperature, *Vishay Precision Group*, **2014**, Malvern, PA, USA.
34. S. Gurusideswar, N. Srinivasan, R. Velmurugan, and N.K. Gupta, Tensile Response of Epoxy and Glass/Epoxy Composites at Low and Medium Strain Rate Regimes, *Procedia Engineer*, **2017**, 173, 686-693.
35. Raghavan, J.; Meshii, M. Creep of polymer composites. *Compos. Sci. Technol.* **1998**, 57, 1673–1688.

## 6 Conclusions

High-velocity and long-lifetime operating conditions of modern high-speed energy storage flywheel rotors may create the necessary conditions for failure modes not included in current quasi-static failure analyses. The central hypothesis for this thesis research is that (i) viscoelastic effects and shear stress effects can cause creep rupture, matrix cracking, or hub-rim interfacial failure in composite flywheel rotors, and that (ii) these failure modes can be prevented by employing an appropriate modeling approach in the FESS design process. To investigate this hypothesis, three primary objectives were established. These objectives were first, to create an analytical algorithm, based on existing flywheel rotor models, to simulate the evolution of the stress-strain field in a flywheel rotor during its expected operational lifetime. Second, to conduct simulations to predict the evolution of the stress-strain field in the flywheel rotor subjected to shear stress and viscoelastic stress relaxation. And, finally, to determine the transverse viscoelastic material compliance of filament-wound fiber reinforced polymer composite used to construct flywheel rotor rims.

Addressing the first two objectives was accomplished by developing a computational algorithm based on an accepted analytical model. This model was employed in two different scenarios. In the first scenario, the model was employed to simulate the rotor under steady-state conditions for constant, high angular velocity rotation. The viscoelastic behavior of a FRPC flywheel rotor was determined over a 10-year operational lifetime. The simulations indicate that viscoelastic effects are likely to reduce peak stresses in the FRPC material and the hub-rim interface while simultaneously increasing stress in the metallic hub.

Then, in the second scenario, the computational model was used to describe the transient behavior of radial, circumferential, and shear stresses in FRPC flywheel rotors during constant power demands. This thesis discusses failure predictions using the maximum stress and Tsai-Wu failure criteria. The Tsai-Wu criterion predicted failure to occur at higher loadings compared to a maximum stress threshold. A strength ratio (SR) determined from the Tsai-Wu criterion indicated a changing peak stress location from the inner radius at the start of the rotor acceleration to approximately the center of the rotor thickness at top speed. The results from this study indicate strong variability in the loading conditions, which may promote damage, crack initiation and propagation, and fatigue effects, posing risks to the long-term structural health of composite flywheel rotors.

Predicting the behavior of the flywheel rotor over the lifetime of the system requires a thorough understanding of the evolution of the composite material behavior. To understand the viscoelastic behavior of FRPC, an effective experimental test platform and methodology was developed to conduct elevated temperature tensile creep testing. Glass fiber reinforced polymer composite (GFRP) tube specimens were investigated. Using this methodology, the creep compliance of the GFRP was measured at various elevated temperatures, then, time-temperature superposition was applied to shift the compliance curves along the time axis to create a master curve. The resulting transverse master curve can accurately predict the material compliance over

an approximate 100-year period. Additionally, the compliance values compare well with published values of other similar materials.

Based on the findings and results published in this thesis, necessary evidence is provided to accept the hypothesis. First, high-speed operation of FRPC flywheel rotors can have significantly impact on creep rupture, matrix cracking, and/or hub-rim interfacial stress over a 10-year operational lifetime. However, shear stress induced by angular acceleration during energy transfer was shown to be minimally impactful on the evolution of internal stresses, and, in isolation, is unlikely to lead to rotor failure. Secondly, it was shown that the Tsai-Wu criterion is capable of predicting the strength ratio of all points throughout the flywheel rotor, indicating the failure mode and location. Therefore, the hypothesis that relevant failure modes can be predicted and accounted for by employing appropriate failure models is confirmed based on the simulation results in chapters 3 and 4.

## CONTRIBUTIONS

Recalling the knowledge gaps from the beginning of this thesis, attempts have been made to more comprehensively predict rotor failure by amending the stiffness matrix for the rotor material(s) with progressive damage models, they fail to incorporate viscoelastic behavior and shear stress effects into the stress and failure analysis. The limited work that has been conducted on viscoelastic stress simulations has focused on time frames between  $10^5$  and  $10^{10}$  years which is well outside the presently accepted 10-20 year expected lifetime of FESS systems. Similarly, the impact of shear stress on internal rotor stresses is typically studied by assuming instantaneous loading. Again, this falls outside typical FESS operating conditions where applied shear stress changes continuously as a function of the power demands placed upon it. In both cases this leaves a discontinuity between the operation of FESS and established modeling methods to design and analyze the composite flywheel rotors. This is exacerbated by the limited availability of viscoelastic material properties necessary to conduct accurate simulations of flywheel rotors.

These gaps have been filled by creating the analytical model, conducting viscoelastic and shear stress simulation, and determining the transverse material master curve. Addressing the first two objectives required creating a detailed analytical model capable of accurately simulating the stress behavior of a multi-rim composite flywheel rotor subjected to a variety of operating conditions throughout its expected operational lifetime, the results of which have been discussed extensively in chapter 3 and 4. This analytical model differs from other established models by simulating the dynamic behavior of the flywheel rotor subjected to combined loading conditions including shear stress and viscoelastic behavior. As has been seen in this thesis, these effects can have a significant impact on the stress response of composite flywheel rotors which impacts the safety and reliability of FES systems. It was seen the largest stress changes caused by viscoelasticity occurred in the interface between the rim and hub. This novel result had not been seen in literature previously. Additionally, this model showed shear stress to be negligible compared to the other principle stresses, however it highlighted several key areas where cyclic

stress poses the highest potential risk. This model can be applied to any multi-rim rotor constructed from any combination of materials, provided the requisite assumptions are met. The model is more applicable than previous models, and it can be used to design, analyze, and optimize multi-rim flywheel rotors for future applications. This addresses the knowledge gaps relating to the integration of viscoelastic effects and shear stress effects into existing flywheel rotor design techniques. Similarly, chapter 5 addresses the final objective by developing a method to measure the transverse creep compliance of a GFRP composite applicable to flywheel rotor construction. It has been seen that transverse viscoelastic behavior of composite materials is rarely investigated or reported in literature for a variety of reasons. This thesis develops a simple method to investigate this behavior which only requires elevated temperature testing and does not require an understanding of the activation energy. This innovation lowers the barrier to entry for viscoelastic testing allowing a wider variety of materials to be tested accurately allowing those materials to be incorporated into the necessary design and analysis tools. The viscoelastic material testing in chapter 5 not only expands on the understanding of the GFRP seen here, but also facilitates the future study of a wide array of viscoelastic materials in the future.

## FUTURE WORK

Future work directed toward the analytical model can focus on expanding the existing 2D analysis to include the axial direction. This would provide additional detail on the induced stresses during operation. Additionally, expanding the scope of the failure criteria to include fatigue failure would be extremely beneficial as this is likely a significant failure mode in composite flywheel rotors. Regarding material testing, future work can focus on characterizing systematic errors so they can be accounted for in future testing. It may be beneficial to modify the system to reduce these errors, particularly those seen in the heating chamber and strain measurements. Finally, it may be valuable to modify the testing parameters and temperatures in future studies to ensure the compliance data has a significant overlapping region necessary for shifting.

## 7 References

1. British Petroleum Statistical Review of World Energy globally consistent data on world energy markets and authoritative publications in the field of energy; 2021; Vol. 70;.
2. Chen, H.; Cong, T.N.; Yang, W.; Tan, C.; Li, Y.; Ding, Y. Progress in electrical energy storage system: A critical review. *Prog. Nat. Sci.* 2009, 19, 291–312, doi:10.1016/j.pnsc.2008.07.014.
3. Kåberger, T. Progress of renewable electricity replacing fossil fuels. *Glob. Energy Interconnect.* 2018, 1, 48–52, doi:10.14171/j.2096-5117.gei.2018.01.006.
4. Moriarty, P.; Honnery, D. Can renewable energy power the future? *Energy Policy* 2016, 93, 3–7, doi:10.1016/j.enpol.2016.02.051.
5. Hadjipaschalis, I.; Poullikkas, A.; Efthimiou, V. Overview of current and future energy storage technologies for electric power applications. *Renew. Sustain. Energy Rev.* 2009, 13, 1513–1522, doi:10.1016/j.rser.2008.09.028.
6. Denholm, P.; O'Connell, M.; Brinkman, G.; Jorgenson, J. Overgeneration from Solar Energy in California: A Field Guide to the Duck Chart; Golden, CO;
7. Amiryar, M.E.; Pullen, K.R. A review of flywheel energy storage system technologies and their applications. *Appl. Sci.* 2017, 7, doi:10.3390/app7030286.
8. Sabihuddin, S.; Kiprakis, A.E.; Mueller, M. A numerical and graphical review of energy storage technologies. *Energies* 2015, 8, 172–216, doi:10.3390/en8010172.
9. Ilan, D. The ground stone components of drills in the ancient Near East: Sockets, flywheels, cobble weights, and drill bits. *J. Lithic Stud.* 2016, 3, 261–277, doi:10.2218/jls.v3i3.1642.
10. Skinner, M. Characterization of passive discharge losses in a flywheel energy storage system, University of Alberta, 2017.
11. Luo, X.; Wang, J.; Dooner, M.; Clarke, J. Overview of current development in electrical energy storage technologies and the application potential in power system operation. *Appl. Energy* 2015, 137, 511–536, doi:10.1016/j.apenergy.2014.09.081.
12. Hebner, R.; Beno, J.; Walls, A. Flywheel batteries come around again. *IEEE Spectr.* 2002, 39, 46–51, doi:10.1109/6.993788.
13. Bolund, B.; Bernhoff, H.; Leijon, M. Flywheel energy and power storage systems. *Renew. Sustain. Energy Rev.* 2007, 11, 235–258, doi:10.1016/j.rser.2005.01.004.
14. Krack, M.; Secanell, M.; Mertiny, P. Rotor Design for High-Speed Flywheel Energy Storage Systems. In *Energy Storage in the Emerging Era of Smart Grids*; InTech, 2011.
15. Skinner, M.; Suess, M.; Secanell, M.; Mertiny, P. Design of a Composite Flywheel Rotor For Long-Term Energy Storage in Residential Applications. In *Proceedings of the The Canadian Society of Mechanical Engineering International Congress*; Canadian Society of Mechanical Engineers: Kelowna, BC, Canada, 2016; pp. 1–5.
16. Skinner, M.; Mertiny, P. Effects of Viscoelasticity on the Stress Evolution over the Lifetime of Filament-Wound Composite Flywheel Rotors for Energy Storage. *Appl. Sci.* 2021, 11, 9544, doi:10.3390/app11209544.
17. Pullen, K. The Status and Future of Flywheel Energy Storage. *Joule.* 2019, 3, 1394–1399, doi: 10.1016/j.joule.2019.04.006.
18. The GYROBUS: Something New Under the Sun?". *Motor Trend.* 1952. p. 37.
19. Wakefield, E. *History of the Electric Automobile: Hybrid Electric Vehicles*; Society of Automotive Engineers: Warrendale, PA, 1998; ISBN 978-0-7680-0125-9.
20. Weiss, C.C., Volvo Confirms Fuel Savings of 25 Percent with Flywheel KERS. Available online: <https://newatlas.com/volvo-flywheel-kers-testing/27273/> (accessed on 01/13/2022)
21. Available online: [https://www.porsche.com/international/\\_iceland\\_/motorsportandevents/motorsport/customerracing/racingcars/991-2nd-gt3-r/](https://www.porsche.com/international/_iceland_/motorsportandevents/motorsport/customerracing/racingcars/991-2nd-gt3-r/) (accessed on 01/13/2022)
22. Rupp, A.; Baier, H.; Mertiny, P.; Secanell, M. Analysis of a Flywheel Energy Storage System for Light Rail Transit. *Energy* 2016, 107, 625–638, doi:10.1016/j.energy.2016.04.051.
23. Tarrant, C., Kinetic Energy Storage Wins Acceptance, Available online: <https://www.railwaygazette.com/kinetic-energy-storage-wins-acceptance/27250.article> (accessed on 01/13/2022)
24. NRStor Inc., 2 MW Minto Flywheel Facility: A Fast-Ramping Resource for Grid Regulation and other Electricity Services. Available online: <http://nrstor.com/2019/11/21/2-mw-minto-flywheel-facility-market-impact-case-study-power-advisory/> (accessed on: 01/13/2022)
25. Beacon Power, Operating Plants Stephenton, New York. Available online: <https://beaconpower.com/stephentown-new-york/> (accessed on 01/13/2022)
26. Amber Kinetics, The World's Only Flywheel Innovation Hub. Available online:

- <https://amberkinetics.com/installation/the-worlds-only-flywheel-innovation-hub/> (accessed on 01/13/2022)
27. Genta, G. *Kinetic Energy Storage: Theory and Practice of Advanced Flywheel Systems*; Butterworth-Heinemann: London, UK 2014; ISBN 0-408-01396-6.
  28. Ha, S.K.; Han, H.H.; Han, Y.H. Design and manufacture of a composite flywheel press-fit multi-rim rotor. *J. Reinf. Plast. Compos.* 2008, 27, 953–965, doi:10.1177/0731684407086625.
  29. Kale, V.; Thomas, M.; Secanell, M. On determining the optimal shape, speed, and size of metal flywheel rotors with maximum kinetic energy. *Struct. Multidiscip. Optim.* 2021, 64, 1481–1499, doi:10.1007/s00158-021-02935-x.
  30. Wang, Y.; Dai, X.; Wei, K.; Guo, X. Progressive failure behavior of composite flywheels stacked from annular plain profiling woven fabric for energy storage. *Compos. Struct.* 2018, 194, 377–387, doi:10.1016/j.compstruct.2018.04.036.
  31. Ornaghi, H.L.; Neves, R.M.; Monticeli, F.M.; Almeida, J.H.S. Viscoelastic characteristics of carbon fiber-reinforced epoxy filament wound laminates. *Compos. Commun.* 2020, 21, doi:10.1016/j.coco.2020.100418.
  32. Takkar, S.; Gupta, K.; Tiwari, V.; Singh, S.P. Dynamics of Rotating Composite Disc. *J. Vib. Eng. Technol.* 2019, 7, 629–637, doi:10.1007/s42417-019-00155-8.
  33. Eggers, F.; Almeida, J.H.S.; Azevedo, C.B.; Amico, S.C. Mechanical response of filament wound composite rings under tension and compression. *Polym. Test.* 2019, 78, 105951, doi:10.1016/j.polymertesting.2019.105951.
  34. Rejab, R.; Kumar, N.M.; Ma, Q.; Idris, M.S.; Zhang, B.; Merzuki, M.N.M. Wireless technology applied in 3-axis filament winding machine control system using MIT app inventor. *Wireless technology applied in 3-axis filament winding machine control system using MIT app inventor*. In *Proceedings of the IOP Conference Series: Materials Science and Engineering*; IOP Publishing, 2019.
  35. Wild, P.M.; Vickers, G.W. Analysis of filament-wound cylindrical shells under combined centrifugal, pressure and axial loading. *Compos. Part A Appl. Sci. Manuf.* 1997, 28, 47–55, doi:10.1016/S1359-835X(96)00093-0.
  36. Sayem Uddin, M.; Morozov, E. V.; Shankar, K. The effect of filament winding mosaic pattern on the stress state of filament wound composite flywheel disk. *Compos. Struct.* 2014, 107, 260–275, doi:10.1016/j.compstruct.2013.07.004.
  37. Tzeng, J.T.; Emerson, R.P.; O'Brien, D.J. Viscoelasticity Analysis and Experimental Validation of Anisotropic Composite Overwrap Cylinders. Vol. 8 *Mech. Solids, Struct. Fluids* 2012, 429, doi:10.1115/IMECE2012-87818.
  38. Ertz, G. *Development, manufacturing and testing of a Multi-Rim ( Hybrid ) Flywheel Rotor*, University of Alberta, 2014.
  39. Skinner, M.; Mertiny, P. Experimental Characterization of Low-Speed Passive Discharge Losses of a Flywheel Energy Storage System. *Appl. Mech.* 2021, 2, 1–15, doi:10.3390/applmech2010001.
  40. Kale, V.; Secanell, M. A comparative study between optimal metal and composite rotors for flywheel energy storage systems. *Energy Reports* 2018, 4, 576–585, doi:10.1016/j.egy.2018.09.003.
  41. Zheng, Y.; Bahaloo, H.; Mousanezhad, D.; Mahdi, E.; Vaziri, A.; Nayeb-Hashemi, H. Stress analysis in functionally graded rotating disks with non-uniform thickness and variable angular velocity. *Int. J. Mech. Sci.* 2016, 119, 283–293, doi:10.1016/j.ijmecsci.2016.10.018.
  42. Yeh, K.Y.; Han, R.P.S. Analysis of high-speed rotating disks with variable thickness and inhomogeneity. *J. Appl. Mech. Trans. ASME* 1994, 61, 186–191, doi:10.1115/1.2901396.
  43. Ertz, G.; Twiefel, J.; Krack, M. Feasibility Study for Small Scaling Flywheel-Energy-Storage Systems in Energy Harvesting Systems. *Energy Harvest. Syst.* 2014, 1, 233–241, doi:10.1515/ehs-2013-0010.
  44. Ha, S.K.; Kim, M.H.; Han, S.C.; Sung, T.H. Design and spin test of a hybrid composite flywheel rotor with a split type hub. *J. Compos. Mater.* 2006, 40, 2113–2130, doi:10.1177/0021998306061324.
  45. Hartl, S.; Schulz, A.; Sima, H.; Koch, T.; Kaltenbacher, M. A Static Burst Test for Composite Flywheel Rotors. *Appl. Compos. Mater.* 2016, 23, 271–288, doi:10.1007/s10443-015-9460-5.
  46. Han, Y.; Ren, Z.; Tong, Y. General Design Method of Flywheel Rotor for Energy Storage System. *Energy Procedia* 2012, 16, 359–364, doi:10.1016/j.egypro.2012.01.059.
  47. Mittelstedt, M.; Hansen, C.; Mertiny, P. Design and multi-objective optimization of fiber-reinforced polymer composite flywheel rotors. *Appl. Sci.* 2018, 8, doi:10.3390/app8081256.
  48. Krack, M.; Secanell, M.; Mertiny, P. Cost optimization of hybrid composite flywheel rotors for energy storage. *Struct. Multidiscip. Optim.* 2010, 41, 779–795, doi:10.1007/s00158-009-0469-y.
  49. Skinner, M.; Secanell Gallart, M.; Mertiny, P. Observed Effects of Vibrationally Induced Fretting on Bearing–Shaft Systems in Flywheel Energy Storage Systems. *J. Fail. Anal. Prev.* 2018, 18, doi:10.1007/s11668-018-0469-6.
  50. Allam, M.N.M.; Tantawy, R.; Yousof, A.; Zenkour, A.M. Elastic and viscoelastic stresses of nonlinear rotating functionally graded solid and annular disks with gradually varying thickness. *Arch. Mech. Eng.* 2017, 64, 423–

- 440, doi:10.1515/meceng-2017-0025.
51. Long, Z.; Zhiping, Q. Review of Flywheel Energy Storage System. In Proceedings of ISES World Congress 2007 (Vol. I – Vol. V); Springer: Berlin, Germany, 2008; pp. 2815–2819.
  52. Lai, W.M.; Rubin, D.; Krempl, E. Chapter 5: The Elastic Solid. In Introduction to Continuum Mechanics; 2010; pp. 201–352.
  53. Ding, H.; Chen, W.; Li, Z. Elasticity of Transversely Isotropic Materials; Gladwell, G.M.L., Ed.; Springer: Dordrecht, 2006; ISBN 9781119130536.
  54. Zhao, J.; Song, X.; Liu, B. Standardized compliance matrixes for general anisotropic materials and a simple measure of anisotropic degree based on shear extension coupling coefficient. *Int J Appl Mech* 2011, 8, 1–28.
  55. Lakes, R. Viscoelastic Materials; Cambridge University Press: Edinburgh, Cambridge, UK, 2009; Vol. 1; ISBN 9780511626722.
  56. Buchroithner, A.; Haidl, P.; Birgel, C.; Zarl, T.; Wegleiter, H. Design and experimental evaluation of a low-cost test rig for flywheel energy storage burst containment investigation. *Appl. Sci.* 2018, 8, doi:10.3390/app8122622.
  57. Rojas, J.I.; Nicolás, J.; Crespo, D. Study on mechanical relaxations of 7075 (Al-Zn-Mg) and 2024 (Al-Cu-Mg) alloys by application of the time-temperature superposition principle. *Adv. Mater. Sci. Eng.* 2017, 2017.
  58. Mahdavi, R.; Goodarzi, V.; Jafari, S.H.; Saeb, M.R.; Shojaei, S.; Khonakdar, H.A. Experimental analysis and prediction of viscoelastic creep properties of PP / EVA / LDH nanocomposites using master curves based on time – temperature superposition. *J Appl Polym Sci* 2018, 1–12, doi:10.1002/app.46725.
  59. Barbero, E.J. Time-temperature-age superposition principle for predicting long-term response of linear viscoelastic materials; 2nd ed.; Elsevier Ltd., 2019; ISBN 9780081026014.
  60. Yeow, Y.; Morris, D.; Brinson, H. Time-Temperature Behavior of a Unidirectional Graphite/Epoxy Composite. In Fifth Conference on Composite Materials: Testing and Design; ASTM International: West Conshohocken, PA, 1979; pp. 263-263–19.
  61. Koyanagi, J.; Sato, M. Time and temperature dependence of transverse tensile failure of unidirectional carbon fiber-reinforced polymer matrix composites; 2nd ed.; Elsevier Ltd., 2019; ISBN 9780081026014.
  62. Emerson, R.P. Viscoelastic Flywheel Rotors: Modeling and Measurement, Pennsylvania State University, 2002.
  63. Aniskevich, A.; Glaskova-Kuzmina, T. Effect of moisture on elastic and viscoelastic properties of fiber reinforced plastics: Retrospective and current trends; 2nd ed.; Elsevier Ltd., 2019; ISBN 9780081026014.
  64. Alwis, K.G.N.C.; Burgoyne, C.J. Time-temperature superposition to determine the stress-rupture of aramid fibres. *Appl. Compos. Mater.* 2006, 13, 249–264, doi:10.1007/s10443-006-9017-8.
  65. Sih, S.; Tsai, S. Automated shift for time-temperature superposition. *12th Int. Com. Compos. Mater.* 1999, 51.
  66. Brinson, H.F.; Griffith, W.I.; Morris, D.H. Creep Rupture of Polymer-matrix Composites. *1981*, 57, 329–335.
  67. Brinson, H.F. Mechanical and optical viscoelastic characterization of Hysol 4290. *Exp. Mech.* 1968, 8, 561–566, doi:10.1007/bf02327519.
  68. Williams, M.L.; Landel, R.F.; Ferry, J.D. The Temperature Dependence of Relaxation Mechanisms in Amorphous Polymers and Other Glass-forming Liquids. *J. Am. Chem. Soc.* 1955, 77, 3701–3707, doi:10.1021/ja01619a008.
  69. Krauklis, A.E.; Akulichev, A.G.; Gagani, A.I.; Echtermeyer, A.T. Time-temperature-plasticization superposition principle: Predicting creep of a plasticized epoxy. *Polymers (Basel)*. 2019, 11, doi:10.3390/polym11111848.
  70. Ganß, M.; Satapathy, B.K.; Thunga, M.; Weidisch, R.; Pötschke, P.; Janke, A. Temperature dependence of creep behavior of PP-MWNT nanocomposites. *Macromol. Rapid Commun.* 2007, 28, 1624–1633, doi:10.1002/marc.200700288.
  71. Jain, N.; Verma, A.; Singh, V.K. Dynamic Mechanical Analysis and Creep-recovery behaviour of Polyvinyl Alcohol based cross-linked Biocomposite reinforced with Basalt fiber. *Mater. Res. Express* 2019, 6, doi:10.1088/2053-1591/ab4332.
  72. Gergesova, M.; Zupančič, B.; Saprunov, I.; Emri, I. The closed form t-T-P shifting (CFS) algorithm. *J. Rheol. (N. Y. N. Y.)*. 2011, 55, 1–16, doi:10.1122/1.3503529.
  73. Bradshaw, R.D.; Brinson, L.C. Recovering nonisothermal physical aging shift factors via continuous test data: Theory and experimental results. *J. Eng. Mater. Technol. Trans. ASME* 1997, 119, 233–241, doi:10.1115/1.2812250.
  74. Sullivan, J.L. Creep and physical aging of composites. *Compos. Sci. Technol.* 1990, 39, 207–232, doi:10.1016/0266-3538(90)90042-4.
  75. Lou, Y.C. Viscoelastic Characterization of Nonlinear Fiber-Reinforced Plastic. *J. Compos. Mater.* 1971, 5, 208–234.
  76. Stinchcomb, W.W.; Bakis, C.E. Fatigue Behavior of Composite Laminates. *Compos. Mater. Ser.* 1991, 4, 105–180, doi:10.1016/B978-0-444-70507-5.50008-1.

77. Lekhnitskiy, S.G. *Anisotropic Plates*, Air Force Systems Command: Moscow, 1957.
78. Chdnis, C.C.; Kiruly, L.J. *Rim-Spoke Composite Flywheels - Stress and Vibration Analysis*. 1976.
79. Gabrys, C.W.; Bakis, C.E. *Design and Testing of Composite Flywheel Rotors*. *Compos. Mater. Test. Des.* Thirteen. Vol. ASTM STP 1242 1997, 1–22.
80. Ha, S.K.; Yang, H.-I.; Kim, D.-J. Optimum design of a hybrid composite flywheel with permanent magnet rotor. *J. Compos. Mater.* 1999, 33, 1544–1575.
81. Kelly, P. *Mechanics Lecture Notes* Available online: <http://homepages.engineering.auckland.ac.nz/~pkel015/SolidMechanicsBooks/index.html>.
82. Ha, S.K.; Kim, D.J.; Sung, T.H. Optimum design of multi-ring composite flywheel rotor using a modified generalized plane strain assumption. *Int. J. Mech. Sci.* 2001, 43, 993–1007, doi:10.1016/S0020-7403(00)00047-3.
83. Hearn, C.S.; Flynn, M.M.; Lewis, M.C.; Thompson, R.C.; Murphy, B.T.; Longoria, R.G. Low cost flywheel energy storage for a fuel cell powered transit bus. *VPPC 2007 - Proc. 2007 IEEE Veh. Power Propuls. Conf.* 2007, 829–836, doi:10.1109/VPPC.2007.4544239.
84. Krack, M.; Secanell, M.; Mertiny, P. Advanced optimization strategies for cost-sensitive design of energy storage flywheel rotors. *J. Adv. Mater.* 2011, 43, 65–78, doi:10.1002/lary.24014.
85. Kheawcum, M.; Sangwongwanich, S. A Case Study on Flywheel Energy Storage System Application for Frequency Regulation of Islanded Amphoe Mueang Mae Hong Son Microgrid. In *Proceedings of the 17th International Conference on Electrical Engineering/Electronics, Computer, Telecommunications and Information Technology, ECTI-CON 2020*; 2020; pp. 421–426.
86. Pérez-Aparicio, J.L.; Ripoll, L. Exact, integrated and complete solutions for composite flywheels. *Compos. Struct.* 2011, 93, 1404–1415, doi:10.1016/j.compstruct.2010.11.011.
87. Eraslan, A.N.; Akis, T. On the plane strain and plane stress solutions of functionally graded rotating solid shaft and solid disk problems. *Acta Mech.* 2006, 181, 43–63, doi:10.1007/s00707-005-0276-5.
88. Saleeb, A.F.; Arnold, S.M.; Al-Zoubi, N.R. A study of time-dependent and anisotropic effects on the deformation response of two flywheel designs. *ASTM Spec. Tech. Publ.* 2003.
89. Trufanov, N.A.; Smetannikov, O.Y. Creep of Composite Energy Accumulators. *Strength Mater.* 1991, 23, 671–675.
90. Portnov, G.G. Estimation of Limit Strains in Disk-Type Flywheels Made of Compliant Elastomeric Matrix Composite Undergoing Radial Creep. *Mech. Compos. Mater.* 2000, 36, 55–58.
91. Tzeng, J.T. *Viscoelastic analysis of composite flywheel for energy storage*; Army Research Laboratory, 2001;
92. Ghosh, T.N.; Tzeng, J.T.; Emerson, R.P.; O'Brien, D.J.; Ghosh, T.N. Viscoelasticity Analysis and Experimental Validation of Anisotropic Composite Overwrap Cylinders. *Trans. Ophthalmol. Soc. U. K.* 2012, 101, 200–202, doi:10.1106/002199802021464.
93. *Levistor Boosting Forecourt Grid Power for the Next Generation of Fast Charging Electric Vehicles* Available online: <https://levistor.com/#about>.
94. *Stornetic GmbH Powerful Storage System for Grid Services* Available online: [https://stornetic.com/assets/downloads/stornetic\\_general\\_presentation.pdf](https://stornetic.com/assets/downloads/stornetic_general_presentation.pdf).
95. Tang, S. Note on acceleration stress in a rotating disk. *Int. J. Mech. Sci.* 1970, 12, 205–207, doi:10.1016/0020-7403(70)90020-2.
96. Reddy, T.Y.; Srinath, H. Effects of acceleration stresses on the yielding of rotating disks. *Int. J. Mech. Sci.* 1974, 16, 593–596.
97. Salehian, M.; Shahriari, B.; Yousefi, M. Investigating the effect of angular acceleration of the rotating disk having variable thickness and density function on shear stress and tangential displacement. *J. Brazilian Soc. Mech. Sci. Eng.* 2019, 41, 1–11, doi:10.1007/s40430-018-1523-8.
98. Li, S. The Maximum Stress Failure Criterion and the Maximum Strain Failure Criterion: Their Unification and Rationalization. *J. Compos. Sci.* 2020, 4, doi:10.3390/jcs4040157.
99. Ha, S.K.; Lee, D.G.; Kim, D.J. Optimization of hybrid composite rotor in flywheel battery. *SAE Tech. Pap.* 1998, doi:10.4271/981899.
100. Corbin, C.K. *Burst failure prediction of composite flywheel rotors: A progressive damage approach via stiffness degradation*, Stanford University, 2005.
101. Tsai, S.W.; Wu, E.M. A General Theory of Strength for Anisotropic Materials. *J Comp Mater* 1971, 5, 58–80.
102. Li, S.; Sitnikova, E.; Liang, Y.; Kaddour, A.S. The Tsai-Wu failure criterion rationalised in the context of UD composites. *Compos. Part A Appl. Sci. Manuf.* 2017, 102, 207–217, doi:10.1016/j.compositesa.2017.08.007.
103. Roy, A.K.; Tsai, S.W. Design of Thick Composite Cylinders. *J. Press. Vessel Technol.* 2009, 110, 255,



doi:10.1115/1.3265597.

104. Chen, Q.; Li, C.; Tie, Y.; Liu, K. Progressive Failure Analysis of Composite Flywheel Rotor Based on Progressive Damage Theory. *J. Mech. Eng.* 2013, 49, 1–6.

105. Kotelnikova-Weiler, N.; Baverel, O.; Ducoulombier, N.; Caron, J.F. Progressive damage of a unidirectional composite with a viscoelastic matrix, observations and modelling. *Compos. Struct.* 2018, 188, 297–312, doi:10.1016/j.compstruct.2017.12.067.

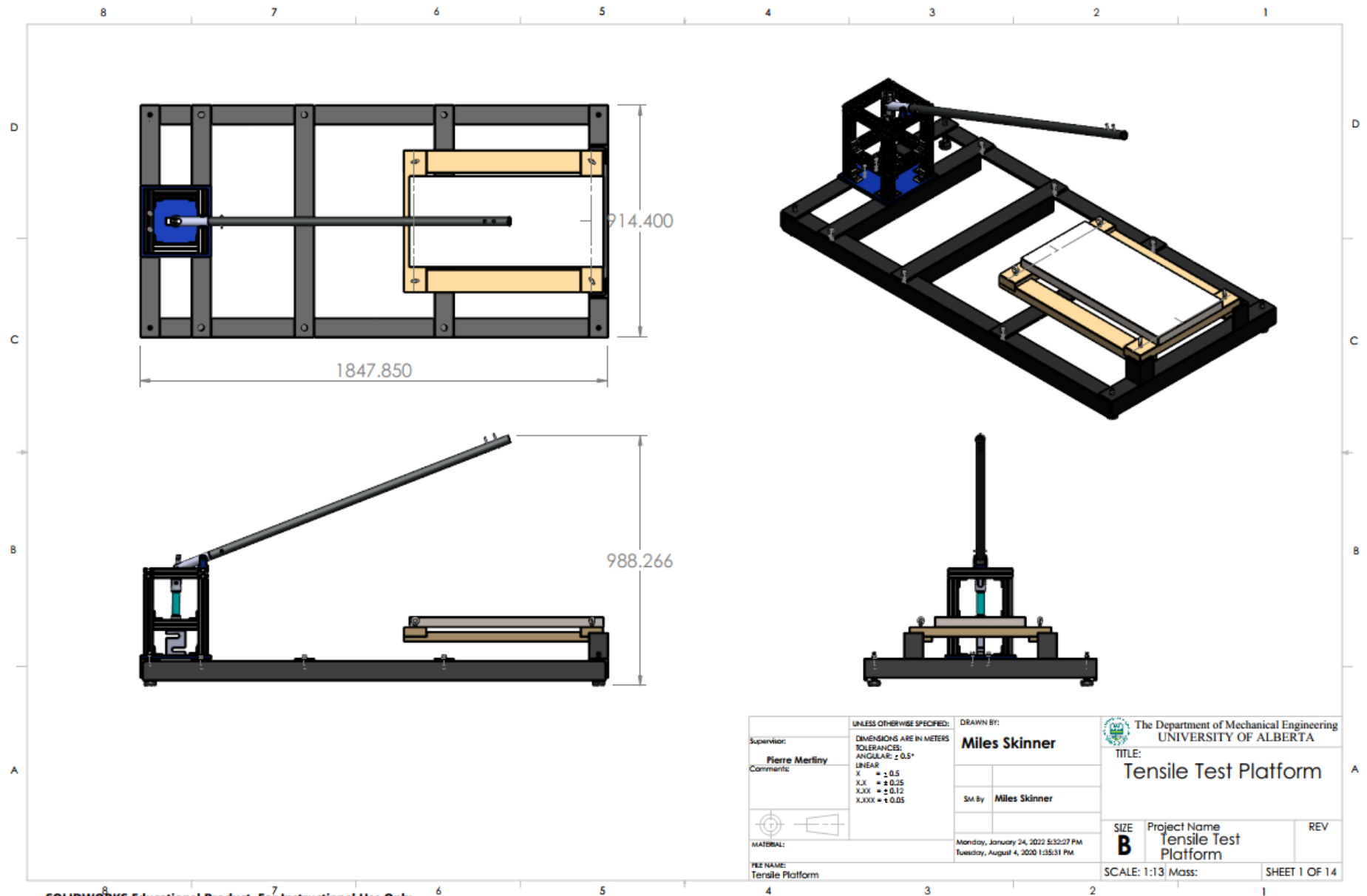
## 8 Appendices

### Appendix I: Burnout Testing Results

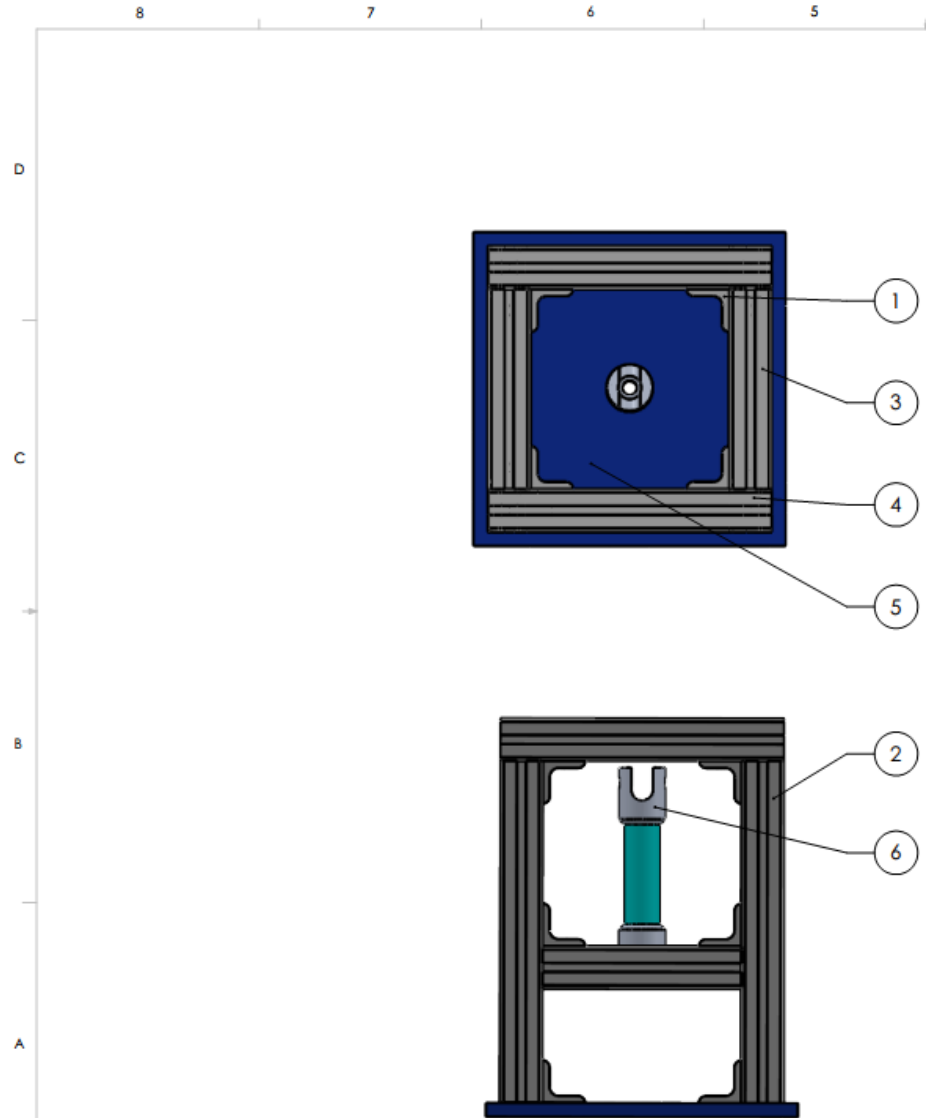
*Table 8.1: Fiber volume fraction results determined from the burn out tests.*

Sample Number	Wt [g]	Post burn out wt [g]	Resin Volume [cm <sup>3</sup> ]	Fiber volume [cm <sup>3</sup> ]	$v_f$
1	11.644	9.486	1.860	3.705	0.666
2	9.825	8.061	1.521	3.149	0.674
3	10.22	8.353	1.609	3.263	0.670
4	9.664	7.874	1.543	3.075	0.666
5	8.952	7.262	1.457	2.837	0.661
				Average	0.667

## Appendix II Viscoelastic Test Platform and Sample Technical Drawings

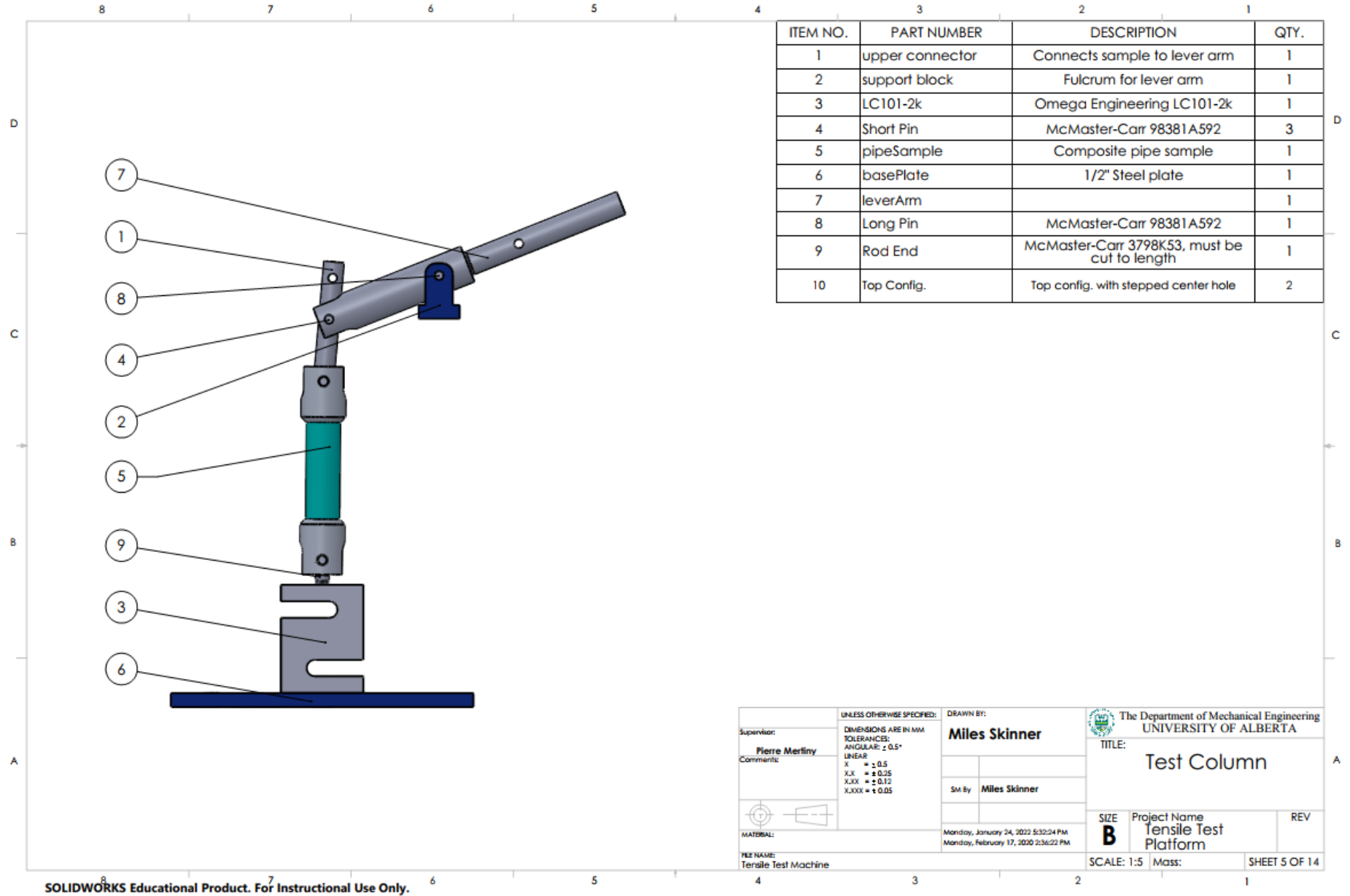


SOLIDWORKS Educational Product. For Instructional Use Only.



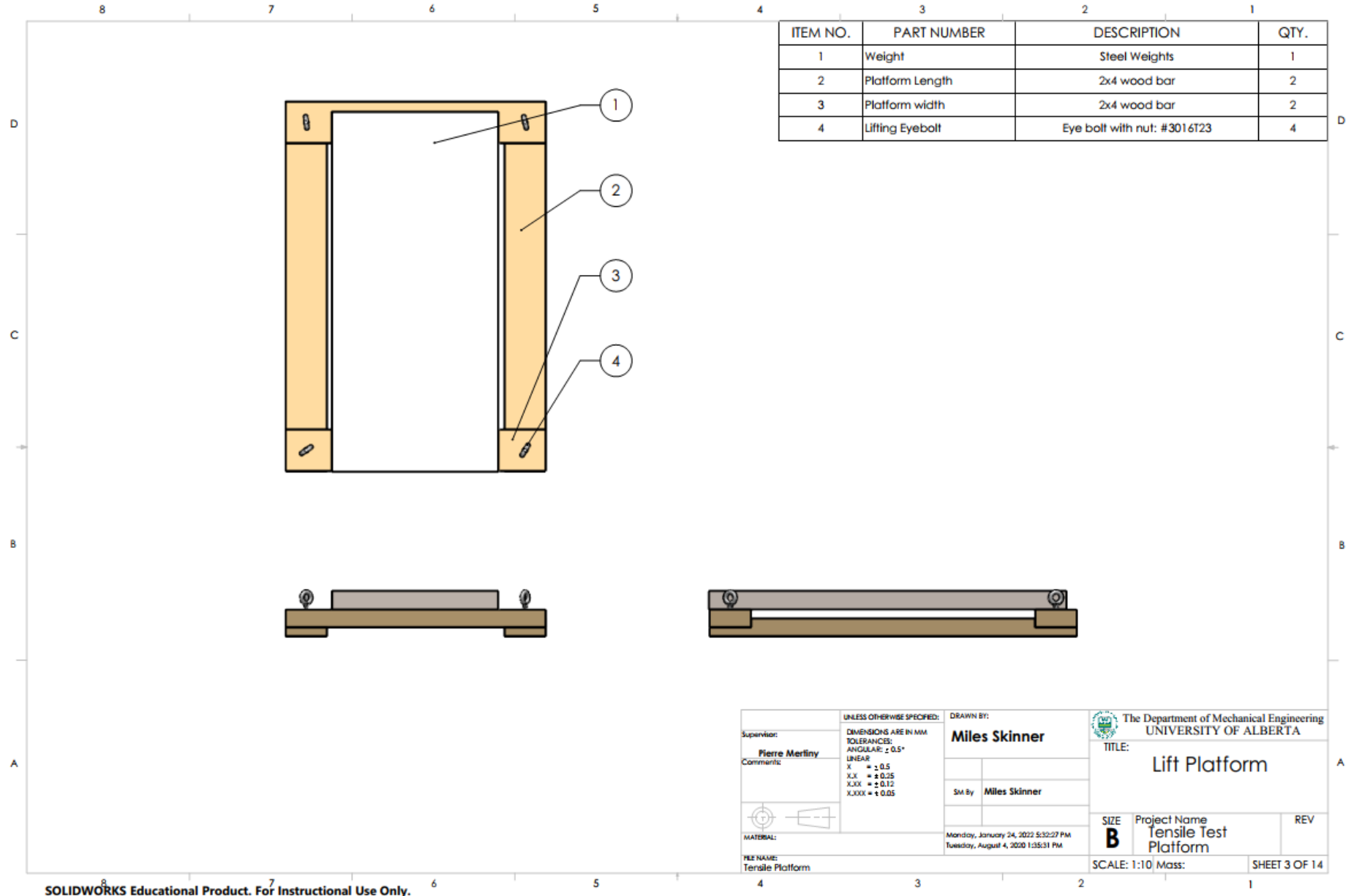
ITEM NO.	PART NUMBER	DESCRIPTION	QTY.
1	L-Bracket	McMaster-Car #47065T845	24
2	T-Slot 12"	McMaster-Carr 47065T102	4
3	T-Slot 7"	McMaster-Carr 47065T102	6
4	T-Slot 10"	McMaster-Carr 47065T102	2
5	basePlate	1/2" Steel plate	1
6	TestSampleAssembly_Single_Piece		1

Supervisor: <b>Pierre Merligny</b> Comments:		UNLESS OTHERWISE SPECIFIED: DIMENSIONS ARE IN MM TOLERANCES: ANGULAR: ± 0.5° LINEAR X = ± 0.5 XX = ± 0.25 XXX = ± 0.12 XXXX = ± 0.05	DRAWN BY: <b>Miles Skinner</b>  SM By <b>Miles Skinner</b>	The Department of Mechanical Engineering UNIVERSITY OF ALBERTA TITLE: <b>Tensile Column Support Frame</b>
MATERIAL: Tensile Test Machine		Monday, January 24, 2022 5:32:24 PM Monday, February 17, 2020 2:36:22 PM	SIZE <b>B</b>	Project Name <b>Tensile Test Platform</b> REV
SCALE: 1:10 Mass:			SHEET 4 OF 14	



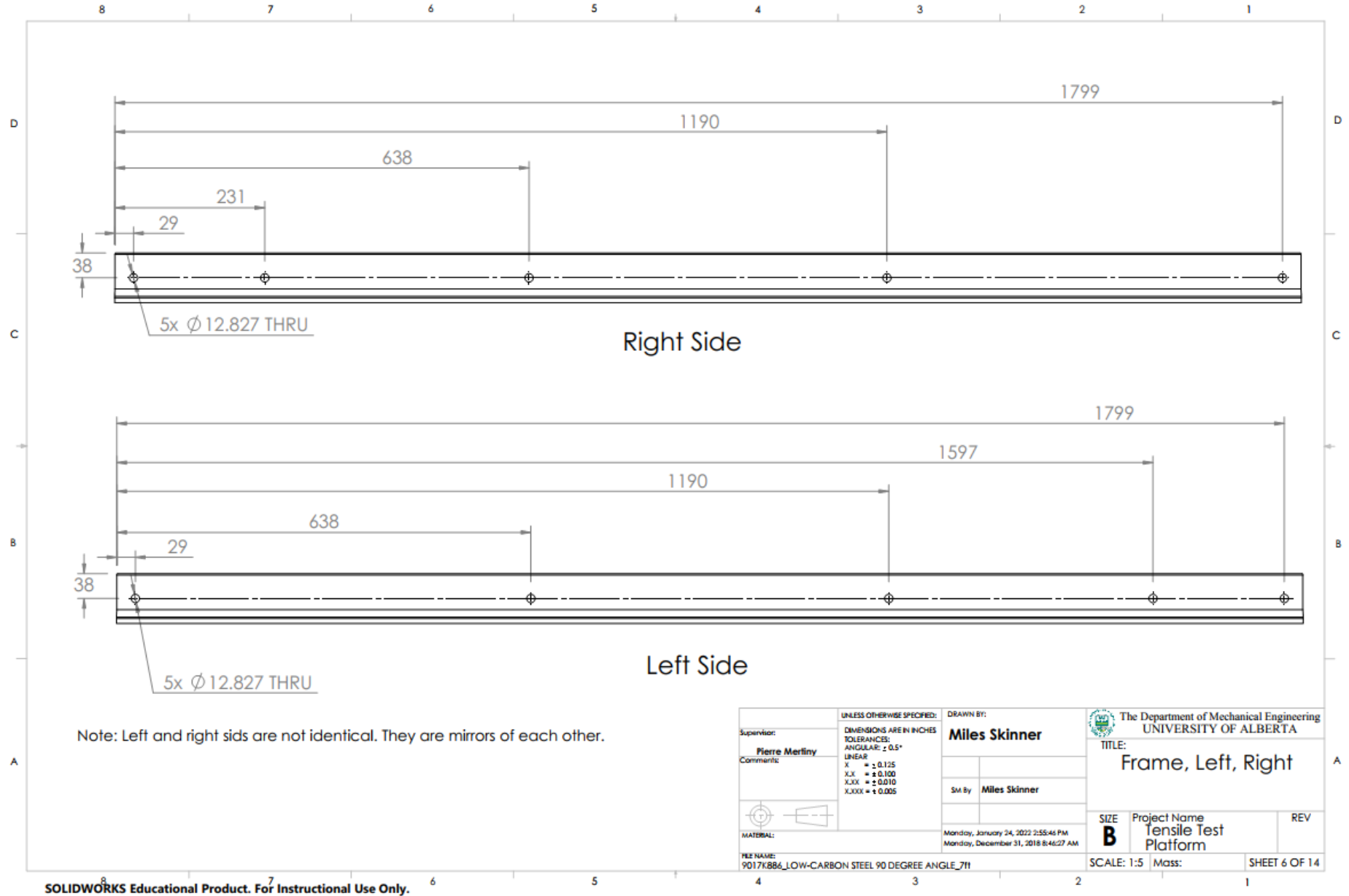
ITEM NO.	PART NUMBER	DESCRIPTION	QTY.
1	upper connector	Connects sample to lever arm	1
2	support block	Fulcrum for lever arm	1
3	LC101-2k	Omega Engineering LC101-2k	1
4	Short Pin	McMaster-Carr 98381A592	3
5	pipeSample	Composite pipe sample	1
6	basePlate	1/2" Steel plate	1
7	leverArm		1
8	Long Pin	McMaster-Carr 98381A592	1
9	Rod End	McMaster-Carr 3798K53, must be cut to length	1
10	Top Config.	Top config. with stepped center hole	2

Supervisor: <b>Pierre Merligny</b>	UNLESS OTHERWISE SPECIFIED: DIMENSIONS ARE IN MM TOLERANCES: ANGULAR: ± 0.5° LINEAR X = ± 0.5 XX = ± 0.25 XXX = ± 0.12 XXXX = ± 0.05	DRAWN BY: <b>Miles Skinner</b>	The Department of Mechanical Engineering UNIVERSITY OF ALBERTA TITLE: <b>Test Column</b>
Comments:		SM By: <b>Miles Skinner</b>	
MATERIAL: Tensile Test Machine		Monday, January 24, 2022 5:32:24 PM Monday, February 17, 2020 2:36:22 PM	SIZE <b>B</b> Project Name <b>Tensile Test Platform</b>
			REV SCALE: 1:5 Mass: SHEET 5 OF 14



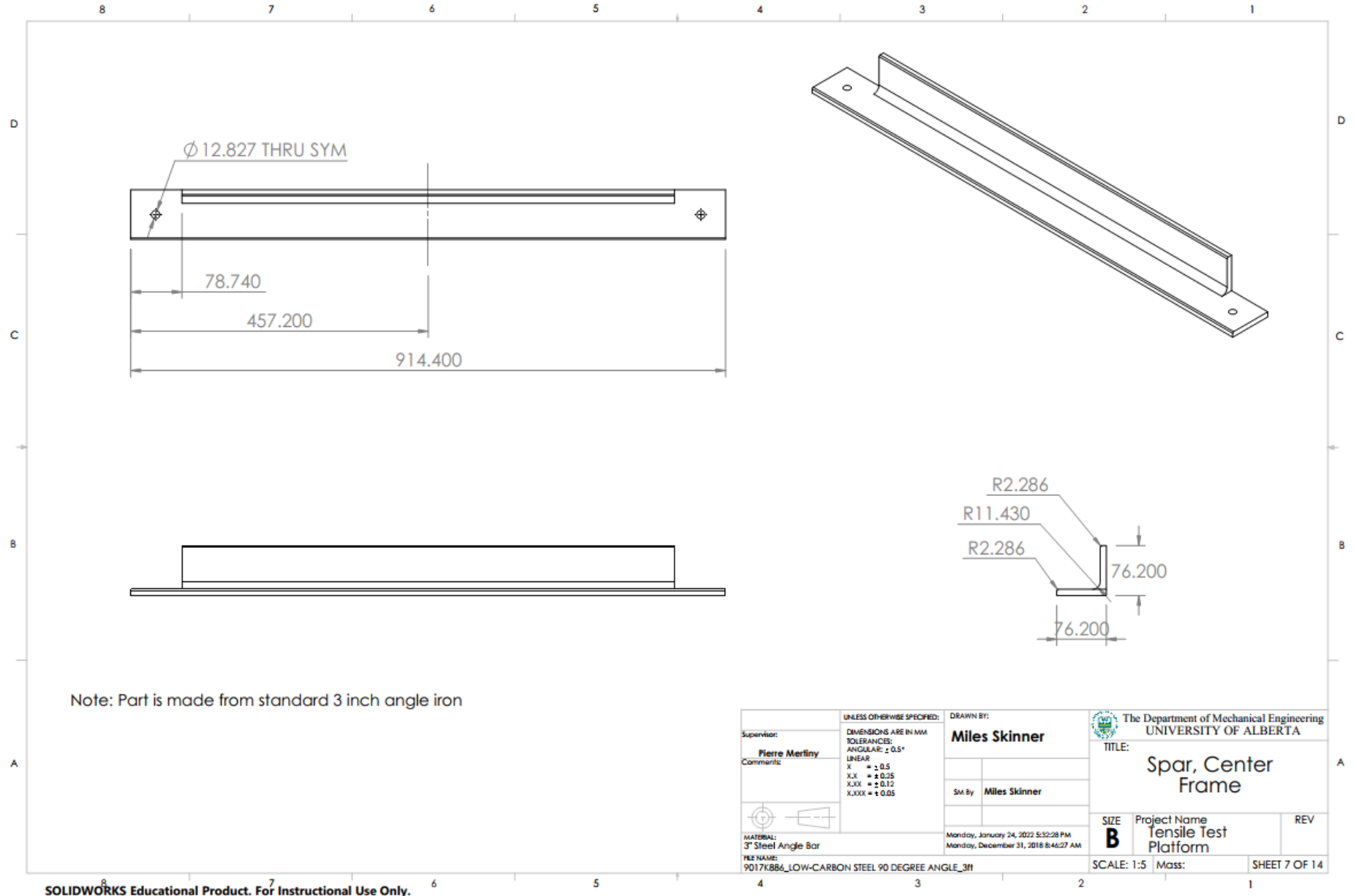
ITEM NO.	PART NUMBER	DESCRIPTION	QTY.
1	Weight	Steel Weights	1
2	Platform Length	2x4 wood bar	2
3	Platform width	2x4 wood bar	2
4	Lifting Eyebolt	Eye bolt with nut: #3016T23	4

Supervisor: <b>Pierre Merliny</b>		UNLESS OTHERWISE SPECIFIED: DIMENSIONS ARE IN MM TOLERANCES: ANGULAR: ± 0.5° LINEAR X = ± 0.5 XX = ± 0.25 XXX = ± 0.12 XXXX = ± 0.05	DRAWN BY: <b>Miles Skinner</b>		The Department of Mechanical Engineering UNIVERSITY OF ALBERTA TITLE: <b>Lift Platform</b>
Comments:			SM By <b>Miles Skinner</b>		
MATERIAL: Tensile Platform		Monday, January 24, 2022 5:32:27 PM Tuesday, August 4, 2020 1:55:31 PM		SIZE <b>B</b>	Project Name <b>Tensile Test Platform</b>
		SCALE: 1:10 Mass:		REV	SHEET 3 OF 14

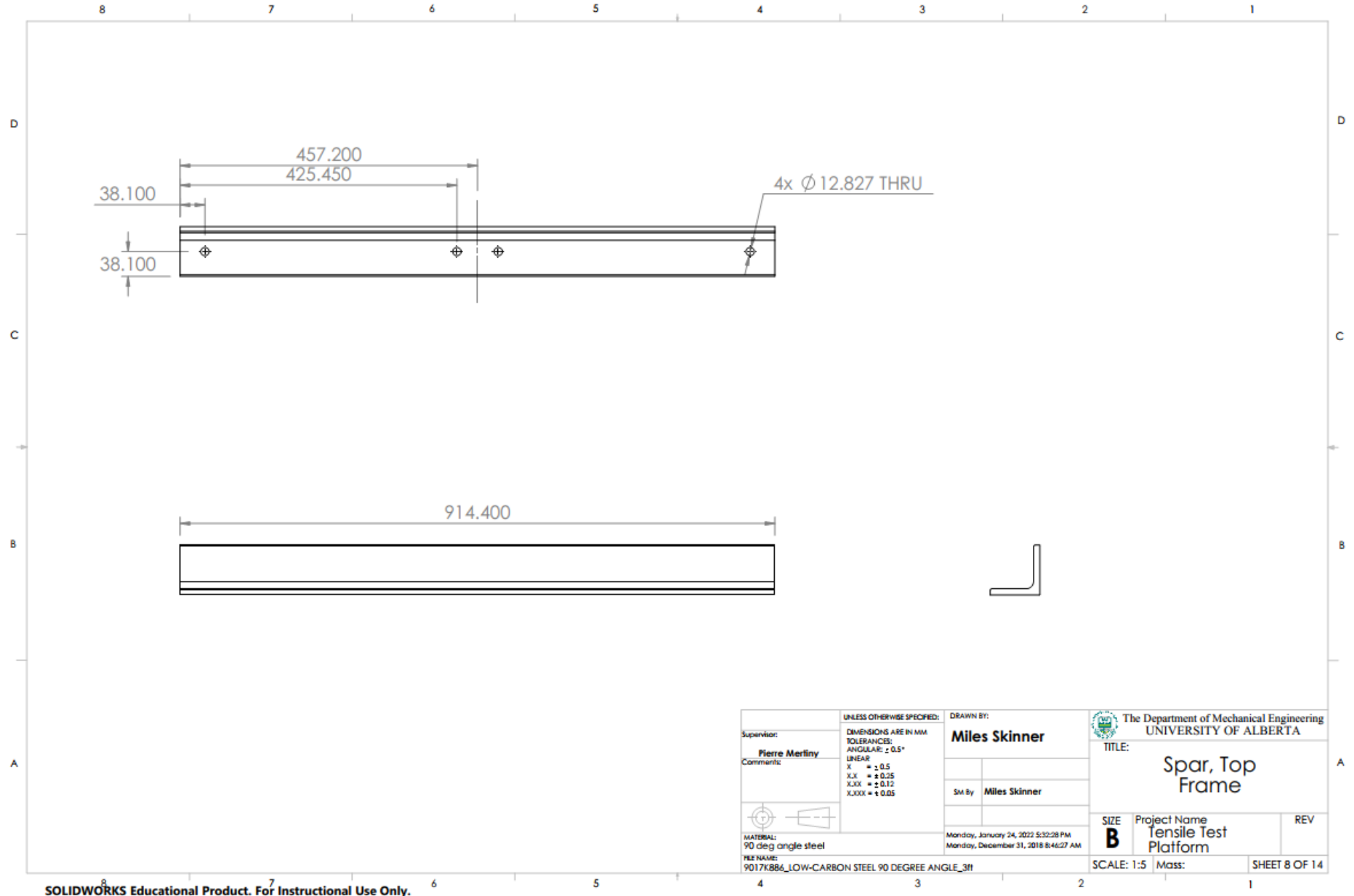


SOLIDWORKS Educational Product. For Instructional Use Only.



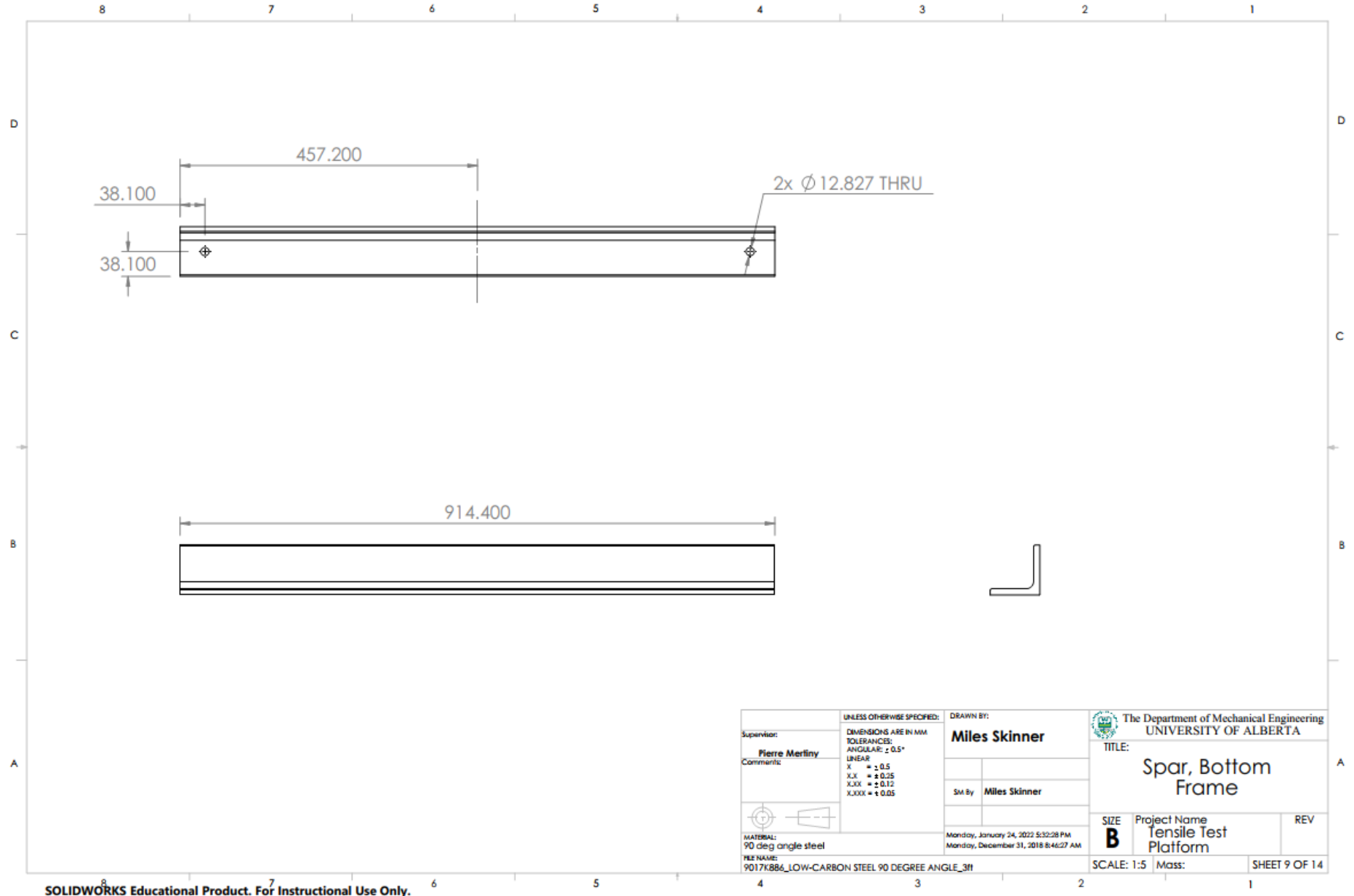


SOLIDWORKS Educational Product. For Instructional Use Only.

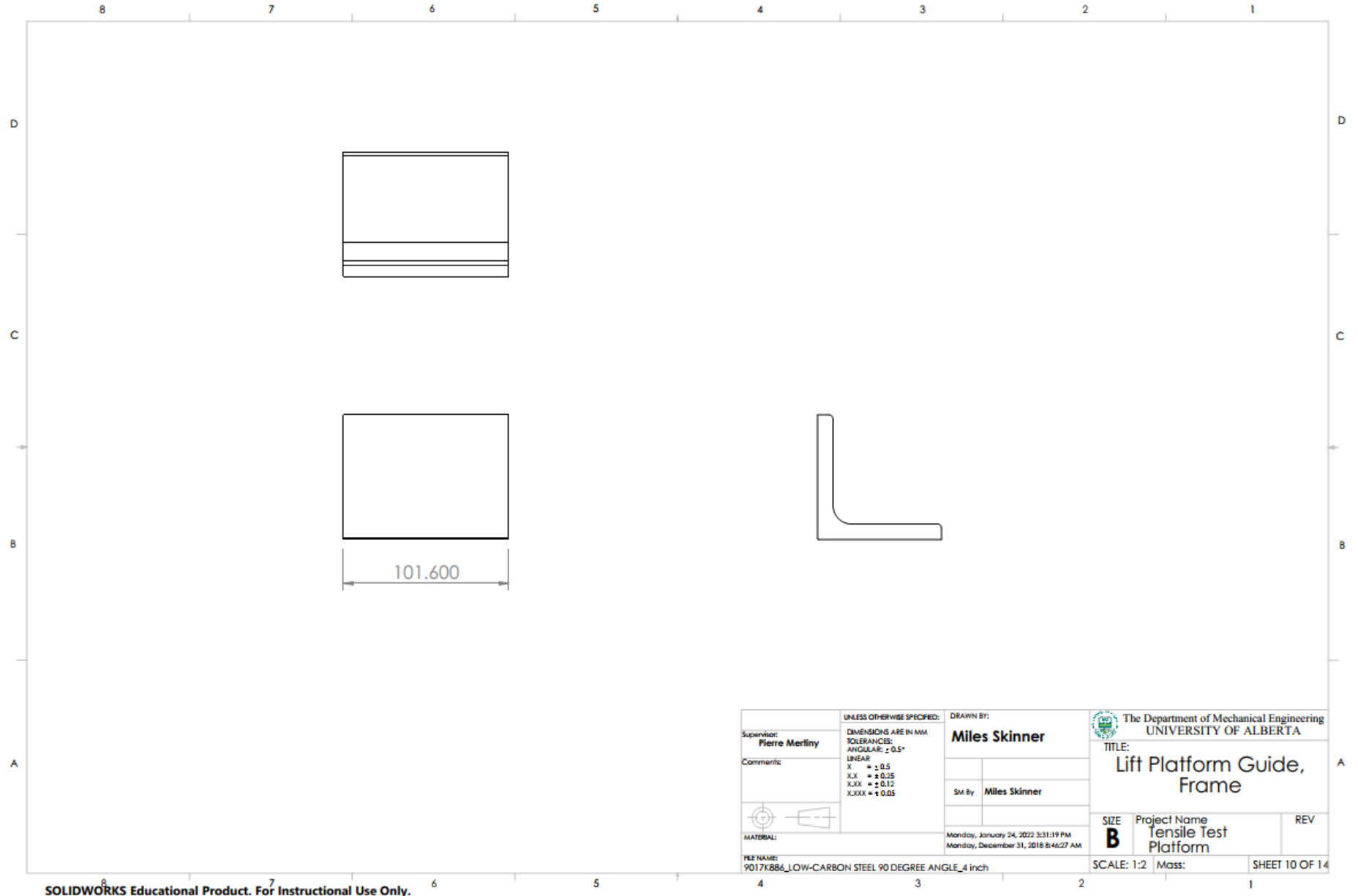


SOLIDWORKS Educational Product. For Instructional Use Only.

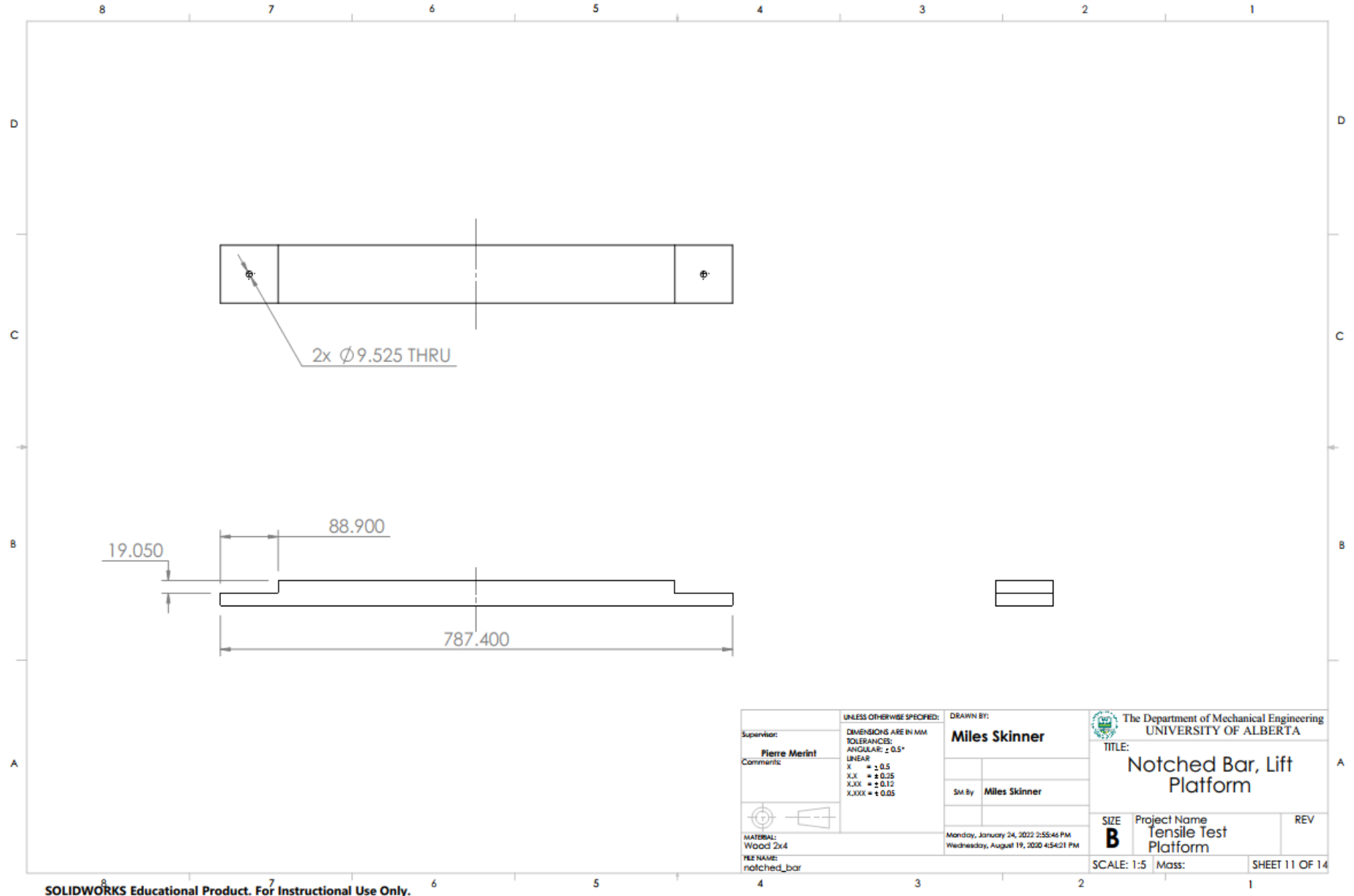
Supervisor: <b>Pierre Merligny</b>		UNLESS OTHERWISE SPECIFIED: DIMENSIONS ARE IN MM TOLERANCES: ANGULAR: $\pm 0.5^\circ$ LINEAR X = $\pm 0.5$ XX = $\pm 0.25$ XXX = $\pm 0.12$ XXXX = $\pm 0.05$		DRAWN BY: <b>Miles Skinner</b>		The Department of Mechanical Engineering UNIVERSITY OF ALBERTA	
Comments:				SM By <b>Miles Skinner</b>		TITLE: <b>Spar, Top Frame</b>	
MATERIAL: 90 deg angle steel		Monday, January 24, 2022 5:32:28 PM		Monday, December 31, 2018 8:46:27 AM		SIZE <b>B</b>	Project Name Tensile Test Platform
Reference: 9017K886_LOW-CARBON STEEL 90 DEGREE ANGLE_3fl		SCALE: 1:5		Mass:		REV	



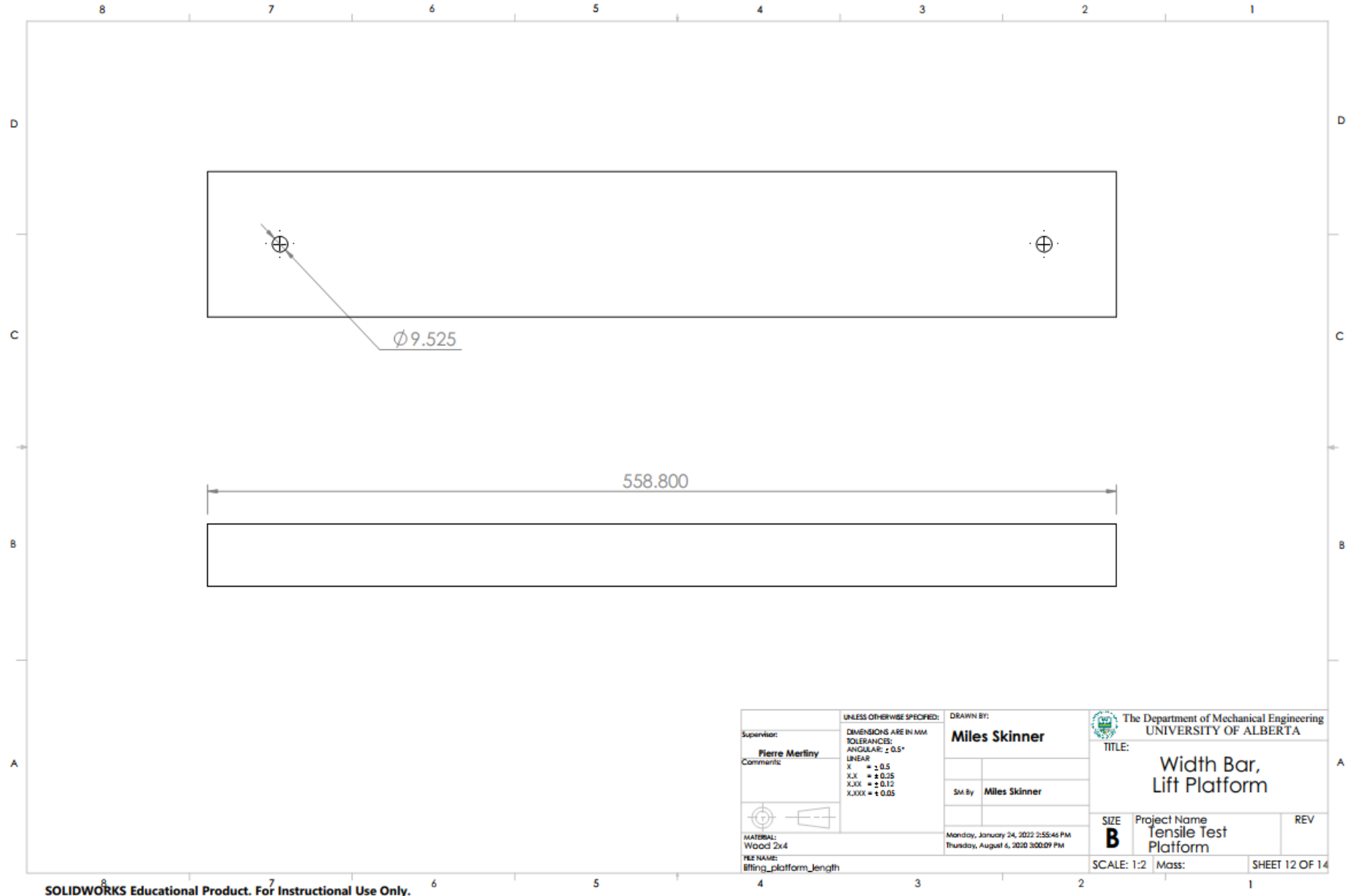
Supervisor: <b>Pierre Merligny</b>		UNLESS OTHERWISE SPECIFIED: DIMENSIONS ARE IN MM TOLERANCES: ANGULAR: ± 0.5° LINEAR X = ± 0.5 XX = ± 0.25 XXX = ± 0.12 XXXX = ± 0.05		DRAWN BY: <b>Miles Skinner</b>		The Department of Mechanical Engineering UNIVERSITY OF ALBERTA	
Comments:				SM By <b>Miles Skinner</b>		TITLE: <b>Spar, Bottom Frame</b>	
MATERIAL: 90 deg angle steel		DATE: Monday, January 24, 2022 5:32:28 PM		REV		SIZE <b>B</b>	
FILENAME: 9017K886_LOW-CARBON STEEL 90 DEGREE ANGLE_3fl		DATE: Monday, December 31, 2018 8:46:27 AM		SCALE: 1:5		Mass:	
				SHEET 9 OF 14			



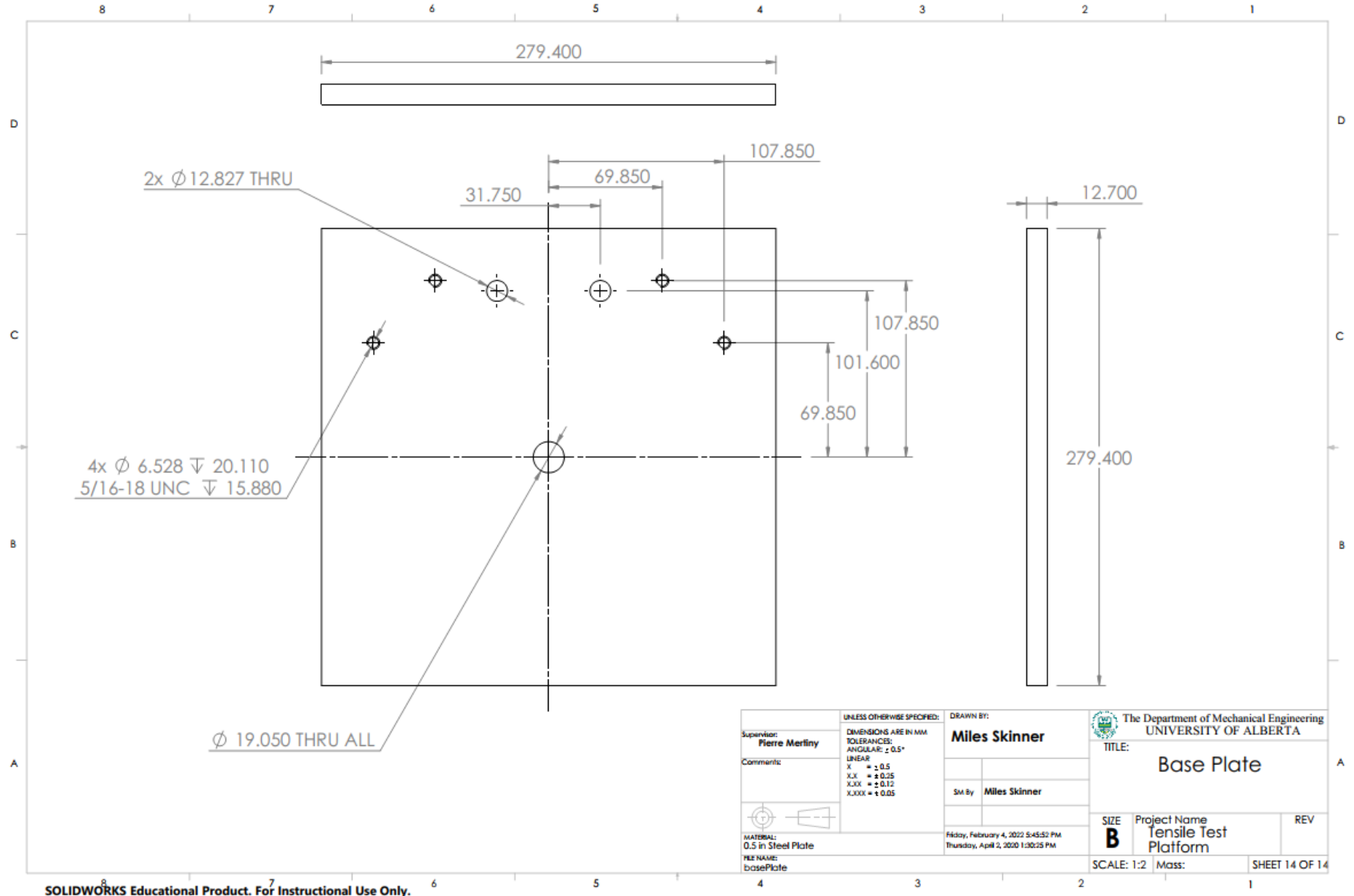
Supervisor: <b>Pierre Merliny</b>		UNLESS OTHERWISE SPECIFIED: DIMENSIONS ARE IN MM TOLERANCES: ANGULAR: ± 0.5°		DRAWN BY: <b>Miles Skinner</b>		The Department of Mechanical Engineering UNIVERSITY OF ALBERTA	
Comments:		LINEAR X = ± 0.5 X.X = ± 0.25 X.XX = ± 0.12 X.XXX = ± 0.05		SM By <b>Miles Skinner</b>		TITLE: <b>Lift Platform Guide, Frame</b>	
MATERIAL: 9017K886_LOW-CARBON STEEL 90 DEGREE ANGLE_4 inch		Monday, January 24, 2022 3:31:19 PM Monday, December 31, 2018 8:46:27 AM		SIZE <b>B</b>		Project Name <b>Tensile Test Platform</b>	
SCALE: 1:2		Mass:		REV		SHEET 10 OF 14	



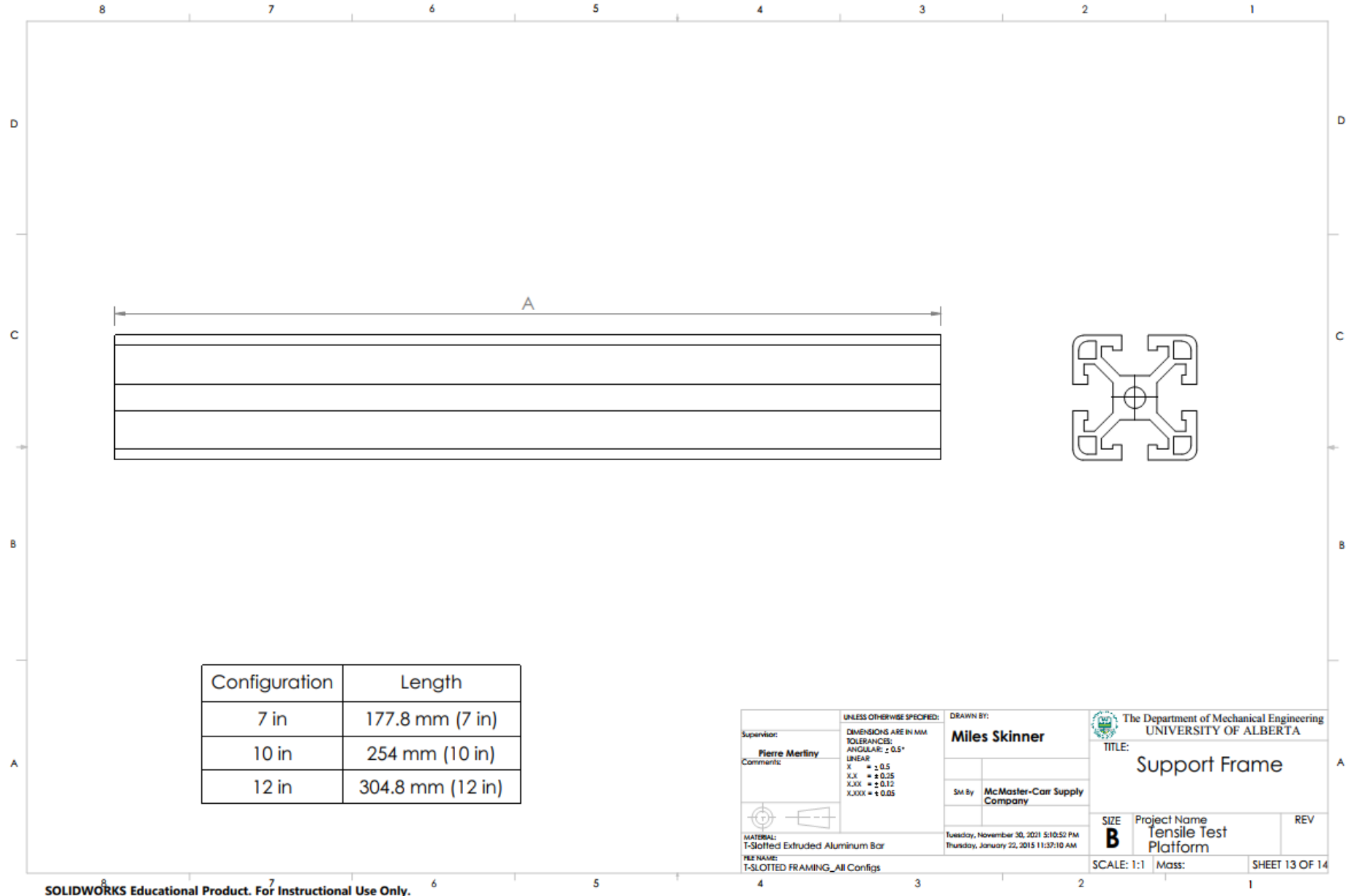
SOLIDWORKS Educational Product. For Instructional Use Only.



SOLIDWORKS Educational Product. For Instructional Use Only.



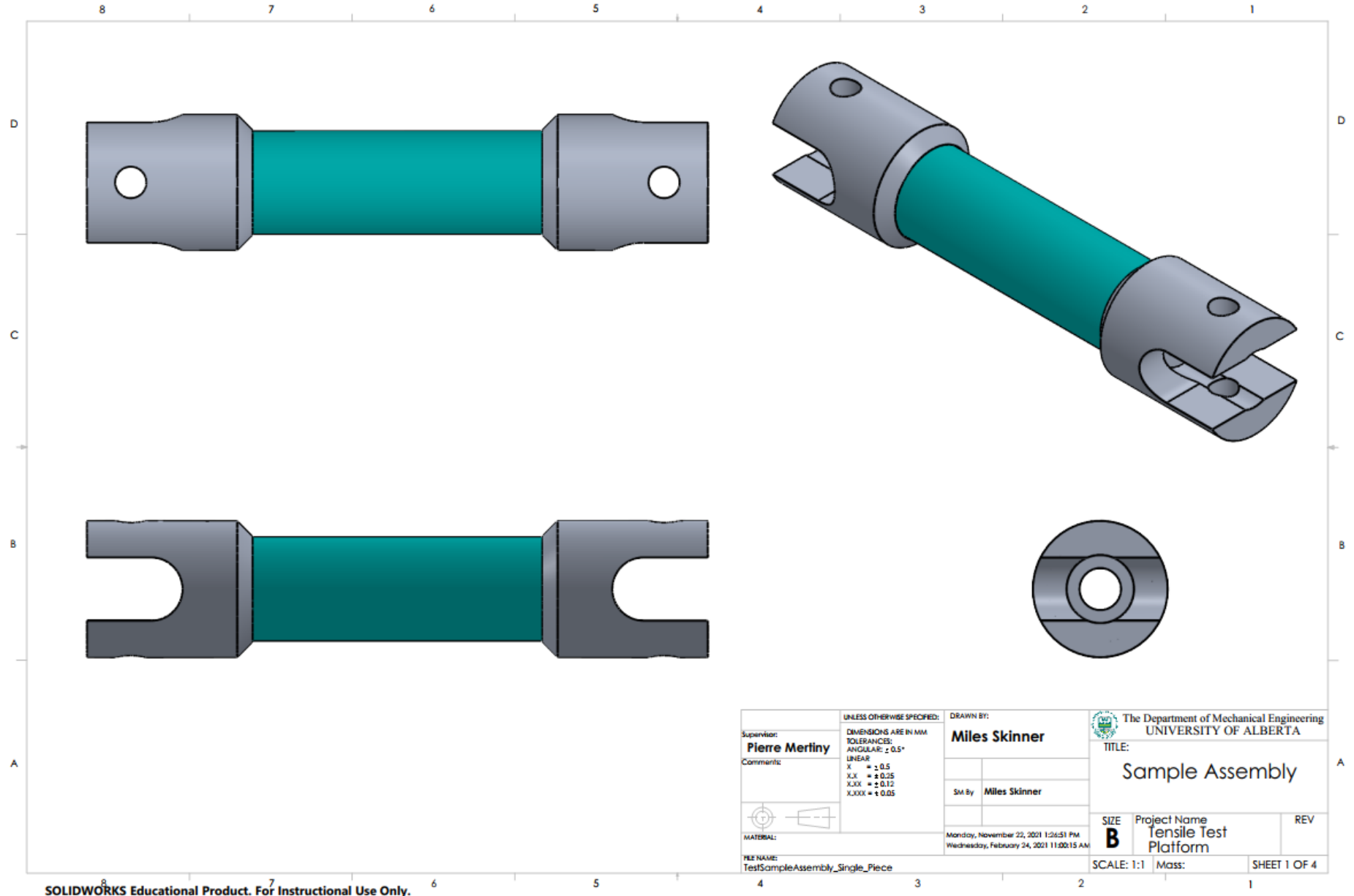
SOLIDWORKS Educational Product. For Instructional Use Only.



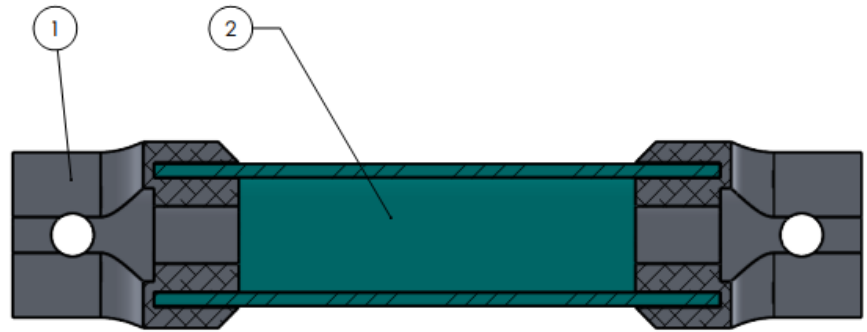
Configuration	Length
7 in	177.8 mm (7 in)
10 in	254 mm (10 in)
12 in	304.8 mm (12 in)

Supervisor: <b>Pierre Merliny</b> Comments:		UNLESS OTHERWISE SPECIFIED: DIMENSIONS ARE IN MM TOLERANCES: ANGULAR: ± 0.5° LINEAR X = ± 0.5 XX = ± 0.25 XXX = ± 0.12 XXXX = ± 0.05	DRAWN BY: <b>Miles Skinner</b>  SM By <b>McMaster-Carr Supply Company</b>	The Department of Mechanical Engineering UNIVERSITY OF ALBERTA TITLE: <b>Support Frame</b>
MATERIAL: T-Slotted Extruded Aluminum Bar FILE NAME: T-SLOTTED FRAMING_All Configs		Tuesday, November 30, 2011 5:10:53 PM Thursday, January 22, 2015 11:37:10 AM	SIZE <b>B</b>	Project Name <b>Tensile Test Platform</b> REV
SCALE: 1:1		Mass:	SHEET 13 OF 14	





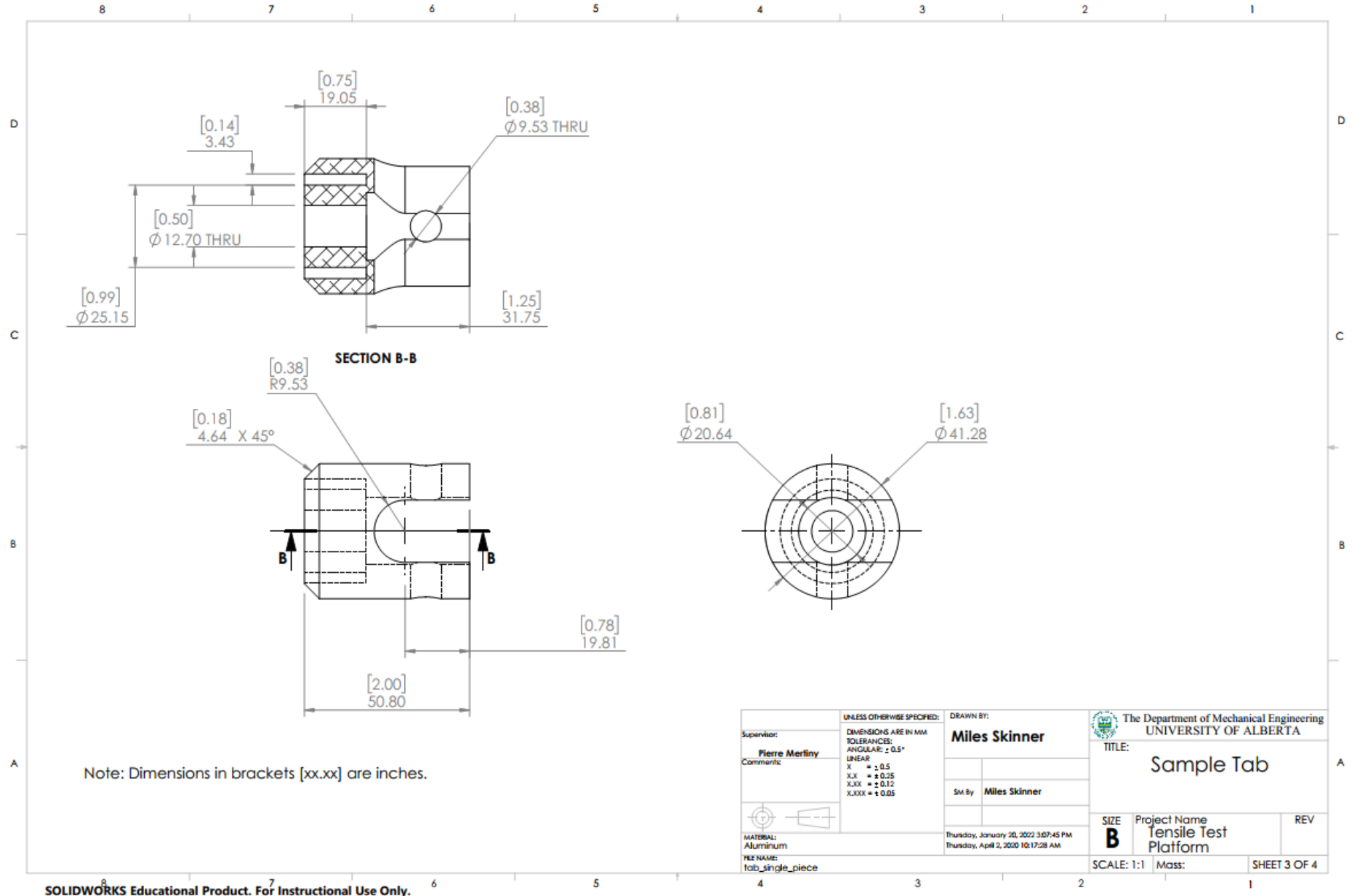
ITEM NO.	PART NUMBER	DESCRIPTION	QTY.
1	Top Config.	Top config. with stepped center hole	2
2	pipeSample	Composite pipe sample	1



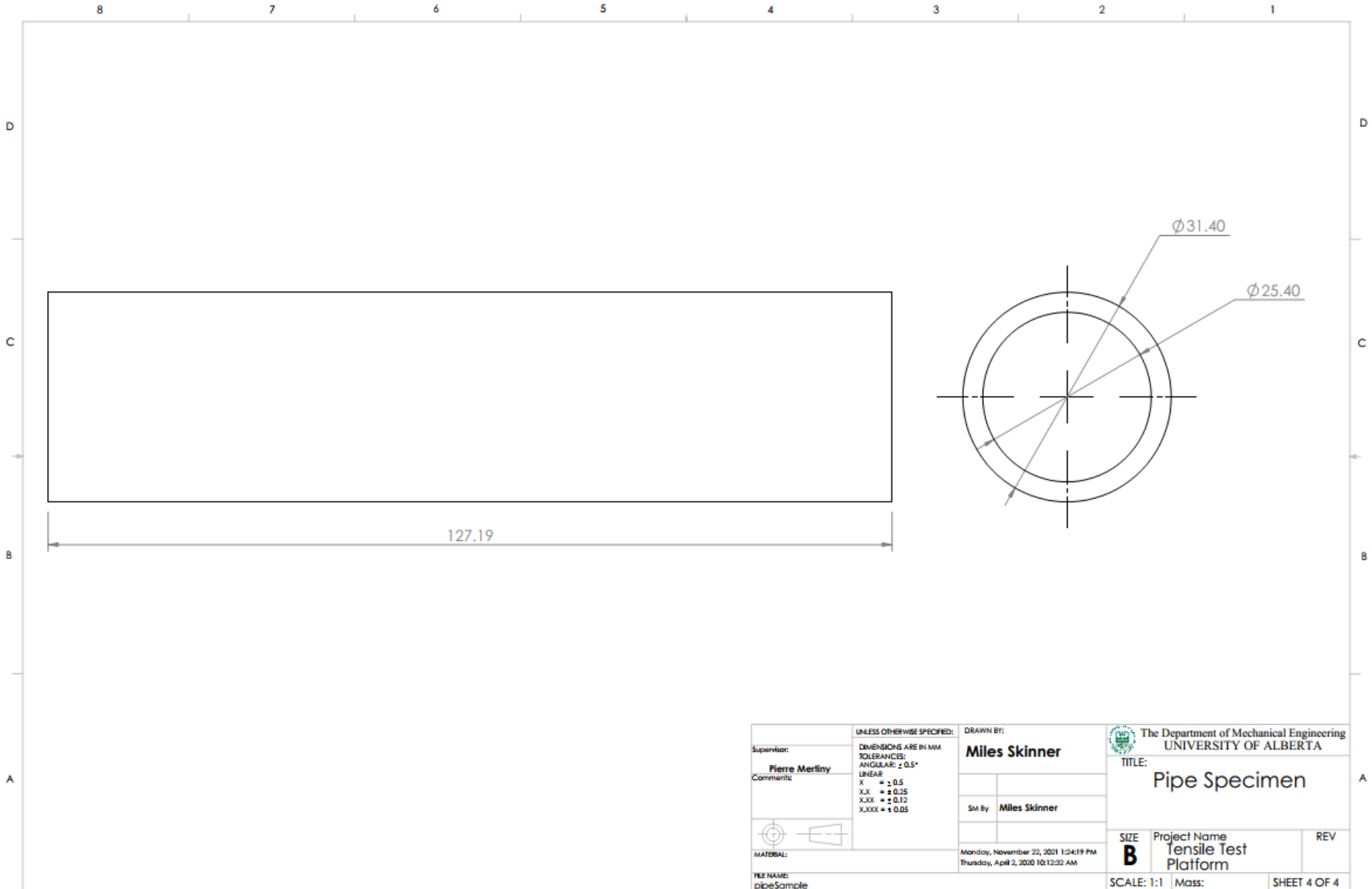
SECTION A-A



Supervisor: <b>Pierre Mertiny</b>		UNLESS OTHERWISE SPECIFIED: DIMENSIONS ARE IN MM TOLERANCES: ANGULAR: ± 0.5° LINEAR X = ± 0.5 X.X = ± 0.05 X.XX = ± 0.12 X.XXX = ± 0.05	DRAWN BY: <b>Miles Skinner</b>		The Department of Mechanical Engineering UNIVERSITY OF ALBERTA
Comments:			SM By: <b>Miles Skinner</b>		
MATERIAL: TestSampleAssembly_Single_Piece		Monday, November 22, 2021 1:26:51 PM Wednesday, February 24, 2021 11:00:15 AM		SIZE <b>B</b>	Project Name <b>Tensile Test Platform</b>
				SCALE: 1:1	REV SHEET 2 OF 4



Supervisor: <b>Pierre Merligny</b>		UNLESS OTHERWISE SPECIFIED: DIMENSIONS ARE IN MM TOLERANCES: ANGULAR: $\pm 0.5^\circ$ LINEAR X = $\pm 0.5$ XX = $\pm 0.25$ XXX = $\pm 0.12$ XXXX = $\pm 0.05$	DRAWN BY: <b>Miles Skinner</b>	The Department of Mechanical Engineering UNIVERSITY OF ALBERTA TITLE: <h1>Sample Tab</h1>
Comments:			SM By: <b>Miles Skinner</b>	
MATERIAL: ALUMINIUM REF NAME: tab_single_piece		Thursday, January 20, 2022 3:07:45 PM Thursday, April 2, 2020 10:17:28 AM	SCALE: 1:1	Mass: SHEET 3 OF 4



Supervisor: <b>Pierre Merliny</b>		UNLESS OTHERWISE SPECIFIED: DIMENSIONS ARE IN MM TOLERANCES: ANGULAR: $\pm 0.5^\circ$ LINEAR X = $\pm 0.5$ X.X = $\pm 0.05$ X.XX = $\pm 0.12$ X.XXX = $\pm 0.05$	DRAWN BY: <b>Miles Skinner</b>		The Department of Mechanical Engineering UNIVERSITY OF ALBERTA	
Comments:			SM By <b>Miles Skinner</b>		TITLE: <b>Pipe Specimen</b>	
MATERIAL: pipeSample		Monday, November 22, 2011 1:24:19 PM Thursday, April 2, 2010 10:12:32 AM		SIZE <b>B</b>	Project Name <b>Tensile Test Platform</b>	REV
SCALE: 1:1				Mass:	SHEET 4 OF 4	

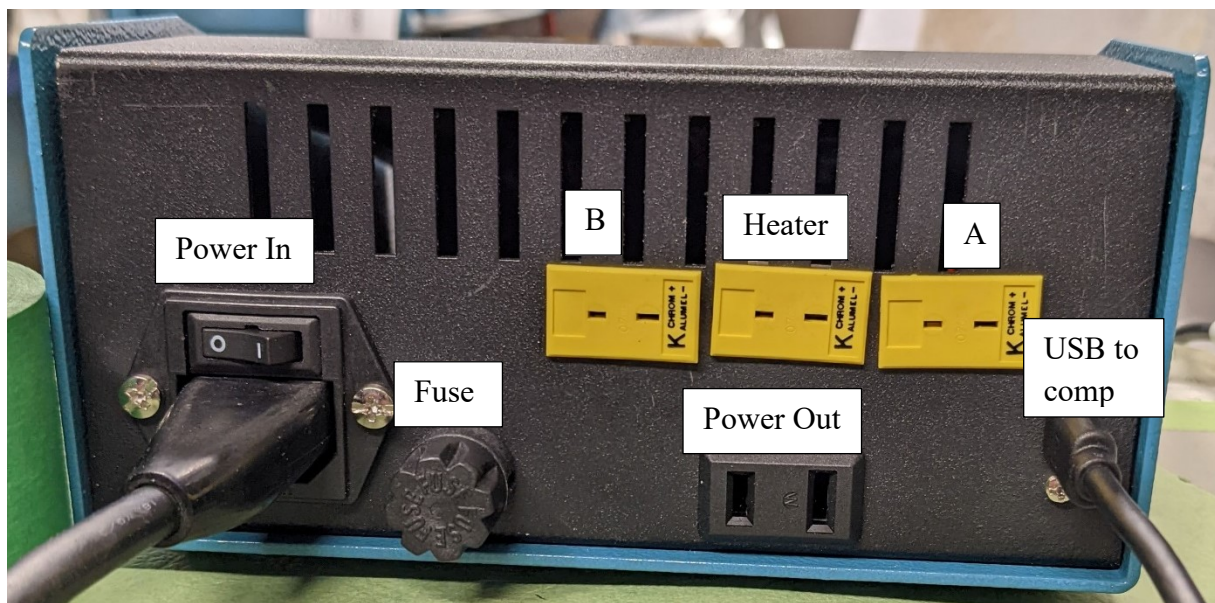
## Appendix III

### Heater Controller Operating Procedure

#### Procedure:

1. Connect all thermocouples to the controller. All thermocouples must be connected for the controller to function. Push the “Power In” switch to the off position.
2. Connect the “Power Out” cable to the heater using the appropriately colored connectors. Note the red and black coloring does not necessarily indicate negative and positive terminals.
3. Connect the USB cable, or reset the controller as needed.
4. Set up RealTerm as needed, see below.
5. Set the min/max for each thermocouple and the heater set temperature as needed.
6. Flip the “Power In” switch to the on position.
7. Begin data collection when ready.

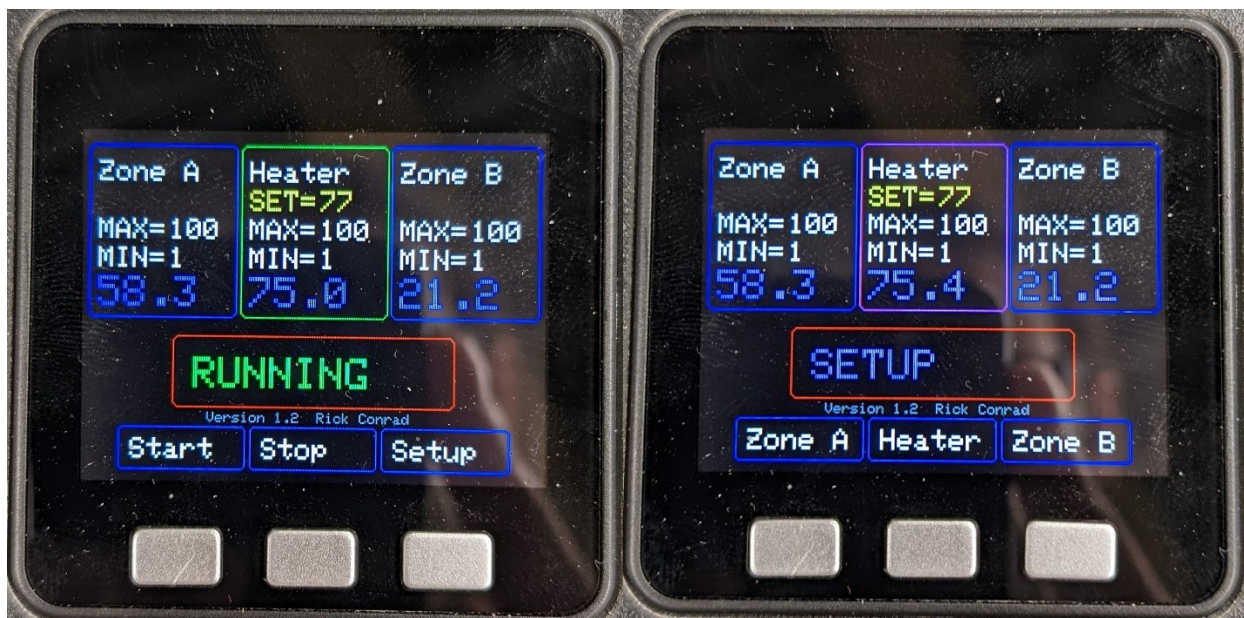
#### Controller Ports:



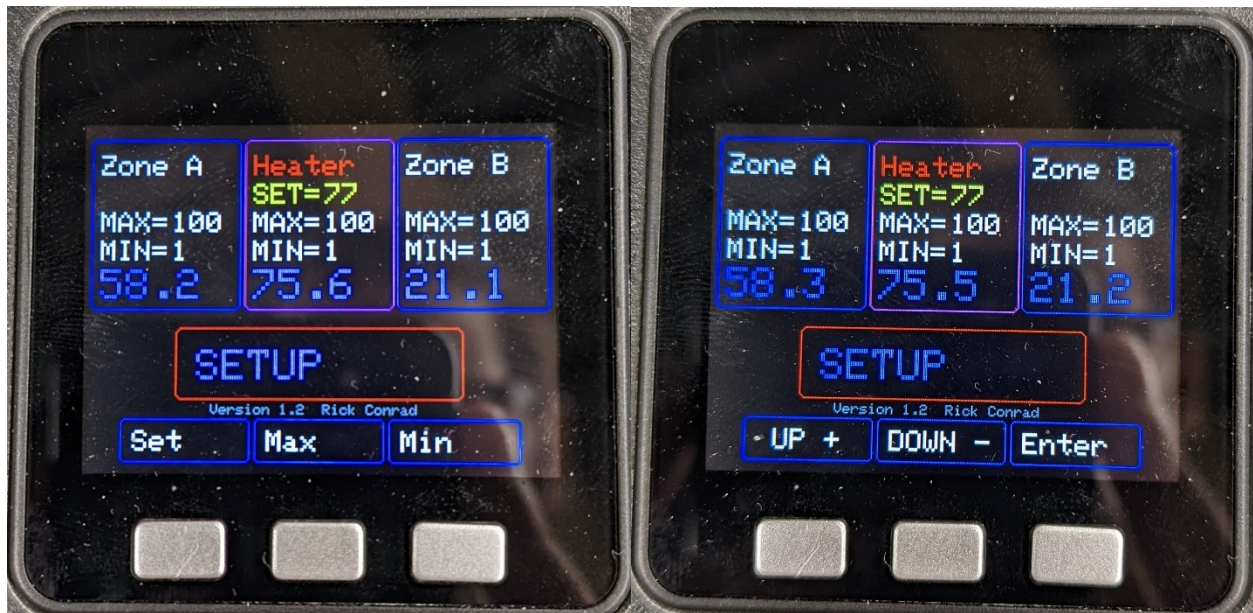
- Thermocouples: A, Heater, B
  - Only the “Heater” thermocouple is used for temperature input to the controller. Ports A and B are data collection only.
  - All thermocouples must be connected for the controller at all times.
- Power In: Power input from a wall outlet.
- Power Out: Power output to the heater controlled by the “Heater” thermocouple.
- USB-C: Communication and data connection to the computer.
- Fuse: It’s a fuse.

Controller Face:

- Red box indicates the current state of the controller: Ready, Running, Setup, Zone X, or Error
- Start/Stop button start and stop the heater control functions. Note, start/stop does not begin data collection only the heater control functions.
- Setup allows the user to set the min/max/set temperature for each thermocouple and the heater set temperature. Hold set up for 3 seconds to open the setup menu.
  - Choose the appropriate Zone to change.
  - Use Up/Down/Enter buttons as necessary to set the values for each temperature range. The figures below show the series of windows seen when changing the heater set temperature.





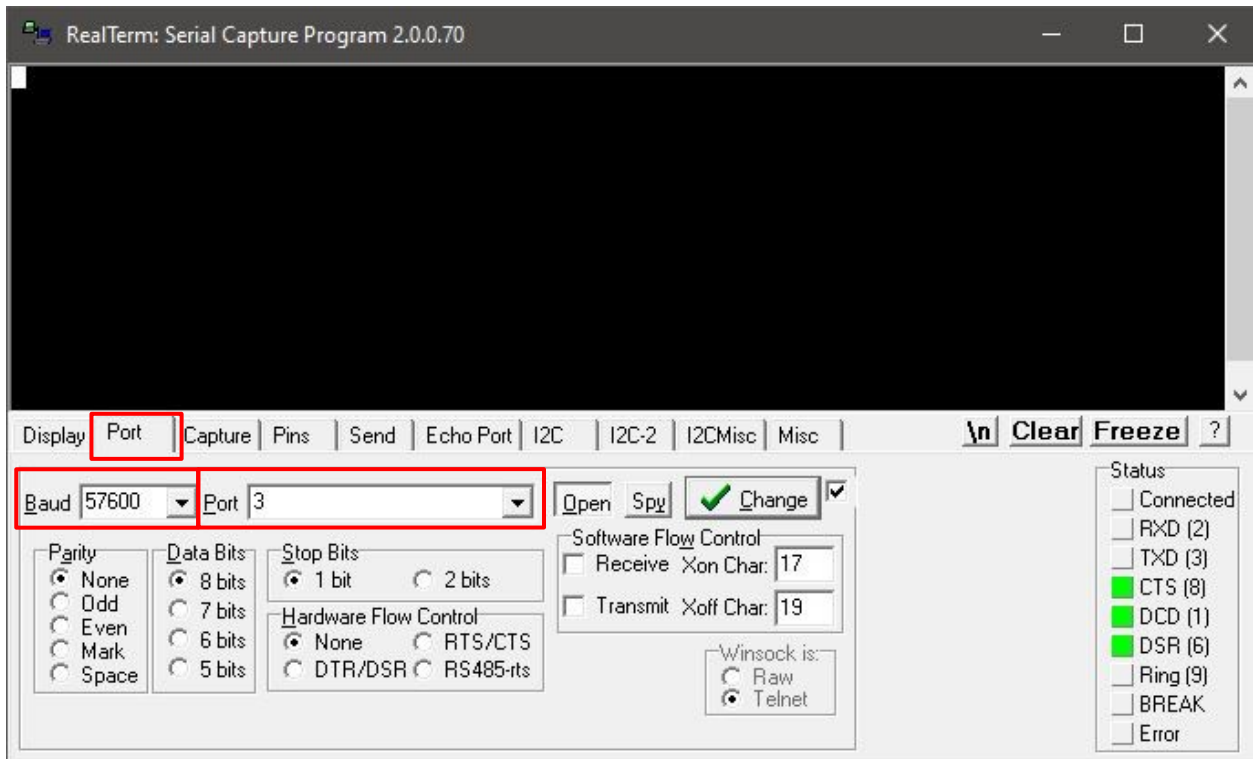


Program: RealTerm, Driver: CP210x SUB to UART Bridge

To begin collecting data check the settings in the following tabs:

Port:

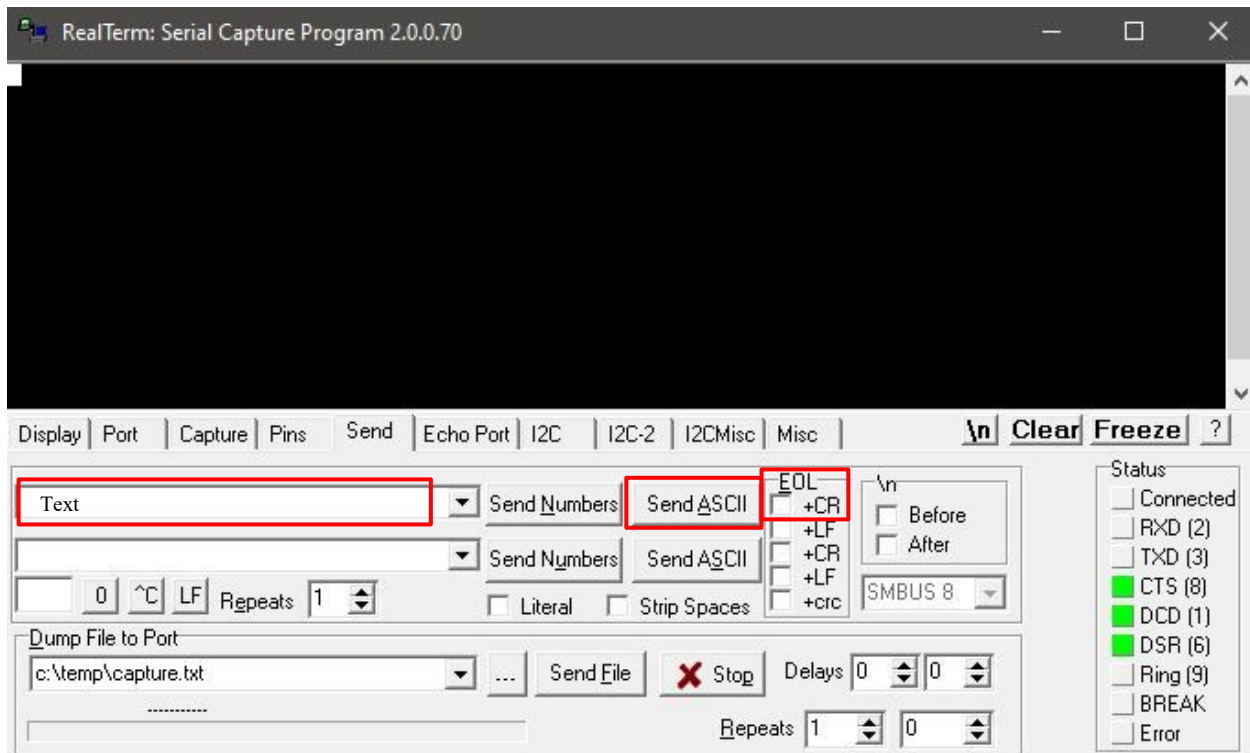
- Baud > 1120
- Port > 4 (Silabser0) [Note: The port can change if the computer or usb port is changed, the particular port can be found by checking the “connected devices” tool in Windows.
- Click “Change” when baud and port settings have been set.



Send:

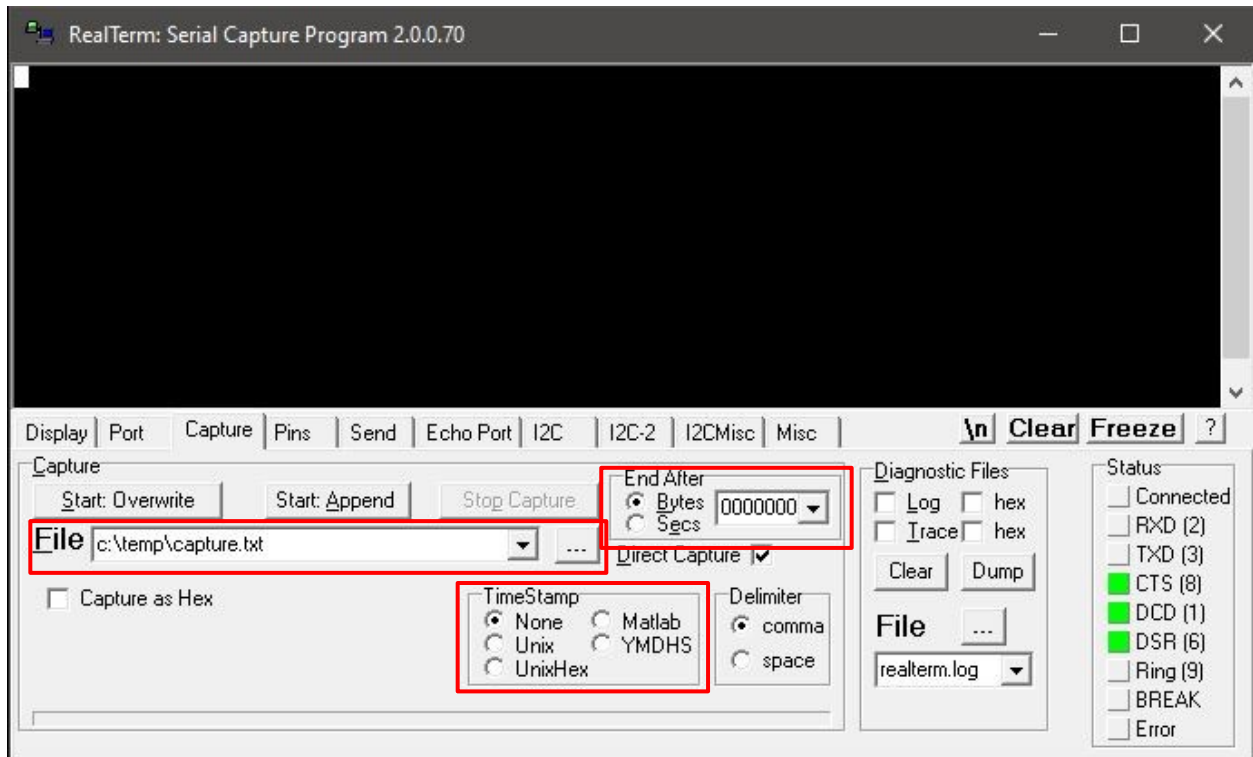
- Can communicate with the controller from this tab by entering commands into the text boxes at the top left.
- Must click the “+CR” check box under end of line (EOL).
- Click “Send ASCII” to send the commands.
- Most useful commands:
  - help: Displays a list of all possible commands.
  - all: Display current settings.
  - out x: Determines the sample rate were x is a numeric value in seconds, i.e. “out 1” samples temperature at 1 Hz. When x is 0 there is no data collection.
  - Reset: Reset the controller after a fault/error.



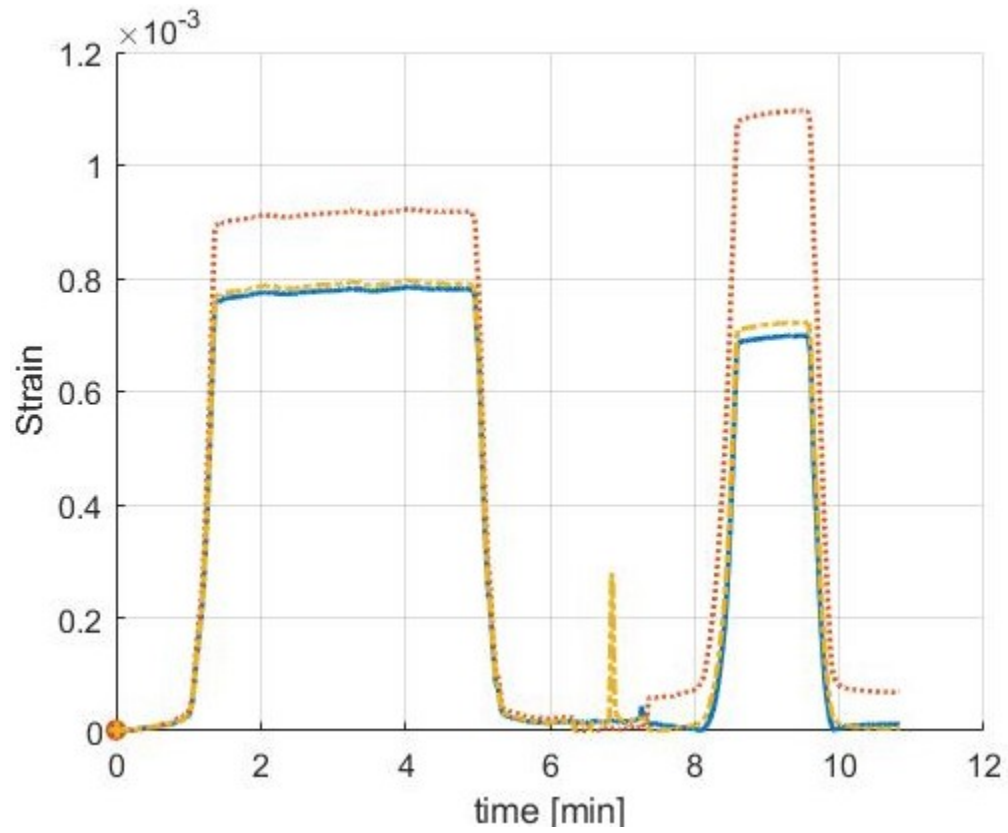


#### Capture:

- Output file name and location is set in the “file” box. Can select a save location with the “...” box right of the window.
- (Optional) Choose to stop data collection after a certain file size or time. To collect continuously choose 0.
- (Optional) Choose the type of time stamp to include in the data file.
- Begin data collection with either “Start: Overwrite” or “Start: Append”. If the file name does not exist in the selected folder the appropriate file will be created. (Note: Data output will not be seen on screen while collecting data.)



#### Appendix IV: Position Test



*Figure 8.1: Stress response from the same sample at constant temperature mounted in position A or position B. Position B is 180° rotation of position A.*